

Theoretical reconstruction of photoelectron spectra and its application to ionic liquids



TECHNISCHE UNIVERSITÄT
ILMENAU

Arbeit zur Erlangung des Grades
Doctor rerum naturalium (Dr. rer. nat.)
vorgelegt von

Dipl.-Ing. Markus Reinmöller
(geboren am 16.06.1984 in Suhl)

an der
Fakultät für Mathematik und Naturwissenschaften
der
Technischen Universität Ilmenau

Gutachter:

Priv.-Doz. Dr. rer. nat. habil. Wichard J. D. Beenken, TU Ilmenau

Univ.-Prof. Dr. rer. nat. habil. Stefan Krischok, TU Ilmenau

Univ.-Prof. Dr. rer. nat. habil. Hans-Peter Steinrück, FAU Erlangen-Nürnberg

Tag der Einreichung: 16.10.2015

Tag der wissenschaftlichen Aussprache: 01.03.2016

urn:nbn:de:gbv:ilm1-2016000114

To Alexander.

You are the most wonderful son that I could ever imagine, although you have enhanced our lives just since a few months.

Abstract

Ionic liquids are a special class of salts that are liquid at temperatures below 100 °C, which provide superior and tunable physicochemical properties, resulting in a broad range of applications. A suitable reconstruction method for X-ray and ultraviolet photoelectron spectra (XPS, UPS) for these molecular systems is developed, which incorporated the photoionization cross sections of atomic orbitals as well as a Gelius intensity approach. This technique is based on quantum-chemical calculations of the respective molecular systems, which are executed by density functional theory (DFT) together with the basis set 6-31G** and hybrid-functional B3-LYP. For this purpose, (most) simple charge- and spin-balanced systems for the investigated ionic liquids, such as ion pairs and small clusters, are utilized for the subsequent reconstruction. The calculated binding energies for the spectra of neat ionic liquids are adapted to the experimental ones by an appropriate rescaling procedure using three parameters, while for the clusters with additional atoms or molecules a fourth parameter is introduced.

This method is applied for the reconstruction of core level and valence band spectra of ionic liquids, which have comprised sets of pure imidazolium- and pyrrolidinium-based ionic liquids as well as those with incorporated metal atoms and with (alkali) metals evaporated onto the liquid. The reconstructed core level spectra have enabled novel insights into the chemical environment, interactions between the ions, and partial charge effects within ionic liquids. Decent hints for the radiation-induced degradation mechanisms of ionic liquids are attained by this method. In addition, reconstructed valence band spectra are compared to experimental ones and have provided a quantitative analysis of the intertwined contributions of the contained ions and elements for the first time. The arrangement and orientation of the ions and selected parts of the ions at the surface and their preferred interaction is analyzed with the aid of reconstructed valence band spectra.

Kurzfassung

Ionische Flüssigkeiten sind eine besondere Gruppe von Salzen, welche für Temperaturen unterhalb von 100 °C in flüssigem Aggregatzustand vorliegen und deren herausragende, einstellbare Eigenschaften zu einem breiten Anwendungsfeld führen. In der vorliegenden Arbeit wurde eine geeignete Rekonstruktionsmethode für die Röntgen- und Ultraviolett-Photoelektronenspektroskopie (XPS, UPS) von molekularen Systemen, zu welchen auch diese Flüssigkeiten zählen, entwickelt. Hierfür werden Atomorbital-spezifische Streuquerschnitte mit einer Intensitätsnäherung nach Gelius kombiniert. Diese Rekonstruktionsmethode baut auf quantenchemischen Berechnungen mittels Dichtefunktionaltheorie (DFT) unter Verwendung des Basissatzes 6-31G** und Hybrid-Funktionals B3-LYP auf. Zu diesem Zweck erfolgte die Berechnung von jeweils kleinsten bzw. kleinen ladungs- und spinkompensierten, molekularen Systemen für die anschließende Rekonstruktion. Die berechneten Bindungsenergien für die reinen ionischen Flüssigkeiten werden durch eine Reskalierung mit drei Parametern an die der experimentellen Spektren angepasst. Für jene Flüssigkeiten mit zusätzlichen Atomen oder Molekülen wird ein vierter Parameter eingeführt.

Diese Methode findet für die Rekonstruktion von Rumpfniveau- und Valenzbandspektren von ionischen Flüssigkeiten Anwendung. Hierbei werden sowohl reine Imidazolium- und Pyrrolidinium-basierte ionische Flüssigkeiten als auch solche mit eingebauten Metallatomen oder aufgedampften Metall- bzw. Alkalimetallatomen untersucht. Die rekonstruierten Rumpfniveauspektren haben neuartige Einblicke in die chemische Umgebung, Wechselwirkungen zwischen den Ionen und Partialladungseffekte offenbart. Für die strahlungsinduzierte Degradation von ionischen Flüssigkeiten konnten deutliche Hinweise auf die zugrundeliegenden Mechanismen gewonnen werden. Der Vergleich zwischen experimentellen und rekonstruierten Spektren liefert erstmalig eine quantitative Bestimmung der ineinander verflochtenen Beiträge der einzelnen Ionen und der Elemente im Valenzband. Weiterhin lassen sich die Anordnung und Orientierung der Ionen und ihrer ausgewählten Bestandteile an der Oberfläche sowie deren bevorzugte Wechselwirkungen mittels der rekonstruierten Valenzbandspektren identifizieren.

Contents

1	Introduction	8
1.1	Ionic liquids and their impact on science and technology	8
1.2	Ionic liquids and surface science	9
1.3	Theoretical calculations of ionic liquids	11
1.4	Theoretical analyses of PES and MIES spectra of ionic liquids . .	13
1.5	Motivation and scope of the present thesis	14
I	Methodical approaches	15
2	Reconstruction of photoelectron spectra	15
2.1	Principle of photoelectron spectroscopy	15
2.2	Details of the experimental techniques	17
2.2.1	XPS and UPS spectroscopy	17
2.2.2	MIES spectroscopy	18
2.3	Relationship between experiment and theory	20
2.4	The reconstruction procedure of photoelectron spectra	21
3	Calculation details, partial charge analysis, and rescaling of calculated binding energies	28
3.1	Details of the quantum-chemical calculations	28
3.2	Natural bond orbital (NBO) partial charge analysis	29
3.3	Stepwise rescaling procedure for the calculated binding energies .	30
II	Results of the reconstruction of core level spectra	36
4	Core level spectra of neat and copper-containing ionic liquids	37
4.1	Core level spectra of imidazolium-based ionic liquids	37
4.2	Core level spectra of pyrrolidinium-based ionic liquids	42
4.2.1	N1s and C1s core level spectra	43
4.2.2	Influence of partial charges and geometrical distances on the binding energy order	55
4.3	Copper-containing ionic liquids	60
4.4	Chapter summary	61
5	Analysis of the degradation of [EMIm]Tf₂N on the atomic scale	64
5.1	Cation degradation	67
5.1.1	Alkyl chain degradation	67
5.1.2	Hydrogen degradation	69
5.2	Anion degradation	73
5.2.1	Fluorine degradation	73
5.2.2	Oxygen degradation	77
5.2.3	Degradation of larger groups	79
5.3	Chapter summary	82

III	Results of the reconstruction of valence band spectra of neat ionic liquids	83
6	Valence band structure of [XMIIm]Tf₂N	83
6.1	Effect of ion pair geometry and anion conformer on the valence band structure of [EMIm]Tf ₂ N	84
6.2	Reconstructed XPS and UPS valence band spectra of [XMIIm]Tf ₂ N	95
6.2.1	XPS and UPS valence band spectra	95
6.2.2	Arrangement of the ions at the surface of [XMIIm]Tf ₂ N . .	103
6.3	Chapter summary	106
7	Valence band structure of [XMIIm]Cl	107
7.1	Reconstructed XPS and UPS valence band spectra	107
7.2	Influence of the geometry of the ion pair and the alkyl chain on the reconstructed valence band spectra	111
7.2.1	Influence of pair geometry of [EMIm]Cl	111
7.2.2	Effect of alkyl chain geometry of [OMIm]Cl	117
7.3	Chapter summary	121
8	Valence band structure of pyrrolidinium-based ionic liquids of [XMPyrr]Tf₂N - in comparison to their imidazolium-based analog	122
8.1	Reconstructed XPS and UPS (He II) valence band spectra	122
8.2	Chapter summary: a comparison to their imidazolium-based analogs	128
IV	Results of the reconstruction of valence band spectra of ionic liquids with metals and alkali metals	129
9	Interaction of ionic liquids with evaporated metal and alkali metal atoms and the resulting valence band spectra	130
9.1	Evaporation of copper onto [EMIm]Tf ₂ N	131
9.2	Evaporation of lithium onto [EMIm]Tf ₂ N	134
9.3	Evaporation of potassium onto [EMIm]Tf ₂ N	136
9.4	Chapter summary	137
10	Valence band spectra of copper-containing ionic liquids	140
10.1	Reconstructed valence band spectra	140
10.1.1	XPS valence band spectra	140
10.1.2	UPS (He II) spectra	142
10.2	Effect of photoionization cross sections and their calculation methods on the valence band spectra	147
10.3	Effect of sample impurities on the valence band spectra	149
10.4	Chapter summary	152

V	Summary and outlook	154
11	Summary	154
12	Outlook	156

1 Introduction

1.1 Ionic liquids and their impact on science and technology

Ionic liquids, as this class of materials should come to be called, were defined by P. Walden [1] about 100 years ago: he stated that these substances possess a melting point below 100 °C and behave like melts of inorganic salts at much higher temperatures. Since these findings, a long time has elapsed until ionic liquids gained noticeable interest. This period began around the turn of the millennium [2, 3]. From the year 2000 on, the number of publications and patents per year has risen exponentially [2]. Ionic liquids have gotten into the focus, because they feature superior chemical and physical properties: liquid state over a broad temperature range, electrical conductivity, large electrochemical window, temperature stability, non-flammability, high solubility for other species, and a very low vapor pressure, to mention only a few [2, 3]. All of the stated and further properties, such as melting point, density, viscosity, heat capacity etc., are tunable within certain ranges by alteration of one or both of the ions (upper and lower limits as well as typical ranges are tabulated in ref. [4]). In Figure 1, a three-dimensional representation of ionic liquids by interaction between anion and cation as well as the variability of their properties by chosen lengths and functionality of the alkyl chain is illustrated (after ref. [5]). The number of suitable combinations of ions is roughly estimated by the order of 10^6 , which can be further elevated to 10^{12} for binary mixtures, and finally could even extend to a theoretically possible number of 10^{18} [2, 6, 7, 8]. All extraordinary properties of these substances and their versatility have enabled a broad spectrum of applications that ranges from chemical reactions and their design (synthesis, catalysis, dissolution, separation, generation of nanoparticles, multiphase reactions), green chemistry (gas storage, purification, conversion of energy), electrochemistry (metal plating, battery electrolytes, fuel cells, solar cells), surface modification (lubricants, coatings), physical chemistry (thermodynamic processes, mixtures), biological and medical applications (cellulose solution, drug fabrication), and a plenty of more [2, 3, 4, 8, 9, 10]. As a result of this enormous number of possible combinations, the playing field for further applications and related studies for chemists, physicists, biologists, and engineers is vast and has yet to see its limitations.

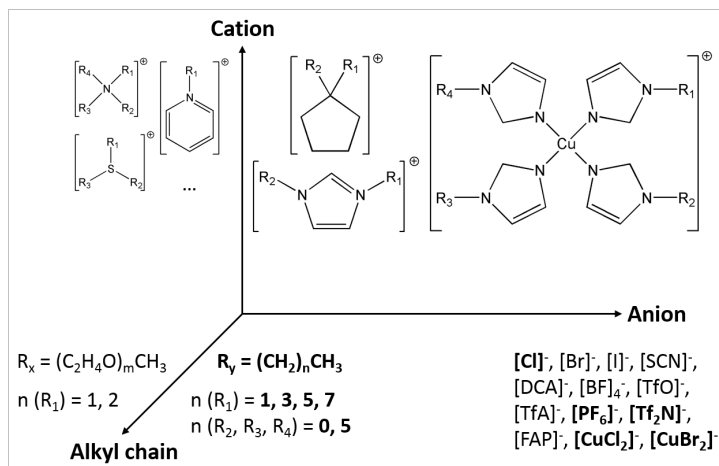


Figure 1: Three-dimensional representation of the composition of ionic liquids by choice of cation and anion with the opportunity of an adjustment of certain properties by variation of the length and functionality of the alkyl chains. All largely displayed cations or bold styled anions and respective cation alkyl chains are investigated in the present thesis. (Referring to the illustration in A. Stark, Top. Curr. Chem. 290 (2009) 41-81, page 44 [5])

1.2 Ionic liquids and surface science

Ionic liquids gained interest in the field of surface science due to the targeted applications in catalysis, electrochemistry, surface modifications etc. (cf. refs. [2, 3, 4, 8, 9, 10]). As a result, a comprehensive understanding of ionic liquid surfaces and interfaces is required. Nevertheless, classical surface science techniques are not applicable to liquids and these substances are in general liquid at room-temperature. However, one of the ionic liquids' superior properties - the very low vapor pressure - enabled the utilization of ultra-high vacuum-based surface science techniques with typical pressures $< 10^{-9}$ mbar [11]. Consequently, ionic liquids can be denoted as exceptional liquid materials, which can be studied by a whole set of well-known surface science techniques [4, 11, 12, 13].

A first group of techniques encompassed (photo-)electron emission spectroscopy using appropriate energy sources, i.e. photons (PES) and metastable atoms (MIES). The methods of X-ray photoelectron spectroscopy (XPS) and angular-resolved X-ray photoelectron spectroscopy (ARXPS) [4, 14, 15, 16, 17, 18, 19, 20, 21, 22, 23, 24, 25, 26, 27, 28, 29, 30, 31, 32, 33, 34, 35, 36, 37, 38], ultraviolet photoelectron spectroscopy (UPS) [18, 23, 28, 29, 37, 39, 40, 41],

and metastable induced electron spectroscopy (MIES) [18, 23, 28, 29, 37, 39] are part of this first set. A second group of methods has comprised of the vibrational analysis of surfaces, which may be accomplished by high-resolution electron energy loss spectroscopy (HREELS) [23] as well as sum frequency generation (SFG) [12, 42, 43, 44, 45, 46, 47, 48]. The third group consists of a set of scattering techniques, which involved X-ray and neutron reflectometry [46, 49, 50] as well as grazing-incidence X-ray reflectometry [51], direct recoil spectroscopy (DRS) [52, 53], neutral impact collision ion scattering spectroscopy (NICISS) [54, 55, 56], time-of-flight secondary ion mass spectroscopy (TOF-SIMS) [16, 57, 58, 59, 60], low energy ion scattering (LEIS) [25, 61], and high-resolution Rutherford backscattering spectroscopy (HRBS) [62, 63]. Ultra-high vacuum conditions are not essential to some of the mentioned methods, i.e. sum frequency generation (SFG) [12, 42, 43, 44, 45, 46, 47, 48], neutral impact collision ion scattering spectroscopy (NICISS) [54, 55, 56], and other techniques, such as surface tension measurements [47, 48, 64, 65]. Besides these studies, classical scanning probe microscopy techniques, like atomic force microscopy (AFM) and scanning tunneling microscopy (STM), have been employed to interfaces between ionic liquids and other materials, inter alia electrodes [66, 67] or pure and oxidic materials [10, 68, 69]. In contrast to the bulk case, in all cases a certain self-assembly of the ions near the interface has occurred due to interactions between solid and ionic liquid (for further details see ref. [10]). The combination of all of these techniques provided a complete picture of the ionic liquid surface (the respective interface to vacuum/gas), since each method typically only covers one or a few aspects.

These measurements consistently revealed that ionic liquid surfaces are in general well ordered, contrasting to their homogeneously distributed bulk. Still, one fundamental question for all surface science studies on ionic liquids remains: in which special manner is the surface of the respective ionic liquid arranged? Several imaginable arrangements of the ions are illustrated in Figure 2. Thus, both the presence of the ions as well as their preferred orientation and relative depth have to be identified for a sufficient picture of an ionic liquid surface. Since this is recognized as intricate for a single experimental technique, a suitable solution may be intended by a combination of these experimental data with the results of theoretical calculations.

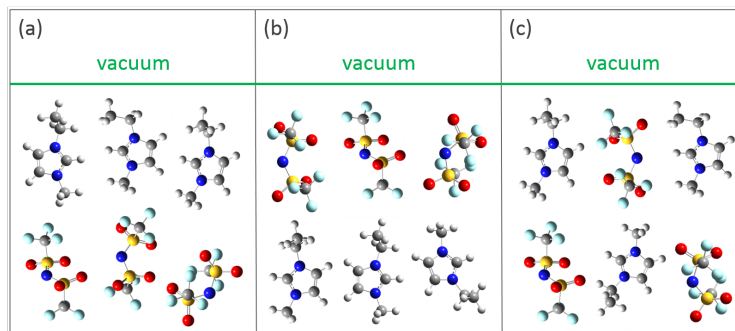


Figure 2: Three hypothetical arrangements of ions at the ionic liquid surface (ionic liquid-vacuum interface): cations are closer to the surface (a), anions are closer to the surface (b) or a mixed arrangement of the ions (c). (Referring to the illustration in C. S. Santos and S. Baldelli, *Chem. Soc. Rev.* 39 (2010) 2136-2145, page 2137 [12])

1.3 Theoretical calculations of ionic liquids

Ionic liquids can be studied by means of theoretical methods of either molecular dynamics simulations or quantum-chemical calculations. The choice of method is dependent on the length scale of various interactions between the ions, which has to be considered for the intended physicochemical property [70] (for more details about the present interactions see references herein and refs. [5, 10, 71, 72]). All interactions within the ions, inter alia Coulomb forces, hydrogen bonding, and dispersion forces [71, 72], as well as steric effects and other molecular characteristics have to be considered with care to achieve a sufficient description of their properties [73, 74].

Molecular dynamics simulations have revealed the basic properties of ionic liquids, e.g. melting point, density, viscosity, electrical conductivity, orientational correlations, and hydrogen bonding strength, which are found in good agreement with the experiment [75, 76]. It has to be noted that clear differences are recognized for the mentioned properties of the imidazolium-based ionic liquids with symmetrical and asymmetrical alkyl chain lengths (cf. refs. [77, 78] and references herein). Molecular dynamics simulations of the interface between ionic liquids and vacuum/gas phase were performed for several imidazolium-based and pyrrolidinium-based ionic liquids [73, 78, 79, 80, 81, 82, 83, 84, 85]. These studies have coincidentally revealed that the cations' longer alkyl chain has predominantly protruded towards the vacuum/gas phase. For these cations

the imidazolium-ring has primarily oriented perpendicular to surface (70 %) and parallel to surface (16 %) [84]. In addition, only 7 % of those with the imidazolium ring oriented perpendicular to surface have directed the longer alkyl chain towards the bulk [84]. Larger anions, e.g. $[\text{Tf}_2\text{N}]^-$, are present at the surface [80]; whereas, small anions, such as $[\text{Cl}]^-$, are buried beneath the cations' alkyl chain [79]. Further surface-related properties for example the surface tension at increased temperatures [80] or the large potential of CO_2 capture as well as the solution properties for different species in ionic liquids around room temperature and elevated temperatures [81, 82, 86], are well reproduced by the molecular dynamics simulations. Since these simulations consider long-ranging Coulomb interactions, the applied calculation box typically contained several hundred ions composed of a few thousand atoms, which have to be treated in a simplified way as a result of their enormous number to achieve reasonable calculation times [73, 74].

An alternative is supplied by the fully quantum-chemical calculation of one or a few ions, which contained up to a maximum of around one hundred atoms [74]. For calculations by means of quantum-chemical methods, i.e. primarily density functional theory, single ion pairs are frequently used [29, 33, 87, 88, 89, 90]. Single ions and/or larger clusters of ions are more rarely applied in these calculations [39, 88, 91, 92, 93]. Evidence for the presence of a considerable number of ion pairs in a neat ionic liquid is given for example by T. Köddermann et al. [88] in a combined study using FTIR spectroscopy and DFT-based calculations. Furthermore, at elevated temperatures and in diluted ionic liquids the number of ion pairs is enhanced [88, 94, 95]. It can be assumed that for asymmetric ions sufficient lifetimes of directional bound ion pairs are responsible for a significant impact on the properties of ionic liquids in their liquid state [96]. On the other hand, it has to be noted that studies investigating ionic liquids with highly symmetric anions have assigned significantly shorter lifetimes and strengths for the bonds inside of ion pairs, which might not lead to the formation of long-time stable ion pairs in those particular liquids [76]. These quantum-chemical calculations have utilized extensive methods, which regularly involved density functional theory (DFT) with large basis sets and appropriate functionals [70, 74]. Thus, the results obtained from single ion pairs can be characterized as highly exact for the estimation of relevant properties of ionic liquids. Recent developments in computer technology and methodical approaches have outlined that future calculations will cover a combination of quantum-chemical methods together with molecular dynamics [70, 74].

1.4 Theoretical analyses of PES and MIES spectra of ionic liquids

Since 2005, a number of researchers have started to analyze their measured spectra from photoelectron spectroscopy (XPS and UPS) and metastable induced electron spectroscopy (MIES) with the aid of theoretical calculations [18, 23, 28, 29, 33, 36, 39, 40, 41, 90, 91, 92, 97]. For this purpose, gas phase calculations of single ions or a single ion pair composed of both ions are commonly executed. In most cases density functional theory (DFT) [98] is applied for the quantum-chemical calculations combined with appropriate functionals, e.g. the hybrid exchange-correlation functional B3-LYP [99, 100, 101, 102], and sufficiently large basis sets, e.g. 6-31G plus additional polarization and diffuse functions (cf. ref. [103]). Nevertheless, the B3-LYP functional is accompanied by differences for the ion pair binding energy due to an inaccuracy in the description of dispersion interactions, which can be adjusted by means of dispersion-corrected functionals [70, 104].

In general, the electronic structure is obtained from binding energies of the calculated eigenstates of the optimized ion or ion pair and their respective occupation. The density of states (DOS), which is obtained from the equally weighted summation of all occupied eigenstates and a subsequent broadening with respect to the experimental resolution, is utilized for ionic liquids in a number of studies [18, 23, 28, 29, 39, 40, 41, 92]. D. Yoshimura et al. [41] have interpreted their experimental spectra by means of the partial density of states (pDOS) of the respective ions. Herein, the Madelung potential for an ionic liquid is estimated from the shift, which has to be introduced between the calculated pDOSes of cation and anion relative to the experimental spectrum. Furthermore, the Madelung potential has distinctly determined the shape of the ion pair (cf. ref. [95]). In the study by D. Strasser et al. [105], the valence band structure of trapped single ion pairs is measured. A good agreement between the related experimental spectra and the DOS obtained from the calculation of a single ion pair (presented in S. Krischok et al. [29]) is recognized. This fact has most probably resulted from the good comparability due to an identical system of an isolated ion pair under similar conditions between gas phase calculation and the trapped one, where the surrounding of other ions is missing compared to a regular ionic liquid.

The normalization of these DOS-based spectra onto the experimental spectra is obtained by means of absolute shifts in binding energy [23, 29, 39, 105]. A

similar adaption procedure is accomplished for open shell metal-phtalocyanines [106]. The DOS, which is achieved from quantum-chemical calculations of basic units of various polymers, is normalized onto the respective experimental spectra by a multiplicative scaling factor and an overall shift of the calculated binding energies [107].

1.5 Motivation and scope of the present thesis

The experimentally measured photoelectron spectra and metastable induced electron spectra have contained multifaceted information about the surface structure (inter alia depth, layering, and orientation), the related electronic properties of several atomic, molecular or ionic species as well as the interactions in between those (e.g. chemical environment, charge state, bond type, and preferred bonding partners). Thus, results obtained from quantum-chemical calculations are associated with the advantage of an intrinsic analysis of these wide-ranging information from the experimental spectra. Otherwise, these facts may only be achieved from the comparison with supplementary experimental methods. The valence band spectra are shaped by intertwined contributions of several atoms of the ionic liquid, which have to be deconvoluted to extract all relevant data about the surface structure. This information can only be achieved with the aid of theoretical calculations. However, up to now only a qualitative comparison of the experimental spectra was carried out by use of the shifted and scaled DOS or the respective partial DOS. Thus, a demand for a quantitative analysis of experimental PES spectra as a powerful in-depth tool is recognized and has configured the core of the present thesis. This kind of analysis is enabled, since the essential details for a subsequent attainment of the signal intensities, i.e. the binding energies and the occupancy data, are provided by the quantum-chemical calculations. Herein, a method for the reconstruction of PES spectra by means of element-specific pDOS weighted by the photoionization cross sections is developed, which could fulfil the previously mentioned requirements. Nonetheless, the binding energies in their status 'as calculated' are frequently found far off the reality. Consequently, these have to be adapted to the experiment by a suitable rescaling procedure for ionic liquids, since they have represented charged systems for which a much more complex treatment is needed in comparison to uncharged molecules.

Part I

Methodical approaches

Here, the theoretical approaches for the developed reconstruction method for surface sensitive spectra from X-ray and ultra-violet photoelectron spectroscopy (XPS, UPS) will be illustrated. The complex mechanism of photoelectron emission is reduced to a summation of photoionization cross sections, which are specific for the contained atomic species. For this reconstruction method only a few details of the experimental setup are taken into account as well as an appropriate adaptation for the calculated binding energies of the reconstructed spectra is depicted.

2 Reconstruction of photoelectron spectra

2.1 Principle of photoelectron spectroscopy

Photoelectron spectroscopy is based on the photoelectric effect, where electrons are emitted from a surface due to an exposure to electromagnetic radiation. These techniques have provided information about the occupied electronic states present near the sample surface. Two photoelectron spectroscopy methods are distinguished depending on the photon energy of impinging radiation: X-ray photoelectron spectroscopy ($\hbar\omega \gtrsim 100$ eV), which is also named electron spectroscopy for chemical analysis (ESCA), and ultra-violet photoelectron spectroscopy ($\hbar\omega \approx 10 - 100$ eV). Due to its higher photon energy XPS can be utilized to study both the core levels (deeply bound states) and the valence band (weakly bound states). Whereas, for UPS it is possible to study the weakly bound states only, since the maximum investigatable binding energy of an emitted electron is limited by the energy of the impinging photon (one electron approximation). The core levels studied by XPS can provide for example information about the stoichiometry, chemical environment, charge state as well as layering and depth of certain species. Valence band spectra studied by both techniques have contained inter alia details about the band structure of the highest occupied states and the kind of chemical bonding between the involved species.

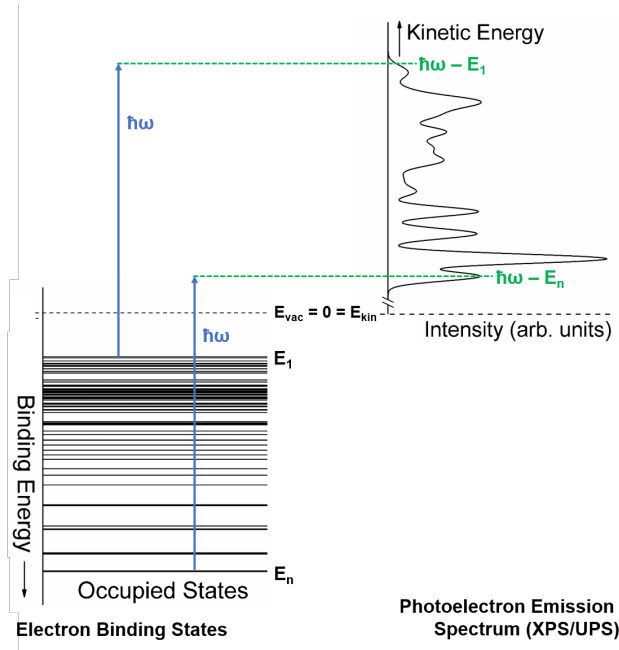


Figure 3: Illustration of the idealized principle of photoelectron spectroscopy (one electron approximation) for a molecular system, like ionic liquids.

The fundamental photoelectron emission process is illustrated in Figure 3. In the most simple case, photoemission can be regarded as a one electron process: a single electron with an initial binding energy E_i (relative to E_{vac}) is emitted by the impinging photon with the energy $\hbar\omega$ into the final state of a free electron with the kinetic energy $E_f = E_{kin}$. All other electrons inside the atom/molecule have remained at their initial binding energy during this emission process (adiabatic behavior). It is assumed in this simplified picture that any internal relaxation process, which may be caused by the reduced number of electrons ($N - 1$ electron system), has not occurred until the electron is emitted. Thus, its measured binding energy is not affected by relaxation terms and can be calculated from the detected kinetic energy of its final state $E_{kin} = \hbar\omega - E_i$. The related density of the initial states $\rho(E_i)$ can be described as a stick spectrum, i.e. expressed by a sum of Dirac delta functions at the respective initial binding energies $\delta(E - E_i)$ (cf. Figure 3), and a specific final state density $\rho(E_f)$. This final state density has featured no significant shape for XPS. On the contrary, the structure of the inconstant final state density could reveal a considerable

effect especially for the resulting UPS (He I) spectra. For an analysis of the respective spectra of ionic liquids this fact has to be addressed later.

2.2 Details of the experimental techniques

All experimental spectra were provided by the research group of Prof. Dr. S. Krischok, those are measured in particular by Dr. A. Ulbrich as well as to a lesser extent by Assoc.-Prof. Dr. T. Ikari, Dr. M. Himmerlich, and A. Zühlsdorff. The displayed experimental spectra are partially published in refs. [28, 33, 36, 37, 90, 108].

2.2.1 XPS and UPS spectroscopy

In the PES experiments three different radiation sources are applied: XPS is measured by means of the Al K_α line, which has offered a photon energy of 1486.7 eV. For UPS photons with energies of 40.8 eV (He II) and 21.2 eV (He I) are utilized. The experimental setup and the main geometric parameters are displayed in Figure 4. For the experimental spectrum and its subsequent reconstruction only the angles between radiation/excitation source and detector direction γ as well as the electron detection angle θ_e (with respect to the surface normal) have to be taken into account. For γ values of 80° (XPS) and 42.5° (UPS) have resulted from the experimental setup. The emitted electrons of all employed techniques are detected under the same angle θ_e , which is fixed to 53° in the setup.

The electron emission angle θ_e and the photon energy $\hbar\omega$ have strongly affected the information depth for photoelectron emission, which is given by $3 \cdot \lambda_e(\hbar\omega) \cdot \cos(\theta_e)$. Herein, λ_e is the inelastic mean free path of the electrons, which are emitted from the respective surface. For kinetic energies at around 50 eV (close to the photon energy provided by UPS (He II)) the mean free path of the electrons is found in the order of 0.5-0.8 nm, while for 1000-1500 eV has been identified at about 3-4.5 nm for several organic compounds [109]. Thus, approximately 95 % of the signal intensity of a photoelectron spectrum resulted from a depth of the first $3 \cdot \lambda_e$ along the detector direction, i.e. for an emission along the surface normal information depths of about 1.5-2.5 nm for UPS (He II) and around 9-13.5 nm for XPS using Al K_α radiation. By angular-resolved XPS, where the electrons are detected under wide angles relative to the surface normal,

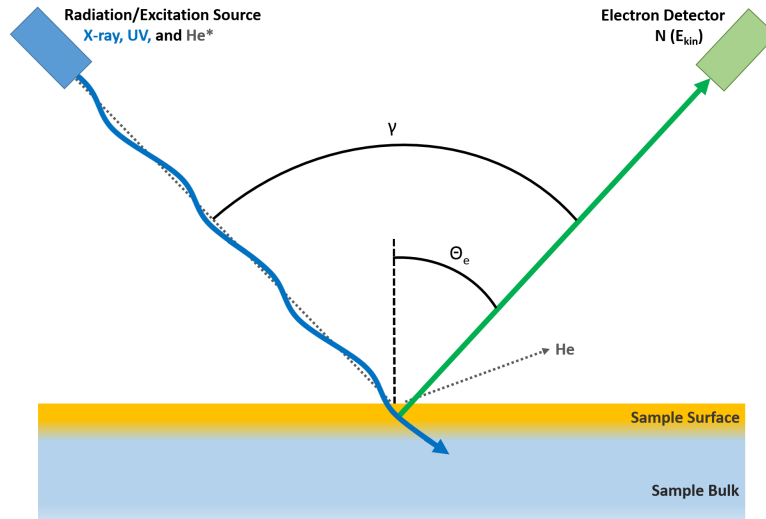


Figure 4: Experimental setup for the executed XPS, UPS, and MIES investigation with indication of the relevant geometrical parameters (angles γ and θ_e) for reconstruction and comparison to experimental spectra.

for example for an electron emission angle θ_e of 80° information depths of about 1-1.5 nm are obtained [15]. The information depth of the experimental spectra recorded under $\theta_e = 53^\circ$, which are used for comparison in the present thesis, is estimated in the order of 5.5-8 nm for XPS and 1-1.5 nm for UPS (He II) (cf. ref. [33]).

2.2.2 MIES spectroscopy

In addition, spectra from metastable induced electron spectroscopy are partially analyzed by the spectral information obtained from executed quantum-chemical calculations. The MIES signal can be shaped by more than one process [110]. Moreover, the dominating process is determined by the electronic properties of the investigated material, i.e. isolating, semiconducting or conducting behavior, and its degree of periodicity, i.e. crystalline/solid or non-crystalline/isotropic, which has resulted from the material itself as well as the respective state. In the literature, only a limited number of descriptions for the MIES processes for molecular systems based on quantum-chemical calculations is found, e.g. in refs. [110, 111]. The readers attention might be directed towards an extensive

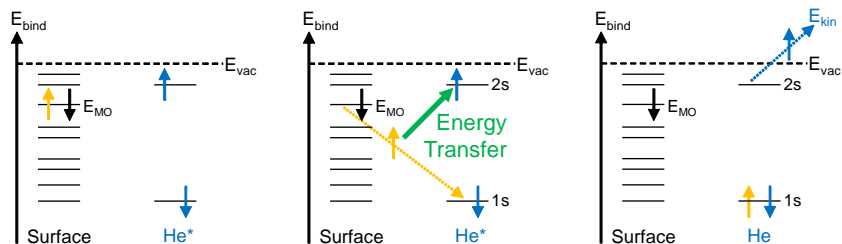


Figure 5: Schematical illustration of the steps within the Auger deexcitation (AD) process: initial state (left), energy transfer/exchange interaction (middle), and final state (right).

review about the whole field of MIES spectroscopy by Y. Harada et al. [110].

The most appropriate process for the class of ionic liquids is the Auger deexcitation (AD), also named as Penning ionization, since these materials are slightly conducting non-crystalline molecular materials [110]. This process schematically illustrated in Figure 5 is described by an initial state of the metastable helium atom (He^*) with one electron in its 1s and the other in the 2s state as well as a certain structure of valence states in the probed sample. During the approach of the He^* towards the surface, typically with a distance in between 1 and 0.2 nm [112], the interaction between the metastable atom and the surface has occurred by filling the half occupied 1s state in He^* with an electron from the sample surface. This interaction probability is characterized by the size of the overlap between the two orbitals. The electron originating from the valence band is finally located in a lower state with an energy difference of $E_{1s} - E_{MO}$ (absolute values) compared to the initial one. Thus, this redundant energy is transferred to the electron in the He^* 2s state due to the reason of the conservation of energy (see Figure 5, middle). This additional energy amount has led to the emission of the He^* 2s electron. The transition probability for the electron emission is determined by an exchange type term in a quantum-chemical description [110].

The MIES experiment has made use of metastable He^* atoms, which have possessed an excitation energy of 19.8 eV ($\text{He}^* 2^3\text{S}$) and 20.6 eV ($\text{He}^* 2^1\text{S}$), respectively. For these two types of He^* an intensity ratio of 7:1 (triplet:singlet) is present. The He^* atoms approach to the surface by grazing incidence and the electrons are detected under/close to normal emission conditions $\gamma \simeq 90^\circ$ (cf. schematical illustration in Figure 4). An extreme surface sensitivity of MIES is caused due to the requirement of a substantial overlap between the orbitals

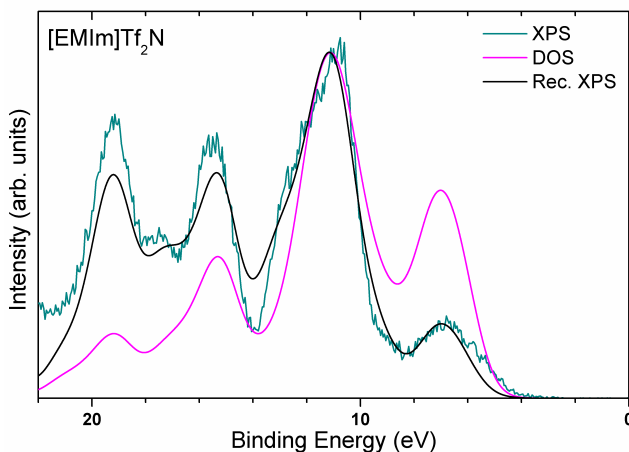


Figure 6: The density of states (DOS) calculated from a single ion pair of [EMIm]Tf₂N is related to the experimental XPS valence band spectrum (all spectra are taken from the illustration in M. Reinmöller et al., Phys. Chem. Chem. Phys., 13 (2011) 19526-19533, page 19530 [90]). For comparison the reconstructed XPS spectrum is displayed, which is obtained according to the reconstruction method described in Chapter 2.4. DOS and reconstructed XPS valence band spectrum are normalized to the peak at approximately 11 eV. The binding energies of DOS and reconstructed XPS spectrum are modified according to the rescaling procedure described in Chapter 3.3 with the parameters $f = 1.02838$, $\Delta E = -1.36$ eV, and $\Delta\Delta E_{\text{Cation}-\text{Anion}} = -1.10$ eV.

of He* and those of species at the surface. Thus, only those orbitals directed towards the vacuum are probed, since the deexcitation of all He* has occurred up to at a distance of 0.2 nm in front of the surface [112].

2.3 Relationship between experiment and theory

For an analysis of photoelectron spectra the density of states (DOS) or a partial density of states (pDOS) has been utilized up to now [18, 23, 28, 29, 39, 40, 41, 92]. In Figure 6, the experimental XPS valence band spectrum of [EMIm]Tf₂N is compared to the DOS obtained from a single ion pair of this ionic liquid. Herein, a strong discrepancy between the intensities of the DOS and the experimental spectrum can be recognized for the peaks at circa 7 and 19 eV as well as partially for those at about 15 and 17 eV.

The differences in the respective binding energies in Figure 6 are already cor-

rected by a rescaling procedure, which is described in Chapter 3.3. Nevertheless, only the energy scale used is improved, but the recognized differences in intensities still remain (cf. unscaled DOS in refs. [28, 29]). Therefore, any comparison based on the DOS is limited to qualitative statements. Due to the presence of inappropriate intensities, information about the surface structure, such as orientation, layering or partial coverage of some components of an ionic liquid can not be extracted by this method. For an in-depth analysis of the experimental spectra a novel approach is required, which is described hereinafter.

2.4 The reconstruction procedure of photoelectron spectra

In this chapter a simple, but appropriate reconstruction approach for photoelectron spectra using X-ray (XPS) and ultra-violet radiation (UPS (He II)/(He I)) is presented.¹ All results of quantum-chemical calculations of basic units (single ion pairs or small clusters for ionic liquids with evaporated metal and alkali metal atoms) are combined with tabulated photoionization cross sections from literature under consideration of only a few experimental details. The differences in the intensities between the DOS and the experimental spectrum have to be compensated by a suitable procedure, which is adapted to the conditions of the executed experiment.

First of all, the photoelectron emission can be characterized as an emission of a bound electron (initial state) into an unbound state (final state). A related quantum-mechanical approach is stated by Fermi’s Golden Rule, which is characterized by a transition probability $\Gamma(f, i, V)$ depending on the related initial state i and final one f as well as the matrix element of the respective interaction potential V :

$$\Gamma(f, i, V) = \frac{2\pi}{\hbar} |\langle f | V | i \rangle|^2. \quad (1)$$

¹Parts of this chapter have been published in the following peer-reviewed articles:
M. Reinmöller, A. Ulbrich, T. Ikari, J. Preiß, O. Höfft, F. Endres, S. Krischok, W. J. D. Beenken, “Theoretical reconstruction and elementwise analysis of photoelectron spectra for imidazolium-based ionic liquids”, Physical Chemistry Chemical Physics, 13 (2011) 19526-19533.

A. Ulbrich, M. Reinmöller, W. J. D. Beenken, S. Krischok, “Photoelectron spectroscopy on ionic liquid surfaces - theory and experiment”, Journal of Molecular Liquids, 192 (2014) 77-86.

A first quantum-mechanical description of the photoeffect was given by A. Einstein [113] in his *anno mirabilis* (1905). The central condition of energy conservation, which can be expressed with an absolute value of the binding energy for the initial molecular orbital, is stated as follows:

$$\frac{\hbar^2 k^2}{2m} = \hbar\omega - E_{MO}. \quad (2)$$

Herein, the energy terms are the kinetic energy $E_{kin} = \hbar^2 k^2 / 2m$, the binding energy of the respective molecular orbital E_{MO} , and the photon energy $\hbar\omega$. The transition probability can be written accordingly by use of a Dirac delta function, which has considered the energy conversion:

$$\Gamma(f, i, V, E_{MO}, \hbar\omega) = \frac{2\pi}{\hbar} |\langle f | V | i \rangle|^2 \delta \left(\frac{\hbar^2 k^2}{2m} + E_{MO} - \hbar\omega \right). \quad (3)$$

By incorporation of the respective wave functions of initial molecular orbital and final plane wave of the emitted electron the transition probability can be stated as follows:

$$\Gamma(r; k, \psi_{MO}, V, E_{MO}, \hbar\omega) = \frac{2\pi}{\hbar} |(\exp(-ikr) | V | \psi_{MO})|^2 \delta \left(\frac{\hbar^2 k^2}{2m} + E_{MO} - \hbar\omega \right). \quad (4)$$

This kind of calculation is performed by other authors, e.g. F. J. Himpsel [114] or P. Puschnig et al. [115]. Another opportunity for the reconstruction of PES spectra could be provided by a linear combination of atomic orbitals (LCAO) together with a Gelius intensity approach, which has covered the applied method in the present thesis.

The related PES signal has corresponded to a current of emitted electrons ($dI(E_{kin})/dE_{kin}$). This electron current is generated under precondition of a homogeneous illumination $\Phi(\hbar\omega)$ of a surface area with the size L^2 . All photons have impinged on the surface under an angle θ_γ with respect to the surface normal as well as a detector with an aperture Ω_D and a spatial sensitivity along this direction $d\eta(\Omega, E_{kin})/d\Omega$ is used for the analysis. The electron current is described in ref. [116] as a function of photoionization cross sections σ :

$$\begin{aligned} \frac{dI(E_{kin})}{dE_{kin}} &= \int_{\Omega_D} d\Omega \int_{-L/2}^{L/2} dx \int_{-L/2}^{L/2} dy \int_{-\infty}^0 \Phi(\hbar\omega) \exp \frac{z}{\lambda_\gamma(\hbar\omega, x, y, z) \cos \theta_\gamma} \quad (5) \\ &\times \left(\sum_M \frac{d\sigma_M(\hbar\omega, E_{kin}, \theta_\gamma, \theta_e)}{d\Omega dE_{kin}} \rho_M(x, y, z) \right) \exp \frac{z}{\lambda_e(E_{kin}) \cos \theta_e} \cdot \frac{d\eta(\Omega, E_{kin})}{d\Omega} dz. \end{aligned}$$

The photoionization cross sections are given in their differential expression with a scattering angle γ between photon source and detector direction, the two angles for the impinging photons θ_γ and for the emitted electrons θ_e are considered. Herein, the photon absorption length λ_γ according to Lambert's absorption law and the inelastic mean free path of the emitted electrons λ_e have to be taken into account. It has to be noted that λ_γ could be sensitive to the density of the included molecules M along all coordinates $\rho_M(x, y, z)$ and the respective cross sections for photon absorption $\sigma_M^{abs}(\hbar\omega)$ according to:

$$\lambda_\gamma(\hbar\omega, x, y, z) = \sum_M \sigma_M^{abs}(\hbar\omega) \rho_M(x, y, z). \quad (6)$$

The photon absorption length λ_γ is typically much larger than λ_e and a further dependence of intensity with depth has been neglected. A thorough discussion of the resulting information depth based on the inelastic mean free path of electrons for the different kinetic energies is performed in Chapter 2.2. The reconstruction of photoelectron spectra is performed by means of a linear combination of the molecular orbitals MO inside these molecules M regarding the related photoionization cross sections σ_{MO} described as:

$$\frac{d\sigma_M(\hbar\omega, E_{kin}, \gamma)}{d\Omega dE_{kin}} = \sum_{MO \in M} \frac{d\sigma_{MO}(\hbar\omega, \gamma)}{d\Omega} \delta(E_{kin} + E_{MO} - \hbar\omega). \quad (7)$$

The MO-specific photoionization cross sections σ_{MO} , which are only depending on the photon energy, kinetic energy, and angle between impinging radiation and electron emission direction, have resulted from a linear combination of the atomic orbitals AO using the Gelius intensity approach [117, 118], which can

be extracted from the following equation:

$$\frac{d\sigma_{MO}(\hbar\omega, \gamma)}{d\Omega} = \sum_{AO} |\langle MO|AO\rangle|^2 \frac{d\sigma_{AO}(\hbar\omega, \gamma)}{d\Omega} \quad (8)$$

AO-based photoionization cross sections have offered the same dependencies as the molecular ones. Herein, the related asymmetry parameter β_{AO} has consulted this spatial orientation of an atomic orbital and the angle γ , which is determined by the experimental setup. These facts can be incorporated into the photoionization cross sections by an additional term:

$$\frac{d\sigma_{AO}(\hbar\omega, \gamma)}{d\Omega} = \frac{d\sigma_{AO}(\hbar\omega)}{4\pi} \left(1 + \frac{\beta_{AO}(\hbar\omega)}{2} \left(\frac{3}{2} \sin^2 \gamma - 1 \right) \right). \quad (9)$$

The illustrated reconstruction method has reduced the complex description of the transition of electrons from bound states inside of a molecule into a free state into a simple summation of photoionization cross sections adapted to the experiment. This method is based on the calculated eigenvectors from the quantum-chemical methods using a single ion pair from neat ionic liquids and a small cluster for those with additional atoms. Related photoionization cross sections are tabulated, e.g. from J. J. Yeh and I. Lindau [119] or I. M. Band et al. [120]. These AO-specific photoionization cross sections for XPS, UPS (He II), and UPS (He I) with consideration of the parameters β_{AO} and γ are listed for typical elements of ionic liquids in Table 1 and Table 2 according to Equation 9. Herein, the photoionization cross sections from the two sources are calculated from partially different approaches, which are thoroughly discussed in Chapter 10, where the results of both methods are directly compared. In all other parts of the present thesis only the photoionization cross sections from Table 1 (based on the data of J. J. Yeh and I. Lindau [119]) are employed for the spectra reconstruction.

The UPS (He II) the spectrum has originated from the superposition of two optical transitions within helium (α - and β -line). Herein, the β -line is shifted in energy relative to the α -line, but no significant differences within the associated photoionization cross sections are expected due to almost the same photon energies for both. Consequently, the reconstructed UPS (He II) spectrum is a signal, which is mainly shaped from the α -line combined with a

Element	Atomic orbital	XPS	UPS (He II)	UPS (He I)	Element	Atomic orbital	XPS	UPS (He II)	UPS (He I)
H	1s	2.91	197995.92	1292587.47	Cl	2s	32004.92	-	-
	1s	1149.27	-	-		2p	39508.05	-	-
Li	2s	12.51	94410.92	329034.71	3s	3636.92	275222.54	-	
	1s	18912.00	-	-	3p	2398.13	666781.90	9964167.20	
C	2s	960.15	801020.84	842098.83	2s	43643.08	-	-	
	2p	8.74	1430037.15	4864100.67	2p	68654.76	-	-	
N	1s	34914.46	-	-	3s	5528.12	-	-	
	2s	1600.25	743511.65	-	3p	6286.05	1054484.79	n.a.	
O	2p	74.72	3371277.07	8050373.35	2s	109107.68	-	-	
	1s	58190.76	-	-	2p	454451.83	-	-	
F	2s	2764.06	571121.01	-	3s	18912.00	-	-	
	2p	268.34	5408051.21	9430852.08	3p	44330.57	-	-	
P	1s	87286.14	-	-	3d	14780.46	9866643.64	7760945.59	
	2s	4073.35	423445.63	-	4s	392.79	28069.96	24646.80	
S	2p	776.75	6877423.41	8933053.63	3s	29095.38	-	-	
	2s	23276.30	-	-	3p	91070.92	-	-	
Br	2p	19972.86	-	-	3d	48701.59	-	-	
	3s	2036.68	310686.54	117346.13	4s	3636.92	129943.38	-	
Br	3p	619.04	470274.14	924671.26	4p	6132.05	755469.51	11192502.18	
	2s	27640.61	-	-					
S	2p	27767.84	-	-					
	3s	2764.06	307605.69	-					
S	3p	1251.94	591099.15	3067635.48					

Table 1: Asymmetry-corrected photoionization cross sections (in barn) are calculated by use of the parameters from J. J. Yeh and I. Lindau [119] for atomic orbitals of all elements, which are incorporated in ionic liquids investigated in the present thesis. The photoionization cross sections are tabulated for three radiation sources: XPS Al K α ($\hbar\omega=1486.7$ eV, $\gamma=80^\circ$), UPS (He II) ($\hbar\omega=40.8$ eV, $\gamma=42.5^\circ$), and UPS (He I) ($\hbar\omega=21.2$ eV, $\gamma=42.5^\circ$).

Element	Atomic orbital	XPS	Element	Atomic orbital	XPS
H	1s	8.80	Cl	2s	33750.65
C	1s	19784.86		2p	19927.59
	2s	945.60		3s	3666.02
	2p	23.22		3p	1484.43
N	1s	35641.85	K	2s	45388.81
	2s	1716.63		2p	34977.70
	2p	96.56		3s	5659.05
O	1s	58190.78		3p	3162.00
	2s	2778.61	4s	274.95	
	2p	221.19	Cu	2s	109544.14
F	1s	88449.98		2p	229252.71
	2s	4189.74		3s	19057.48
	2p	445.23		3p	22846.88
S	2s	28368.00	3d	4912.77	
	2p	14350.07	4s	883.05	
	3s	2909.54			
	3p	994.95			

Table 2: Asymmetry-corrected photoionization cross sections (in barn) are calculated by use of the parameters from I. M. Band et al. [120] for atomic orbitals of selected elements of ionic liquids. These are listed for XPS using Al K_{α} radiation ($\hbar\omega=1486.7$ eV, $\gamma=80^{\circ}$).

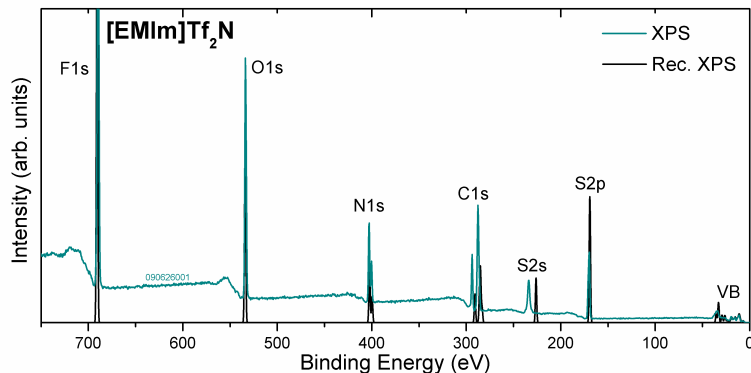


Figure 7: A comparison of the reconstructed XPS core level and valence band spectrum of [EMIm]Tf₂N together with the experimental spectrum. Binding energies are rescaled according to Chapter 3.3 with the parameters $f = 1.02838$, $\Delta E = -1.36\text{eV}$, and $\Delta\Delta E_{\text{Cation}-\text{Anion}} = -1.10\text{eV}$. Slight deviations might be caused by the background in the experimental spectrum and potentially different broadening mechanisms for core levels and valence band. The experimental spectrum is obtained from personal communication with Dr. A. Ulbrich.

small contribution from the β -line. The latter is simply reproduced by the initial α -line spectrum together with incorporation of a respective shift of -7.56eV in binding energy and a relative signal height of 4 % of the initial α -line.

Finally, the resulting stick spectra are convoluted with Gaussian type functions to simulate the obtained experimental broadening (cf. Figure 6). In the present thesis the width of Gaussian peaks is found in the range of $0.45\text{-}0.65\text{eV}$ (FWHM), which is chosen with respect to the experimental resolution. It has to be mentioned that these spectra are found in good agreement with the experimental XPS and UPS (He II) spectra, which might partially contain other peak shapes, e.g. with minor percentage Lorentzian type, too. These reconstructed XPS spectra can be utilized to study both core levels (cf. Figure 7) and valence band spectra (cf. Figure 6 and Figure 7). However, clear differences compared to the experiment are recognized for the reconstructed UPS (He I) spectra due to a strong influence of the final state density. For XPS and UPS (He II) a constant final state density is assumed. While, this fact should be corrected for UPS (He I) by a further convolution with the final state density if this kind of information is available. In addition, a rescaling procedure is developed in Chapter 3.3 to adapt the calculated binding energies to those of the experiment.

3 Calculation details, partial charge analysis, and rescaling of calculated binding energies

In this chapter the methodical details of the performed quantum-chemical calculations are outlined. A discussion about an appropriate quantum-chemical charge analysis method is performed with consideration of ionic liquids. Deviations in the binding energies, which are observed from the comparison between the experimentally measured and theoretically reconstructed spectra, have resulted from various reasons, i.e. methodical/calculational imperfections, differences in their respective zero points, induced shifts due to surface charging, and effects of the Madelung potential. As a result of the mentioned facts a suitable rescaling procedure for the binding energies is developed to enable a direct comparison between measured and reconstructed spectra hereinafter.

3.1 Details of the quantum-chemical calculations

The quantum-chemical calculations were executed with the software package Gaussian09 [121].² All optimizations of single ion pairs have utilized density functional theory [98]. Herein, the basis set 6-31G** is applied together with the hybrid functional B3-LYP [99, 100, 101, 102], which has combined the description of the exchange energy of Becke with a suitable approximation for the correlation energy by Lee, Yang, and Parr. The choice of the basis set is basically difficult: a small one might lead to wrong results, since it is too stiff. While, for an extremely large basis set, which is very flexible, the results are affected by an arbitrary assignment of contributions in the LCAO analysis, related problems will be discussed later. Thus, by application of 6-31G** approximately the golden mean with less of these effects is selected (cf. Chapter A.1 in the Appendix).

The geometry of the ions was previously optimized with their ideal charge state of +1 or -1 e/ion , which has guaranteed a satisfying closed-shell calculation. For the different possible geometries similar total energies are recognized,

²For some of the quantum-chemical calculations of single ion pairs of [EMIm]Tf₂N two versions Gaussian09 [121] and Gaussian03 [122] are utilized. A general tendency that quantum-chemical calculations from the same input file have frequently resulted in identical geometries and total energies independent of the respective Gaussian version is observed. But it cannot fully be excluded that the calculated results, i.e. total energies, can be only compared within the same version of the Gaussian software package. Consequently, this is indicated in the respective tables for ion pairs of [EMIm]Tf₂N.

which have frequently varied in order of kT between the global minimum and the diverse local minima. Subsequently, optimized ions with the respective lowest total energy are assembled to an overall neutral single ion pair, which is optimized again to regard the related interactions within this ion pair. Two previously optimized ion pairs are utilized to shape a cluster for [EMIm]Tf₂N ionic liquids interacting together with two metal or alkali metal atoms. This has provided a system that is balanced in both charge and spin in each case.

3.2 Natural bond orbital (NBO) partial charge analysis

The estimation of charges from the quantum-chemical calculations can be performed by different methods [103, 123]. In a very simple way, this is executed by means of Mulliken or Löwdin population analysis [123]: herein, the results are obtained from single electron wave functions and their related population $c_{i\mu}$. Thus, the overall charge of the single atom A within a molecular structure is estimated by $q_A = Z_A - \sum_{\mu \in A} (PS)_{\mu\mu}$ using the number of positive charges in the nucleus Z_A and a summation limited to the basis functions concentrated on this atom. The other dependencies are the density matrix P and the overlap matrix S . In a similar way, the Löwdin population analysis is obtained by $q_A = Z_A - \sum_{\mu \in A} (S^{\frac{1}{2}}PS^{\frac{1}{2}})_{\mu\mu}$, where a symmetrically orthogonalized basis set is considered.

A more complex method for the charges is provided by the population analysis of natural bond orbitals (NBO). The compact description of this approach is given by F. Weinhold and C. R. Landis [124] (see also references therein): for this method orthonormal single electron wave functions, which are intrinsic for the N electron system, are used to describe the valence hybrids h_A and h_B for two atoms. Thus, a binding NBO $\sigma_{AB} = c_A h_A + c_B h_B$ and an anti-binding NBO $\sigma_{AB}^* = c_A h_A - c_B h_B$ are formed within the bond orbital picture. The character of this bond is strongly affected by the polarization coefficients: for $c_A \simeq c_B$ a covalent bond between the atoms A and B is shaped; while, for $c_A \gg c_B$ or vice versa an ionic bonding character is addressed. These calculations have operated with an occupation close to two electrons in the binding NBO (donor) and nearly zero in the anti-binding one (acceptor). In case of a perceptible occupation of the anti-binding NBO, this would lead to a non-Lewis type structure due to a present delocalization. In general, this method has established the most appropriate natural Lewis structure and has provided a very

good agreement with those structures of organic molecules. Consequently, this model has seemed as suitable for the charge analysis of ionic liquids, since these are dominated by organic species, e.g. organic rings inside of common cations, where the electrons are partially delocalized. It can be assumed that this population analysis could provide suitable charges for the relevant atoms, like carbon and nitrogen, within these organic species. Reliable results were obtained by the NBO population analysis in other studies on ionic liquids [87].

3.3 Stepwise rescaling procedure for the calculated binding energies

The calculated binding energies have differed from the experimentally determined ones due to the following reasons:³

- The calculated binding energies of the core levels are systematically underestimated by a few percent [103]. Whereas, the binding energies of the reconstructed valence band states are frequently overestimated in the order up to 2 eV compared to the experiment.
- Clear differences are recognized for the respective zero points in the binding energy: for the calculation the vacuum level is used as zero point, while in the experiment the Fermi level is applied as the reference [90]. Thus, this difference has corresponded to a relative shift between the two binding energy scales.
- Surface charging is induced by positive charges remaining in the near surface region after emission of electrons due to the photoelectric effect in XPS, UPS as well as the interaction in MIES. The positive charges are accumulated due to the slow transportation of compensating charges to the surface. Thus, the electron emission is accompanied by a time-dependent shift of the peaks towards higher binding energies in the experimental

³Parts of this chapter have been published in the following peer-reviewed articles:

A. Ulbrich, M. Reinmöller, W. J. D. Beenken, S. Krischok, "Photoelectron spectroscopy on ionic liquid surfaces - theory and experiment", *Journal of Molecular Liquids*, 192 (2014) 77-86.

M. Reinmöller, A. Ulbrich, T. Ikari, J. Preiß, O. Höfft, F. Endres, S. Krischok, W. J. D. Beenken, "Theoretical reconstruction and elementwise analysis of photoelectron spectra for imidazolium-based ionic liquids", *Physical Chemistry Chemical Physics*, 13 (2011) 19526-19533.

spectrum [35], which has resulted from a variation in the surrounding potential in the near surface area. The application of a charge compensation might not lead to an entirely unaffected system due to a limited charge transport and decomposition effects, which might generate new charged species with time [125].

- The electrostatic interactions within the employed single ion pair are obviously varied from the real ionic liquid, where the respective ion would be surrounded by several other ions of identical and opposite charge. This charge related effect is denoted as the Madelung potential, which is initially defined by the regularly placed charges in an ionic crystal. For ionic liquids this potential can be determined on the basis of quantum-chemical calculations of single ions [41]. An extensive discussion about the surrounding potential effects of an ion pair compared to a real ionic liquid is performed in ref. [36] (see also references therein). Additionally, the most simple description of the photoelectron emission is given by an adiabatic behavior, but in reality relaxation processes might occur. It is assumed that the relaxation energy of the residual $N - 1$ electron system is partially transferred to the emitted electron [126]. According to ref. [126] the effective binding energy of the detected electron $E_{bind,eff}$ can be written as: $E_{bind,eff} = E_{bind,AO} + \Delta E_{chem} + \Delta E_{Madelung} + \Delta E_{relax}$. Both the binding energy of the respective atomic orbital $E_{bind,AO}$ and the chemical environment ΔE_{chem} are already reflected by the quantum-chemical calculation. The other two terms have caused an additional deviation between experimental and reconstructed spectrum. Nevertheless, the detailed effect of these two reasons has remained uncertain and both are covered by the extracted absolute and relative shifts described hereinafter.

Due to the noticed deviations a suitable rescaling method is required for a direct comparison between experimental and reconstructed spectra. A stepwise rescaling procedure is developed, for this purpose compare the different steps in Figure 8. The choice of peaks is highly relevant for this method, since the calculated binding energies of the utilized peaks have to fulfill the following conditions: on the one hand these have to be clearly separated in the core levels, i.e. the N1s spectrum is preferred instead of a more convoluted C1s states, and on the other the valence states of the same atoms employed for the rescaling in the core levels have to be present inside of the maximum or any

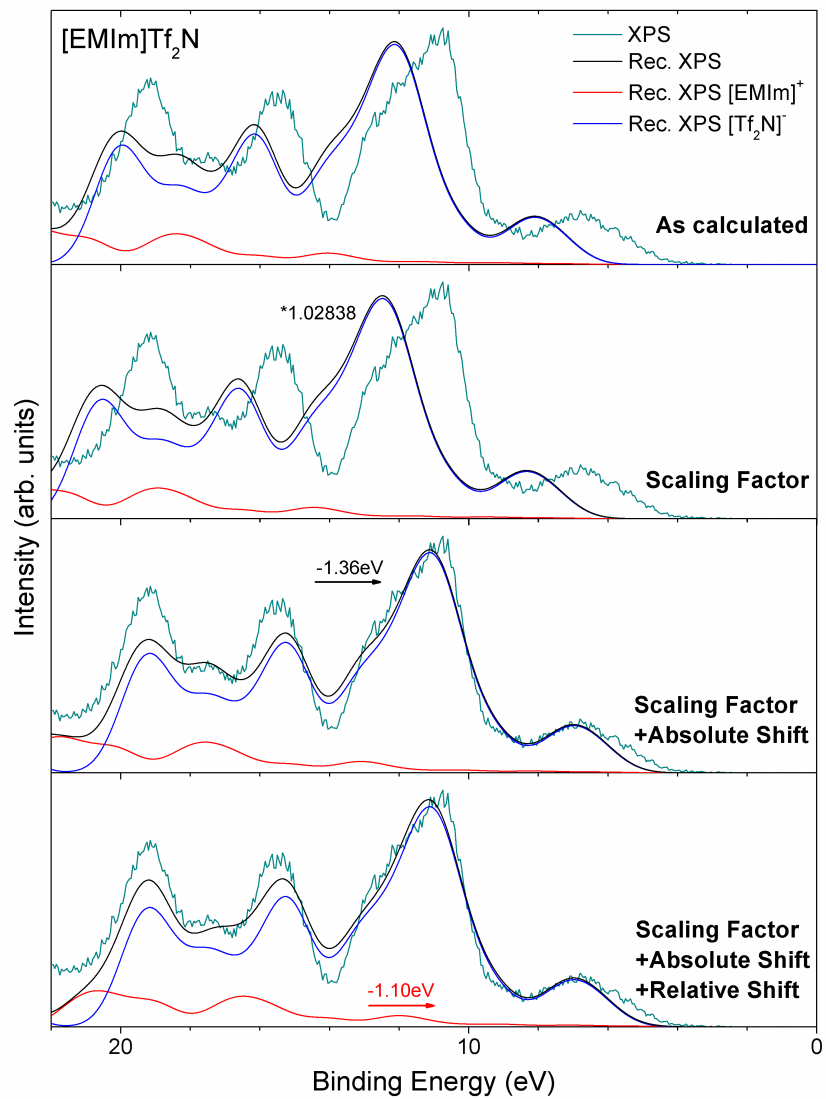


Figure 8: Illustration of the effects of the three steps of the rescaling procedure for the calculated binding energies of [EMIm]Tf₂N with introduction of a scaling factor $f = 1.02838$, an absolute shift $\Delta E = -1.36 \text{ eV}$, and a relative ion shift $\Delta\Delta E_{\text{Cation}-\text{Anion}} = -1.10 \text{ eV}$. The experimental and reconstructed spectra are taken from the illustration in M. Reinmöller et al., Phys. Chem. Chem. Phys., 13 (2011) 19526-19533, page 19530 [90].

other significant structure of the valence band, too. The fact of assignable core levels and valence states within the same element is provided by nitrogen atoms, which are frequently present inside of one or two of the ions within a broad range of common ionic liquids. Additionally, the assignment of nitrogen at lower binding energies in the valence band spectra is found as defined compared to carbon (cf. detailed deconvolution of different carbon atoms in the reconstructed UPS (He II) spectra in Figure 65 in Chapter A.2 in the Appendix). Hereinafter, a phenomenological description of the compensation method is performed, for the respective view point from a Coulomb charge and Madelung potential behind this adaptation see ref. [36].

An appropriate rescaling procedure should compensate all the previously discussed deviations. First of all, the evident underestimation of the binding energies of the core levels and the overestimation of the valence band states can be corrected by a multiplicative scaling factor f . This factor is determined by means of the binding energies from experiment and theory in both ranges of states, i.e. the N1s core levels and the valence band (VB), as follows:

$$f = \frac{N1s^{exp} - VB^{exp}}{N1s^{theo} - VB^{theo}}. \quad (10)$$

The scaling factor is regularly found in the order between 1.024 and 1.032 using 6-31G** and B3-LYP for the investigated ionic liquids (see Table 16 in the Appendix for the rescaling parameters of all investigated ionic liquids). Nevertheless, this is strongly dependent on the respective functional and basis set employed in the quantum-chemical calculation (cf. ref. [103]). By this factor the relative distance between core levels and valence band is generated. Such a multiplicative approach is applied for the comparison of the DOS with the XPS spectra of organic and polymeric compounds [107]. But this correction has only considered the methodical imperfection of the DFT calculation, while other effects are simultaneously present in ionic liquids.

The differences caused by unequal zero points in the respective energy scale [90] as well as charge effects of the surface [35] have relatively shifted these scales. Surface charging effects have accumulated additional charges, which have modified the surrounding potential for the ions in the near surface region. Thus, both effects can be jointly compensated by an absolute and uniform binding energy shift ΔE of the whole reconstructed spectra (concerning all states). This shift is determined by use of one ion (typically the anion) for which the binding

energy can be more exactly determined from the core level states compared to the valence band according to the following equation:

$$N1s_{Anion}^{exp} = f \cdot N1s_{Anion}^{theo} + \Delta E. \quad (11)$$

This absolute shift ΔE also can be determined from the cation if nitrogen is only present in this ion. After rescaling according to Equation 11 the binding energies of the reconstructed spectrum of the opposite ion (typically the cation) might not agree with the experimental values. Thus, a relative shift $\Delta\Delta E_{Cation-Anion}$ has to be introduced into the already modified binding energies of the opposite ion to adapt the related core level and valence band spectra in terms of:

$$N1s_{Cation}^{exp} = f \cdot N1s_{Cation}^{theo} + \Delta E + \Delta\Delta E_{Cation-Anion}. \quad (12)$$

In case that nitrogen is not present inside of the opposite ion, the determination of the relative shift $\Delta\Delta E_{Cation-Anion}$ can be achieved from the respective peaks in the valence band spectra in a similar way:

$$VB_{Cation}^{exp} = f \cdot VB_{Cation}^{theo} + \Delta E + \Delta\Delta E_{Cation-Anion}. \quad (13)$$

According to the Equations 10-13, the scaling factor as well as absolute and relative shift can be estimated by means of the information about the binding energies of the same peaks. The binding energies for neat ionic liquids are already adapted to experiment after incorporation of these three parameters into the reconstructed spectra. Thus, a direct quantitative comparison of the intensities of experimentally measured and theoretically reconstructed spectra at virtually identical binding energy positions is enabled.

The previously described rescaling procedure might be insufficient for an analysis of the spectra for ionic liquids interacting with other substances, e.g. evaporated (alkali) metal atoms, encapsulated liquids or dissolved species. These interactions are exemplarily investigated in the present thesis for copper evaporated onto [EMIm]Tf₂N and [EMIm]Cl with incorporated water. Thus, another relative shift has to be incorporated due to the reason that the calculated charges of those additional species might differ from the experimental

ones, which are accompanied by an additional potential, and so their related binding energies are varied. This shift is preferentially identified from the respective states in the valence band, since the core levels for example of copper are strongly affected by the partially unknown charge state as well as shake-up processes. The core levels of these additional species are not available for the rescaling procedure, since these have only rarely contained the element nitrogen, which is required for an exact determination of this extra shift $\Delta\Delta E_{AddSpecies}$ relative to those of the reference ion (typically the anion). A clear distinction between the additional states from those of the typical elements in the ionic liquids is achieved, since these are frequently found as a single one or only a few peaks in the valence band. Consequently, the binding energies of this contribution by the additional species have to be rescaled according to:

$$VB_{AddSpecies}^{exp} = f \cdot VB_{AddSpecies}^{theo} + \Delta E + \Delta\Delta E_{AddSpecies}. \quad (14)$$

The previously mentioned methodical imperfections and deviations to the experiment are compensated by the illustrated rescaling procedure. This has enabled a first comprehensive comparison between reconstructed spectra from small systems (single ion pairs or small clusters balanced in charge and spin) to the experimentally measured spectra. It has to be noted that for small uncharged systems, like benzene, very recent developments using Koopmans-compliant functionals demonstrated highly coincident results by a piecewise linearity interfering with the total energy functional for partially removed electrons [127]. This kind of quasiparticle states are not considered in the present thesis.

Part II

Results of the reconstruction of core level spectra

Core levels contain detailed information about the stoichiometry, charge states as well as chemical environment and bonding partners. Herein, the states of certain types of atomic species, except of the very light elements interfering with the valence band, are clearly separated (cf. Figure 7). Those states of elements, which are frequently present in both ions, like nitrogen and carbon, are of particular interest for an analysis with the aid of the reconstructed XPS spectra. Thus, the N1s states are commonly utilized for the rescaling of the binding energies of the reconstructed spectra, the exact method is described in Chapter 3.3. The absolute peak heights might marginally differ due to a partial contribution from Lorentzian functions to the Gaussian ones in experiment (e.g. see ref. [28]), while only Gaussian peaks are used for the reconstruction. All spectra were compared to the experimental binding energies after realization of the rescaling procedure.

For the imidazolium- and pyrrolidinium-based ionic liquids the C1s core levels have demonstrated a certain substructure, which is expected due to the different carbon positions inside the cation and anion. Thus, the reconstructed spectra can be utilized to identify the underlying origin for the respective order of states. For the copper-containing ionic liquids [128, 129], which are interesting for example in catalytic applications [128], the influence of the number of imidazolium rings attached to the central copper atom on the N1s core levels is of particular relevance. A further application of the reconstructed XPS spectra is found for the systematic analysis of the radiation-induced degradation of ionic liquids, since the respective binding energy shifts are simulated by fragments of an ion pair of [EMIm]Tf₂N through a targeted removal of selected atoms and groups from the ions. Fragments formed during the degradation in the experiment are potentially identified by means of the comparison performed. Herein, only charge- and spin-balanced clusters are regarded, which have provided closed-shell calculations. These calculations have offered reliable results for the binding energies, which have enabled a direct assignment of molecular species and indirect also on the time scale with respect to the experiment (cf.

ref. [125]). Finally, the identification of corresponding fragments allows for the conclusion of the present degradation mechanisms.

4 Core level spectra of neat and copper-containing ionic liquids

4.1 Core level spectra of imidazolium-based ionic liquids

Imidazolium-based ionic liquids composed of [XMIIm]Tf₂N have featured melting points of -17 °C (in other studies between -21 and -15 °C) for [EMIm]Tf₂N, -2 °C (in other studies from -6 to -3 °C) for [BMIm]Tf₂N, and -6 °C for [HMIm]Tf₂N (see refs. [130, 131] and references therein). The lowest melting points are typically discerned for longer alkyl chains with six to eight carbons, while for selected samples this minimum has ranged from four to ten alkyl carbons [132]. Thus, these ionic liquids are present in their liquid state at room temperature, which has made them interesting for a profound investigation and different applications. However, other imidazolium-based ionic liquids, such as [EMIm]Cl with a melting point of 41 °C [130], have remained in their solid state at room temperature, since this class of materials is defined by melting temperatures below 100 °C [1]. For the investigated liquids, high densities of around 1.52 g/cm³ ([EMIm]Tf₂N) and approximately 1.33 g/cm³ ([OMIm]Tf₂N) are recognized at room temperature [130]; in general, the density of ionic liquids is lowered by the choice of a smaller anion and prolongation of the alkyl chain length [130, 131]. Further properties of [XMIIm]Tf₂N, such as viscosity and conductivity, are typically found in the medium range compared to other ionic liquids [133].

The reconstructed N1s core level spectra are commonly utilized for the normalization of the reconstructed spectra to the experiment (cf. Chapter 3.3).⁴ In the N1s core levels of [EMIm]Tf₂N and [OMIm]Tf₂N, two peaks are identified at about 399.7 eV and 402.3-402.4 eV with twice the intensity of the first one

⁴Parts of this chapter have been published in the following peer-reviewed articles:

M. Reinmöller, A. Ulbrich, T. Ikari, J. Preiß, O. Höfft, F. Endres, S. Krischok, W. J. D. Beenken, "Theoretical reconstruction and elementwise analysis of photoelectron spectra for imidazolium-based ionic liquids", Physical Chemistry Chemical Physics, 13 (2011) 19526-19533.

T. Ikari, A. Keppler, M. Reinmöller, W. J. D. Beenken, S. Krischok, M. Marschewski, W. Maus-Friedrichs, O. Höfft, F. Endres, "Surface electronic structure of imidazolium-based ionic liquids studied by electron spectroscopy", e-Journal of Surface Science and Nanotechnology, 8 (2010) 241-245.

[28] (see Table 3). The peak at lower binding energy is assigned to the central nitrogen atom within the $[\text{Tf}_2\text{N}]$ anion and the second peak has resulted from the two nitrogen atoms in the imidazolium ring of the cation.

A further core level structure, which has also contained convoluted contributions in a very different chemical environment, is the C1s spectrum. In the experimental spectra in ref. [28], an isolated peak at 293.15 eV as well as a double structure with peaks at about 287.0 eV for both ionic liquids and 285.6 eV for $[\text{EMIm}]\text{Tf}_2\text{N}$ or 285.2 eV for $[\text{OMIm}]\text{Tf}_2\text{N}$ are identified, respectively. The first peak is assigned to carbons in the CF_3 groups of the $[\text{Tf}_2\text{N}]$ anion. Whereas, the double peak structure is caused by the imidazolium-based cation. Inside this peak at higher binding energy the carbon atoms in the imidazolium ring as well as the first one in the longer alkyl chain and from the methyl group are localized [14, 15, 28]. The peak at lower binding energy is shaped from the further carbon atoms within the alkyl chain [14, 15, 28]. Herein, a shift towards lower binding energies and an increase in peak height is recognized with increasing alkyl chain length. This shift is present up to a number of approximately ten carbons in the alkyl chain [14], since the influence of the imidazolium ring is reduced for these remote carbons in the longer chain. In what follows, the C1s core level peaks are decomposed from a single ion pair calculation to verify and understand the supposed order from experimental data.

The two single ion pairs of $[\text{EMIm}]\text{Tf}_2\text{N}$ and $[\text{OMIm}]\text{Tf}_2\text{N}$, which are used for the subsequent analysis, are visualized in Figure 9 (top left). Both ion pairs have featured a position of the $[\text{Tf}_2\text{N}]$ anion in vicinity of the central carbon atom of the imidazolium ring (C^1), which is energetically favored (see discussion performed in Chapter 6.1 for the relative ion pair geometry). For $[\text{EMIm}]\text{Tf}_2\text{N}$ an ion pair with the cis conformer of the $[\text{Tf}_2\text{N}]$ anion is utilized. Whereas, for $[\text{OMIm}]\text{Tf}_2\text{N}$ an anion with the respective trans conformer is preferred. However, the cis and trans conformer of the $[\text{Tf}_2\text{N}]$ anion are identified to be in equilibrium at room temperature [134, 135] and during the optimization of the ion pairs composed of preoptimized single ions the effect of conformational change was observed in both directions.

The density of states (DOS) for the C1s core level spectrum is illustrated in Figure 9, which can be used for comparison to the intensity of the experimental XPS spectra for $[\text{EMIm}]\text{Tf}_2\text{N}$ and $[\text{OMIm}]\text{Tf}_2\text{N}$. However, the DOS does not represent a reconstructed XPS spectrum, but the DOS and reconstruction of an XPS core level spectrum of a single element have only varied by a multiplicative factor known as photoionization cross section. This factor is constant for the

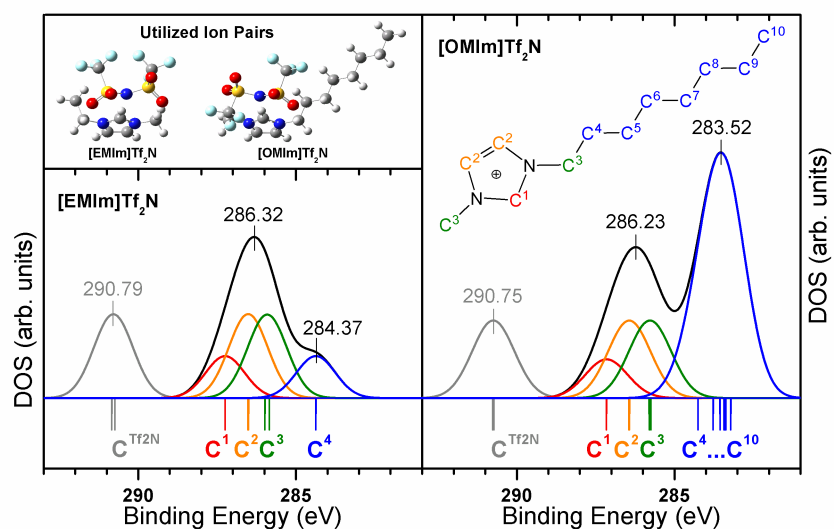


Figure 9: The DOS of the C1s core level spectra for [EMIm]Tf₂N (left) and [OMIm]Tf₂N (right) obtained from the single ion pairs visualized in the top left. Signatures of different carbon positions C¹-Cⁿ (see inset) within the imidazolium-based cations are grouped together depicted by means of similar color. Rescaling of the calculated binding energies is performed with parameters of $f = 1.02838$, $\Delta E = -1.36 \text{ eV}$ for [EMIm]Tf₂N and $\Delta E = -1.39 \text{ eV}$ for [OMIm]Tf₂N, while here $\Delta\Delta E_{\text{Cation}-\text{Anion}} = 0 \text{ eV}$. (With the courtesy of: The Royal Society of Chemistry, M. Reinmöller et al., Phys. Chem. Chem. Phys., 13 (2011) 19526-19533, page 19527 [90])

states belonging to the same atomic orbital. Thus, the DOS is as useful as the fully reconstructed spectrum for a single core level structure, e.g. solely the C1s or N1s states, since they both are arbitrarily adjusted to the experimental intensity subsequently. Nevertheless, for a quantitative comparison between core level structures, which have originated from different elements, the consideration of photoionization cross sections is mandatory.

An analogous peak structure as found in the experimental C1s spectra of [XMIm]Tf₂N (cf. refs. [14, 15, 28]) is determined by the respective DOS in Figure 9. Whereas, the binding energies in the DOS are observed at about 0.8 and 2.4 eV lower than in the experimental spectra. The assignment of the single peak at higher binding energy to the [Tf₂N] anion and the double peak to the imidazolium-based cation of [EMIm]⁺ or [OMIm]⁺ is verified by the DOS, respectively. Furthermore, the previously stated general separation of the double peak into the carbon atoms on one hand within the imidazolium ring plus first carbon atom from both alkyl chains and on the other into the residual alkyl chain is confirmed by the DOS. A certain energetic order is revealed by a more detailed view onto C1s core level spectra of the cation-related peak at higher binding energy: the central carbon atom (C¹) within the imidazolium ring is discerned at the highest binding energy position, the other two carbons in the ring (C²) are located at about 0.7 eV below (see tabulated binding energies in Table 3). Finally, the first carbon atom of both alkyl chains (C³) has occupied a binding energy position about 0.6 eV below those of C². This order has immediately resulted from the distance of each carbon atom to the two imidazolium nitrogens: C¹ is directly neighbored by both nitrogens and, consequently, found at the highest binding energy position. The C² carbons are recognized at lower binding energy due to the fact that they are directly neighbored by only one nitrogen, while the other is their second next neighbor. C³ carbons are eventually located at the lowest binding energy in this peak, since they are only directly bound to one nitrogen and further on are not significantly influenced by the second one. However, the binding energy distance between the two C³ carbons is estimated to be very small (≤ 0.15 eV) even though both are located in relatively different chemical environments, i.e. pure terminal methyl group vs. head group of a longer alkyl chain. This fact has additionally supported the suggestion that only the distance to the nitrogens is the dominating effect for the present energetic order rather than the general classification into 'aromatic' and 'aliphatic' carbons as performed in other studies [14, 15] or charge-related effects [87].

Atom	[EMIm]Tf ₂ N		[OMIm]Tf ₂ N		[OMIm] ⁺
	Calc. Binding Energy (eV)	Exp. Binding Energy (eV)	Calc. Binding Energy (eV)	Exp. Binding Energy (eV)	Calc. Binding Energy (eV)
N ^{Tf2N}	399.70 ^{&}	399.7 ^{&}	399.70 ^{&}	399.7 ^{&}	
N ^{Im}	403.54	402.3	403.48	402.4	403.50
	403.44		403.35 [#]		403.35 [#]
C ^{Tf2N}	290.84	293.2	290.76	293.2	
	290.75		290.73		
C ¹	287.24	287.8	287.16	287.8	287.53
C ²	286.53	287.2	286.44	287.1	286.19
	286.50		286.42		286.16
C ³	285.98	286.7	285.80	286.7	285.94
	285.84		285.75		285.76
C ⁴	284.37	285.6	284.25	285.2	283.91
C ⁵			283.77		283.15
C ⁶			283.56		282.56
C ⁷			283.43		282.11
C ⁸			283.40		281.79
C ⁹			283.37		281.61
C ¹⁰			283.21		281.26

Table 3: Rescaled binding energies for the N1s and C1s core levels obtained from ion pairs of [EMIm]Tf₂N and [OMIm]Tf₂N (displayed in Figure 9) together with those of the single cation [OMIm]⁺ in comparison to the experimental values. The nomenclature for all positions within the imidazolium-based cations is depicted in Figure 9 (top right). ([&]) A normalization of the binding energies from [EMIm]Tf₂N and [OMIm]Tf₂N onto the experimental N^{Tf2N} core level is performed by a scaling factor of $f = 1.02838$ and respective absolute shifts of $\Delta E = -1.36 \text{ eV}$ for [EMIm]Tf₂N and $\Delta E = -1.39 \text{ eV}$ for [OMIm]Tf₂N. A relative shift is not incorporated at this stage ($\Delta\Delta E_{\text{Cation-Anion}} = 0 \text{ eV}$). ([#]) The normalization of the binding energies for the isolated cation of [OMIm]⁺ is achieved by the identical scaling factor and a shift of $\Delta E = -4.90 \text{ eV}$. (With the courtesy of: The Royal Society of Chemistry, M. Reinmöller et al., Phys. Chem. Chem. Phys., 13 (2011) 19526-19533, page 19529 [90])

The enhancement of the peak intensity and a shift to lower binding energy is determined for the peak at the lower energy side of the double structure. For the carbon atoms inside the longer alkyl chain (C^4-C^n , see inset in Figure 9), which have shaped this peak, a certain energetic order is detected (cf. Table 3): the binding energy has decreased with the distance of the respective carbon atom to the nitrogen (equivalent to the whole imidazolium ring). From the binding energy values in Table 3, it is perceived that the related shifts in binding energy have clearly proceeded through the whole alkyl chain. This energetic order is discovered for both the ion pair of [OMIm]Tf₂N as well as the isolated [OMIm] cation. It is verified by an identical energetic order for [OMIm]⁺ that this effect is not only accidentally present in this particular ion pair. Nevertheless, the charges of the involved carbon atoms have not clearly varied within the alkyl chain and, thus, have not significantly influenced the binding energies. The influence of the charges in the imidazolium ring onto the carbon atoms in the alkyl chain has rapidly decreased by the distance [30]. For a longer alkyl chain of the [XMIIm] cation the carbons far away from nitrogen have featured a chemical environment similar to pure alkanes. A shift towards lower binding energies is decelerated by the distance to the imidazolium ring with marginal binding energy differences of about 0.03 eV between the neighboring carbons within C⁷-C⁹. This is in agreement with the stop of any further shift in experiment at a number of circa ten carbons in the alkyl chain [14].

4.2 Core level spectra of pyrrolidinium-based ionic liquids

The main physico-chemical properties of pyrrolidinium-based ionic liquids are outlined by S. Men et al. [136] (see also references therein): the melting points are similar in pyrrolidinium- and imidazolium-based ionic liquids and for example the viscosities and conductivities of pyrrolidinium-based ionic liquids are slightly increased compared to their imidazolium-based analogs.

The fundamental structural analysis of [XMPyrr]Tf₂N is given from O. Borodin and G. D. Smith [137], J. N. Canongia Lopes et al. [138] as well as Y. Umebayashi et al. [139] by means of molecular dynamics simulations. In these studies, it was identified that both conformers of [Tf₂N] anion are present in approximately an energetical equilibrium. For the pyrrolidinium-based cations three different conformers are ascertained, which are visualized in Figure 10. All of those conformers recognized in molecular dynamics simulations are observed

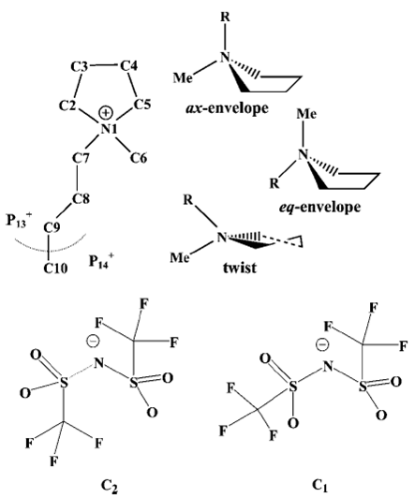


Figure 10: Conformers of the [N-alkyl-N-methylpyrrolidinium] cation and [Tf₂N] anion. (With the courtesy of: The American Chemical Society, Y. Umebayashi et al., J. Phys. Chem. B, 113 (2009) 4338-4346, page 4339 [139])

in the quantum-chemical calculations utilizing single ion pairs, too. Three-dimensional isosurfaces for elements of the [Tf₂N] anion around those of the [PMPyrr] cation calculated by O. Borodin and G. D. Smith [137] are illustrated in Figure 11. A transition between the conformers of the [Tf₂N] anion, as it was recognized for [EMIm]Tf₂N, is not observed for [BMPyrr]Tf₂N in the quantum-chemical calculation. Only the tendency to form intermediate states between both conformers is identified. This may lead to the assumption that the energy barrier for transition between cis and trans conformer of the [Tf₂N] anion is higher in a pyrrolidinium-based ionic liquid compared to the imidazolium-based analog, which is somehow in contrast to the statements given by E. Bodo et al. [135]. The C1s core level spectra of a set of [XMPyrr]Tf₂N ionic liquids are analyzed in depth subsequently.

4.2.1 N1s and C1s core level spectra

The core level spectra from nitrogen and carbon are of special interest due to the fact that these elements are present in both ions of [XMPyrr]Tf₂N ionic liquids. For the experimental N1s states two peaks are observed at about 403.8 eV and 400.6 eV. Herein, the peak at higher binding energy is assigned to pyrrolidinium-based cation. Whereas, the second peak has originated from the [Tf₂N] anion.

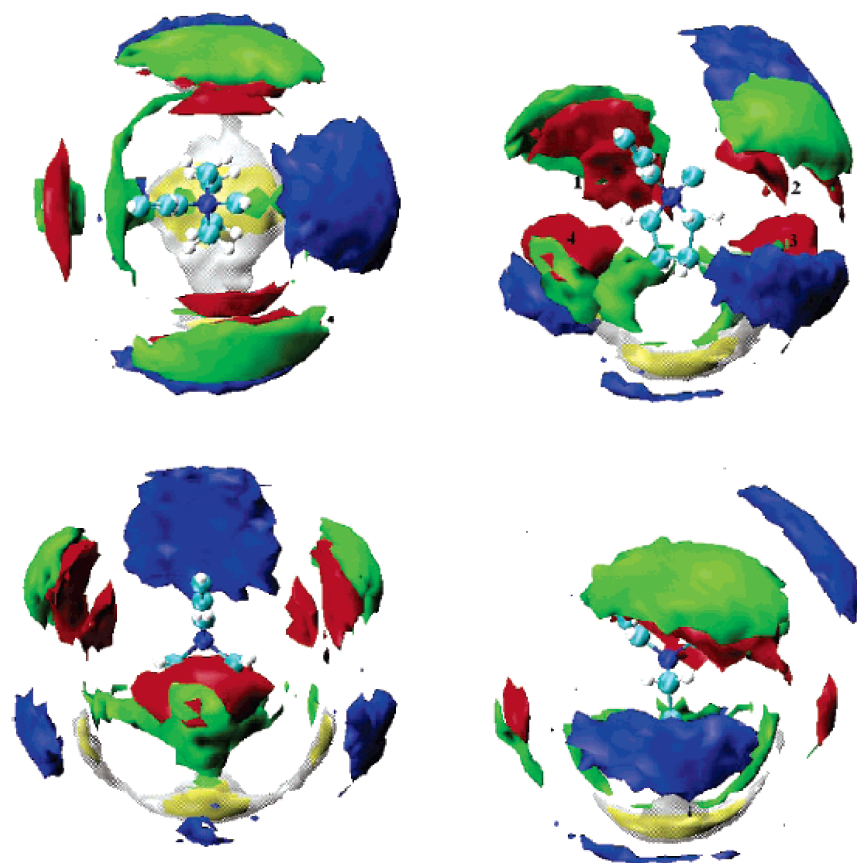


Figure 11: Three-dimensional isosurfaces of the density of different elements in [PMPyrr]Tf₂N, which are also denoted as spatial distribution functions (SDF): nitrogen (isovalue: 4.0, color: red), fluorine (2.1, green), carbon from [Tf₂N]⁻ (2, silver/yellow), and carbons of the neighboring pyrrolidinium-based cation (2.2, blue). (With the courtesy of: The American Chemical Society, O. Borodin and G. D. Smith, *J. Phys. Chem. B*, 110 (2006) 11481-11490, page 11486 [137])

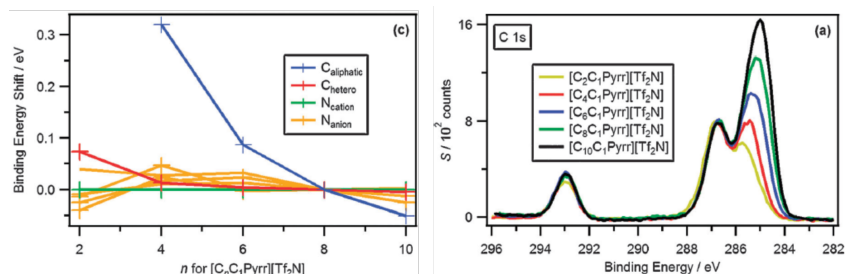


Figure 12: Normalization of experimental C1s binding energies to those of [OMPyr][Tf₂N] (left) and C1s core level spectra from a set of pyrrolidinium-based ionic liquids [XMPyr][Tf₂N] with varied alkyl chain length (right). (With the courtesy of: The Royal Society of Chemistry, S. Men et al., Phys. Chem. Chem. Phys., 13 (2011) 15244-15255, page 15250 [136])

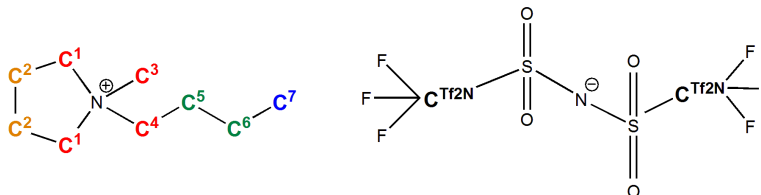


Figure 13: Nomenclature for the different carbon atoms in [BMPyr][Tf₂N]: C¹-C⁷ in the [BMPyr] cation (left) and C^{Tf2N} inside the [Tf₂N] anion (right), which is modified compared to the assignment in S. Men et al. [136].

In the experimental C1s core level spectra, two structures are identified: an isolated peak at around 294 eV and a double peak structure at about 288 and 286.5 eV. The single peak at higher binding energy is assigned to the two carbon atoms in the [Tf₂N] anion. While, the double peak structure has arisen from the pyrrolidinium-based cation. A possible normalization of the experimental spectra due to charge effects is stated by S. Men et al. [136]: the peak originating from the longer alkyl chain in [OMPyr][Tf₂N] is fixed to a binding energy of 285 eV (a similar procedure is known for imidazolium-based ionic liquids [30]). All other peaks in the spectra have to be shifted according to this charge-adapted normalization (cf. Figure 12, left). A suitable nomenclature for C1s states of the pyrrolidinium-based cation using a three-step model is given by S. Men et al. [136] (see different carbon positions in Figure 13): 'C^{hetero}' (C¹, C³, and C⁴), 'C^{inter}' (C² and C⁵), and 'C^{aliphatic}' (C⁶-C¹¹), where the latter peak is set to

285 eV. This normalization is not required for a comparison to the experimental spectra due to the applied rescaling procedure of the binding energies for the reconstructed spectra. The underlying nomenclature is borrowed from ref. [136] and the arrangement in groups will be modified with respect to results of the subsequent spectra reconstruction.

A theoretical analysis of the C1s core level spectra has enabled deeper insights into core level spectra for which a relationship between the position of the respective carbon atom within the ion pair and its binding energy can be concluded. For this purpose, a number of approximately 40 ion pairs was calculated using different relative geometries between the ions as well as both conformers of the [Tf₂N] anion according to Figure 10. The reconstructed C1s core level spectra for three different ion pair geometries, which are in congruence with the spatial distribution functions (SDF) in Figure 11, are jointly illustrated in Figure 14. Herein, a surprising nature is recognized for the reconstructed C1s core levels of the [BMPyrr] cation and three different shapes are discovered: a peak with a shoulder (Figure 14, top), a broad single peak (middle), and a double peak structure (bottom). For the cations' C1s structure, which has exhibited a peak together with a shoulder at lower binding energy (Figure 14, top), this shoulder has originated from the alkyl carbons (C⁵-C⁷, see Figure 13), whereas C¹-C⁴ have contributed to the main peak. This peak shape is observed for ion pairs, where either the central nitrogen atom of the [Tf₂N] anion is found in vicinity of the nitrogen in [BMPyrr] cation or the [Tf₂N] anion is placed around the edge of the pyrrolidinium ring, which has corresponded to a potential parallel alignment to the alkyl chains. In case that only a single peak is detected for the cation (Figure 14, middle), the noticed order of the underlying contributions has strongly altered: the C² carbons are shifted to a binding energy position in between the alkyl positions of C⁵⁺⁶ at higher and C⁷ at lower binding energy. The carbon C⁴ has simultaneously taken the highest energy position. This is related to an anion position in between pyrrolidinium rings face and the methyl group. It is found in contrast to the order, which is assigned by S. Men et al. [136]. The third case of a double peak structure (Figure 14 bottom) is discovered for ion pairs, where the [Tf₂N] anion is placed in a position between the pyrrolidinium rings face and the longer butyl chain, which is additionally slightly favored from an energetical view point. This position is fully covered by the anion in the SDF displayed in Figure 11, which is in contrast to the other positions, where both anion and cation could be found as neighboring

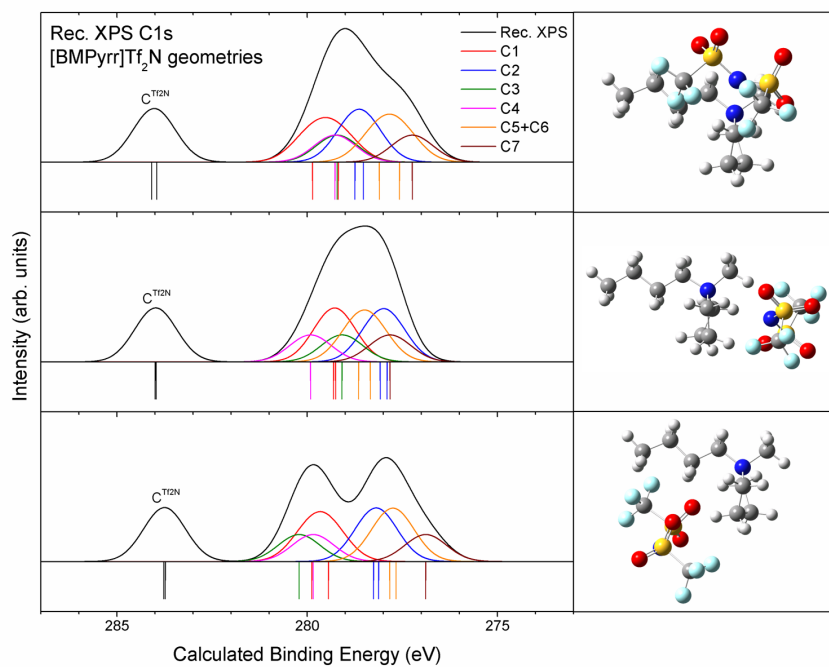


Figure 14: Reconstructed C1s spectra (left) in comparison to the respective ion pair geometry (right). All utilized ion pairs have featured a twist conformer of the [BMPyrr] cation (see nomenclature in Figure 10) for sake of comparison. Herein, the calculated binding energies are utilized due to the reason that a rescaling procedure can only be executed for a particular ion pair, since the related parameters (f , ΔE , and $\Delta\Delta E_{Cation-Anion}$) might change and will be incomparable to those of ion pairs with significantly different geometry.

interaction partners. Hereinafter, only those ion pairs, which have exhibited a clear splitting in the C1s structure related to $[\text{BMPyrr}]^+$, will be considered for a detailed analysis. This effect is further identified to be independent of the respective conformer of the $[\text{Tf}_2\text{N}]$ anion (cf. Figure 15 and Figure 16).

In Figure 15, the reconstructed C1s core level spectra of eight ion pairs, which are visualized in Figure 16, are deconvoluted into the contributions of the contained carbon atoms. Several peaks are encountered in the reconstructed C1s core level spectra from the ion pairs of $[\text{BMPyrr}]\text{Tf}_2\text{N}$. Herein, the binding energies are used as calculated, i.e. no scaling factor, relative or absolute shifts are incorporated. As previously described the peak at highest binding energy (around 284 eV) can be assigned to the $[\text{Tf}_2\text{N}]$ anion. For the double peak structure, which has originated from the respective $[\text{BMPyrr}]$ cation, a particular substructure with an intrinsic order is identified by deconvolution for all ion pairs (for applied nomenclature see Figure 13): the single methyl group (C^3) is detected at the highest binding energy. For most of the calculated ion pairs, the next state is assigned to the first carbon atom of the butyl chain (C^4), which is directly linked to the cations nitrogen. These are followed by the other two carbon atoms bound to the nitrogen within the pyrrolidinium ring (C^1), which have only occupied a binding energy position similar to or slightly higher than C^4 for one of the investigated ion pairs. Thus, all four carbon atoms, which are directly connected to nitrogen, have shaped the peak at higher binding energy inside the C1s double peak structure of $[\text{BMPyrr}]^+$. Finally, the peak at lower binding energy has resulted from carbon atoms, which are not directly bound to nitrogen. At the higher binding energy side of this peak the other two carbon atoms inside the pyrrolidinium ring (C^2) are found, since both are second and third next-neighbored by the cations' nitrogen. This double interaction with the nitrogen might be the consequence for the clear energetical separation between C^2 and the further carbons of the butyl chain (C^{5-7}), which are only influenced once by nitrogen. The further carbon atoms of the butyl chain (C^{5-7}) are localized at lower binding energy and their exact position first of all is dependent on the distance to the nitrogen atom, which has resulted in the following energetic order: C^5 is present at the highest binding energy, the terminal carbon of the butyl chain (C^7) is found at lowest binding energy, while C^6 is noticed in between. Surprisingly, these energetic positions are not homogeneously distributed for nearly all ion pairs, since the distance between C^5 and C^6 is comparatively small, whereas it is large between C^6 and C^7 . Consequently, the distance to the nitrogen has seemed not exclusively responsible for this fact. In all of the

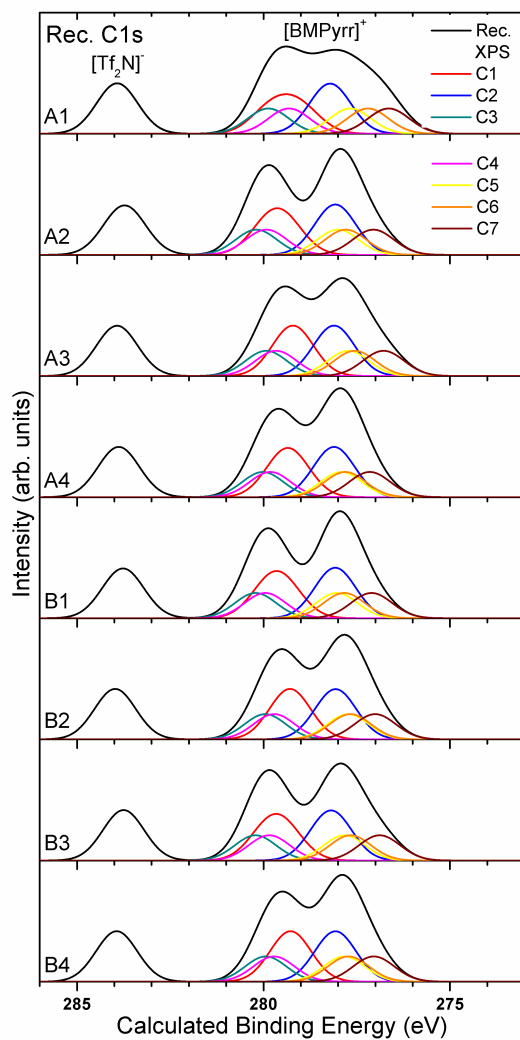


Figure 15: Reconstructed C1s core level spectra of different ion pairs from [BMPyrr][Tf₂N] (visualized in Figure 16), which have featured a distinct double peak structure in the contributions of the cation. A deconvolution of the contributions of carbon atoms in different chemical environment within the [BMPyrr] cation is executed (for the respective nomenclature see Figure 13). Herein, the calculated binding energies are utilized due to the reason that a rescaling procedure can only be executed for a particular ion pair, since the related parameters (f , ΔE , and $\Delta\Delta E_{\text{Cation-Anion}}$) might slightly vary for the ion pairs investigated here.

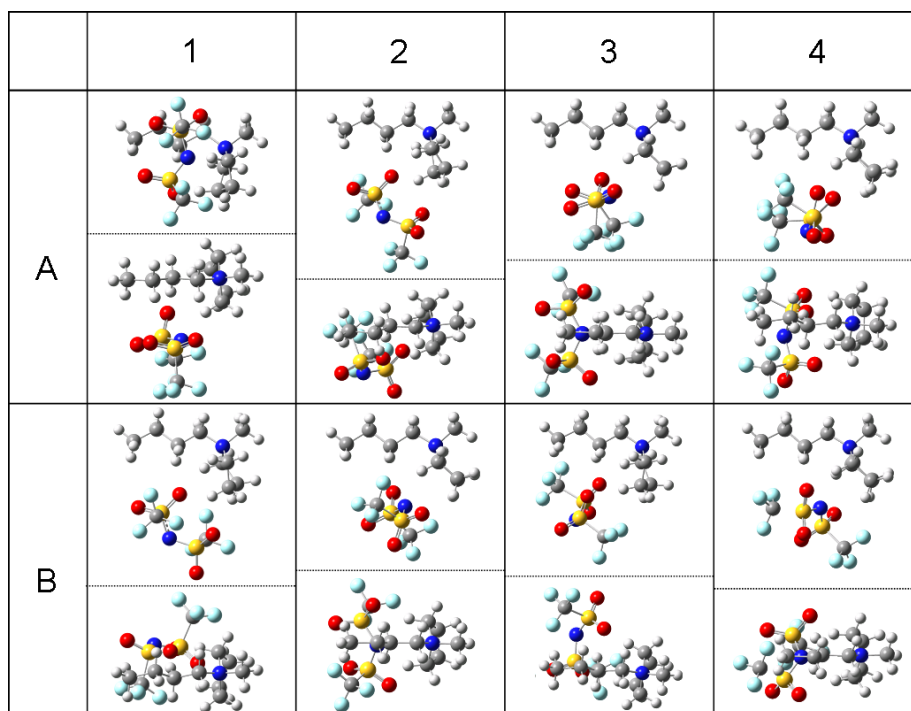


Figure 16: Ion pairs from [BMPyrr]Tf₂N, which have featured a distinct double peak structure in their reconstructed C1s core level spectra (see Figure 15), are visualized by two different directions (side and top view, separated by a dotted line). The ion pairs in line A have offered a cis conformer of the [Tf₂N] anion, while those with a trans conformer are depicted in line B.

considered ion pairs, the geometrical distance between alkyl carbons (C^{5-7}) and the $[Tf_2N]$ anion is identified to be close, which might lead to the conclusion that the interaction between the butyl chain (or the cation in general) and the $[Tf_2N]$ anion is not entirely negligible. This effect will be discussed in detail hereinafter.

For sake of comparison, the core level positions for a similar ion pair with an extended alkyl chain, i.e. octyl instead of butyl, are calculated to assure that the utilized $[BMPyrr]^+$ might not result in a wrong order of binding energies due to its relatively short alkyl chain length. The ion pair with the alkyl chain prolonged by four CH_2 groups is abbreviated as $[OMPyrr]Tf_2N$. In Figure 17, the respective C1s core level spectra are shown. The related binding energies for N1s and C1s core levels of the utilized ion pairs $[BMPyrr]Tf_2N$ (B2 in Figure 16) and $[OMPyrr]Tf_2N$ (analog to this ion pair) are listed in Table 4. Herein, reconstructed C1s spectra are modified, based on the N1s peaks at 403.84 eV from $[BMPyrr]^+$ and 400.61 eV from $[Tf_2N]^-$ as well as the valence band in the experimental spectra from $[BMPyrr]Tf_2N$. Hence, all binding energies of the reconstructed spectra are adapted by a scaling factor $f = 1.02963$, an absolute shift of $\Delta E = -0.79 \text{ eV}$ as well as a relative one between the contributions from $[BMPyrr]$ cation and those of the $[Tf_2N]$ anion ($\Delta\Delta E_{Cation-Anion} = -1.47 \text{ eV}$). For the reconstructed spectra of $[OMPyrr]Tf_2N$, these modifications, i.e. scaling factor and relative shift between the ions are equally utilized, while an absolute shift of $\Delta E = -0.77 \text{ eV}$ is integrated due to a small deviation in the calculated N1s binding energies of the N^{Pyrr} .

The binding energy positions of the single and the double peak structure in the reconstructed C1s spectra in Figure 17 are identified at about 291.62 eV, 285.53 eV, and 283.80 eV for $[BMPyrr]Tf_2N$ or 283.15 eV for $[OMPyrr]Tf_2N$, respectively. In contrast to this, the experimental spectra from $[BMPyrr]Tf_2N$ are found at binding energies in the order of 2.5-3 eV higher (around 294.06 eV and a double peak structure at about approximately 287.80 and 286.65 eV). Due to this reason one could not directly compare the binding energies of experimental and reconstructed spectra by their absolute values, but qualitative assignments by use of the relative energetic differences and the order of states in the double peak structure are reasonable. The distance in binding energy between the C^{Tf_2N} and the peak at higher binding energy side of the double peak structure is estimated by about 6.1 eV, this fact is supported by a difference of circa 6 eV in the experimental spectra. In the reconstructed C1s spectrum, the carbon of the methyl group (C^3) is found at an equal binding energy for both ionic liquids

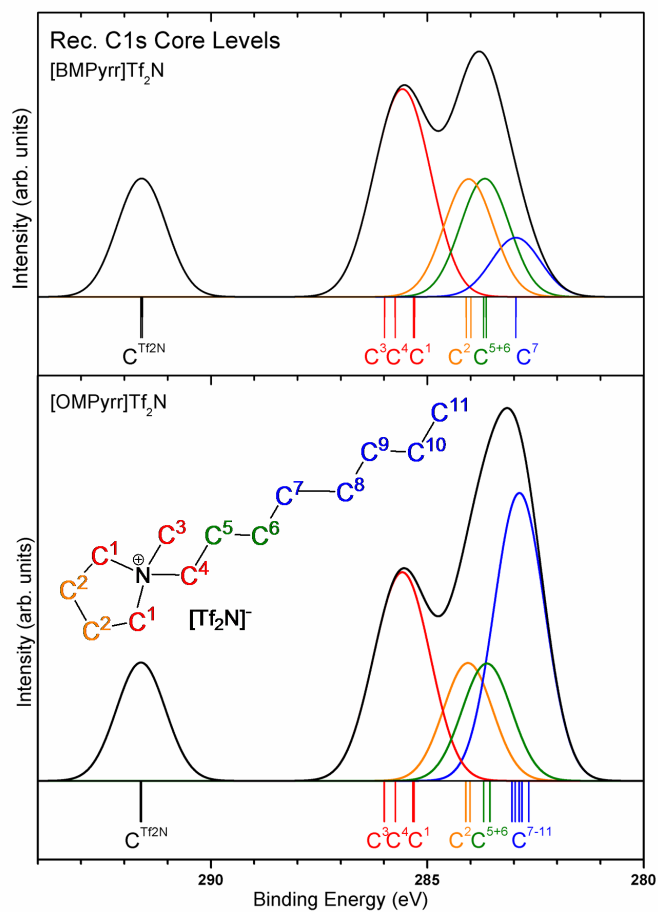


Figure 17: Reconstructed C1s core level spectra of [BMPyrr]Tf₂N and [OMPyrr]Tf₂N (carbon atoms in a conformable chemical environment are grouped together according to the inset). Herein, the binding energies are modified by the rescaling parameters $f = 1.02963$, $\Delta E = -0.79 \text{ eV}$ for [BMPyrr]Tf₂N and $\Delta E = -0.77 \text{ eV}$ for [OMPyrr]Tf₂N, respectively, and $\Delta\Delta E_{\text{Cation}-\text{Anion}} = -1.47 \text{ eV}$ for both ionic liquids.

Atom	[BMPyrr]Tf ₂ N		[BMPyrr] ⁺	[OMPyrr] Tf ₂ N	[OMPyrr] ⁺
	Exp. Binding Energy (eV)	Calc. Binding Energy (eV)	Calc. Binding Energy (eV)	Calc. Binding Energy (eV)	Calc. Binding Energy (eV)
N ^{Pyrr}	403.84 [#]	403.84 [#]	403.84 [#]	403.84 [#]	403.84 [#]
N ^{Tf₂N}	400.61 [#]	400.61 [#]		400.62	
C ^{Tf₂N}	294.06	291.62 291.59		291.63 291.61	
C ¹	287.80	285.32 285.29	285.62 285.61	285.33 285.31	285.62 285.61
C ³		285.99	285.58	286.00	285.59
C ⁴		285.74	285.58	285.74	285.56
C ²	286.65	284.10 283.99	284.26 284.25	284.11 284.01	284.27 284.26
C ⁵		283.70	283.93	283.70	283.89
C ⁶		283.64	283.22	283.55	283.08
C ⁷		282.96	282.41	283.04	282.40
C ⁸					282.97
C ⁹				282.81	281.56
C ¹⁰				282.88	281.35
C ¹¹				282.66	280.98

Table 4: Rescaled binding energies of the different carbon atoms in the reconstructed core level spectra of [BMPyrr]Tf₂N and [OMPyrr]Tf₂N in Figure 17 with a partial comparison to the experimental data. For the positions within the pyrrolidinium cations see inset in Figure 17. (#) The value of N^{Tf₂N} in [BMPyrr]Tf₂N is utilized as reference for the rescaling procedure. Herein, the binding energies are adapted by the following rescaling parameters: a scaling factor of $f = 1.02963$, an absolute shift of $\Delta E = -0.79 eV$ for [BMPyrr]Tf₂N and $\Delta E = -0.77 eV$ for [OMPyrr]Tf₂N, and a relative shift of $\Delta\Delta E_{Cation-Anion} = -1.47 eV$. The binding energies of the neat pyrrolidinium-based cations are obtained by an identical scaling factor as used for [BMPyrr]Tf₂N and they are finally shifted by $\Delta E = -5.66 eV$ for [BMPyrr]⁺ and $\Delta E = -5.61 eV$ for [OMPyrr]⁺ to match the value of N^{Pyrr} of the ion pair.

and the initial carbon of the alkyl chain (C^4) is identified approximately 0.25 eV below. Whereas, the two pyrrolidinium carbons directly bond to nitrogen (C^1) have possessed a binding energy of circa 0.7 eV below those of the methyl group at highest position. Thus, the contributions of these four carbon atoms can be clustered together (see Figure 17), since they are ascertained to be very close to each other, which is in the order of experimental peak broadening. However, for the neat cations, $[BMPyrr]^+$ and $[OMPyrr]^+$, a reverse order of the positions C^1 , C^3 , and C^4 (from highest to lowest binding energy) is found. The total energetical splitting between these four carbon atoms is identified as 0.04 eV for $[BMPyrr]^+$ and 0.08 eV for $[OMPyrr]^+$. Thus, one may assume that a distinct effect of the $[Tf_2N]$ anion onto binding energy of certain carbon positions is present.

Further on, the distance between the lower energy side of this first peak (C^1) and the next binding energy position C^2 is encountered to be approximately 1.2 eV. The energetic distance between the further two carbons within the pyrrolidinium ring (C^2) and the alkyl carbon (C^5), which both are not directly bound to nitrogen, is determined to be in the range of 0.3-0.5 eV. While, a separation between C^5 and the next carbon (C^6) in the order of ≤ 0.15 eV is recognized. The energetic distance to the proximate alkyl carbon (C^7), i.e. the terminal methyl group in the butyl chain of $[BMPyrr]Tf_2N$ or the fourth carbon in the octyl chain of $[OMPyrr]Tf_2N$, is located at circa 0.6-0.7 eV, which is close to the applied peak broadening. A separation between C^2 and C^5 in the same order is detected for the neat cations $[BMPyrr]^+$ and $[OMPyrr]^+$. In these the binding energy position for the first alkyl carbons not directly bound to nitrogen (C^5 , C^6 , and C^7) has shifted approximately 0.7-0.8 eV towards lower binding energy per each atom further away from the nitrogen in the cations. This is ascertained in contrast to the energetic order in $[XMIm]Tf_2N$ (cf. Table 3). In comparison to the ion pair, where C^5 and C^6 are only separated by maximum 0.15 eV, the influence of the anion is obviously perceptible. Consequently, on the one hand the carbons C^2 and C^{5+6} from the ion pair calculation may be clustered either as one single peak or two interleaved peaks and on the other all further alkyl carbons starting at C^7 have to be treated as a further group of states. For binding energy positions from C^7 to C^{11} in $[OMPyrr]Tf_2N$ a smaller shift in the order of -0.10 eV per atom is assigned, since these carbons are less affected by nitrogen due to their increased distance. This shift is observed in similar way in the experimental C1s structure together with an enhanced peak intensity (cf. Figure 12, right). However, this effect has not homogeneously

propagated through the whole alkyl chain, as found for the isolated [OMPyrr] cation or for the imidazolium-based ionic liquids. A slight deviation in the order is recognized for C⁹ and C¹⁰, which have changed their positions. The respective energetic distance between these two carbons is discovered to be about 0.1 eV, which is in the order of exactness of calculated binding energies as well as a slightly different chemical environment for C¹⁰ due to the neighboring terminal methyl group. In addition, the shift in binding energy of the carbons to lower values with increased distance to the nitrogen atom is confirmed to propagate through the part of the alkyl chain far away from nitrogen of the single [OMPyrr] cation. A nearly constant value of around -0.35 eV per additional atom is existent here. The distance between C^{Tf₂N} and the lower binding energy peak in the cations double peak structure is experimentally derived with about 7.4 eV for [BMPyrr]Tf₂N, whereas in the reconstructed spectra using a single ion pair a marginally increased distance of circa 7.8 eV is observed. The enlarged distance between the carbons directly bound to nitrogen and the further carbons in the alkyl chain in the theoretical reconstruction compared to the experiment was previously identified for imidazolium-based ionic liquids, too. This may be interpreted as an effect of the interaction beyond a single ion pair, which is not considered in the utilized single ion pair calculation. The origin of the recognized binding energy order in ion pairs from [XMPyrr]Tf₂N is subsequently analyzed further.

4.2.2 Influence of partial charges and geometrical distances on the binding energy order

The deviations in binding energy of carbon atoms are observed for the ion pair and the isolated cation, which could potentially be caused by different partial charges found in both molecular systems. This is based on the NBO charge analysis of the various carbons in Table 5. The NBO partial charges from a comparison between the same carbon atoms in [OMPyrr]Tf₂N and [OMPyrr]⁺ have varied at maximum by an absolute value of 0.012 e or a relative one of less than 4 %. However, the biggest deviations in the partial charges between ion pair and neat cation are recognized for the first carbon atoms of the alkyl chain (C⁴-C⁶), which have featured a clear interaction with the [Tf₂N] anion. In relation to this the partial charge of the cations' central nitrogen atom, which is used as reference for rescaling, has only changed by 0.001 e and, thus, an inappropriate comparison of the binding energies can be excluded. Additionally, these

	[OMPyrr]Tf ₂ N	[OMPyrr] ⁺
Atom	NBO partial charge (e)	
N ^{Pyrr}	-0.299	-0.300
C ¹	-0.263	-0.259
	-0.255	-0.260
C ²	-0.497	-0.500
	-0.498	-0.499
C ³	-0.480	-0.484
C ⁴	-0.249	-0.258
C ⁵	-0.499	-0.487
C ⁶	-0.453	-0.456
C ⁷	-0.460	-0.458
C ⁸	-0.456	-0.458
C ⁹	-0.460	-0.460
C ¹⁰	-0.458	-0.460
C ¹¹	-0.685	-0.687

Table 5: NBO partial charges (in e) for different carbons of the [OMPyrr]Tf₂N ion pair and the isolated cation [OMPyrr]⁺. For respective nomenclature of carbon atoms see inset in Figure 17.

perceptible shifts of the alkyl chain carbons (not directly bound to nitrogen) have not resulted from different partial charges (cf. discussion performed later). The NBO charge analysis has provided nearly equal partial charges for all alkyl carbons C⁶-C¹⁰ except for the terminal carbon C¹¹. An approximately 0.225-0.230 e higher negative partial charge is offered by this terminal carbon than found for the others. This carbon also possessed an additional hydrogen atom, which has typically featured a positive partial charge in the order of +0.23 e. Under consideration of this aspect, the partial charge of the terminal carbons is similar to those of the other alkyl carbons, which are CH₂ groups instead of CH₃. A charge-related shift in binding energy of the C1s states in the order of 6 eV/e is assigned in ref. [126]. The maximum shift caused by the detected differences in partial charges is below 0.08 eV for all carbon atoms in the ion pair compared to those of the neat cation. Thus, the main contributions of these binding energy shifts have resulted from another reason. Since the considered NBO charges have not revealed the complete answer to the changes in the C1s core levels between ion pair and neat cation, the interaction between cation and anion has to be examined further.

First hints are obtained in the order of binding energies of the carbons directly bound to nitrogen, which have altered their order in the [BMPyrr]Tf₂N

	N ^{Tf2N}	O ¹	O ²	F
Atom	Distance (Å)			
N ^{Pyrr}	3.94	4.21	4.68	4.58
C ¹	3.49	3.29	4.77	5.16
	3.37	4.54	3.37	3.70
C ²	3.52	4.00	4.25	5.48
	3.49	4.77	3.00	4.68
C ³	5.36	5.56	5.81	5.84
C ⁴	4.32	4.22	5.33	4.34
C ⁵	3.58	3.40	4.93	3.45
C ⁶	4.86	4.40	6.19	4.14
C ⁷	4.93	4.42	6.39	4.09

Table 6: The geometrical distances (in Å) between the atoms within the [BMPyrr] cation and selected atoms of the [Tf₂N] anion, which are tabulated for the utilized ion pair from [BMPyrr]Tf₂N (for the affiliation of the carbon atoms see inset in Figure 17).

and [OMPyr]Tf₂N ion pairs compared to the neat cations (cf. Table 4). A reason of the selective interactions between different carbon atoms within the cation and the [Tf₂N] anion might be found in the geometric relationship between the respective carbon and the [Tf₂N] anion. In Table 6, the distances between all carbon atoms within the [BMPyr] cation and the nearest atoms in the [Tf₂N] anion of the utilized ion pair are listed. An effect onto the carbons C¹, C³, and C⁴, which are previously detected at nearly the same energy, is recognized from Table 6: one or both C¹ carbons are typically localized closer to all considered atoms of the anion than those of C³ and C⁴. Thus, one is enabled to suppose that this effect is accompanied by a higher interaction for C¹, which has led to a shift to a lower binding energy, while those of C³ and C⁴ are less influenced and shifted in the opposite direction relative to the states in [BMPyr]⁺. However, for the carbons C⁵ and C⁶ the energetic difference in the order of 0.7-0.8 eV is detected in the neat cation, whereas it is reduced to 0.06 and 0.15 eV in the respective ion pair. Fluorine and oxygen from the [Tf₂N] anion are identified as the nearest atoms for these carbons, which are followed by the further oxygen and the central nitrogen. Due to these interaction partners a formation of hydrogen bondings may be presumed. The distance to all of the analyzed atoms of the [Tf₂N] anion is ascertained to be 0.7-1.3 Å smaller for C⁵ than for C⁶. Thus, the interaction between cation and anion has led to a readjustment of the binding energies of the states with comparable chemical environment. The

changes in the C1s binding energy positions and their order within the pyrrolidinium ring have provided a fingerprint of the preferred interaction between cation and anion, since these shifts are correlated with the respective distances of the carbons to the nearest atoms of the [Tf₂N] anion. In addition, it might be assumed that for the imidazolium-based cation the distance effect is not relevant, since the anion is present in a symmetrical position (close to C¹) relative to all other carbons. While, for the pyrrolidinium-based cation the anion is located in an asymmetric position to the alkyl chains. These conclusions are not in contradiction to the results of A. R. Santos et al. [140], which have noticed a stronger interaction between cation and anion for pyrrolidinium-based ionic liquids due to a charge localization on the central nitrogen atom compared to their imidazolium-based analog with a charge distribution over both nitrogens.

The binding energies of carbon atoms inside of the cations and their geometric distances to the anion in ion pairs of [OMPyrr]Tf₂N and [OMPyrr]Cl are listed in Table 7. Herein, all binding energy positions are normalized for reason of comparison to the nitrogen in the pyrrolidinium-based cation. The respective distances between atoms of the [OMPyrr] cations and the central nitrogen atom in the [Tf₂N] or the chlorine anion are added in Table 7. A similar order and comparable differences of the relative binding energy positions are identified in [OMPyrr]Tf₂N and [OMPyrr]Cl for the two groups of carbon atoms C¹-C⁵ and C⁹-C¹¹, whereas for C⁶-C⁸ stronger deviations are noted. The alkyl chain of the cation in [OMPyrr]Cl is twisted from the ideal zigzag structure, which is present in [OMPyrr]Tf₂N, and as a result the alkyl carbons have featured a slight π electron system. This π electron contribution might also lead to the almost degeneration of the binding energies of the carbons C⁵ and C⁶ as well as C⁷ and C⁸. In addition, nearly identical distances are featured between the atoms in the cation (N^{Pyrr} and C¹-C¹¹) and the central atom in the anion (N^{Tf₂N} or Cl). The related values are typically similar, but around 0.1 Å smaller for [OMPyrr]Cl compared to [OMPyrr]Tf₂N. Perceptible deviations are only detected for the carbons C⁶, C⁸, and C¹⁰ due to the twisted alkyl chains. This means that the positions of the centers of both anions are comparable. As a consequence of this comparison between [OMPyrr]Tf₂N and [OMPyrr]Cl, it can be concluded that the previously found changes in the energetic order and binding energy positions of the pyrrolidinium-based cations are induced by the [Tf₂N] anion, while the interaction can be reduced to a simple cation-anion distance effect.

	[OMIm]Tf ₂ N	[OMIm]Cl	N ^{Tf₂N}	Cl
Atom	Calculated binding energies (eV)		Distance (Å)	
N ^{Pyrr}	403.84 [#]	403.84 [#]	3.94	3.82
C ³	286.00	286.10	5.36	5.25
C ⁴	285.74	285.79	4.32	4.18
C ¹	285.33	285.26	3.38	3.37
	285.31	285.20	3.48	3.29
C ²	284.11	284.17	3.51	3.54
	284.01	284.08	3.51	3.43
C ⁵	283.70	283.72	3.58	3.51
C ⁶	283.55	283.73	4.87	4.64
C ⁷	283.04	283.32	4.95	4.87
C ⁸	282.97	283.31	6.46	6.26
C ⁹	282.81	283.22	7.02	6.93
C ¹⁰	282.88	283.30	8.55	8.38
C ¹¹	282.66	283.11	9.33	9.25

Table 7: The binding energies (in eV) of the carbon atoms of the [OMPyr] cation, which have shaped a similar ion pair together with an anion of [Tf₂N]⁻ or [Cl]⁻, are related to the respective geometrical distances (in Å) to the anion. (#) All reconstructed spectra are normalized onto the binding energy value of N^{Pyrr} for [BMPyr]Tf₂N in Table 4. Herein, an identical scaling factor of $f = 1.02963$ and for the pyrrolidinium-based cation in [OMPyr]Tf₂N an absolute of $\Delta E = -0.77 \text{ eV}$ as well as a relative shift of $\Delta\Delta E_{\text{Cation-Anion}} = -1.47 \text{ eV}$ are employed. In contrast to this, the contributions of [OMPyr]Cl are modified by an overall shift $\Delta E = -1.75 \text{ eV}$.

4.3 Copper-containing ionic liquids

Parallel to the evaporation of metals onto ionic liquids, which will be discussed in Chapter 9.1, and the subsequent degradation of the ionic liquid to generate nanoparticles for catalytic applications another possibility for catalytic applications may be provided by intrinsic incorporation of metal atoms into the ionic liquid (cf. refs. [128, 141]). The respective metal atoms are integrated in the cation, the anion or both, and a frequently central coordinating position surrounded by functional groups known from neat ionic liquids is featured [128, 129]. A set of copper-containing ionic liquids is utilized for catalytic applications, such as the oxidative carbonylation of methonal, which is typically accompanied by a handful of disadvantages, inter alia selectivity problems due to undesired side reactions and a low conversion rate [128]. These ionic liquids have exhibited a certain crystal structure in their solid state, which is illustrated in Figure 18. Herein, the ionic liquid is separated into on one hand charged centers with the copper atoms and on the other an area of alkyl crystals, while in the latter van der Waals interactions are relevant. The two imidazolium rings in the $[\text{Cu}(\text{Im}^{12})_2]$ cation are twisted out of plane and the two copper atoms are found with a distance between each other, which is only slightly higher than found in metallic copper [128]. Thus, a significant interaction between these two charged copper atoms is present inside of those substances. Ionic liquids of this type with a shorter alkyl chain are investigated hereinafter.

In Figure 19 (right), the reconstructed and experimental N1s core level spectra are jointly displayed. Herein, the separation of the two different nitrogen

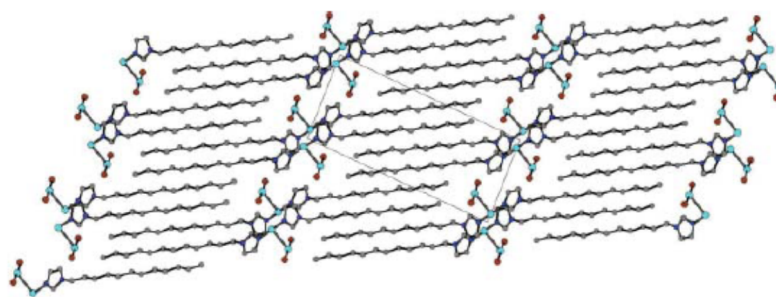


Figure 18: Crystal structure of $[\text{Cu}(\text{Im}^{12})_2]\text{CuBr}_2$ with indication of the unit cell. (With the courtesy of: The Royal Society of Chemistry, M. Stricker et al., Green Chem. 12 (2010) 1589-1598, page 1591 [128])

states has become evident. This is expected from the different chemical environment inside the cations' imidazolium groups depending on the respective bonding partners (see molecular structure in Figure 19, left): the first nitrogen of the imidazolium ring is bound to the central copper atom and the second one is connected to the alkyl chain. In the experimental spectra, the nitrogen at the alkyl site is detected at 401.1 eV for $[\text{Cu}(\text{Im}^6)_2]\text{CuCl}_2$ and at 401.3 eV for $[\text{Cu}(\text{Im}^6)_4]\text{PF}_6$ (cf. 402.3 eV for $[\text{EMIm}]\text{Tf}_2\text{N}$ and 402.4 eV $[\text{OMIm}]\text{Tf}_2\text{N}$ [90]), which are used as references for the rescaling procedure. The nitrogen at the copper site is ascertained in the experiment at circa 400.0 eV for $[\text{Cu}(\text{Im}^6)_2]\text{CuCl}_2$ and 400.1 eV for $[\text{Cu}(\text{Im}^6)_4]\text{PF}_6$, while in the reconstruction both are located at around 399.7 eV. A position, where the contributions of the anions, e.g. $[\text{Tf}_2\text{N}]^-$, are regularly found in other ionic liquids [90], has resulted from the charge neutralization of the imidazolium ring compared to a cation of $[\text{XMIm}]^+$. The calculated separation in the N1s spectra is recognized as larger for the $[\text{Cu}(\text{Im}^6)_4]^+$ than for the $[\text{Cu}(\text{Im}^6)_2]^+$ analog, which is also verified by the experimental spectra. An energetic distinction in between N^{Cu} and N^{Alkyl} of circa 1.4 and 1.6 eV is not exclusively caused by the varied number of imidazolium species in the cation. This fact has also resulted from a different shift in binding energy due to significant distinctions in the mean NBO partial charges of the N^{Cu} of -0.627 e for $[\text{Cu}(\text{Im}^6)_2]^+$ and -0.585 e for $[\text{Cu}(\text{Im}^6)_4]^+$. While, the mean partial charge of the N^{Alkyl} atom is found as similar in both with -0.374 e for $[\text{Cu}(\text{Im}^6)_2]^+$ and -0.380 e for $[\text{Cu}(\text{Im}^6)_4]^+$, respectively. The resulting charge differences between N^{Cu} and N^{Alkyl} are calculated as 0.253 e for $[\text{Cu}(\text{Im}^6)_2]\text{CuCl}_2$ and 0.205 e for $[\text{Cu}(\text{Im}^6)_4]\text{PF}_6$. Thus, the differences in the separation of the two N1s peaks are dominated by the obvious distinction in their partial charges according to the estimated shift of around 6 eV/e [126]. This would lead to a difference in the separation of the N1s states in the order of 0.25-0.30 eV between both ionic liquids, which is in good agreement with the experimentally found disparity of about 0.2 eV. The influence of the unequal anions in both liquids is not regarded here. Nevertheless, no significant differences are observed between the $[\text{Cu}(\text{Im}^6)_2]$ cation combined with the counterions of $[\text{CuCl}_2]^-$ and $[\text{CuBr}_2]^-$.

4.4 Chapter summary

For ionic liquids of $[\text{XMIm}]\text{Tf}_2\text{N}$, we have revealed by means of the employed deconvolution of the C1s core level spectra that the distance to the nitrogen

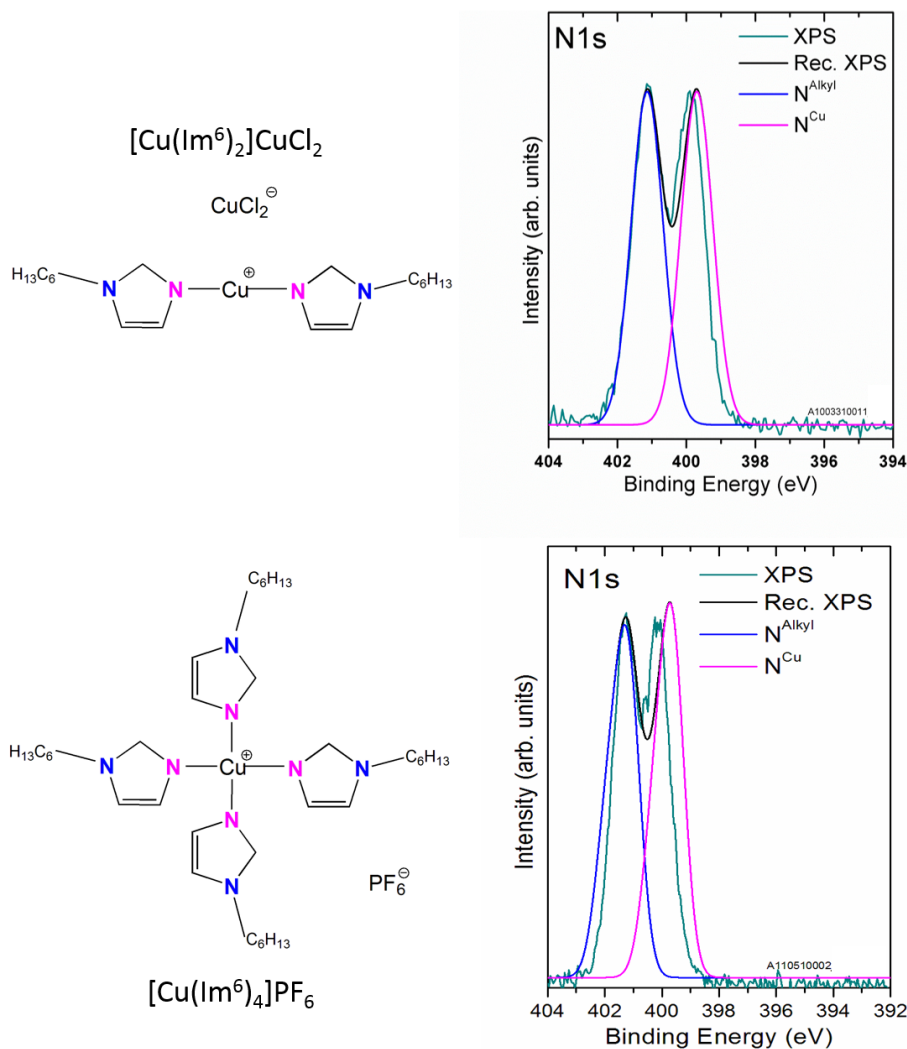


Figure 19: Structure (left) and reconstructed N1s core levels together with the experimental spectrum (right) of the copper-containing ionic liquids $[\text{Cu}(\text{Im}^6)_2]\text{CuCl}_2$ (top) and $[\text{Cu}(\text{Im}^6)_4]\text{PF}_6$ (bottom). The reconstructed spectra are normalized to the peak N^{Im} and, thus, the related rescaling parameters of $f = 1.03045$, $\Delta E = -3.02 \text{ eV}$, and $\Delta\Delta E_{\text{Cation}-\text{Anion}} = -1.05 \text{ eV}$ for $[\text{Cu}(\text{Im}^6)_2]\text{CuCl}_2$ as well as $f = 1.02427$, $\Delta E = +0.25 \text{ eV}$, and $\Delta\Delta E_{\text{Cation}-\text{Anion}} = -0.60 \text{ eV}$ for $[\text{Cu}(\text{Im}^6)_4]\text{PF}_6$ are employed. The experimental spectra of $[\text{Cu}(\text{Im}^6)_2]\text{CuCl}_2$ and $[\text{Cu}(\text{Im}^6)_4]\text{PF}_6$ are obtained from personal communication with Dr. M. Himmerlich and Dr. A. Ulbrich, respectively.

atoms in the imidazolium ring is the dominating effect for the detected binding energy positions [90]. This effect has fully propagated through all carbons, while the very local chemical environment of the carbon (CH, CH₂ or CH₃ group) has not affected the exact binding energy position. In comparison to this, the binding energies of the C1s states of a set of pyrrolidinium-based ionic liquids [XMPyrr][Tf₂N] have not exclusively resulted from the distance to the central nitrogen atom. Herein, a distinct fingerprint of an interaction between [Tf₂N] anion and the cations' carbon atoms within the pyrrolidinium ring and the first ones of the longer alkyl chain is recognized, which has primarily resulted from a cation-anion distance effect. This is not in contradiction to ref. [140], where a principally stronger interaction between both ions due to an intensified localization of charge is assigned in contrast to the imidazolium-based analog. Thus, the model for a deconvolution of the C1s core level spectra of pyrrolidinium-based ionic liquids, which was sketched by S. Men et al. [136], is verified in principle by the reconstruction method. This model can be modified due to the interaction between the ions by use of the peak 'C^{inter}', which is composed of C², C⁵, and C⁶ instead of the indicated assignment, where the latter peak was attributed to the regular alkyl chain in ref. [136]. For the copper-containing ionic liquids of [Cu(Im⁶)₂][CuCl₂] and [Cu(Im⁶)₄][PF₆], the separation of the N1s core level states are substantially influenced by the different partial charges found for N^{Cu} in the ionic liquids with two and four imidazolium rings attached to the central copper atom.

5 Analysis of the degradation of [EMIm]Tf₂N on the atomic scale

The degradation of materials is an omnipresent process, which is caused by the exposure of a material to specific environmental conditions. For certain applications this phenomenon is desired, whereas for others the degradation has to be understood as a limiting factor. In green chemistry using ionic liquids, the degradation, which is realized by natural processes (biodegradability), is favored for an environmentally friendly disposal after a common technological utilization period (cf. refs. [142, 143]). The degradation due to the existent environment is observed as a limitation for the application, e.g. in case of temperature-induced degradation [144] as well as degradation of an ionic liquid in the presence of other chemical substances, like H₂O₂ [145, 146]. The latter can additionally be employed as a method for disposal of ionic liquids. A desired degradation of ionic liquids for example caused by a plasma treatment is applied to generate metal nanoparticles from the substances, which are previously dissolved or incorporated in ionic liquids [147, 148]. Degradation of ionic liquids due to radiation is not only perceived under extreme application conditions [149], while its impact is already found in common radiation-based measurement techniques [38, 125].

Experimental results of the relevance of X-ray radiation during XPS measurements for the standard ionic liquid of [EMIm]Tf₂N have been obtained by A. Keppler et al. [125]. The influence of measurement time and radiation source, where monochromatic and non-monochromatic Al K_α radiation are used, onto the resulting experimental spectra is investigated in this study. Respective core level spectra (N1s, C1s, and S2p), which are recorded as a function of measurement time and have enabled a comparison between different radiation sources, are visualized in Figure 20. Herein, the following changes in the core level spectra are recognized: in the C1s core levels the peak related to [Tf₂N]⁻ has disappeared over time and the residual peak is slightly shifted towards higher binding energies. The shoulder at the lower binding energy of the [EMIm] cations' C1s states is enhanced in height and the related peak width is clearly broadened. In the N1s states, the initial height ratio of 2:1 between cation and anion related peaks is equalized to the same height and the initial gap between the two peaks is filled. The latter can only be achieved by the states of newly formed species. Additionally, after 12 h of radiation exposure the N1s as well as the C1s peak of

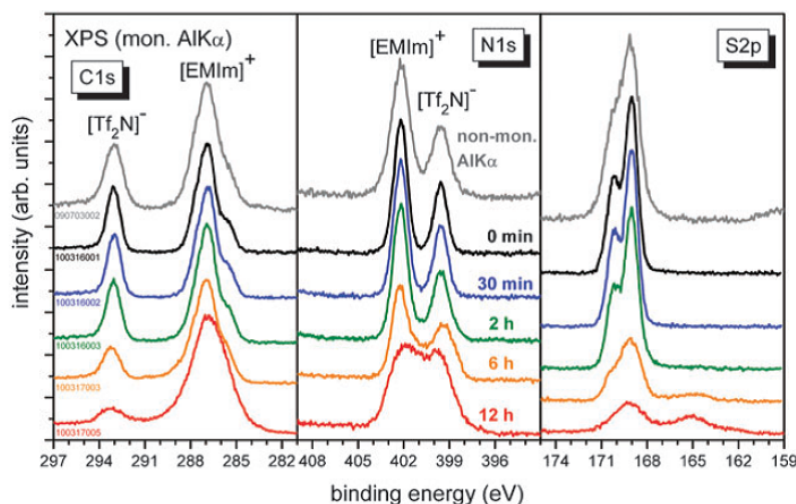


Figure 20: Experimental core level spectra indicating the degradation of [EMIm]Tf₂N by treatment of monochromated X-rays over time with comparison to the respective non-monochromated radiation. (With the courtesy of: The Royal Society of Chemistry, A. Keppler et al., *Phys. Chem. Chem. Phys.*, 13 (2011) 1174-1181, page 1177 [125])

the [EMIm] cation have seemed to be broadened at their higher binding energy sides. The same has slightly occurred at the higher binding energy side of C1s and at the lower of N1s for the [Tf₂N]⁻ anion. In the S2p core levels, the peak intensity is decreased over time compared to the other states, i.e. N1s, and parallel to this a new peak has appeared at a binding energy in the order of 4-5 eV lower than the initial S2p state. These changes in the core level spectra by exposure to monochromatic radiation are interpreted as fingerprints of the remaining species after degradation, which can be identified by means of reconstructed spectra of the related fragments. Finally, the degradation mechanisms can be extracted from the reconstruction by a comparison of the C1s, N1s, and S2p core level spectra of the residual constituents with those of the neat ion pair if similar shifts are provided by the experiment.

For a profound analysis of reconstructed core level spectra a previous optimization of potential fragments of the original ion pair has required the consideration of the following facts:

- A systematical removal of the respective atoms or groups from one ion of the initial ion pair, which might occur during the degradation processes, is performed.
- For the calculation a system balanced in both charge and spin is essential. This condition has resulted from the reason of comparability of the resulting binding energies to the initial ion pair for which uncontrolled effects by overall charged molecular systems (open-shell calculation) have to be avoided. Due to this reason in some cases the calculation is executed for fragments without the respective counterion.
- The binding energies of the calculated fragments are modified using identical rescaling parameters, i.e. scaling factor f , absolute shift ΔE , and relative shift $\Delta\Delta E_{\text{Cation}-\text{Anion}}$, as applied for the binding energies of the initial ion pair of [EMIm]Tf₂N (cf. Chapter 3.3 and Chapter 4.1). Absolute binding energies, which are not fully reproduced by the reconstruction except of the core levels used for normalization, are less important for the identification of potential fragments than the relative shifts herein. In addition, it has to be noted that the separation in the S2p states due to spin-orbit coupling cannot be reproduced by the quantum-chemical calculation.

Hints for present the degradation mechanisms of cation and anion were concluded in the experimental studies in refs. [38, 125]: for example a neutralization of the imidazolium cation is assumed. The imidazolium ring is identified as highly stable in the experiment. This is reproduced by the quantum-chemical calculation, since every incorporated ring opening/bond interruption is reconnected during subsequent optimization. Thus, for the cation degradation the removal of alkyl chains and hydrogen atoms will be considered for the degradation analysis. For the [Tf₂N] anion a significantly stronger impact by degradation is recognized. Herein, especially the detachment of the CF₃ groups, oxygen atoms, and bond breakage between nitrogen and sulfur is assumed. In consequence, the degradation of imaginable anion parts, such as single fluorine or oxygen atoms as well as CF₃ and larger groups, will be analyzed afterwards.

5.1 Cation degradation

The reconstructed N1s and C1s spectra of potential remaining fragments with removal of segments of the alkyl chains and single hydrogen atoms are displayed in Figures 21-23. If the respective binding energy shifts previously observed in the experiment are also recognized in the reconstructed spectra of certain fragments one has found a significant hint. Additionally, the removed part from the respective ion should not be in contradiction to the mass spectroscopy results (cf. ref. [125]), since this part is most probably released into the gas phase and will be detected by the mass spectrometer. The S2p states of $[\text{Tf}_2\text{N}]^-$ are not visualized, since the anion is only present in a very few calculated systems due to the reason of charge and spin balance as well as major changes herein are primarily expected during the anion degradation.

5.1.1 Alkyl chain degradation

The degradation of the cations' alkyl chains, i.e. the methyl group, ethyl chain or both, is displayed in Figure 21. Herein, the removed parts are indicated and their reconstructed N1s and C1s core levels as well as the optimized residual fragment of $[\text{EMIm}]\text{Tf}_2\text{N}$ are displayed in comparison to the initial ion pair. In the N1s peak, where one of both alkyl chains is detached, the nitrogen with remaining alkyl chain is shifted into the gap between two initial peaks of the neat $[\text{EMIm}]\text{Tf}_2\text{N}$ with a position more directed towards the former $[\text{Tf}_2\text{N}]^-$ anion. Whereas, those without alkyl chain are located at a binding energy approximately 5 eV beneath the initial N^{EMIm} . These are accompanied by a peak shift in the C1s states towards lower binding energies, which has occupied the position of the shoulder of the initial cation peak assigned to the carbon C^4 . These facts are found in strong agreement with the experimental observations.

The removal of the CH_3 tail group of the ethyl chain has resulted in a single N1s peak structure from the $[\text{EMIm}]$ cation, which is shifted in the order of 2 eV towards lower binding energies into the gap between the two N1s peaks in neat $[\text{EMIm}]\text{Tf}_2\text{N}$. Herein, no significant separation between the nitrogens with CH_3 and remaining CH_2 group is recognized, which has further supported the strong influence of the nitrogens in imidazolium-based ionic liquids (cf. Chapter 4.1). In contrast, the C1s peaks of the carbons inside the imidazolium ring and the methyl group are discovered at around the initial C^4 position, while those of the CH_2 group is shifted about 2.5 eV towards lower binding energies. For the

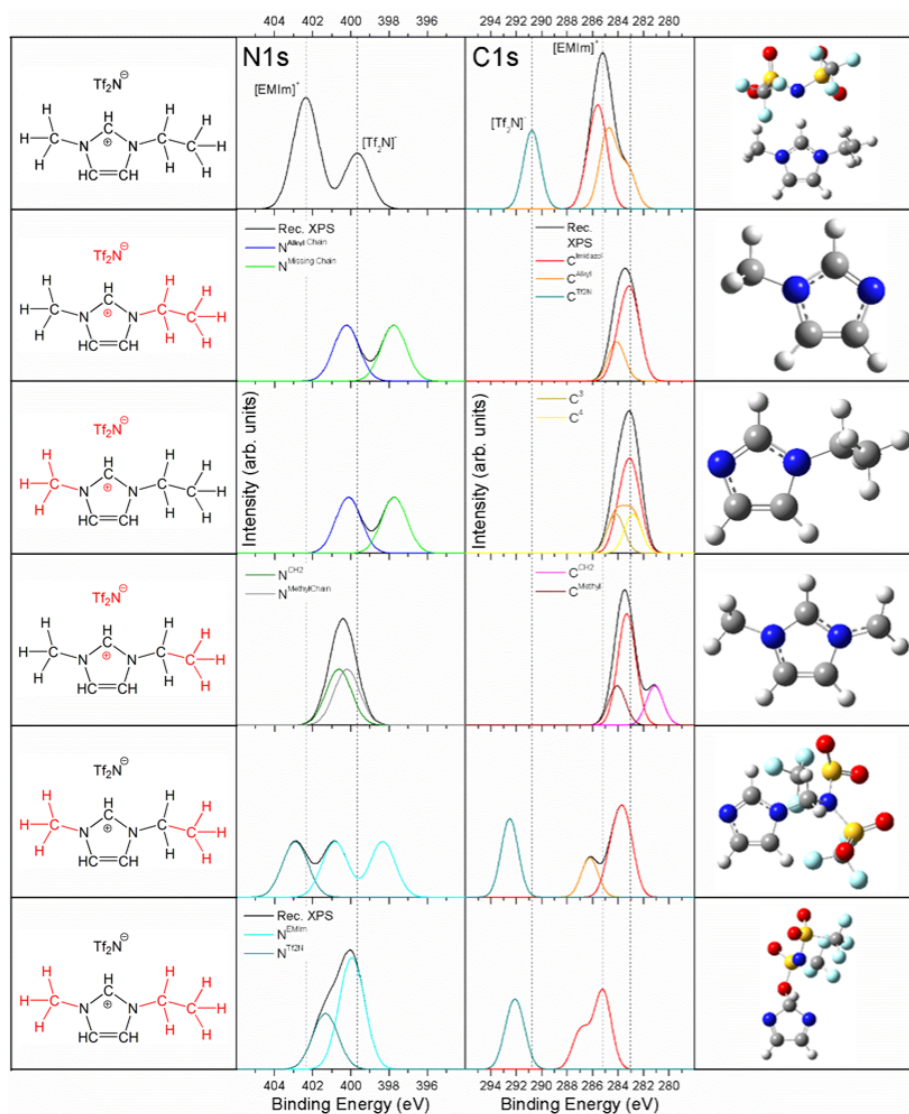


Figure 21: Reconstructed XPS core level spectra (N1s and C1s) for the degradation of the alkyl chain of the [EMIm] cation in [EMIm]Tf₂N. The alkyl parts, which are removed, are indicated (left) and the calculated geometry of the residual fragment is depicted (right). For comparison the spectra and geometry of the reference ion pair are displayed (top line) and the initial peak positions of [EMIm]Tf₂N are illustrated by guidance lines. All spectra are modified by the same rescaling parameters as used for [EMIm]Tf₂N ($f = 1.02838$, $\Delta E = -1.36 \text{ eV}$, and $\Delta\Delta E_{\text{Cation}-\text{Anion}} = -1.10 \text{ eV}$).

removal of the CH_3 groups of both alkyl chains the cations' N1s peak is displaced to lower binding energies and are separated into comparable positions of the previously described fragments with one removed alkyl chain. On the contrary, the N1s peak of the $[\text{Tf}_2\text{N}]$ anion is found at higher binding energies even slightly above the initial N^{EMIm} peak, which could result from a neutralization of the anion.

If both alkyl chains are entirely removed the N1s peaks of the cation and anion have nearly changed their initial positions. The C^2 from the main C1s peak has remained at its initial position, while a the state of the C^1 carbon is shifted towards higher binding energies. These results are distinctly influenced by the strong interaction between the $[\text{Tf}_2\text{N}]$ anion and the central C^1 , which has complicated any exact assignment.

The N1s core level spectra have revealed that in all cases of alkyl degradation a state in between the initial peaks can be found, which would be able to fill the previously mentioned gap. For the C1s states a clear shift of the carbons inside imidazolium ring and partially the remaining alkyl carbons is detected for all cases except for the entire degradation of both alkyl chains, where the residual cation fragment is strongly affected by the anion interaction. Nevertheless, all alkyl degradations have featured decent hints that these might be present during the experimental radiation exposure of $[\text{EMIm}]\text{Tf}_2\text{N}$. In the measured mass spectra peaks are identified at respective m/z values of 15 and 29 for the alkyl chains, which notwithstanding might have contained more than one potential group.

5.1.2 Hydrogen degradation

Another case of degradation of the $[\text{EMIm}]$ cation is assumed by the removal of hydrogen atoms from the carbons at the imidazolium ring and the alkyl chains. For this purpose, single hydrogens at all cation carbons are systematically removed. In Figure 22, the reconstructed N1s and C1s spectra of the cation with removed hydrogen from the ethyl chain and the central carbon (C^1) are depicted. The N1s contribution of the cation is shifted into the gap present between the initial peaks related to $[\text{EMIm}]^+$ and $[\text{Tf}_2\text{N}]^-$ for the hydrogen removal at the C^3 carbon in the ethyl chain. Nearly all C1s peaks are accompanied by a shift towards lower binding energies and a slight change of the intrinsic order, where the C^3 with a missing hydrogen is now found at a similar binding energy position as the C^4 (for nomenclature see Figure 9). A strong kink (in plane with

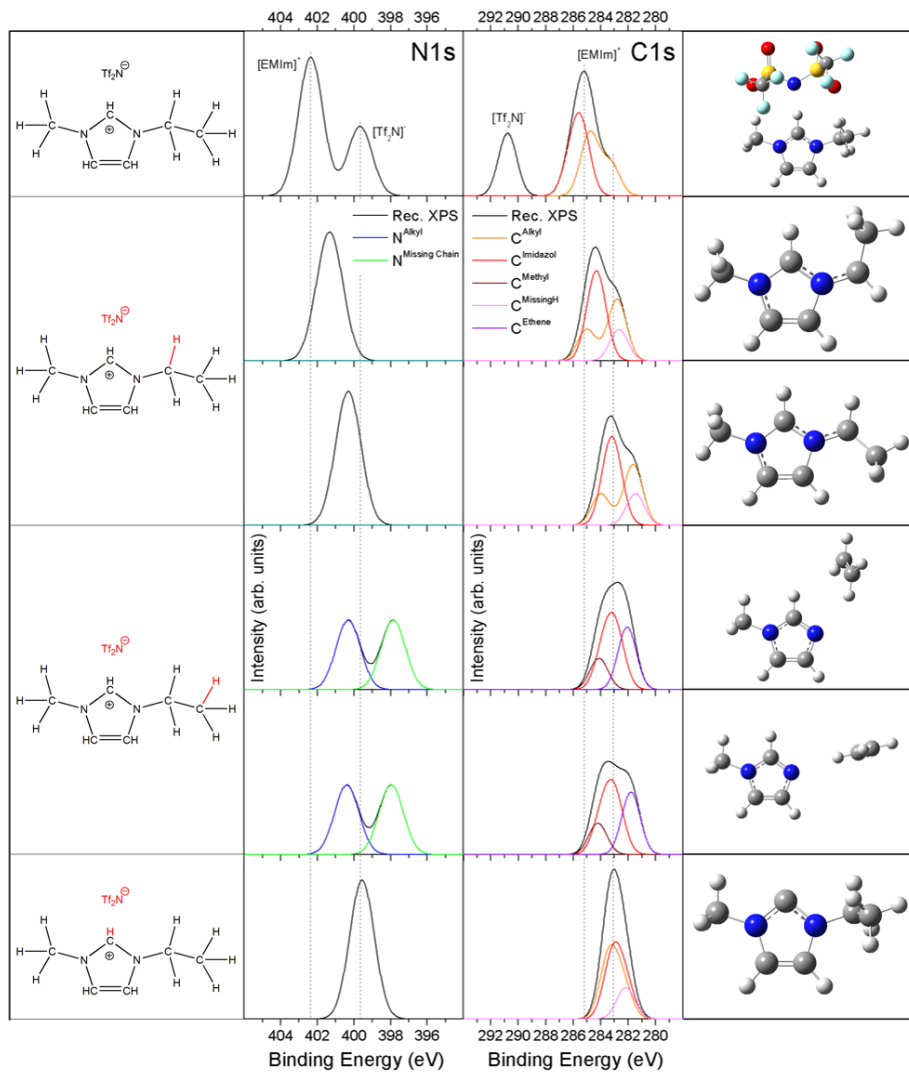


Figure 22: Reconstructed XPS core level spectra (N1s and C1s) for the degradation of a single hydrogen atom of the [EMIm] cation in [EMIm]Tf₂N. The hydrogen atom, which is removed, is indicated (left) and the calculated geometry of the residual fragment is depicted (right). For comparison the spectra and geometry of the reference ion pair are displayed (top line) and the initial peak positions of [EMIm]Tf₂N are illustrated by guidance lines. All spectra are modified by the same rescaling parameters as used for [EMIm]Tf₂N ($f = 1.02838$, $\Delta E = -1.36 \text{ eV}$, and $\Delta\Delta E_{\text{Cation}-\text{Anion}} = -1.10 \text{ eV}$).

the imidazolium ring) in the ethyl chain at the less hydrogen-containing carbon is observed. In comparison to this, for the respective ion pair the ethyl chain is directed out of plane.

In the second case, where a hydrogen atom is removed from the ethyl chains' terminal CH_3 group, the residual alkyl chain (C_2H_4) is detached from the imidazolium ring and most probably released into the gas phase. Thus, the reconstructed N1s states with a split and shift towards lower binding energies as well as the C1s spectra of the remaining fragment with a position at approximately the initial C^4 are found in strong agreement to the previously discussed case, where a whole alkyl chain is removed (cf. Chapter 5.1.1). An additional peak from the separated ethene is detected at binding energies in the range between 282 and 281 eV, which is located slightly below the initial C^4 state. This C_2H_4 group will be primarily transferred into the gas phase and as a result will not be detected experimentally if it is not dissolved in the ionic liquid.

If the single hydrogen from the central carbon of the imidazolium ring (C^1) is removed the N1s peak is discovered at a binding energy of the initial $\text{N}^{\text{Tf}_2\text{N}}$ due to the less positive charge or a neutralization of the imidazolium ring (cf. Figure 22). For the C1s spectrum, only one sharp single peak is detected at approximately the initial position of the C^4 . All carbon atoms of imidazolium ring and the alkyl chains are found at a similar position in contrast to the initial ion pair, while the C^1 has shaped the lower binding energy edge due to the missing hydrogen.

In Figure 23, a hydrogen atom is detached from the methyl group. Herein, the remaining CH_2 group has seemed to be bound stronger to the nitrogen by formation of a contribution of π electrons. The respective N1s peak is recognized in the gap of the two peaks from the $[\text{EMIm}]\text{Tf}_2\text{N}$ ion pair with a location more directed towards the initial $\text{N}^{\text{Tf}_2\text{N}}$ peak. A significant shift in the C1s structure has occurred to approximately the binding energy of the initial C^4 carbon. Additionally, this peak has offered a shoulder, which has resulted from the C^3 position, where the hydrogen was removed.

For the removal of the hydrogen in the two C^2 positions, the N1s peak is located at the same position in between the two initial peaks in $[\text{EMIm}]\text{Tf}_2\text{N}$ as found for hydrogen removal at the C^1 and C^3 carbons. The related C1s spectrum is ascertained with states between the initial main peak and its shoulder, while also a second peak at lower binding energies is present herein. However, the removed hydrogen from this position has caused a stronger shift of this

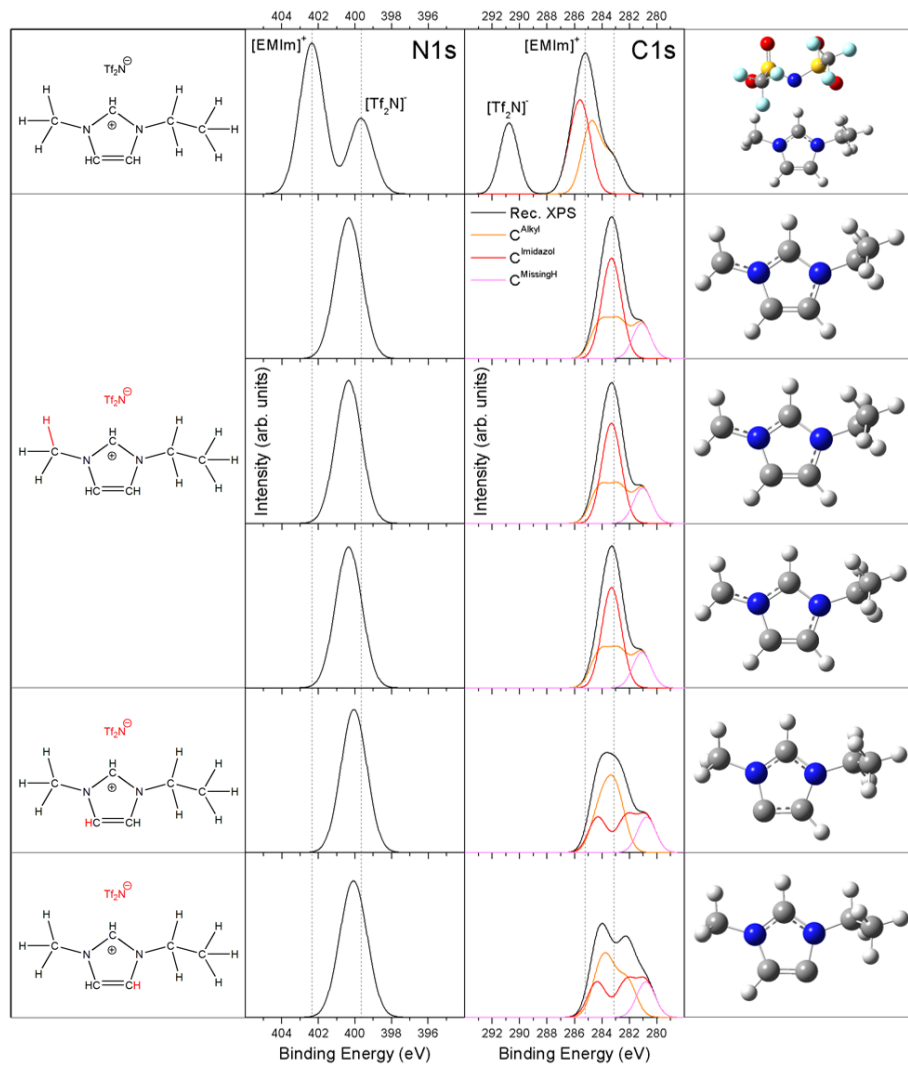


Figure 23: Reconstructed XPS core level spectra (N1s and C1s) for the degradation of a single hydrogen atom of the [EMIm] cation in [EMIm]Tf₂N. The hydrogen atom, which is removed, is indicated (left) and the calculated geometry of the residual fragment is depicted (right). For comparison the spectra and geometry of the reference ion pair are displayed (top line) and the initial peak positions of [EMIm]Tf₂N are illustrated by guidance lines. All spectra are modified by the same rescaling parameters as used for [EMIm]Tf₂N ($f = 1.02838$, $\Delta E = -1.36 \text{ eV}$, and $\Delta\Delta E_{\text{Cation}-\text{Anion}} = -1.10 \text{ eV}$).

carbon towards a lower binding energy. In addition, the peak structures of the imidazolium ring and the alkyl parts have partially changed their positions compared to all other cases of hydrogen removal.

For all resulting spectra with hydrogen removal the N1s state related to the cation is located in between the two initial peaks as found experimentally. All C1s structures have offered a main peak at the initial C⁴, which has designated hydrogen detachment as a possible degradation mechanism. These results are not found in contrast to the mass spectroscopy results, where peaks are present at the m/z values for pure hydrogen and C₂H₄.

5.2 Anion degradation

For the degradation of the [Tf₂N] anion different mechanisms are imaginable, these could comprise the detachment of single terminal atoms, i.e. fluorine and oxygen, or larger groups, for example CF₃, CF₃SO₂ or CF₃SO₂N. Prior to the consideration of the degradation, the decomposition energies along the different bonds inside the anion were determined by a scan along the respective bond. These scans have offered the following overview: the decomposition barriers for the bonds inside the CF₃ and SO₂ groups are determined as slightly higher (in the order of 1 eV) compared those in between carbon and sulfur as well as sulfur and nitrogen. Nevertheless, this in principle means that degradation or bond opening could occur any part of the [Tf₂N] anion. The core level spectra (N1s, C1s, and S2p) are reconstructed for several possible fragments of the [Tf₂N] anion from the initial ion pair of [EMIm]Tf₂N and their relative shifts are subsequently correlated to the previously discussed experimental shifts.

5.2.1 Fluorine degradation

For this type of degradation, a number of different systems have to be considered. A signal, which can be related to a single fluorine atom, is frequently detected in the experimental mass spectra. Nevertheless, these could result from a further degradation of a larger group and, thus, an additional view will be given to the cases of two, three, and six fluorine atoms detached from the [Tf₂N] anion.

The reconstructed XPS core level spectra (N1s, C1s, and S2p) for the case of a single fluorine detachment are displayed in Figure 24. In the N1s core levels, a shift of the [Tf₂N] anion state to a position around the initial N^{EMIm} is recognized. The C1s states of the anion are slightly separated into one with three

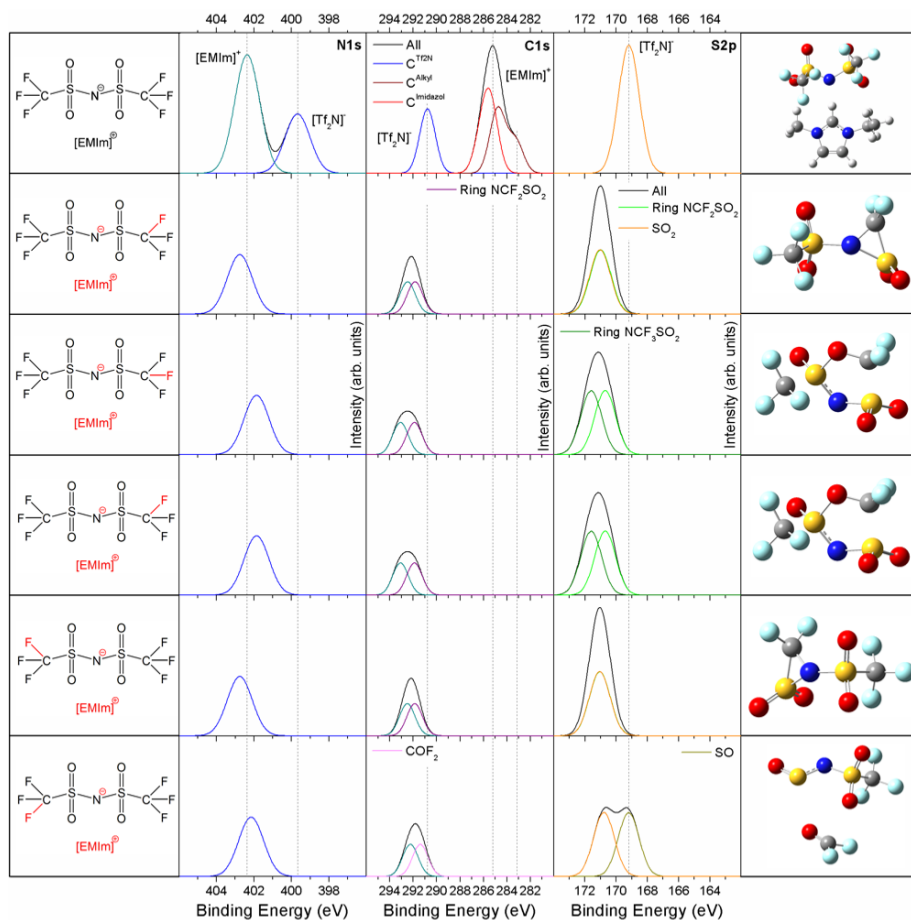


Figure 24: Reconstructed XPS core level spectra (N1s, C1s, and S2p) for the degradation of a single fluorine atom of the $[\text{Tf}_2\text{N}]$ anion in $[\text{EMIm}]\text{Tf}_2\text{N}$. The fluorine atom, which is removed, is indicated (left) and the calculated geometry of the residual fragment is depicted (right). For comparison the spectra and geometry of the reference ion pair are displayed (top line) and the initial peak positions of $[\text{EMIm}]\text{Tf}_2\text{N}$ are illustrated by guidance lines. All spectra are modified by the same rescaling parameters as used for $[\text{EMIm}]\text{Tf}_2\text{N}$ ($f = 1.02838$, $\Delta E = -1.36 \text{ eV}$, and $\Delta\Delta E_{\text{Cation}-\text{Anion}} = -1.10 \text{ eV}$).

fluorine atoms at higher binding energy and the other with two fluorine atoms, which has partially undergone a NCF_2SO_2 ring formation, at lower values. This has caused a broader peak, which is located at circa 1.5 eV above the initial $\text{C}^{\text{Tf}_2\text{N}}$. For the S2p spectrum, a position at higher binding energies is estimated, while only SO has remained at a similar position as the initial SO_2 state due to the neutralization of the anion. A comparable shift to the experimental spectra is exclusively observed in the C1s core levels, which is regarded as an approximate hint. In addition, some of the residual anion fragments have formed a ring structure and it cannot finally be excluded that the missing cation has influenced the core level spectra, since nearly all states are found at higher binding energies. In the experiment it may be assumed that a degradation of a single fluorine will cause a further cascade of detachments from the particular anion fragment.

For the removal of several fluorine atoms, the reconstructed XPS core level spectra (N1s, C1s, and S2p) are depicted in Figure 25. Herein, further reactions, like an oxygen transfer from SO_2 to the CF group, an interaction between the unsaturated carbon and the central nitrogen, a further detachment of SO_2 or the formation and subsequent detachment of CO groups within the residual structure of the anion are recognized.

The reconstructed N1s and C1s spectra for the removal of two fluorine atoms are found in agreement to the initial ion pair of $[\text{EMIm}]\text{Tf}_2\text{N}$, since they have remained at similar positions. Only the formation of CFO or CF groups has led to a shift towards increased binding energies of this C1s state as well as in the N1s core level due to the interaction with the CF group. No significant deviations in the binding energies are observed for the SO_2 groups, which are linked to either CF_3 or CF group. Herein, the SO group has revealed a shift, which is directed to lower binding energies in the order of 2.5 eV.

For the removal of three fluorine atoms, the $\text{N}^{\text{Tf}_2\text{N}}$ state is located at approximately the position of the initial N^{EMIm} , which might result from the reduced negative charge compared to the entire anion. In a similar way, the C1s core level states of the remaining CF_3 and terminal carbon, which is triple bound to the nitrogen in this fragment now, are accompanied by a shift of around 2 eV towards higher binding energies. Analogously, the SO_2 group within this fragment is shifted to a binding energy position about 2.5 eV increased to the state found for the initial sulfur. In contrast, the terminal SO_2 group, which is detached from the fragment and transferred into the gas phase, has located slightly below the initial state, but might be unavailable for the XPS analysis.

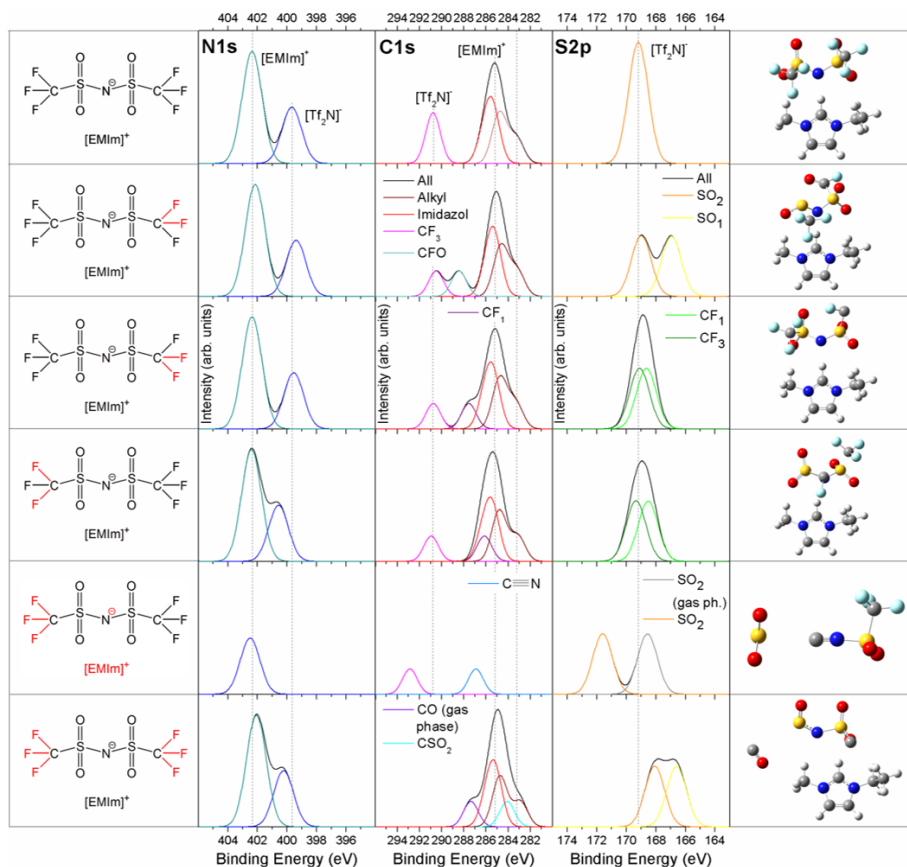


Figure 25: Reconstructed XPS core level spectra (N1s, C1s, and S2p) for the degradation of multiple fluorine atoms of the $[\text{Tf}_2\text{N}]$ anion in $[\text{EMIm}]\text{Tf}_2\text{N}$. The fluorine atoms, which are removed, are indicated (left) and the calculated geometry of the residual fragment is depicted (right). For comparison the spectra and geometry of the reference ion pair are displayed (top line) and the initial peak positions of $[\text{EMIm}]\text{Tf}_2\text{N}$ are illustrated by guidance lines. All spectra are modified by the same rescaling parameters as used for $[\text{EMIm}]\text{Tf}_2\text{N}$ ($f = 1.02838$, $\Delta E = -1.36 \text{ eV}$, and $\Delta\Delta E_{\text{Cation}-\text{Anion}} = -1.10 \text{ eV}$).

In case that all fluorine atoms are removed from the [Tf₂N] anion, the related N1s state is present at slightly higher binding energies, while the N^{EMIm} is detected at the same position as in the initial ion pair. Both anion-related carbon states are located close to or within the C1s contributions of the [EMIm] cation. The S2p core levels are shifted by approximately 1 eV (SO₂ group) and 2.5 eV (SO group) towards lower binding energies.

By means of the observed shifts for the fragments with the removal of several fluorine atoms no distinct hints for this kind of degradation mechanism are observed. A marginal formation of F₂ might be attained in the mass spectroscopy analysis. Thus, it can be assumed that the degradation of single or multiple fluorine atoms is not a dominating degradation process. Nonetheless, the detachment of several fluorine atoms could be present in a further cascade of the anion degradation.

5.2.2 Oxygen degradation

The reconstructed N1s, C1s, and S2p core level spectra for an ion pair with different numbers of removed oxygens are illustrated in Figure 26. No significant differences in the N1s and C1s core levels to neat [EMIm]Tf₂N are recognized for all investigated fragments. Herein, only a slight decrease of the binding energies is present for the anion states, which is found within the typical order of peak width. Significant changes are observed for the S2p state: a position about 2.5 eV lower in binding energy is detected for the SO states, while the SO₂ groups are only marginally shifted to lower values with respect to their initial binding energies. Whereas, the removal of both oxygen atoms from sulfur has caused a shift in the order of nearly -5 eV relative to the initial position of [EMIm]Tf₂N. This particular sulfur shift has provided a significant hint for the degradation of the oxygen atoms, which was detected after a long measurement period of 12 h in the experiment (cf. ref. [125]). The results are additionally supported by the mass spectra. In the experiment, no distinct peak for the degradation of a single oxygen atom is present approximately 2.5 eV below the initial S2p state. Thus, it may be concluded that the degradation of both oxygen atoms from the anions' SO₂ group has occurred simultaneously.

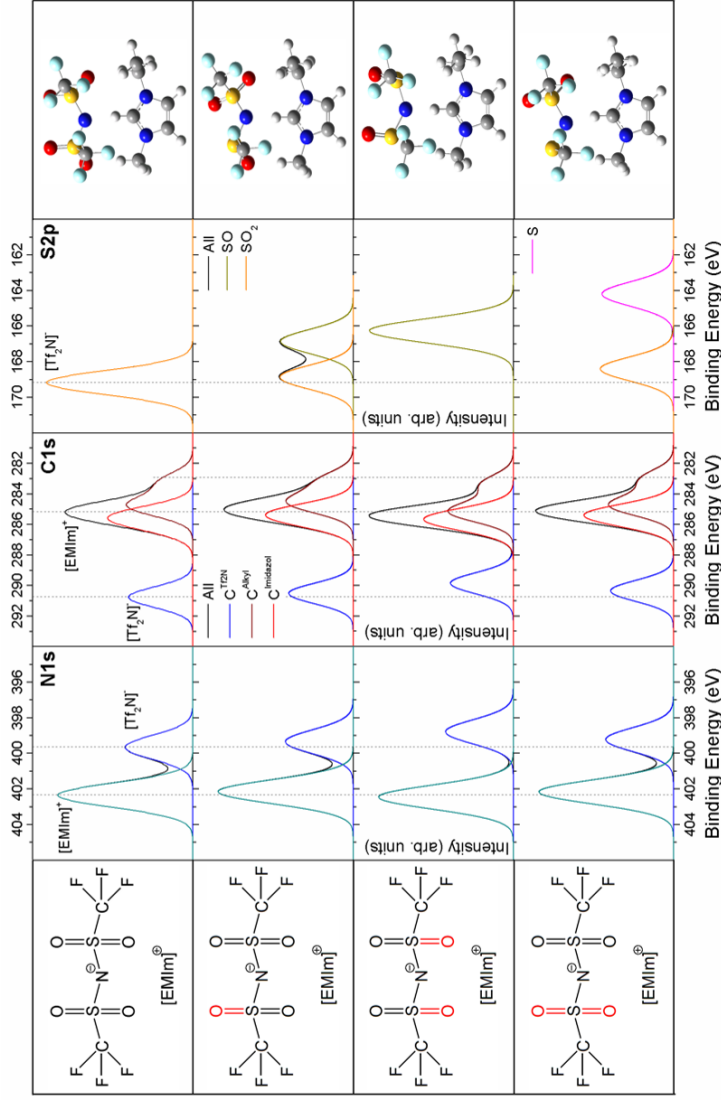


Figure 26: Reconstructed XPS core level spectra (N1s, C1s, and S2p) for the degradation of the oxygen atoms of the $[\text{Tf}_2\text{N}]$ anion in $[\text{EMIm}][\text{Tf}_2\text{N}]$. The oxygen atoms, which are removed, are indicated (left) and the calculated geometry of the residual fragment is depicted (right). For comparison the spectra and geometry of the reference ion pair are displayed (top line) and the initial peak positions of $[\text{EMIm}][\text{Tf}_2\text{N}]$ are illustrated by guidance lines. All spectra are modified by the same rescaling parameters as used for $[\text{EMIm}][\text{Tf}_2\text{N}]$ ($f = 1.02838$, $\Delta E = -1.36 \text{ eV}$, and $\Delta\Delta E_{\text{Cation-Anion}} = -1.10 \text{ eV}$).

5.2.3 Degradation of larger groups

The degradation of the $[\text{Tf}_2\text{N}]$ anion is not limited to the removal of fluorine and oxygen atoms, since a detachment of several larger groups, e.g. CF_3 , CF_3SO_2 , $\text{CF}_3\text{SO}_2\text{N}$ etc., is also imaginable. The N1s, C1s, and S2p core levels of the remaining fragments after removal of trifluoromethyl groups (CF_3) from a reference ion pair of $[\text{EMIm}]\text{Tf}_2\text{N}$ are illustrated in Figure 27. For these fragments the $\text{N}^{\text{Tf}_2\text{N}}$ is recognized slightly above the initial N^{EMIm} state, which might be a result of the anion neutralization. In the C1s core level, the carbon state is present at minimally higher binding energy positions, too. Such effects might also be observed in the experiment by a slight peak broadening and shift of $\text{C}^{\text{Tf}_2\text{N}}$. The S2p states of the SO_2 group surrounded by the regular anion atoms and the terminal SO_2 group have slightly separated and are shifted due to the same reason towards increased binding energies by about 2 and 3 eV, respectively.

After the removal of both trifluoromethyl groups, the cation and anion states have occupied the same positions in the N1s core levels with only a marginal shift towards lower binding energies compared to the ion pair. No significant deviations are observed in the C1s states of the cation, whereas those of the remaining CF_3 group are typically located about 1.5 eV higher. In the S2p states, which are further separated into SO_2N and SO_2 group, related shifts of about -1 eV and -2 eV are detected.

The reconstructed spectra (N1s, C1s, and S2p) for the degradation of CF_3 groups and together with further parts of the $[\text{Tf}_2\text{N}]$ anion from the single ion pair of $[\text{EMIm}]\text{Tf}_2\text{N}$ are depicted in Figure 28. For the detachment of species of CF_3O_2 and CF_3SO_2 , the N1s core level spectra are located above or around the initial N^{EMIm} . Whereas, the C1s core levels have offered a slight shift towards higher binding energies due to a neutralization of the anion. The S2p states are recognized at increased binding energies, while a separation between SO_2 and S in the order of 4 eV is observed.

In case of $\text{CF}_3\text{SO}_2\text{N}$ detachment from the $[\text{Tf}_2\text{N}]$ anion, the N1s state of the cation is detected at slightly decreased binding energies. On the one hand a shift of the anion-related state of around -1.5 eV is observed in the C1s core levels, while on the other the contributions of the cation have remained at their initial binding energy positions. The terminal SO_2 group has offered a binding energy in the order of 3.5 eV beneath the S2p states of $[\text{EMIm}]\text{Tf}_2\text{N}$.

The deviations from the initial ion pair are evaluated as marginal for the re-

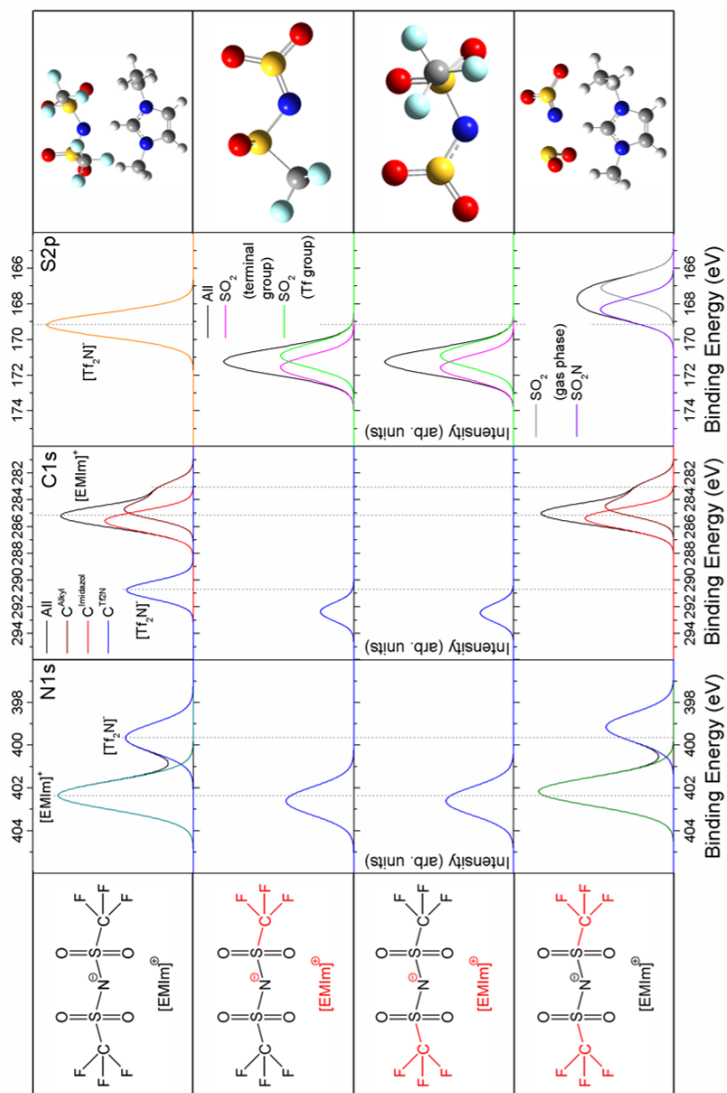


Figure 27: Reconstructed XPS core level spectra (N1s, C1s, and S2p) for the degradation of trifluoromethyl groups of the $[\text{Tf}_2\text{N}]$ anion in $[\text{EMIm}]\text{Tf}_2\text{N}$. The CF_3 groups, which are removed, are indicated (left) and the calculated geometry of the residual fragment is depicted (right). For comparison the spectra and geometry of the reference ion pair are displayed (top line) and the initial peak positions of $[\text{EMIm}]\text{Tf}_2\text{N}$ are illustrated by guidance lines. All spectra are modified by the same rescaling parameters as used for $[\text{EMIm}]\text{Tf}_2\text{N}$ ($f = 1.02838$, $\Delta E = -1.36 \text{ eV}$, and $\Delta\Delta E_{\text{Cation}-\text{Anion}} = -1.10 \text{ eV}$).

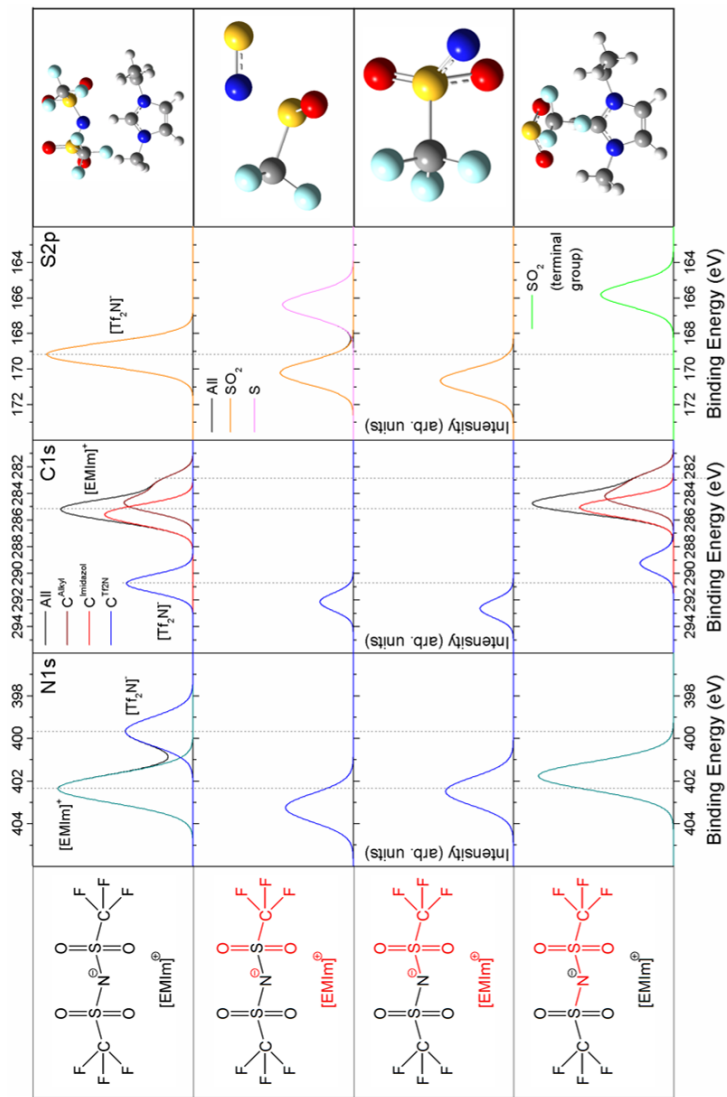


Figure 28: Reconstructed XPS core level spectra (N1s, C1s, and S2p) for the degradation of larger groups of the $[\text{Tf}_2\text{N}]$ anion in $[\text{EMIm}]\text{Tf}_2\text{N}$. The groups, which are removed, are indicated (left) and the calculated geometry of the residual fragment is depicted (right). For comparison the spectra and geometry of the reference ion pair are displayed (top line) and the initial peak positions of $[\text{EMIm}]\text{Tf}_2\text{N}$ are illustrated by guidance lines. All spectra are modified by the same rescaling parameters as used for $[\text{EMIm}]\text{Tf}_2\text{N}$ ($f = 1.02838$, $\Delta E = -1.36 \text{ eV}$, and $\Delta\Delta E_{\text{Cation}-\text{Anion}} = -1.10 \text{ eV}$).

removal of CF_3 groups and are only observed in the respective S2p states. Related signals of CF_3 are detected in the mass spectra, too. These could also result from a further degradation cascade of larger groups, which is indicated from the mass spectra, where additional signals related to the SO_2 and CF_3SO groups are obtained. The latter results are supported by the reconstructed spectra of larger groups, while especially the removal of $\text{CF}_3\text{SO}_2\text{N}$ has seemed to be one of the dominating anion degradation mechanism.

5.3 Chapter summary

Distinct changes in peak positions and heights of the N1s, C1s, and S2p core level spectra caused by radiation-induced degradation are recognized in the experimental spectra (cf. ref. [125]), while similar binding energy shifts are ascertained with the aid of a spectra reconstruction of potential fragments originating from cation and anion. For the [EMIm] cation these mechanisms have not resulted in a total degradation of the ion, since the imidazolium ring is designated as highly stable. The degradation of the alkyl chains and the hydrogens are identified as potential mechanisms. On the contrary, a severe degradation of the [Tf_2N] anion is attributed. Herein, the detachment of oxygen and larger groups, such as CF_3O_2 , CF_3SO_2 , and especially $\text{CF}_3\text{SO}_2\text{N}$, are identified as the main mechanisms. Following this, these larger species have potentially undergone a cascade of further degradation into CF_3 , SO_2 , and also down to their single atoms, since the degradation of single fluorine atoms or the detachment of independent trifluoromethyl groups have not resulted from the reconstructed spectra. Thus, the degradation mechanisms specified in A. Keppler et al. [125] are confirmed by the reconstruction method. In addition, decent hints are found for further co-occurring degradation mechanisms, e.g. the hydrogen detachment has provided similar shifts as detected for the degradation of the cations' alkyl chains and for the [Tf_2N] anion degradation cascades as well as a simultaneous detachment of both oxygen atoms from the sulfur may take place.

Part III

Results of the reconstruction of valence band spectra of neat ionic liquids

The valence band spectra have contained detailed information about the highest occupied states and preferred interaction sites of the present species as well as the related bond type. Thus, the influence of respective interaction sites, which can be caused by different ion pair geometries or variance of the anion conformer, have to be studied prior to a reconstruction of the valence band spectra. The reconstruction is executed for three sets of neat imidazolium- or pyrrolidinium-based ionic liquids of [XMIm]Tf₂N and [XMIm]Cl as well as [XMPyrr]Tf₂N. Finally, the reconstructed XPS, UPS (He II), and partially UPS (He I) valence band spectra are compared to the experimental ones. A decomposition of the reconstructed spectra into the contributions of the related ions and elements is achieved, which was not performed as quantitative analysis previously.

6 Valence band structure of [XMIm]Tf₂N

In this chapter, the valence band spectra are reconstructed for the two imidazolium-based ionic liquids of [EMIm]Tf₂N and [OMIm]Tf₂N. The results for different ion pair geometries and anion conformers in [EMIm]Tf₂N are compared to the preferred interaction sites obtained by molecular dynamics simulations of this ionic liquid. A subsequent reconstruction of the XPS, UPS (He II), and UPS (He I) valence band spectra for these preferred ion pairs is performed. The reconstructed valence band spectra are deconvoluted into the contributions of the ions and the different contained elements, which have offered a specific sensitivity for the respective radiation sources due to the varied photoionization cross sections. In addition, different alkyl chain lengths are investigated to reveal their influence onto the arrangement of the ions in the near surface region.

6.1 Effect of ion pair geometry and anion conformer on the valence band structure of [EMIm]Tf₂N

Single ion pairs are commonly used in quantum-chemical studies to analyze fundamental properties of ionic liquids. A number of possible ion pair geometries for imidazolium-based ionic liquids have been illustrated in the literature [74, 75, 87, 89, 90, 95, 150]. Herein, a preferred position of the anion around the central carbon atom (C¹ position in Figure 29, left) is identified. Nevertheless, also positions in vicinity of the other two carbons within the imidazolium ring (C^{2M} and C^{2E} in Figure 29, left) are detected [87, 88, 89, 150]. The orientation between both ions is typically mediated by hydrogen bonding [75, 87, 89, 150].

The ion pairs of [EMIm]Tf₂N investigated for the purpose of ion pair geometry and preferred anion conformer are composed of previously optimized single ions, which are identified to possess the highest total energy and for the [Tf₂N] anion have offered the respective cis and trans conformer. A preference for the [Tf₂N] anion at positions in vicinity of the imidazolium ring was detected in the molecular dynamics simulations by B. Qiao et al. [75] (see Figure 30). In addition, the opportunity for a rapid change in the [Tf₂N]⁻ conformer for imidazolium-based ionic liquids in their liquid state is recognized inter alia from K. Fujii et al. [134] and E. Bodo et al. [135]. K. Fujii et al. [134] have ascertained a marginal temperature dependence and, in consequence, have concluded that cis and trans conformer of the [Tf₂N] anion are present in an equilibrium. Therefore, one might infer that the barrier for change in the [Tf₂N] conformer is comparably low and in the order of kT . Total energies of [EMIm]Tf₂N ion pairs with the anion in vicinity of the carbon in C¹ position are listed in Table 8. In between these ion pairs, differences in total energy of 0.134 eV (maximum B4 and minimum B1 in Figure 31) are estimated. Ion pairs, which have featured the trans or partially intermediate (i.e. in between cis and trans) conformer of the [Tf₂N] anion, are energetically slightly favored compared to the respective cis conformer. This effect has already been recognized for the trans conformer of an isolated [Tf₂N] anion. For the calculated ion pairs in Figure 32, which have featured the [Tf₂N] anion in vicinity of C^{2M} and C^{2E} carbons, the total and relative energy differences are tabulated in Table 9. These geometries are frequently discriminated against the C¹ position in the order of 400 meV per ion pair or around 40 kJ/mol, but they are ranging over values of approximately 360-580 meV per ion pair or 35-56 kJ/mol, respectively. The lowest differences are noted for those ion pairs, where multiple interactions are present. In con-

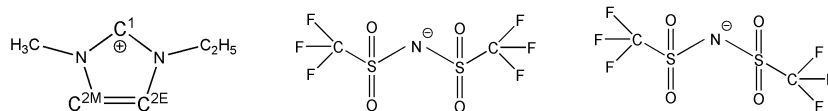


Figure 29: Nomenclature for the preferred carbon positions inside the imidazolium ring in $[\text{EMIm}]^+$ (left) with distinction of the C^2 carbons into the one closer to the methyl group, denoted as $\text{C}^{2\text{M}}$, and the other closer to the ethyl chain, denoted as $\text{C}^{2\text{E}}$, as well as cis conformer (middle) and trans conformer (right) of the $[\text{Tf}_2\text{N}]^-$ anion.

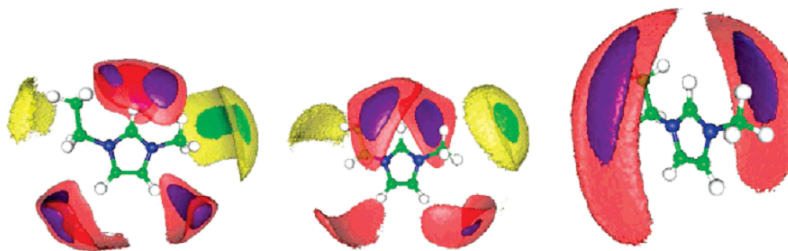


Figure 30: Three-dimensional spatial distribution function (SDF) for the anion around the $[\text{EMIm}]$ cation obtained from molecular dynamics simulations of ionic liquids with the anions of $[\text{Cl}]^-$ (left), $[\text{BF}_4]^-$ (middle), and $[\text{Tf}_2\text{N}]^-$ (right). Isovalues for the closest distances between the geometrical centers of the ions ($r = 0 - 0.54 \text{ nm}$) are drawn as ten-times the average density (blue) and five-times the average density (red). While, areas with a larger distance between the centers of cation and anion ($r = 0.54 - 0.66 \text{ nm}$) are indicated by densities of eight-times (green) and four-times the average density (yellow). The simulations were performed with a number of 288 ion pairs per calculation box and at temperatures of 450, 380, and 350 K, respectively. (With the courtesy of: The American Chemical Society, B. Qiao et al., *J. Phys. Chem. B*, 112 (2008) 1743-1751, page 1746 [75])

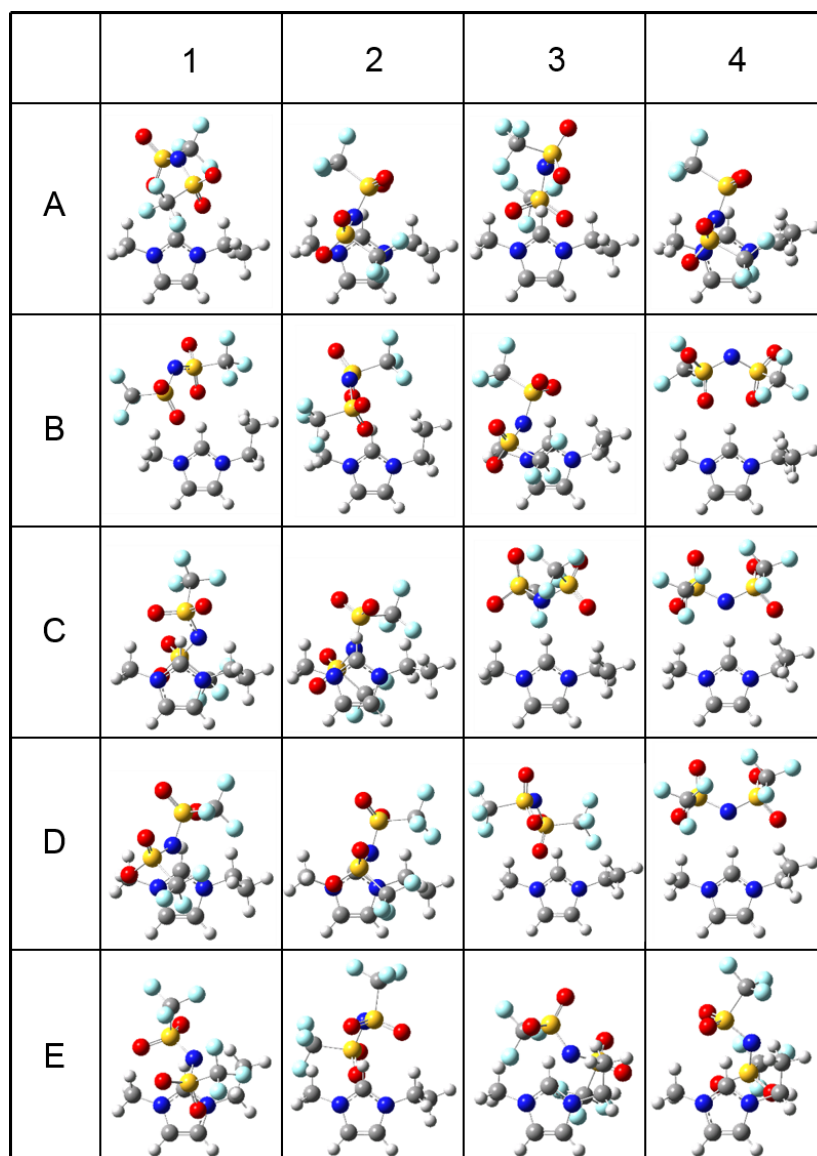


Figure 31: Different ion pair geometries of [EMIm]Tf₂N with the [Tf₂N] anion in vicinity of the C¹ carbon (total energy and relative differences as well as the respective anion conformers and interaction sites are listed in Table 8).

Ion pair	Conformer of [Tf ₂ N] ⁻	Interaction site (atom/atoms in [Tf ₂ N] ⁻)	Total energy (eV)	Difference (eV)
A1 [#]	trans	H ¹ (O)	-59097.370	+0.036
A2 [#]	trans	C ¹ (N)	-59097.397	+0.009
A3 [#]	cis	H ¹ (O)	-59097.380	+0.026
A4 [#]	trans	H ¹ (O) / C ¹ (N)	-59097.382	+0.024
B1 [#]	trans	H ¹ (O)	-59097.272	+0.134
B2 [#]	trans	H ¹ (O)	-59097.291	+0.115
B3 [#]	trans	H ¹ (O)	-59097.382	+0.024
B4 [#]	trans	H ¹ (O)	-59097.406 [#]	0.000 [#]
C1 [#]	intermediate	H ¹ (O)	-59097.338	+0.068
C2 [#]	cis	C ¹ (N)	-59097.326	+0.080
C3 [#]	trans	H ¹ (N)	-59097.395	+0.011
C4 [#]	cis	H ¹ (N)	-59097.363	+0.043
D1 [#]	cis	C ¹ (N)	-59097.367	+0.039
D2 [#]	cis	C ¹ (N)	-59097.353	+0.053
D3 [#]	trans	H ¹ (O)	-59097.326	+0.080
D4 [#]	cis	H ¹ (N)	-59097.367	+0.039
E1 [§]	cis	H ¹ (O)	-59097.340	+0.085
E2 [§]	intermediate	H ¹ (O/O)	-59097.410	+0.015
E3 [§]	cis	H ¹ (O)	-59097.304	+0.121
E4 [§]	intermediate	H ¹ (O)	-59097.425 [§]	0.000 [§]

Table 8: Total energy and relative difference (in eV) of different ion pair geometries of [EMIm]Tf₂N featuring a position in vicinity of the central carbon atom (C¹ position). The respective conformer of the [Tf₂N] anion is indicated as cis, trans or intermediate (i.e. in between the other two distinct cases). ([#]) An optimization of the ion pairs A1-D4 was performed by means of the Gaussian03 program package [122] and the respective energy difference is estimated related to the ion pair geometry B4 in Figure 31. ([§]) For all ion pairs E1-E4 the optimization was executed by the Gaussian09 program package [121] and, thus, the energy difference is accomplished according to the ion pair E4 in Figure 31.

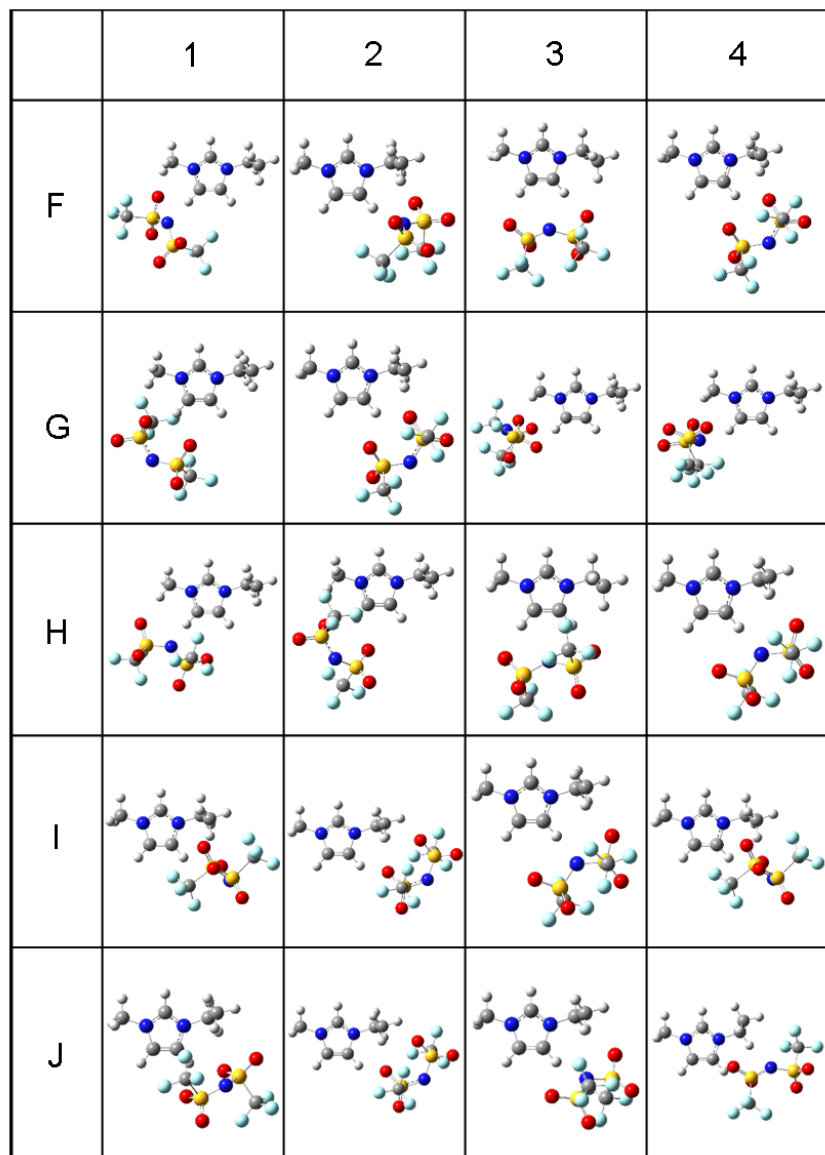


Figure 32: Different ion pair geometries of [EMIm]Tf₂N with the [Tf₂N] anion in vicinity of the C^{2M} and C^{2E} carbons (total energy and relative differences as well as the respective anion conformers and interaction sites are listed in Table 9).

Ion pair	Conformer of $[\text{Tf}_2\text{N}]^-$	Interaction site (atom/atoms in $[\text{Tf}_2\text{N}]^-$)	Total energy (eV)	Difference (eV)
F1	trans	$\text{H}^{2\text{M}}$ (N)	-59096.975	+0.450
F2	cis	$\text{H}^{2\text{E}}$ (N)	-59096.995	+0.430
F3	cis	$\text{H}^{2\text{M}}/\text{C}^{2\text{M}/2\text{E}}/\text{H}^{2\text{E}}$ (O/N/O)	-59097.046	+0.379
F4	cis	$\text{H}^{2\text{E}}$ (O)	-59096.980	+0.445
G1	cis	$\text{H}^{2\text{M}}$ (O/O)	-59096.930	+0.495
G2	cis	$\text{H}^{2\text{E}}$ (O/O)	-59096.980	+0.445
G3	cis	$\text{H}^{2\text{M}}$ (O)	-59097.005	+0.420
G4	cis	$\text{H}^{2\text{M}}$ (N)	-59096.980	+0.445
H1	trans	$\text{H}^{2\text{M}}$ (N)	-59096.996	+0.429
H2	trans	$\text{H}^{2\text{M}}$ (O)	-59096.978	+0.447
H3	trans	$\text{H}^{2\text{M}}/\text{C}^{2\text{M}/2\text{E}}/\text{H}^{2\text{E}}$ (O/N/O)	-59097.060	+0.365
H4	trans	$\text{H}^{2\text{E}}$ (N)	-59097.044	+0.381
I1	trans	$\text{H}^{2\text{E}}$ (O)	-59097.066	+0.359
I2 ^{&}	trans	$\text{H}^{2\text{E}}$ (O)	-59096.913	+0.512
I3	trans	$\text{H}^{2\text{E}}$ (N)	-59097.046	+0.379
I4 ^{&}	trans	$\text{H}^{2\text{E}}$ (O)	-59097.066	+0.359
J1 ^{&}	trans	$\text{H}^{2\text{E}}$ (O)	-59096.979	+0.446
J2 ^{&}	trans	$\text{H}^{2\text{E}}$ (O)	-59096.913	+0.512
J3 ^{&}	trans	$\text{H}^{2\text{E}}$ (N)	-59097.041	+0.384
J4 ^{&}	trans	$\text{H}^{2\text{E}}$ (O)	-59096.847	+0.578

Table 9: Total energy and relative difference (in eV) of different ion pair geometries of $[\text{EMIm}]\text{Tf}_2\text{N}$ featuring a position in vicinity of the carbon atoms at the imidazolium rings' bottom ($\text{C}^{2\text{M}}$ and $\text{C}^{2\text{E}}$ position). The respective conformer of the $[\text{Tf}_2\text{N}]^-$ anion is indicated as cis or trans, while an intermediate shape (i.e. in between the other two distinct cases) is not observed here. Optimization of the ion pairs was performed by means of the Gaussian09 program package [121]. The energy difference is calculated relative to the favored geometry of E4 (Figure 31) and Table 8. (&) A further interaction is established in particular between the $[\text{Tf}_2\text{N}]^-$ anion and hydrogens of the ethyl chain rather than the methyl group.

trast to this, in other studies (cf. ref. [89] and references therein) the different positions are only discerned by about 2-10 kJ/mol. Although the positions of C^{2M} and C^{2E} are less strongly represented in the spatial distribution function in Figure 30 (right), they are found nearly as feasible as the geometry with C^1 position. Hereinafter, the influences onto the reconstructed valence band spectra by on the one hand various ion pair geometries (C^1 and C^{2M}/C^{2E} position) and on the other the respective $[Tf_2N]^-$ conformer will be studied.

The reconstructed XPS and UPS (He II) valence band spectra of the ion pairs, which have featured the $[Tf_2N]^-$ anion in vicinity of the C^1 or C^{2M}/C^{2E} position of the $[EMIm]$ cation, are depicted in Figure 33. The peak shapes of all ion pairs are found as similar and, in consequence, these are independent from the particular ion pair geometry. In contrast to this, for the unscaled density of states of various ion pairs of $[EMIm]Tf_2N$ the peak shapes and heights as well as their positions have revealed strong variances, which agrees with the results of a set of $[XMIIm]Tf_2N$ ionic liquids (cf. ref. [28]). Thus, the incorporation of photoionization cross sections has led to the matching of the different atomic contributions in the XPS and UPS (He II) valence band structure. In the spectra, no significant differences between cis or trans conformer of the $[Tf_2N]^-$ anion are recognized. The XPS and UPS (He II) valence band spectra of $[EMIm]Tf_2N$ are dominated by the $[Tf_2N]^-$ anion, which will be demonstrated in detail later, and, in consequence, this argument is justified. The reconstructed spectra for the positions of C^{2M} and C^{2E} are ascertained to be equal. However, an obvious difference between these and the C^1 position is identified: all peak positions of the ion pair with the anion in C^{2M}/C^{2E} position are found at binding energies that are around 0.30 eV for XPS and about 0.35 eV for UPS (He II) below those of the ion pairs with $[Tf_2N]^-$ in C^1 position. Herein, all peaks are shifted by an approximately uniform value, which might lead to the assumption that all relative binding energies in both geometries are similar and are only affected by a global shift. This is accompanied with the introduction of the rescaling parameter ΔE , which inter alia would compensate this effect for different ion pair geometries. In Figure 34, this shift for the respective cases of different ion pair geometry is illustrated, which has supported the previous assumption. In addition, it is exhibited that for an intermediate position of the $[Tf_2N]^-$ anion in front of the imidazolium ring, i.e. between C^1 and C^{2M}/C^{2E} (see inset in Figure 34), the related reconstructed XPS and UPS (He II) valence band spectra are discovered among the positions directly associated with one of the imidazolium carbons.

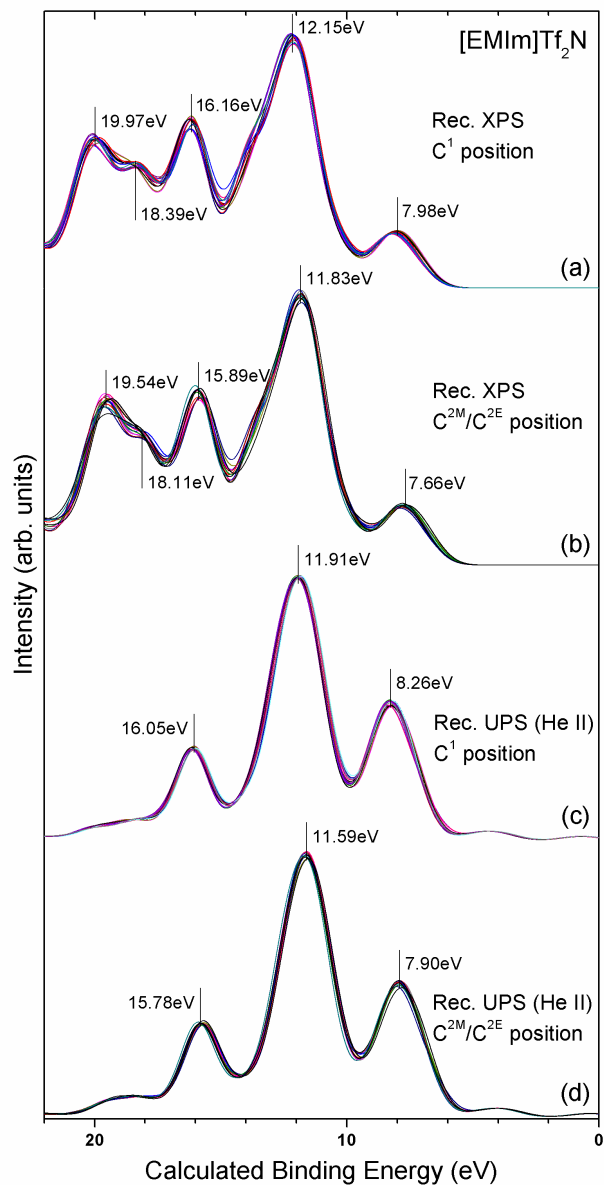


Figure 33: Reconstructed XPS and UPS (He II) valence band spectra from ion pairs of [EMIm]Tf₂N with the [Tf₂N] anion in C¹ (a, c) and C^{2M}/C^{2E} position (b, d). A rescaling procedure is not applied for the binding energy scale of the reconstructed spectra due to potentially different values for the scaling factor f , absolute binding energy shift ΔE , and relative binding energy shift between both ions $\Delta\Delta E_{Cation-Anion}$.

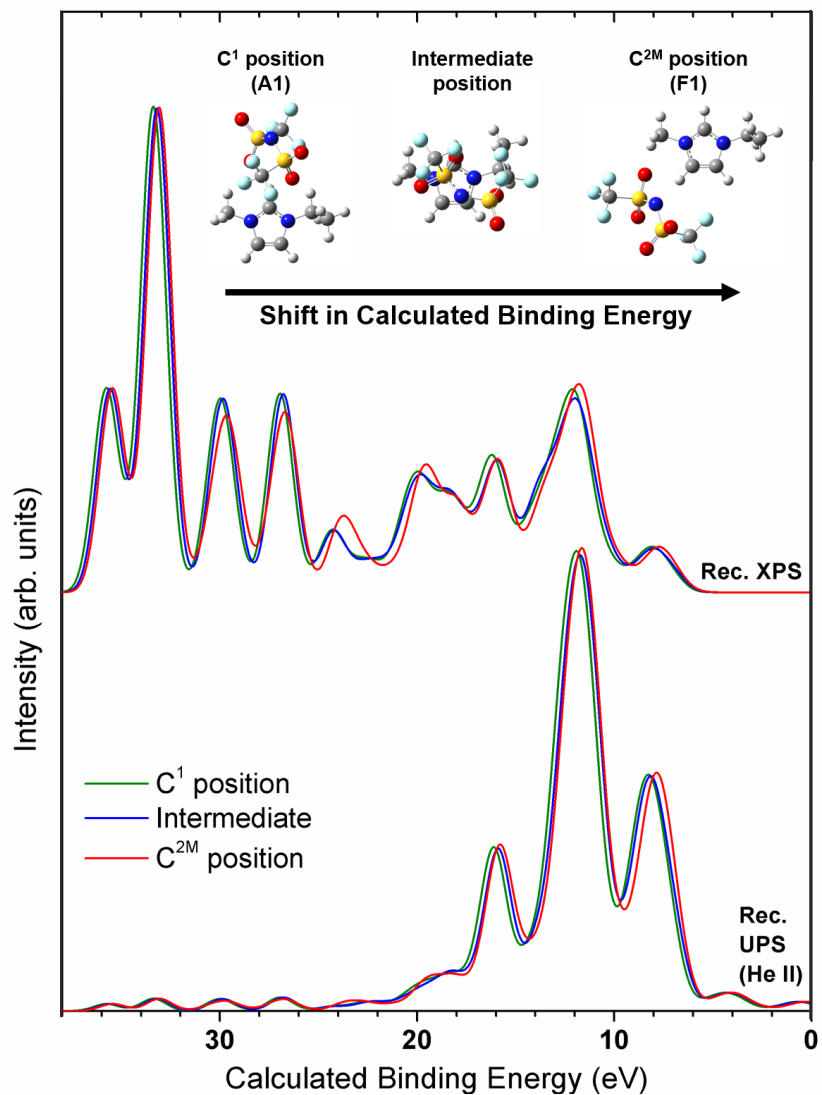


Figure 34: Reconstructed XPS valence band spectra (top) and UPS (He II) spectra (bottom) for visualization of the nearly uniform shifts in the binding energy positions for the three limiting cases of ion pair geometry (C¹ position (A1), C^{2M} position (F1), and an intermediate position, which does not belong to any of those groups of geometries depicted in Figure 31 and Figure 32).

In Figure 34, a distinct difference between the reconstructed XPS valence band spectra of the three ion pairs is recognized in the binding energy range from 22 to 25 eV. This binding energy range is examined in detail in Figure 35. Herein, the binding energies of the anion contributions are shifted towards lower values from C^1 over intermediate to C^{2M} . A contrary behavior for the contributions of the [EMIm] cation relative to those of the dominating [Tf₂N] anion is found. Thus, for an ion pair with the anion in C^{2M} position the cation contributions have overlapped with those of the anion, which has led to a relocalization of the peak to a binding energy of 23.5 eV compared to its initial value of circa 24.5 eV. For the other two ion pair geometries (C^1 and intermediate) the cation contributions are present at lower energies and, in consequence, this peak is only shaped from the anion contributions. The different cation-related contributions of carbon and nitrogen are shifted by similar values. This uniform shift for the contributions of the cation relative to those of the anion can be understood as a further evidence for the relative shift $\Delta\Delta E_{Cation-Anion}$, which was introduced in the rescaling procedure of calculated binding energies. A potentially different value for $\Delta\Delta E_{Cation-Anion}$ for various ion pair geometries has corrected their specific shifts in binding energy with respect to the experimental spectra.

Thus, the applied reconstruction method for XPS and UPS (He II) will provide reliable results for the use of all potential ion pairs of [XMIm]Tf₂N. The reconstructed spectra of all ion pairs of [EMIm]Tf₂N can be utilized for an analysis of the experimental valence band spectra, while different rescaling parameters might occur. This method has provided a tool for a deconvolution into the respective contributions and a further quantitative analysis of the surface electronic structure of ionic liquids for the first time, which is performed hereinafter.

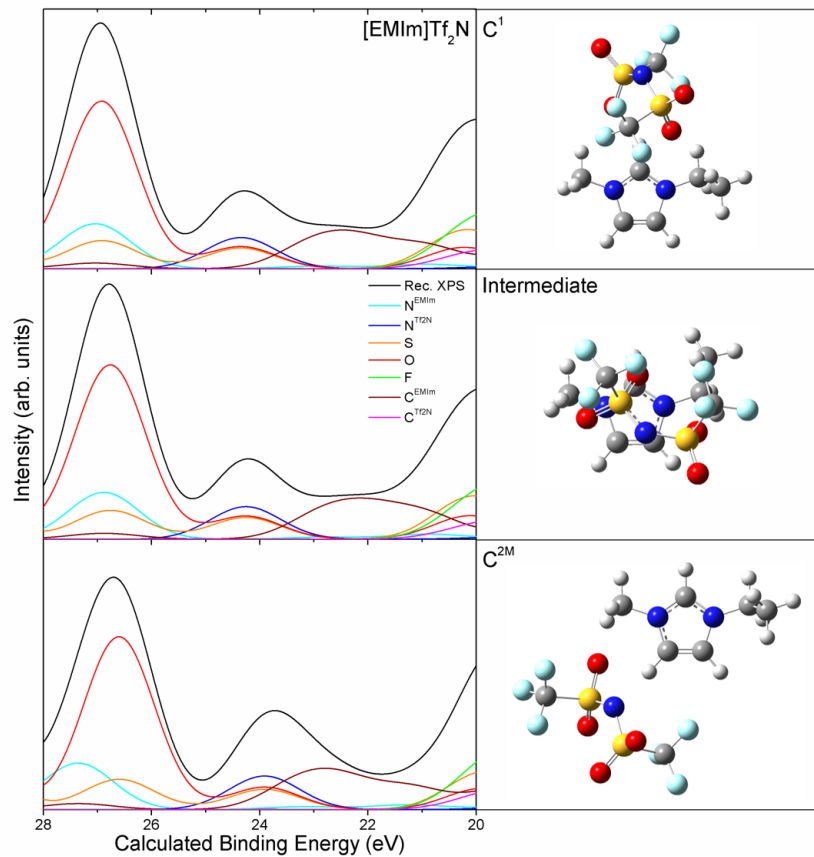


Figure 35: Reconstructed XPS valence band spectra in the binding energy range between 20 and 28 eV with a decomposition of the spectra displayed in Figure 34 into the contained elements. Herein, the three limiting cases of ion pair geometry are illustrated: C¹ position (A1, top), C^{2M} position (F1, bottom), and an intermediate position, which does not belong to any of the groups of ion pair geometry depicted in Figure 31 and Figure 32.

6.2 Reconstructed XPS and UPS valence band spectra of [XMIm]Tf₂N

The XPS, UPS (He II), and UPS (He I) valence band spectra are deconvoluted by means of the reconstructed spectra.⁵ For this purpose, the reconstructed valence band spectra are used as a basis for the normalization of the experimental spectra, which have enabled the calculation of difference spectra. The surface structure is concluded from the reconstructed valence band spectra and the calculated difference spectra subsequently.

6.2.1 XPS and UPS valence band spectra

The reconstructed XPS valence band spectra are depicted in comparison to the experimental spectra in Figure 36. Herein, a very good agreement of peak positions and height ratios between the reconstructed and experimental XPS valence band spectra of [EMIm]Tf₂N and [OMIm]Tf₂N is achieved in Figure 36 (top). The density of states (DOS), which was the state of the art up to the development of the reconstruction method illustrated here, is given for reason of comparison in Figure 36 (top). Obvious differences between the DOS and reconstruction of the XPS valence band spectra are demonstrated. In the DOS the peak at the valence band edge is clearly overestimated, whereas the peaks between 15 and 20 eV are underestimated, since only the unweighted number of states is contained. From the very good agreement, the significant advantage of the reconstruction method is unveiled by the ability of quantitative assignments instead of merely qualitative ones.

A difference between reconstructed and experimental spectrum is observed at

⁵Parts of this chapter have been published in the following peer-reviewed articles:

M. Reinmöller, A. Ulbrich, T. Ikari, J. Preiß, O. Höfft, F. Endres, S. Krischok, W. J. D. Beenken, "Theoretical reconstruction and elementwise analysis of photoelectron spectra for imidazolium-based ionic liquids", *Physical Chemistry Chemical Physics*, 13 (2011) 19526-19533.

A. Ulbrich, M. Reinmöller, W. J. D. Beenken, S. Krischok, "Photoelectron spectroscopy of ionic liquid surfaces - theory and experiment", *Journal of Molecular Liquids*, 192 (2014) 77-84.

T. Ikari, A. Keppler, M. Reinmöller, W. J. D. Beenken, S. Krischok, M. Marschewski, W. Maus-Friedrichs, O. Höfft, F. Endres, "Surface electronic structure of imidazolium-based ionic liquids studied by electron spectroscopy", *e-Journal of Surface Science and Nanotechnology*, 8 (2010) 241-245.

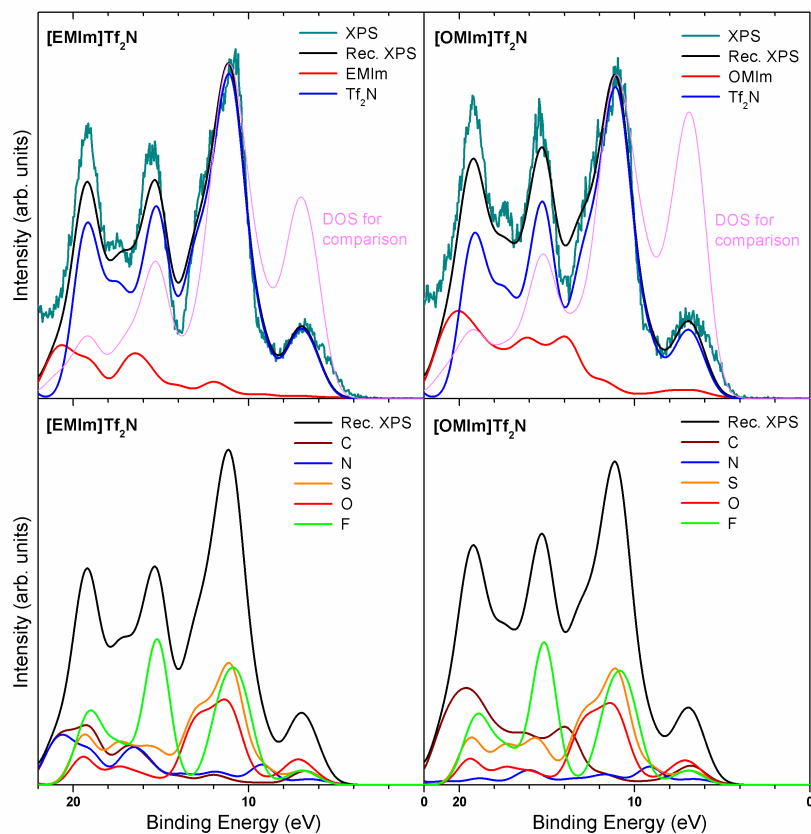


Figure 36: Reconstructed XPS valence band spectra of [EMIm]Tf₂N (left) and [OMIm]Tf₂N (right) with a deconvolution into the ions in comparison to the experiment (top) and into the contained elements (bottom). The comparison with the calculated density of states (DOS), which is broadened by the peak width of the reconstructed spectra, is performed for both ionic liquids (top). All spectra are normalized in height to the most prominent peak at about 11 eV. The contributions of hydrogen are not displayed, since their photoionization cross section is marginal compared to those of the other elements. Herein, rescaling parameters of $f = 1.02838$, $\Delta E = -1.36$ eV for [EMIm]Tf₂N and $\Delta E = -1.39$ eV for [OMIm]Tf₂N as well as $\Delta\Delta E_{\text{Cation}-\text{Anion}} = -1.10$ eV are applied. (With the courtesy of: The Royal Society of Chemistry, M. Reinmüller et al., Phys. Chem. Chem. Phys., 13 (2011) 19526-19533, page 19530 [90])

the valence band edge, where the peak has started at around 4 eV in experiment, while the valence band edge is located at about 5 eV in the reconstruction. This could be caused by potential contributions from additional species, since the estimated composition of ionic liquids has partially resulted in higher carbon contents compared to the stoichiometric value relative to the other elements (cf. refs. [33, 36]). In a valence band study of different carbonaceous species [151], a contribution starting at approximately 3-4 eV is detected with similar shape of a gradual increase as recognized in the experimental spectra, which is further in agreement with the related density of states. This signal is assigned to the C2p orbitals with a π character and partially the highest of the σ states of these additional substances. Moreover, the intensity of this difference is higher for UPS (He II) spectrum in comparison to XPS due to the increased cross section of the C2p states. Additional spectral features are estimated at binding energies of approximately 5-7, 9-10, and 13-14 eV in the experimental UPS (He II) spectra of [XMIIm]Tf₂N, which are close to the binding energies of the peaks and respective states found for the investigated carbonaceous species [151].

In Figure 36 (top), the reconstructed XPS spectrum is decomposed into the contributions of imidazolium-based cations and [Tf₂N] anion. The valence band spectra for both ionic liquids are clearly dominated by the [Tf₂N] anion, which is caused by the high photoionization cross sections of the constituents fluorine, oxygen, and sulfur for XPS (cf. Table 1). For the peaks at lower binding energies up to 12 eV the contributions of the imidazolium-based cations are recognized to be negligible due to the very low photoionization cross sections of the N2p and C2p orbitals, which are two or three orders of magnitude smaller than those of the major constituents in [Tf₂N]⁻. Substantial amounts of the cation are localized to start at about 15 eV for [EMIm]Tf₂N and circa 12 eV for [OMIm]Tf₂N, since the cross sections for the N2s and C2s state are approximately one order of magnitude higher than those of their respective 2p orbitals. In addition, no significant differences are observed up to 12 eV in the reconstructed spectra between [EMIm]Tf₂N and [OMIm]Tf₂N due to the same reason. An increased intensity of the cation contribution is noticed in the reconstructed spectrum of the [OMIm]Tf₂N at higher binding energies. This effect is caused by the higher number of carbon atoms in the alkyl chain of [OMIm]⁺ compared to [EMIm]⁺.

The reconstructed XPS valence band spectra are decomposed into their contained elements in Figure 36 (bottom). In general, the elements fluorine, oxygen, and sulfur have dominated the spectra. Enlarged contributions for [OMIm]Tf₂N

at higher binding energies are distinctly assigned to the carbon atoms. However, the nitrogen contributions in the reconstructed spectra from [EMIm]Tf₂N and [OMIm]Tf₂N have changed significantly above approximately 14 eV. This effect is caused during the calculation by a 'shoveling around' of contributions from different atomic orbitals, while combining them to molecular orbitals with minimum energy. Herein, most probably only the 2s orbitals from carbon and nitrogen are affected, whereas the contributions of fluorine, oxygen, and sulfur are not recognizably varied. Nevertheless, this effect can be present for other polyvalent or complex elements, too.

The peak at the lowest binding energy at about 7 eV is considerably dominated by the element oxygen, which is followed by nearly equal contributions from fluorine, sulfur, and carbon. Significant amounts from fluorine, sulfur, and oxygen are localized in the highest peak in the XPS valence band spectra at around 11 eV. This peak has featured a shoulder at its higher binding energy side, which has almost exclusively resulted from the elements oxygen and sulfur. Thus, this shoulder can be directly assigned to the SO₂ groups in the [Tf₂N] anion. The peak at approximately 15 eV has originated from fluorine, whereas contributions from sulfur and carbon are also present with lower intensity. A further peak at circa 17.5 eV is nearly equally shaped by amounts from fluorine, sulfur, and carbon. For the peak at about 20 eV fluorine and carbon are the dominating species, while smaller contributions from sulfur and oxygen are additionally found. In all of the latter three peaks significant amounts of nitrogen are assigned only in [EMIm]Tf₂N, which is induced by the previously described effect of 'shoveling around' contributions from carbon and nitrogen.

The reconstructed UPS (He II) and UPS (He I) valence band spectra of both ionic liquids, i.e. [EMIm]Tf₂N and [OMIm]Tf₂N, are illustrated in Figure 37 and Figure 38, respectively. A good agreement between the reconstructed and experimental UPS spectra is obtained for a wide range, up to binding energies of circa 15 eV for UPS (He II) and 12 eV for UPS (He I). Above those values, strong discrepancies are detected between the spectra. The fact of a mismatching of the peak heights is caused by the following reasons:

- The experimental spectra are significantly affected by inelastically scattered electrons [153, 154], which are associated with a significant background starting at binding energies of around 12 eV.
- In addition, the photoionization cross sections for the C2s orbitals are

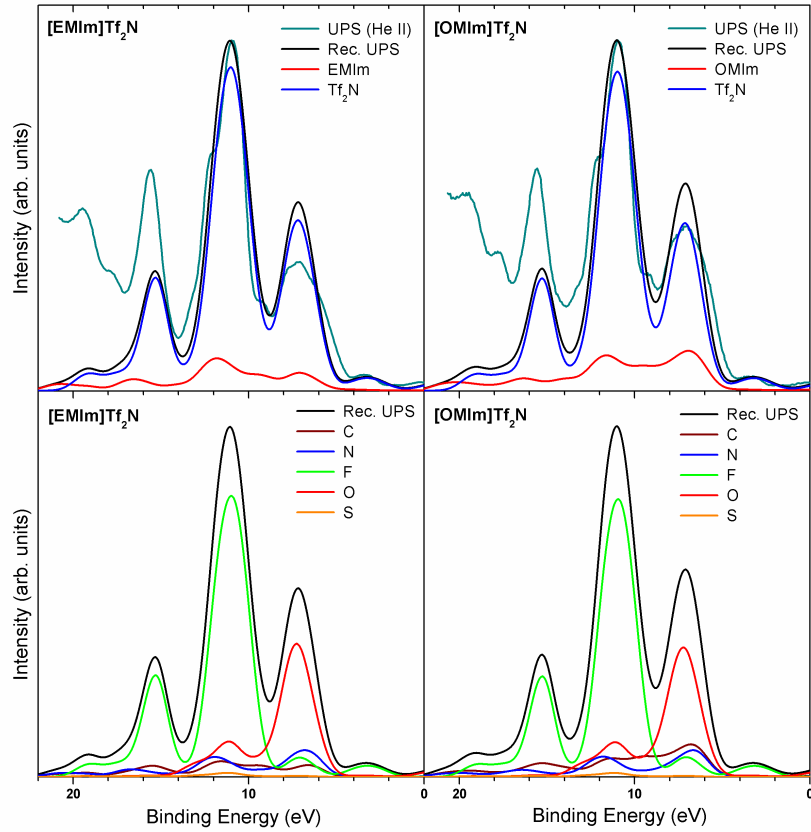


Figure 37: Reconstructed UPS (He II) spectra of [EMIm]Tf₂N (left) and [OMIm]Tf₂N (right) with a deconvolution into the ions in comparison to the experiment (top) and into the contained elements (bottom). All spectra are normalized in height to the most prominent peak at about 11 eV. The presence of the He II β -line is considered by means of a duplicate of the reconstructed He II α -line combined with a shift of -7.56 eV and a height of 4% of the initial α -line intensity in the reconstruction. Herein, rescaling parameters of $f = 1.02838$, $\Delta E = -1.26$ eV for [EMIm]Tf₂N and $\Delta E = -1.29$ eV for [OMIm]Tf₂N as well as $\Delta\Delta E_{Cation-Anion} = -1.10$ eV are applied. (With the courtesy of: The Royal Society of Chemistry, M. Reinmüller et al., Phys. Chem. Chem. Phys., 13 (2011) 19526-19533, page 19531 [90])

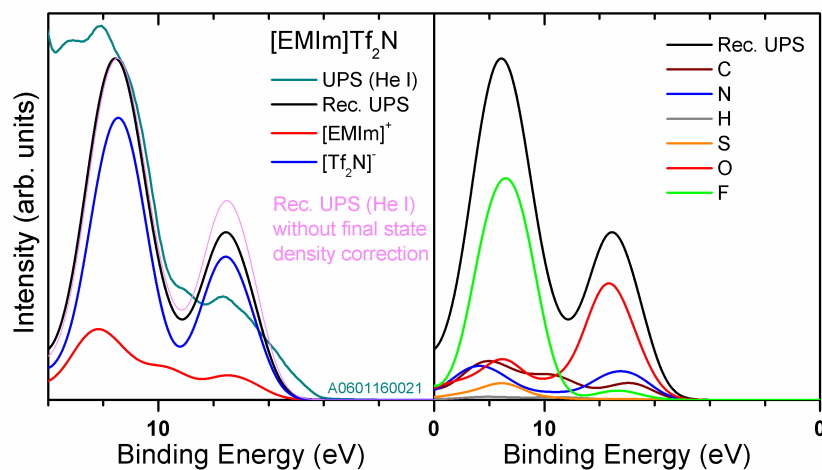


Figure 38: Reconstructed UPS (He I) spectrum of [EMIm]Tf₂N in comparison to the experimental spectrum (left) and with a decomposition into the contributions of the ions (left) and the respective elements (right). The binding energies of the reconstructed spectra are modified by identical values of $f = 1.02838$ and $\Delta\Delta E_{Cation-Anion} = -1.10$ eV applied for XPS and UPS (He II) as well as a different absolute shift of $\Delta E = -0.90$ eV. The intensity of the reconstructed spectra has considered the final state density by means of a multiplicative factor using the approximation $1/\rho_f \approx 1/\sqrt{E_{kin}} \approx 1/\sqrt{\hbar\omega - E_{bind}}$, since the approximation $\rho_f \approx \sqrt{E_{kin}}$ is valid for the experimental spectra (cf. ref. [152]). The experimental spectrum is obtained from personal communication with Dr. M. Himmerlich.

ascertained approximately one order lower than for the C2p orbitals near the valence band edge. For other elements, such as nitrogen, oxygen, and sulfur, no data about the photoionization cross sections are available for the respective N2s, O2s, and S3s states in the UPS (He I) spectra (cf. ref. [119]). These states are located at a defined binding slightly above the photon energy in this reference and might partially contribute in a broader range overlapping with the investigated binding energies. Thus, this has led to significantly reduced contributions from the ionic liquid in the related binding energy range, which nonetheless has indicated the dominating effect of the background in the experimental spectra caused by the inelastically scattered electrons.

- Final state effects are not taken into account for the reconstructed XPS spectra, since the kinetic energies of different electrons recorded from the valence band are varied imperceptibly. Whereas, these effects can become important for the UPS spectra due to the reason that the valence band electrons have covered both the minimum and maximum of the kinetic energy. Thus, a dominating impact in particular on the experimental UPS (He I) spectra is assigned to the exact shape of the final state density. An approximation of the final state density for UPS spectra is given by $\rho_f \approx \sqrt{E_{kin}}$ according to ref. [152]. The initially reconstructed UPS (He I) spectra using the photoionization cross sections from Table 1 have to be corrected by the approximation of $\rho_f \approx \sqrt{\hbar\omega - E_{bind}}$ for the final states, which can be related to the rescaled binding energy for any state. However, this correction has not affected the relative intensities of different elements within one peak, even though the influence of incorporated relative shifts between anion and cation are deemed marginal. This correction is exemplarily applied for the reconstructed UPS (He I) spectrum in Figure 38.

The reconstructed UPS (He II) spectra of [EMIm]Tf₂N as well as [OMIm]Tf₂N are displayed in Figure 37. Herein, the spectra are deconvoluted into the contributions of the two ions (top) and contained elements (bottom). These spectra are significantly dominated by the [Tf₂N] anion. In comparison to the reconstructed XPS spectra, the photoionization cross sections of carbon and nitrogen near the valence band edge are perceived to be only one order of magnitude lower than the primarily present elements in the [Tf₂N] anion. Major differ-

ences between [EMIm]Tf₂N and [OMIm]Tf₂N are identified in a binding energy range from 5 to 10 eV. Thus, these changes can be attributed to the additional carbon atoms due to the extended alkyl chain length of [OMIm]⁺ compared to the [EMIm]⁺ analog.

The reconstructed UPS (He II) spectra are decomposed into the respective elements in Figure 37 (bottom). A general domination of the elements fluorine and oxygen is found. For the peak near the valence band edge at around 7 eV, a clearly prevalent contribution by oxygen is discovered, which is followed by contributions of nitrogen, carbon, and fluorine. An increase in intensity starting at about 5 eV is detected for carbon exclusively and, thus, is eventuated from the additional carbon due to the extended alkyl chain in [OMIm]Tf₂N. The most prominent peak at about 11 eV is provoked on the one hand by a dominant fluorine contribution and on the other by the participation of oxygen, carbon, and nitrogen with much lower intensity. However, the intense contribution by sulfur in the XPS valence band spectra for this peak and the shoulder at the higher binding energy side has nearly completely disappeared. This has resulted from the fact that the large photoionization cross section for XPS is now around one order of magnitude lower than those of most other elements. For the peak at about 15.5 eV a dominating amount of fluorine is observed, while only trace contributions from carbon and nitrogen are existent herein. An assignment of the peaks at higher binding energies has to be apprehended as vague due to the high intensity caused by inelastically scattered electrons. The obtained knowledge of different element-specific intensities and their origin within the ions will be used in Chapter 6.2.2 to access the surface structure at the ionic liquid-vacuum interface of [XMIm]Tf₂N.

The reconstructed UPS (He I) spectrum of [EMIm]Tf₂N is illustrated in Figure 38. Herein, the reconstructed spectrum and its ion and element contributions are modified by the final state density of $\rho_f \approx \sqrt{\hbar\omega - E_{bind}}$ according to ref. [152]. This modification has enabled a slightly better agreement between reconstructed and experimental spectrum, although the height of the peak at approximately 7.5 eV is still overestimated. In this context, it has to be noted that the experimental spectrum is affected by inelastically scattered electrons, too. Both main peaks at circa 7.5 and 11.5 eV are shaped by the [Tf₂N] anion (see Figure 38, left). Nevertheless, the cation has contributed to these peaks with a higher relative intensity than in the respective UPS (He II) and XPS valence band spectra, which has resulted from the photoionization cross sections of nitrogen comparable to those of fluorine, oxygen, and sulfur as well as carbon

with the half value.

The contributions of the different elements to the peaks are distinguished by use of the deconvoluted UPS (He I) spectrum in Figure 38 (right). The previously described order of photoionization cross sections has led to following contributions in the two peaks: oxygen has dominated the peak at approximately 7.5 eV, while also contributions of nitrogen and carbon are present. On the contrary, the peak at 11.5 eV is mainly shaped by fluorine, but also all other elements (except of hydrogen) have participated in this peak by a substantial share. Hereinafter, it will be demonstrated, how the reconstructed valence band spectra can be used for a surface analysis of ionic liquids.

6.2.2 Arrangement of the ions at the surface of [XMIIm]Tf₂N

The experimental UPS (He II) and MIES spectra have contained significant information about the arrangement and orientation of the different species at the surface, since they have offered the highest surface sensitivities of the utilized methods from the set of (photo-)electron emission spectroscopy. Hence, these data have to be attained from the experimental spectra. An important question that has to be answered: how can the information be extracted from experimental spectra by means of the reconstruction method? The reconstructed spectra have comprised absolute values for the spectra heights, which can be utilized for the normalization of experimental spectra, and this method has enabled a deconvolution into specific groups or single atoms of the investigated molecular systems for a detailed analysis.

In Figure 39 (left), the experimental spectra of [EMIIm]Tf₂N and [OMIIm]Tf₂N are depicted after a normalization to the most prominent peak of the reconstructed UPS (He II) spectra of both ionic liquids. In addition, a difference spectrum on the basis of the MIES spectra is obtained. The experimental MIES spectra are normalized onto each other at the shoulder at around 12.5 eV in Figure 39 (right). This position is preferred due to the reason that this shoulder is exclusively shaped by the contributions of the carbons C¹-C³, where spectral features of the further part of the longer alkyl chain have not interfered in this binding energy range (cf. Chapter A.2 in the Appendix). The difference spectra for UPS (He II) and MIES are obtained by subtraction the normalized experimental spectra of [EMIIm]Tf₂N from those of [OMIIm]Tf₂N.

The UPS (He II) difference spectrum is found in a range from about 5 eV to

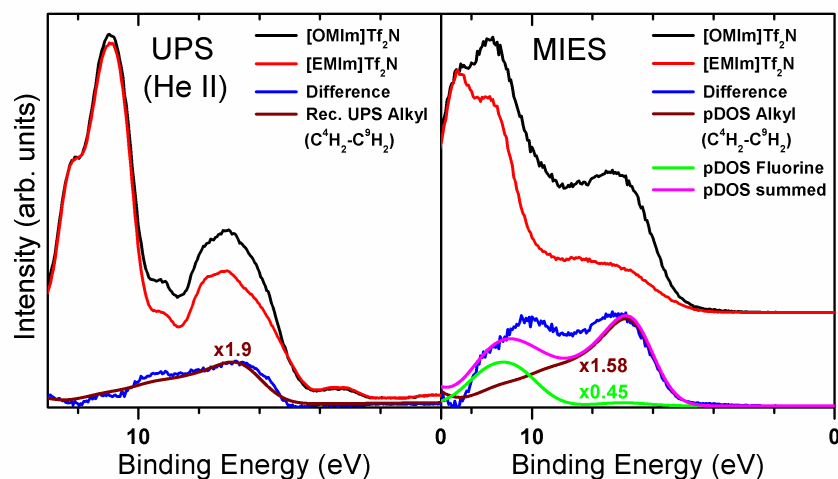


Figure 39: Difference spectra between [OMIm]Tf₂N and [EMIm]Tf₂N obtained from the normalized experimental UPS (He II) spectra (left) and MIES spectra (right) are compared to the reconstructed UPS (He II) spectra and partial density of states (pDOS) of selected parts of the ions. For UPS (He II) the experimental spectra are normalized onto the most prominent peak at about 11 eV of the respective reconstructed spectrum (left) and for MIES onto each other using the shoulder present at circa 12.5 eV (right). The binding energies of the depicted contributions of the additional alkyl chain (C⁴H₂-C⁹H₂) and the fluorine atoms in [OMIm]Tf₂N are rescaled by the parameters of $f = 1.02838$, $\Delta E = -1.29$ eV, and $\Delta\Delta E_{\text{Cation-Anion}} = -1.10$ eV for both methods. (With the courtesy of: The Royal Society of Chemistry, M. Reinmöller et al., Phys. Chem. Chem. Phys., 13 (2011) 19526-19533, page 19532 [90])

approximately 12 eV and has featured a maximum at around 7 eV. The reason for this difference might be easily presumed remembering the difference between [OMIm]Tf₂N and [EMIm]Tf₂N: both ionic liquids differ in the length of their alkyl chains; in a conceptual model, it is assumed that the [OMIm] cation is identical to the [EMIm] cation, but with six more CH₂ groups incorporated prior to the terminal CH₃ group of the alkyl chain. Thus, the difference spectrum should directly be related to the reconstructed UPS (He II) spectrum of these six CH₂ groups within the alkyl chain, which have included the carbons C⁴-C⁹ with the associated hydrogens in [OMIm]Tf₂N (for respective nomenclature see inset in Figure 9). The general shape of the reconstructed spectrum of those CH₂ groups has matched the difference spectrum very well. However, the intensity of the reconstructed UPS (He II) spectrum has to be enlarged by a factor of 1.9 to obtain a full agreement. This has given a first hint for the presence of the alkyl chain at the surface, since all parts of the ions at the surface are accompanied by an increased intensity due to the surface sensitivity of this method. The suggested surface arrangement with the longer alkyl chains protruding towards the vacuum is proclaimed in the literature, for example in the studies in refs. [14, 15, 63, 79, 80, 84, 155]. In addition to this, from a strong contribution of the [Tf₂N] anion in Figure 37 its presence at the surface is determined by the experimental spectra and verified by the reconstruction. This conclusion is exemplarily supported by the studies in refs. [63, 84, 135].

In the MIES difference spectrum in Figure 39 (right), a double structure with peaks at about 7 and 11 eV is recognized. The peak at about 7 eV has originated from the additional part of the alkyl chain C⁴-C⁹ with the related hydrogens in [OMIm]Tf₂N. For this purpose, the partial density of states (pDOS) of these constituents from the ions is applied. Thus, similar to the UPS (He II) difference spectra it can be concluded that the alkyl chain from [OMIm]Tf₂N is present at the surface as based on the corresponding pDOS. However, by utilization of this partial density of states of the additional alkyl chain a gap in the energy range between 9 and 12 eV is perceived. In this binding energy range the contributions of especially fluorine are present and, in consequence, this difference could be caused by a slightly higher number of fluorine atoms pointing towards the vacuum in [OMIm]Tf₂N compared to [EMIm]Tf₂N. This for example could result either from a conformational change in the [Tf₂N] anion dependent on the alkyl chain length of the cation or a different relative depth of the anion. However, a contrasting conformational change was noticed at the surfaces of [EMIm]Tf₂N and [HMIm]Tf₂N in a HRBS study from K. Nakajima et al. [63].

Nevertheless, the MIES spectra have additionally indicated the presence of the [Tf₂N] anion taking account of the significantly higher surface sensitivity. The onset positions of the difference spectra and the spectra from the additional part of the alkyl chain are identified to match very precisely. Thus, the requirement of another shift $\Delta\Delta E_{Cation-Anion} = -1.10\text{eV}$ between cation and anion contributions in the reconstructed spectra is emphasized by this very good agreement. Moreover, this shift was introduced with the aim to compensate the differences in the split of the experimental and reconstructed N1s core levels, which were already modified by a scaling factor of $f = 1.02838$ and the absolute shift of $\Delta E = -1.29\text{eV}$ for UPS (He II) and MIES spectra of the utilized ion pair of [OMIm]Tf₂N.

6.3 Chapter summary

In principle, all optimized ion pairs of [XMIm]Tf₂N ionic liquids can be utilized for the subsequent spectra reconstruction. By the deconvolution of the experimental XPS, UPS (He II), and UPS (He I) spectra into the contributions of the contained ions and elements with the aid of the reconstruction method, we have provided a quantitative analysis of their respective proportions for the first time [90]. A preferred orientation of the longer alkyl chain of the [OMIm] cation towards the vacuum as well as the presence of the [Tf₂N] anion at the surface is concluded from the UPS (He II) difference spectrum, which is additionally supported by the MIES difference spectrum.

7 Valence band structure of [XMIm]Cl

The set of ionic liquids from [XMIm]Cl have offered varied thermochemical properties inter alia a higher melting point, a lower density, a lower heat capacity, a lower decomposition temperature, and a higher viscosity compared to their [XMIm]Tf₂N analogs [130, 132]. An analysis of ionic liquids with the [Cl] anion has provided the opportunity to study the influence of the cation and its longer alkyl chain on the valence band spectra in detail, since the anion contribution is limited to a few states here.⁶ In comparison to the larger [Tf₂N] anion, the impact of a small anion on the resulting surface structure can be investigated, where some differences between [Cl]⁻ and [Tf₂N]⁻ in the preferred ion pair geometry and the surface arrangement are observed from molecular dynamics simulations [75, 79, 80].

7.1 Reconstructed XPS and UPS valence band spectra

The single ion pairs displayed in Figure 40 are utilized for the subsequent reconstruction of the valence band spectra for XPS and UPS (He II) as well as the DOS. All of these ion pairs have featured a similar position of the [Cl] anion above the hydrogen at the central carbon atom (C¹) and slightly moved towards the methyl group. This geometry was identified to be favored in other studies as well [87]. Other possible ion pair geometries and their related energies are listed in Chapter 7.2.1 as well as the effect of the alkyl chain geometry is further investigated in Chapter 7.2.2.

The experimental and reconstructed XPS and UPS (He II) valence band spectra are illustrated for a series of [XMIm]Cl ionic liquids in Figure 41. No significant changes are recognized in the experimental XPS spectra as well as for the reconstructed ones. The marginal differences within the experimental and reconstructed spectra due to the varied alkyl chain length have resulted from the small photoionization cross sections for the N2p and C2p orbitals compared to the dominating Cl3p state at about 3.7 eV (cf. Table 1). The XPS valence band of [EMIm]Cl is noticeably broadened in contrast to all other experimental

⁶Parts of this chapter have been published in the following peer-reviewed article:

A. Ulbrich, M. Reinmöller, W. J. D. Beenken, S. Krischok, "Surface electronic structure of [XMIm]Cl probed by surface-sensitive spectroscopy", *ChemPhysChem*, 13 (2012) 1718-1724.

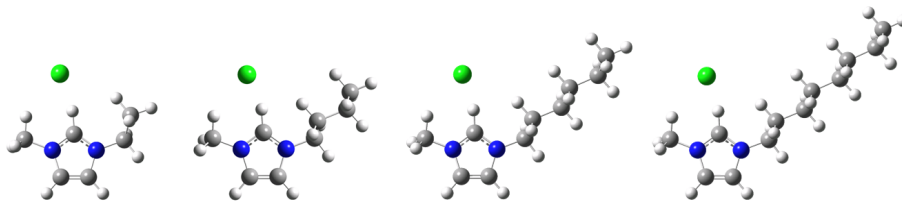


Figure 40: Calculated ion pairs from a series of [XMIm]Cl (from left to right): [EMIm]Cl, [BMIm]Cl, [HMIm]Cl, and [OMIm]Cl.

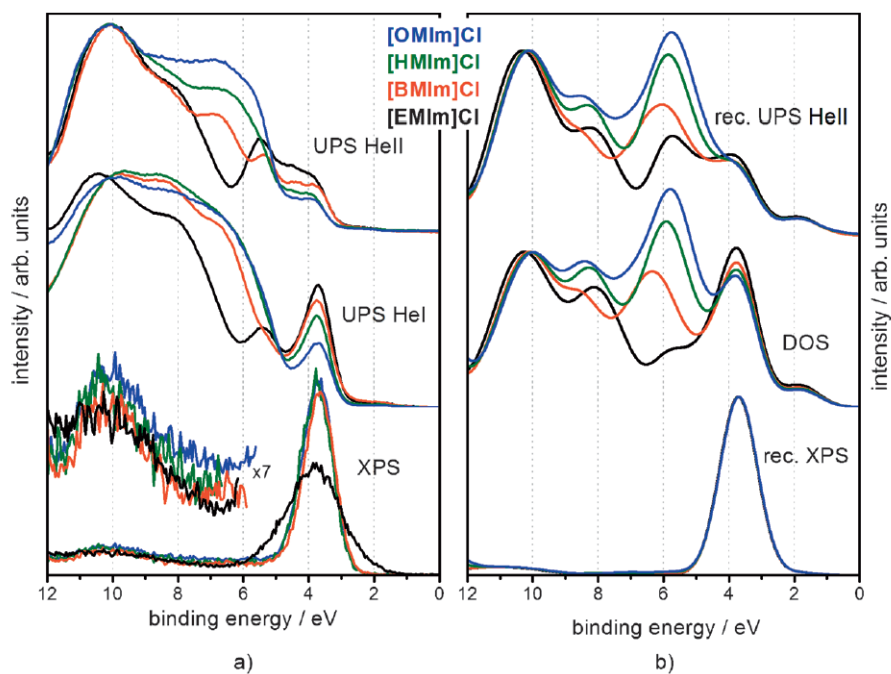


Figure 41: Experimental XPS, UPS (He I), and UPS (He II) valence band spectra (left) and reconstructed XPS and UPS (He II) valence band spectra as well as the respective density of states (DOS) (right) of [XMIm]Cl. All experimental and reconstructed spectra are normalized to the intensity at about 10 eV. The binding energies of the reconstructed spectra of XPS, UPS (He II), and the DOS are modified by a scaling factor of $f = 1.03040$, an identical absolute shift of $\Delta E = -1.41$ eV, and an equivalent relative shift between the ions of $\Delta\Delta E_{\text{Cation}-\text{Anion}} = -1.95$ eV. (With the courtesy of: Wiley-VCH, A. Ulbrich et al., ChemPhysChem, 13 (2012) 1718-1724, page 1721 [33]).

spectra due to sample charging [33].

For the experimental UPS (He I) spectra, respective changes are identified in a binding energy range between 5 and 10 eV. Similar differences in the density of states (DOS) are recognized in an identical binding energy range. The photoionization cross sections in UPS (He I) and UPS (He II) for the chlorine states in the valence band are found in the same order or even smaller than for the 2s and 2p orbitals of the dominating constituents nitrogen and carbon (cf. Table 1). In contrast to the XPS spectra, the contributions of the [XMIIm] cations and effects of the increasing alkyl chain length can be clearly detected in both UPS (He II) and UPS (He I) spectra.

Significant differences are noticed in a binding energy range of approximately 5 to 9 eV in the experimental UPS (He II) spectra, which are already related to the varied alkyl chain length. These changes due to an increased alkyl chain length relative to [EMIm]Cl are accompanied by a shift from circa 6.8 eV for [BMIm]Cl to approximately 6.0 eV for [OMIm]Cl. This shift has featured a parallel enhancement in height of the UPS (He II) spectra in this range, which is caused by the increased number of CH₂ groups in the alkyl chain. These facts are further proven by the partial density of states (pDOS) for respective parts of the alkyl chain of [OMIm]Cl displayed in Figure 42. Herein, enhanced intensities and respective shifts for the differences are observed from the pDOS with increasing alkyl chain length compared to the experimental UPS (He II) spectra. This shift is decelerated with an increase in distance to the imidazolium ring. A similar behavior was already recognized in the C1s core level spectra of imidazolium-based ionic liquids (see Chapter 4.1). Thus, it can be concluded that the distance to the imidazolium ring and its nitrogen atoms has dominated the binding energy positions of the different alkyl carbons in the valence band, too. Moreover, the contributions of encapsulated or dissolved water are noticed in the same binding energy range as the longer alkyl chain (cf. Chapter A.3 in the Appendix).

The intensity of the Cl3p peak is found with equal intensity for all four ionic liquids in their reconstructed UPS (He II) spectra. This reconstruction method has not incorporated any depth dependence, since all elements are considered as equally distributed in the probed sample volume. In contrast to this, the intensity of the Cl3p peak is constantly reduced from [EMIm]Cl to [OMIm]Cl in the experimental UPS (He II) spectra. This decrease of the related intensity is caused by an increased distance of the [Cl] anion from the surface. This has provided hints for the surface structure of [XMIIm]Cl ionic liquids, which can

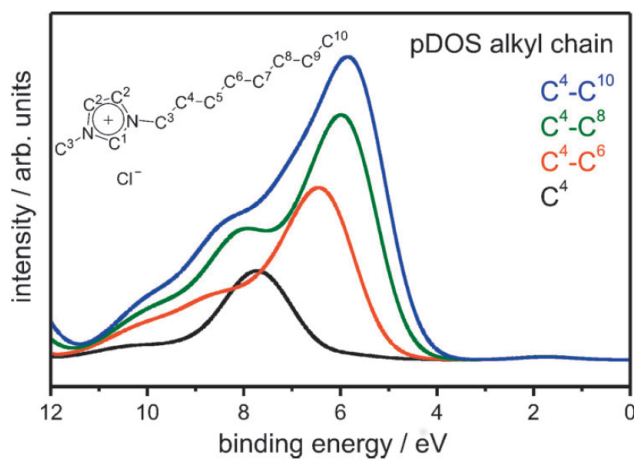


Figure 42: The partial density of states (pDOS) from the outer part of the alkyl chain (C^4H_3 or $C^4H_2-C^nH_3$) of $[XMIm]Cl$ ionic liquids. Herein, the binding energies are modified by the rescaling parameters of $f = 1.03040$, $\Delta E = -1.41 eV$, and $\Delta\Delta E_{Cation-Anion} = -1.95 eV$. (With the courtesy of: Wiley-VCH, A. Ulbrich et al., *ChemPhysChem*, 13 (2012) 1718-1724, page 1721 [33]).

be sketched as follows: the longer alkyl chains are present at surface protruding towards the vacuum, while the $[Cl]^-$ is found below/apart from the surface and might potentially be located in vicinity of the imidazolium ring. Similar surface structures were concluded in other experimental and theoretical studies, such as angular-resolved X-ray photoelectron spectroscopy [15] and molecular dynamics simulations [79].

An additional peak at approximately 5.5 eV is detected in the experimental UPS (He II) spectrum of $[EMIm]Cl$. This peak is exclusively caused by the imidazolium ring with its carbon atoms C^1 and C^2 (see Figure 65 in Chapter A.2 in the Appendix) and the contained two nitrogen atoms. For the other ionic liquids from the $[XMIm]Cl$ set, this peak at 5.5 eV is hidden by contributions caused by the enlarged alkyl chain. This fact has additionally supported the conclusion that the changes in the experimental spectra have predominantly resulted from differences in the ionic liquids' longer alkyl chains. However, the reconstructed UPS (He II) spectra have featured a slightly different shape than the experimentally measured spectra in this binding energy range of the alkyl chains. This could be caused by a number of potentially different ion pair geometries and alkyl chain geometries probed in the real ionic liquid compared to the specific one utilized for the reconstruction. Hereinafter, the influences of six

different ion pair geometries and various alkyl chain geometries with artificially generated kinks and torsions onto the reconstructed XPS and UPS (He II) valence band spectra are analyzed.

7.2 Influence of the geometry of the ion pair and the alkyl chain on the reconstructed valence band spectra

In this chapter it is investigated, how different geometries for the ion pairs of [EMIm]Cl and the alkyl chain in [OMIm]Cl have influenced the reconstructed spectra. As a consequence, those ion pair geometries and alkyl chain shapes are of particular interest, which might result in a better agreement with the experimental spectra compared to the ion pairs used in Chapter 7.1.

7.2.1 Influence of pair geometry of [EMIm]Cl

The spatial distribution function (SDF) for [EMIm]Cl, which was obtained from molecular dynamics simulations, is depicted in Figure 30 (left). Herein, the positions with increased density of the [Cl] anion around the [EMIm] cation are illustrated. The [Cl] anion is found in three preferred positions in vicinity of the C¹, C^{2M}, and C^{2E} carbons (see Figure 29 (left) for respective nomenclature). A separation of the area with a very high density into two ranges is detected for the C¹ position. However, these high density areas are recognized apart from the hydrogen atom in C¹ position and are slightly moved towards the methyl group or ethyl chain. All of these preferred positions of the [Cl] anion around the [EMIm] cation are discovered for the ion pairs of [EMIm]Cl in Figure 43, too. However, other positions are not perceived by the ion pair calculations as well as those, which did not feature significant densities in molecular dynamics simulations, leading to the conclusion that the positions C¹, C^{2M}, and C^{2E} are strongly favored and this is in agreement to refs. [75, 156].

The total and relative energies of the calculated [EMIm]Cl ion pairs are listed in Table 10. Herein, the ion pairs with the [Cl] anion in C¹ position are energetically preferred against C^{2M}/C^{2E} position (cf. ref. [95]). Within the ion pairs in C¹ position a preference by 0.023 eV is exhibited, where the chloride is slightly moved towards the methyl group (A3 in Figure 43), compared to the C¹ position, where the anion is lightly displaced towards the ethyl group (A1 in Figure 43). The position, where the [Cl] anion is slightly shifted out

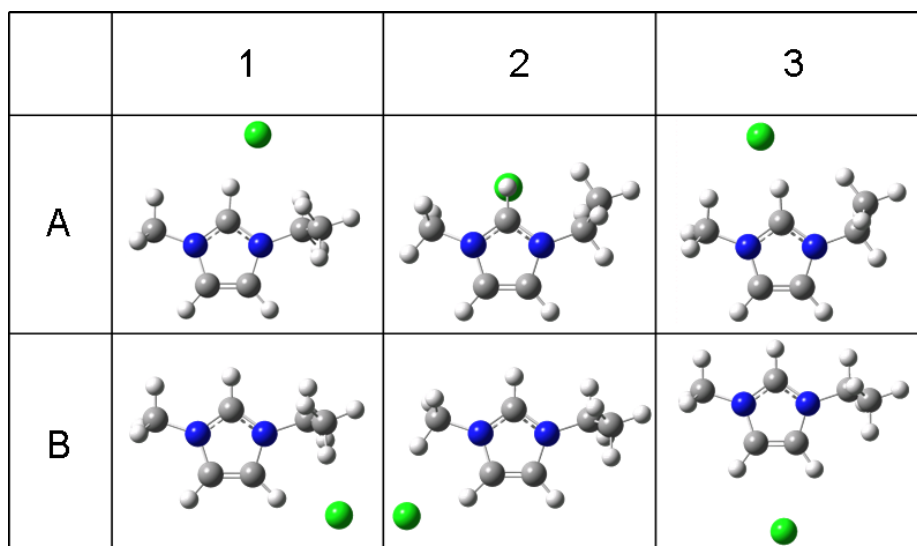


Figure 43: Six different ion pair geometries for [EMIm]Cl (respective total energy and relative difference for the ion pairs are listed in Table 10).

Ion pair	Interaction site	Total energy (eV)	Difference (eV)
A1	H ¹	-21903.336	+0.023
A2	H ¹ /C ¹	-21903.265	+0.094
A3	H ¹	-21903.359	0.000
B1	H ^{2E}	-21903.007	+0.352
B2	H ^{2M}	-21902.981	+0.378
B3	H ^{2M/2E}	-21902.664	+0.695

Table 10: Total energy and relative difference (in eV) of the calculated ion pairs of [EMIm]Cl displayed in Figure 43 in dependence of the respective geometry.

of the image plane (A2 in Figure 43), is associated with a disadvantage of 0.094 eV. For the anion in the C^{2M}/C^{2E} position (B1-B3 in Figure 43) the relative energies are identified between 0.352 and 0.695 eV above A3. This relative energy difference between ion pairs with the [Cl] anion in C^1 position and C^{2M}/C^{2E} position is noticed as obviously high, i.e. even slightly higher than for their [EMIm]Tf₂N analog. It is assumed that this could result from the partially stronger interaction between the imidazolium-based cation and the [Cl] anion. In contrast to this, all of these positions are identified in the respective molecular dynamics simulation [75], while this significant energy gap is maybe only found in ion pair calculations and not in the real ionic liquid with its multiple ion interactions.

The reconstructed XPS valence band spectra from all six calculated ion pairs are illustrated in Figure 44. In the reconstructed spectra, the eye-catching peaks of Cl3s and Cl3p state are observed at 16.3-17.8 eV and 3.9-5.2 eV, respectively. However, the separation of the two prominent peaks is recognized as nearly equal for all ion pairs featuring the C^1 position with a separation of about 12.6-12.7 eV or C^{2M}/C^{2E} position of around 12.4 eV. At this point, the effect of the utilized basis set and functional onto the size of the separation between the Cl3s and Cl3p states (cf. Chapter A.1 in the Appendix) has to be mentioned. This effect might lead to the assumption that only the cases of the [Cl] anion in C^1 and C^{2M}/C^{2E} position have to be distinguished, an identical result was obtained for the ion pairs from [EMIm]Tf₂N in Chapter 6.1. Nevertheless, for the reconstructed valence band spectra of XPS and UPS (He II), which are illustrated in Figure 44 and Figure 45, minor differences are discovered for the ion pairs that have featured a [Cl]⁻ position, which is located outside of the very high density regions in Figure 30. These differences are accompanied by a relative shift of most of the peak positions, where the contributions of the ion pair A2 are shifted by approximately 0.2-0.3 eV to higher binding energy compared to the nearly equal spectra from A1/A3 as well as a shift in the order of 0.6 eV to lower binding energy is detected for those of B3 relative to B1/B2. Herein, the ion pairs of A1 and A3 as well as B1 and B2 have featured similar peak shapes and peak positions. Whereas, the ion pairs of A2 and B3 have offered discernable peak shapes compared to A1/A3 and B1/B2, respectively. Herein, the onset positions of the contributions of the [EMIm] cation are accompanied by relative shifts, too.

Beyond the general curve shape, the relative positions between the contributions of both ions are listed in Table 11. This has provided information about the

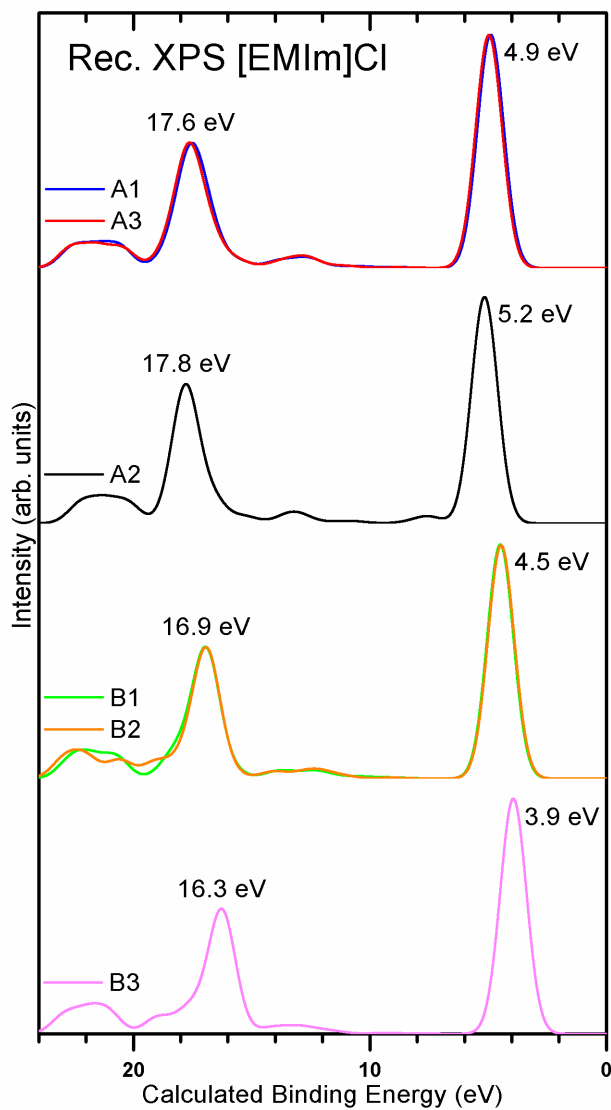


Figure 44: Reconstructed XPS valence band spectra from six different ion pair geometries of [EMIm]Cl (displayed in Figure 43). The calculated binding energies of the Cl3s and Cl3p states are indicated for the reconstructed spectra. A rescaling procedure is not applied here.

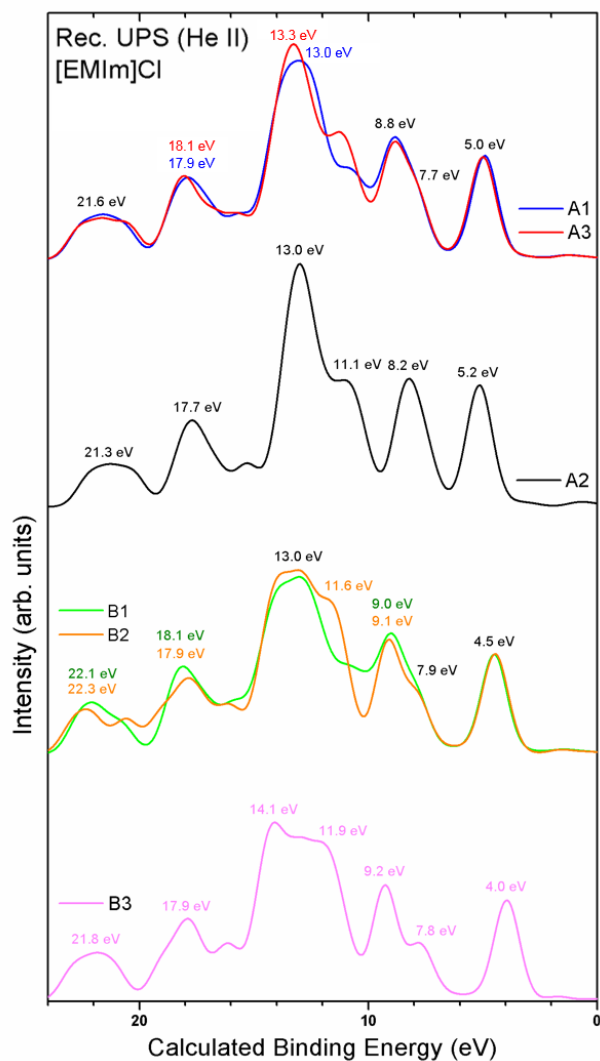


Figure 45: Reconstructed UPS (He II) spectra from six different ion pair geometries of [EMIm]Cl (displayed in Figure 43). The calculated binding energies of the peaks and some related shoulders are indicated for the reconstructed spectra. A rescaling procedure is not applied here.

Ion pair	Lowest [EMIm] ⁺ state (eV)	Cl3p orbital (eV)	Difference (eV)
A1	7.9	5.0	2.9
A2	7.6	5.2	2.4
A3	7.9	5.0	2.9
B1	7.9	4.5	3.4
B2	7.9	4.5	3.4
B3	7.8	4.0	3.8

Table 11: The calculated binding energy positions of the first state related to the [EMIm] cation (at lowest binding energy) and of the Cl3p orbital in the reconstructed UPS (He II) spectra of various ion pair geometries of [EMIm]Cl displayed in Figure 43 as well as the resulting difference between these contributions.

rescaling parameter $\Delta\Delta E_{Cation-Anion}$ and a route towards the determination of the related Madelung potential on the basis of an ion pair. A determination of the Madelung potential was executed with the aid of the pDOS of single ion calculations in relation to the experimental spectra in ref. [41]. The ion pairs A1 and A3, where the [Cl]⁻ interacts with the hydrogen at C¹, have offered a difference of circa 2.9 eV. While, the ion pairs B1 and B2 with the [Cl] anion in vicinity of hydrogen in C^{2M} or C^{2E} position have exhibited a difference of about 3.4 eV, which is exclusively caused by a related shift of the Cl3p state to lower binding energy compared to the geometries A1 and A3. The ion pair A2, where the [Cl] anion is found in interaction with the central carbon atom C¹, has featured a difference of approximately 2.4 eV caused by a shift of the respective contributions towards each other compared to A1 and A3. The last ion pair, which has interacted nearly equally with both hydrogens in C^{2M} and C^{2E} position, a difference of about 3.8 eV is detected (B3), which has resulted from a primary shift of the Cl3p peak position. Those relative shifts have shown to be equal for similar anion positions (A1/A3 and B1/B2) due to symmetry reasons. For the different ion pair geometries of [EMIm]Cl, where the relative shift $\Delta\Delta E_{Cation-Anion}$ has to be compensated by the adaption procedure, four different ion pair geometries have to be distinguished. Additionally, this has led to the conclusion that four distinctions from the Madelung potential are found for [EMIm]Cl. In comparison, for the larger [Tf₂N] anion for which a fewer number of positions are distinguished only two different relative shifts are present for the C¹ and C^{2M}/C^{2E} positions. For qualitative statements, such as the difference spectra, the ion pair geometry has verified an effect onto the shape of the reconstructed spectra. In consequence, the positions within the ion

pairs preferably have to be kept equal for a comparison of ion pairs of different alkyl chain lengths. This has supported the choice of the utilized approximately equal ion pairs of [XMIIm]Tf₂N and [XMIIm]Cl (cf. Figure 9 and Figure 40 as well as refs. [33, 90]).

7.2.2 Effect of alkyl chain geometry of [OMIm]Cl

The structure of the cation is not limited to one preferred geometry, which was found in a similar way for the geometry of the [Tf₂N] anion. Geometrical changes might be present in the imidazolium ring and in the alkyl chains. The imidazolium ring is presumed as comparatively stable, since it has contained contributions of π bonds, which have caused a certain degree of stiffness. Different cases have to be distinguished for the two alkyl chains of the [XMIIm] cation: the methyl group possesses a rotational freedom around the N-C bond. Whereas, for the typically larger alkyl chain a number of conformations may be expected. This fact was proven by Raman spectroscopy, which is supported by quantum-chemical calculations, in which both conformers have featured an equilibrium characterized by different signatures in the range from 200 to 500 cm⁻¹ [157]. Only two independent conformers with planar and nonplanar shape (cf. Figure 46) are found for [EMIm]⁺ due to the fact that the ethyl chain geometry relative to the imidazolium ring is exclusively changed by a rotation around the N-C bond. Quantum-chemical calculations, which are executed in the present thesis, have revealed that the nonplanar conformer of the [EMIm] cation is energetically preferred (see Table 12). The difference between planar and nonplanar conformer of [EMIm]⁺ is estimated by 24 meV, which is in the order of kT at room-temperature. Thus, both conformers are expected to be in an equilibrium in a real ionic liquid under ambient conditions, this finding is supported by the results of Y. Umebayashi et al. [157].

In comparison to the [EMIm] cation, the conformational space of alkyl chain possibilities is much larger if the cation has possessed a longer chain. In particular, the rotational freedom around the N-C bond is determined by the dimension of anion and its interaction with the anion, since the energy difference between the different minima is comparably low for the neat cation (cf. Table 12). For this purpose, possible changes in the longer alkyl chain of the previously used ion pair from [OMIm]Cl, which were artificially incorporated, are illustrated in Figure 47. The related total energies and differences are listed in Table 13. In the ion pairs the [Cl] anion is found in vicinity of the hydrogen atom at the C¹

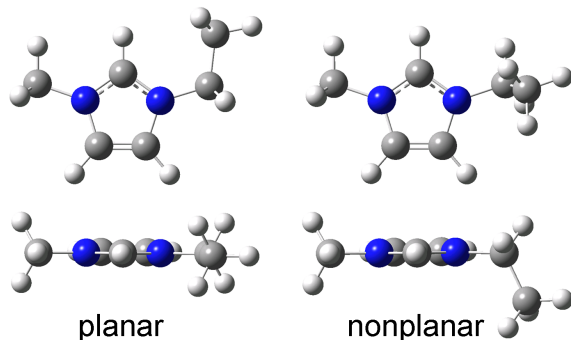


Figure 46: Side view (top) and top view (bottom) of two conformers of the [EMIm] cation with planar (left) and nonplanar geometry (right).

[EMIm] ⁺ conformer	Total energy (eV)	Difference (eV)
planar	-9375.608	+0.024
nonplanar	-9375.632	0.000

Table 12: The total energy and relative difference (in eV) from the planar and nonplanar conformers of the [EMIm] cation displayed in Figure 46.

Ion pair	Changes	Total energy (eV)	Difference (eV)
A1	1 (1T)	28322.217	0.000
A2	2 (1T+1K)	28322.178	+0.039
A3	3 (1K+2T)	28322.145	+0.072
B1 [#]	0	28322.191	+0.026
B2	1 (1K)	28322.143	+0.074
B3 [#]	0	28322.191	+0.026
C1	1 (1K)	28322.185	+0.032
C2	1 (1K)	28322.139	+0.078
C3	1 (1K)	28322.139	+0.078
D1	1 (1K)	28322.139	+0.078
D2	1 (1K)	28322.148	+0.069
D3	2 (2K)	28322.121	+0.096

Table 13: Total energy and relative difference (in eV) of ion pairs of [OMIm]Cl displayed in Figure 47 with artificially incorporated kinks (K) and/or torsions (T) in the longer alkyl chain. ([#]) The ion pairs of B1 and B3 have featured the same total energy due to symmetry reasons, since their octyl chain is rotated around the C-N bond.

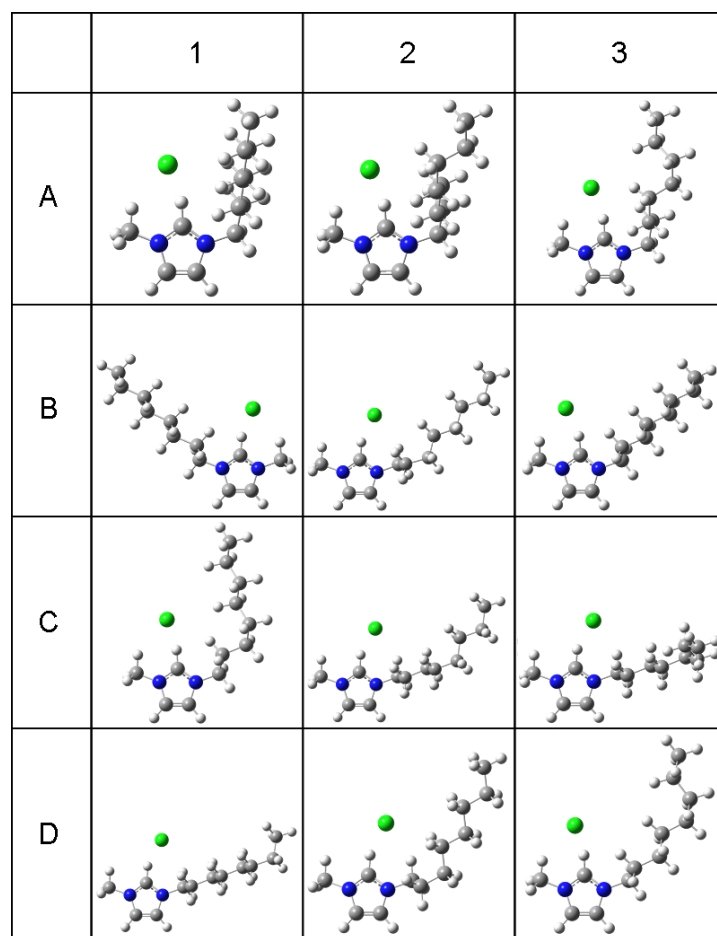


Figure 47: Ion pairs of [OMIm]Cl with artificially incorporated changes, i.e. kinks and/or torsions, in the longer alkyl chain (respective changes as well as total energy and relative difference are listed in Table 13).

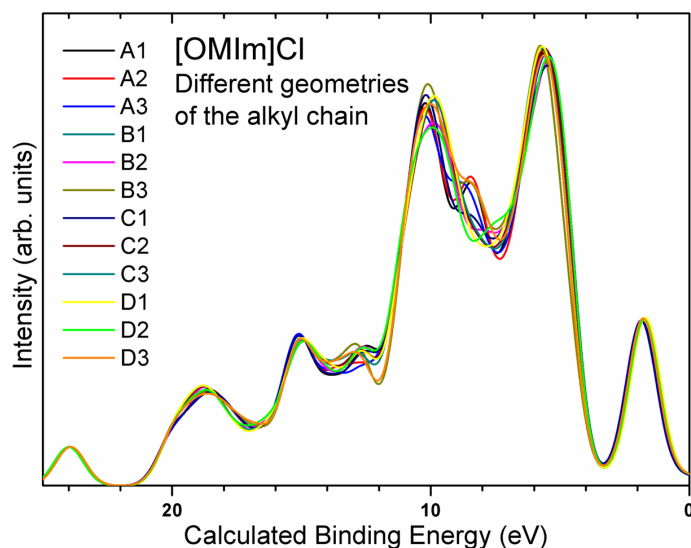


Figure 48: Reconstructed UPS (He II) spectra of ion pairs of [OMIm]Cl with artificially incorporated kinks and torsions (displayed in Figure 47). A rescaling procedure is not applied here.

carbon in two different positions of either slightly moved towards the methyl group or the octyl chain. Herein, it has become obvious that the total energy of an ion pair can be slightly reduced by the incorporation of a torsion around the N-C bond, which might be associated with an additional interaction with the [Cl] anion. In principle, the influence of the alkyl chain geometry is discovered as marginal. The maximum variation in energy is observed in the order of 96 meV. This has led to the conclusion that the presence of a number of possible changes from the ideal alkyl chain might be found at room temperature despite of other influence quantities. The reconstructed UPS (He II) spectra for all ion pairs with different kinks and/or torsions, which are displayed in Figure 47, are illustrated in Figure 48. First of all, the artificial changes in the alkyl chain of [OMIm]Cl have not recognizably influenced the binding energy position of the Cl3p states, which is in agreement with the previous results of ion pair geometry for imidazolium-based ionic liquids. Differences between the valence band spectra of various alkyl chain geometries are detected in the binding energy range from 7 to 14 eV. However, these differences are evaluated as minor. Thus, the differences between the reconstructed and experimental UPS (He II) spectra are most probably not covered by the kinks and torsions within the alkyl

chain. An improvement of the recognized differences between the spectra might be achieved for example by consideration of a certain arrangement of the ions, i.e. layering/stacking with potential shielding effects, in the near surface region or the calculation of a larger cluster of [OMIm]Cl with multiple interactions. A minor influence of final state effects in the experiment cannot be fully excluded. Thus, a final decision about the origin of these differences cannot be made.

7.3 Chapter summary

For the carbon atoms within the cations' longer alkyl chain, a dependence of the respective binding energy positions on the distance to the nitrogen atoms is observed in the valence band. This effect is further decelerated with increasing alkyl chain length, whereas a similar behavior was already found in the Cls core levels of this imidazolium-based cation [90]. For the surface structure of [XMIm]Cl, it is concluded that longer alkyl chains are protruding towards the vacuum, while the small [Cl] anion is burried beneath the alkyl chain (cf. ref. [33]). The assumed surface structure is found in good agreement with other studies [15, 44, 79]. Four different values for relative binding energy positions between cation and anion contributions are detected for the preferred ion pair geometries for which the distinct variations of the rescaling parameter $\Delta\Delta E_{Cation-Anion}$ and likewise deviations from the Madelung potential are expected on the ion pair basis compared to the use of a single ion pair [41]. A minor influence of the specific geometry of the longer alkyl chain is estimated for the reconstructed spectra. As a result, the ascertained differences in the valence band spectra between experiment and reconstruction are potentially caused by the arrangement of the ions at the surface and related shielding effects.

8 Valence band structure of pyrrolidinium-based ionic liquids of [XMPyrr]Tf₂N - in comparison to their imidazolium-based analog

The physicochemical properties of this type of ionic liquids are characterized in relation to the imidazolium-based ionic liquids (cf. refs. [132, 136]): their melting points, densities, and viscosities are similar, while the conductivities of pyrrolidinium-based ionic liquids are slightly decreased compared to their analogs. Pyrrolidinium-based ionic liquids have possessed a non-aromatic ring in the cation in contrast to their imidazolium-based analog, which has offered an aromatic ring. Thus, the pyrrolidinium-based cations have offered a different degree of rotational and geometrical freedom for the calculated ion pair. Appropriate positions for the ion pair geometry are discussed in Chapter 4.2. A profound analysis of the element-specific contributions and the binding energy positions of the states related to the cation in the valence band is performed in comparison to the imidazolium-based cation.

8.1 Reconstructed XPS and UPS (He II) valence band spectra

The reconstructed XPS valence band spectra for the two pyrrolidinium-based ionic liquids [BMPyrr]Tf₂N and [OMPyrr]Tf₂N, which have featured a butyl and octyl chain as the longer one of both, are displayed in Figure 49.⁷ Only the reconstructed valence band spectrum of [BMPyrr]Tf₂N is compared to the experimentally obtained one. Herein, a very good agreement between these spectra is recognized. For the three peaks at about 7, 12, and 16 eV the peak heights are perceived as the same. Whereas, for the peaks at about 18 and 20 eV the experimental spectrum has offered a slightly higher intensity than the reconstructed equivalent, since the experimental spectrum in this energy range is already affected by inelastically scattered electrons. This agreement is evaluated as distinctly better than for the analogous set of ionic liquids from [XMIIm]Tf₂N, where already the peaks at 16 eV as well as at higher binding energies have clearly differed in height. The reason for this effect of the pyrrolidinium-based

⁷Parts of this chapter have been published in the following peer-reviewed article:

A. Ulbrich, M. Reimmöller, W. J. D. Beenken, S. Krischok, "Photoelectron spectroscopy of ionic liquid surfaces - theory and experiment", *Journal of Molecular Liquids*, 192 (2014) 77-84.

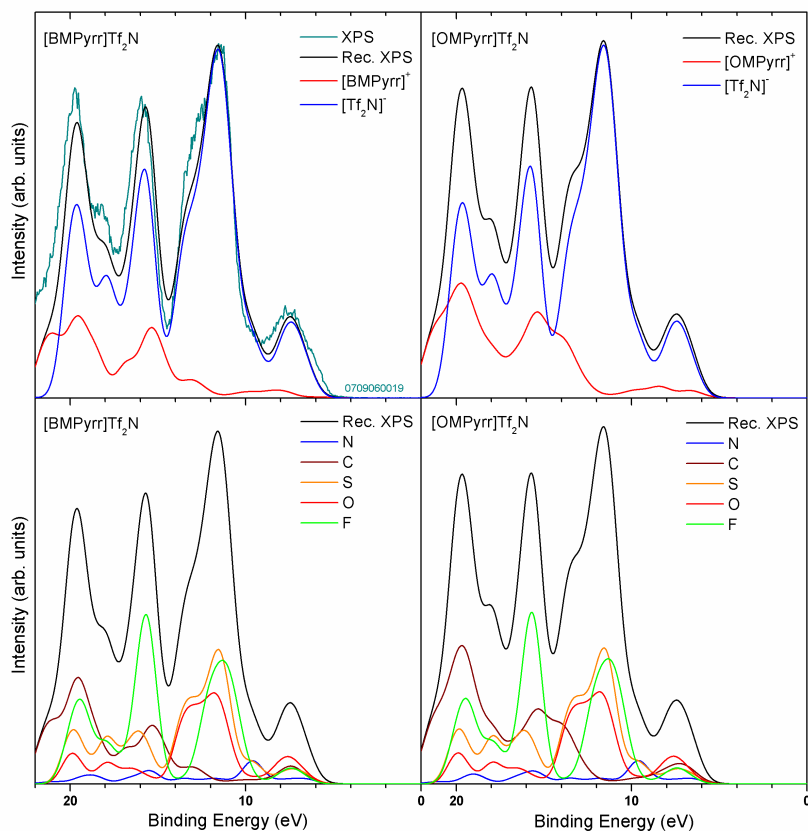


Figure 49: Reconstructed XPS valence band spectrum of [BMPyrr]Tf₂N together with the experimental spectrum (left) and for comparison only the reconstructed spectrum is shown for [OMPyrr]Tf₂N (right). Herein, the reconstructed spectrum is decomposed into the ions (top) and elements (bottom). The reconstructed spectrum of [BMPyrr]Tf₂N is normalized to the respective height of the experimental peak at approximately 12 eV. All reconstructed spectra for [BMPyrr]Tf₂N are modified by the rescaling parameters of $f = 1.02963$, $\Delta E = -0.79$ eV, and $\Delta\Delta E_{Cation-Anion} = -1.47$ eV to fit the value of N^{Tf_2N} . The same values except of $\Delta E = -0.77$ eV (due to minor deviations) are used for [OMPyrr]Tf₂N, since for this ionic liquid no experimental spectra are available. For comparison to ionic liquids of the sets of [XMIIm]Tf₂N and [XMIIm]Cl, the rescaling parameters for ion pairs featuring an analogous geometry are almost identical within one set (cf. Table 16). The experimental spectrum is obtained from personal communication with Dr. M. Himmerlich.

ionic liquid may be found either by a lower background caused by inelastically scattered electrons or a better assignment of the element-specific contributions due to the non-aromatic ring, which might strongly influence the attribution of contributions of carbon and nitrogen. In addition, it has to be noticed that the spectra are broadened by a slightly different FWHM according to the experimental resolution.

The decomposition into the contributions of both ions, i.e. the pyrrolidinium-based cation and the $[\text{Tf}_2\text{N}]$ anion, are visualized in Figure 49 (top) for both investigated ionic liquids. A dominating contribution of the $[\text{Tf}_2\text{N}]$ anion especially near the valence band edge is identified in the reconstructed XPS spectra. The reason for this are the large photoionization cross sections from the 2p or 3p orbitals of elements fluorine, oxygen, and sulfur, which are a few orders of magnitude higher than those of carbon and nitrogen, which have comprised the main constituents of the pyrrolidinium-based cation (cf. Table 1). In consequence, no significant changes in the reconstructed spectra due to the different alkyl chain lengths are obtained between $[\text{BMPyrr}]\text{Tf}_2\text{N}$ and $[\text{OMPyrr}]\text{Tf}_2\text{N}$ near the valence band edge. On the other hand, the contributions of the cation have become more significant at higher binding energies above approximately 12 eV, since the cross sections of their C2s and N2s orbitals are in the same order of magnitude than those from fluorine, oxygen, and sulfur. Two structures containing multiple peaks with their respective maxima at circa 15 and 19 eV are related to the $[\text{XMPyrr}]$ cations. In contrast to this, for the imidazolium-based analog of $[\text{EMIm}]\text{Tf}_2\text{N}$ the cation-related spectra have featured two peaks at around 16 and 21 eV in the reconstructed XPS spectra, while for the $[\text{OMIm}]$ cation a broad plateau in this binding energy range with a further peak at about 14 eV has appeared. The main difference between both cations is detected in a binding energy range of 12 to 15 eV and at around 20 eV, which should be caused by the sufficient C2s cross sections for the additional alkyl carbons. This effect is analyzed by means of elementwise deconvoluted contributions hereinafter. However, it has to be noted that the nitrogen and carbon contributions of ionic liquids of $[\text{XMIm}]\text{Tf}_2\text{N}$ are affected by the 'shoveling around' effect.

In Figure 49 (bottom), the reconstructed XPS valence band spectrum is decomposed into the contained elements. The spectra are in general dominated by fluorine, oxygen, and sulfur due to their previously mentioned high XPS photoionization cross sections. For the peak at lowest binding energy at around 7 eV oxygen is identified as the dominating element, herein further contribu-

tions of fluorine, sulfur, and carbon are present. The contribution of carbon has primarily originated from the [Tf₂N] anion, since the ascertained carbon peak is notably higher than the total contribution of the [BMPyrr] cation as found from the decomposition into the ions in this binding energy region. An analogous result was achieved for the set of ionic liquids from [XMIIm]Tf₂N. The elements fluorine, sulfur, and oxygen are encountered in remarkable amounts in the highest peak for [XMPyrr]Tf₂N at around 12 eV. This peak has featured two shoulders: a first one at the lower binding energy side and a second one at the higher binding energy edge. The shoulder at lower binding energy, which is visible in a range from approximately 9 to 10 eV, might originate from nitrogen and sulfur, since the elementwise analysis has almost exclusively revealed contributions of both elements in this region. Thus, this shoulder is primarily shaped by the central atoms on the main bond axis of the [Tf₂N] anion. In addition, the shoulder at the higher binding energy side of this peak is mainly assigned to sulfur and oxygen, which has led to the same conclusion as for the imidazolium-based ionic liquids that this shoulder is formed by the SO₂ groups of the [Tf₂N] anion. Additional parts of carbon are detected within this shoulder for [OMPyrr]Tf₂N. Contributions from fluorine, sulfur, and carbon are found in the three peaks at higher binding energies in the range of 16-20 eV. The peak at about 16 eV is dominated by fluorine, whereas carbon is found in excess in the peak at about 20 eV. The peak in between at circa 18 eV is equally shared by the three mentioned elements with minor amounts of oxygen and nitrogen. Oxygen has not significantly contributed to these three peaks, since it has featured comparably low photoionization cross sections for its 2s orbital. In contrast to their imidazolium-based analogs, the utilized ion pairs of [XMPyrr]Tf₂N have not demonstrated an apparent effect of 'shoveling around' of the contributions related to different elements in the higher binding energy range of the XPS valence band spectra.

The reconstructed UPS (He II) spectrum of [BMPyrr]Tf₂N is correlated to the experimental spectrum, while the additionally reconstructed spectrum for the ion pair of [OMPyrr]Tf₂N is illustrated only for comparison in Figure 50. A general agreement between reconstructed and experimental spectra is observed. The shoulder peak found at the higher binding energy side of the dominating peak in the experimental spectrum is not reproduced by the reconstruction, which could be an effect of either the utilized peak broadening, final state effects or an insufficient energetical separation of the molecular orbitals in the calculation. A final statement about the percentages of these potential effects

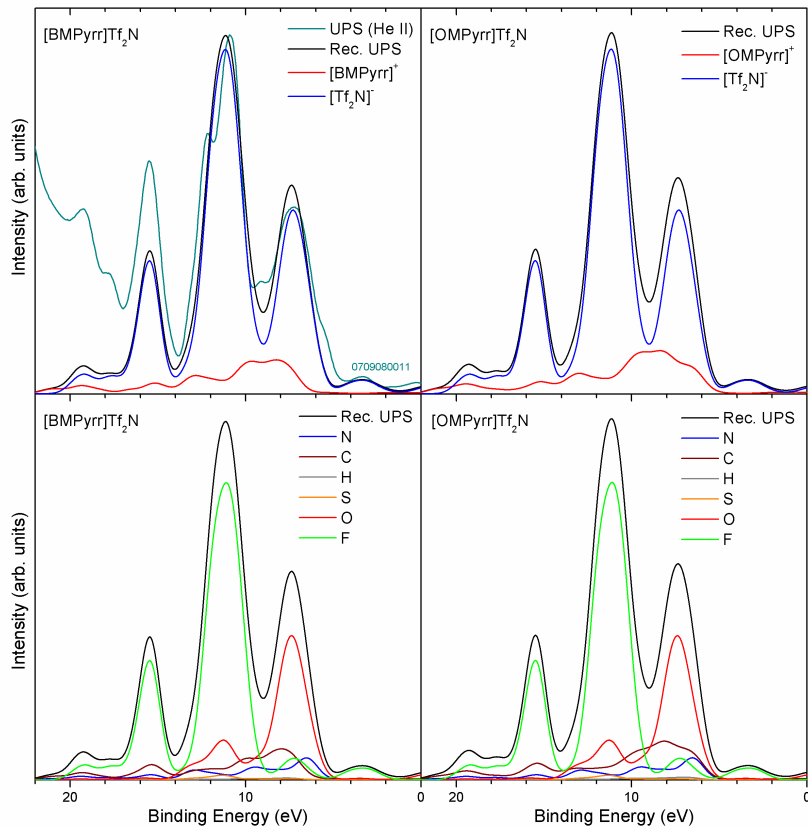


Figure 50: Reconstructed UPS (He II) spectrum of [BMPyrr]Tf₂N together with the experimental spectrum (left) and for comparison only the reconstructed spectrum is shown for [OMPyrr]Tf₂N (right). Herein, the reconstructed spectrum is decomposed into the ions (top) and elements (bottom). The presence of the He II β -line is considered in the reconstructed spectra by means of a duplicate of the reconstructed He II α -line combined with a shift of -7.56 eV and a height of 4% of the initial α -line intensity. The spectrum of [BMPyrr]Tf₂N is normalized to height of the peak at approximately 11 eV. All reconstructed spectra for [BMPyrr]Tf₂N are modified by the rescaling parameters of $f = 1.02963$, $\Delta E = -0.99$ eV, and $\Delta\Delta E_{\text{Cation}-\text{Anion}} = -1.47$ eV to fit the value of $N^{\text{Tf}_2\text{N}}$. The same values are used for [OMPyrr]Tf₂N, since for this ionic liquid no experimental spectra are available. For comparison to ionic liquids of the sets of [XMIIm]Tf₂N and [XMIIm]Cl, the rescaling parameters for ion pairs featuring an analogous geometry are almost identical within one set (cf. Table 16). The experimental spectrum is obtained from personal communication with Dr. M. Himmerlich.

is not possible at this point. The peak heights have not fully matched, which can be attributed to a background of inelastically scattered electrons at the higher binding energies and potentially an influence of final state effects. Nevertheless, the relative intensities of the ions or elements within a single peak are not influenced by the differences between experimental and reconstructed spectra. A dominating proportion of the $[\text{Tf}_2\text{N}]$ anion is identified by means of a deconvolution of the reconstructed UPS (He II) spectra into the ions in Figure 50 (top). The cation has contributed, especially at binding energies in a range approximately from 6 to 11 eV for $[\text{BMPyrr}]\text{Tf}_2\text{N}$ and from 5 to 11 eV for $[\text{OMPyrr}]\text{Tf}_2\text{N}$. No significant contributions near the valence band edge are assigned to the $[\text{BMPyrr}]$ cation. In contrast to this, for the $[\text{OMPyrr}]$ cation contributions near the valence band edge starting at circa 5 eV are perceived, which have consequently originated from the additional outer part of the octyl chain.

A decomposition of the reconstructed UPS (He II) spectra into the respective elements is performed in Figure 50 (bottom). Herein, a dominating effect of either fluorine or oxygen in all peaks is recognized, since both have featured the highest photoionization cross sections compared to all other contained elements in their 2p orbitals (cf. Table 1). The first peak at approximately 7 eV is assigned to mainly oxygen, while further elements, like fluorine, nitrogen, and carbon, are detected herein. The second most intense contribution following the strong oxygen proportion has originated from carbon in both pyrrolidinium-based ionic liquids. A clearly stronger carbon contribution is detected in the first peak at around 7 eV compared to the imidazolium-based analog and, thus, closer to the valence band edge. It can be excluded that this could be a result of a significantly different number of carbon atoms, since both ionic liquids have only varied by one carbon atom in total. The contributions of the increased alkyl chain length are recognized in a binding energy range from 5 to 11 eV for $[\text{OMPyrr}]\text{Tf}_2\text{N}$ compared to those of $[\text{OMIm}]\text{Tf}_2\text{N}$, which are present from 5 to 13 eV. Herein, the carbon contributions are shifted in their onset position within the peak at a binding energy of about 7 eV towards lower values with increasing alkyl chain length, a similar behavior was recognized for the imidazolium-based cation. Differences in the respective peak shapes for the carbon contributions are noticed: for the pyrrolidinium-based ionic liquid of $[\text{OMPyrr}]\text{Tf}_2\text{N}$ a broad plateau with a small tip at around 8 eV is present, while $[\text{OMIm}]\text{Tf}_2\text{N}$ has offered a lower plateau with the highest intensity closer to the valence band edge at circa 6.5-8 eV (cf. Figure 37).

A dominating contribution from fluorine is detected in the highest peak of the UPS (He II) spectrum at approximately 11 eV. Herein, other contributions, which have originated from oxygen, carbon, and nitrogen, are discovered with lower amount, too. The very strong contribution from sulfur, which was previously found in the reconstructed XPS spectra, has nearly disappeared in the UPS (He II) spectra due to its very low cross section as observed for the ionic liquids of [XMIIm]Tf₂N. For the third peak at about 15.5 eV, a dominating fluorine as well as a slight carbon contribution are verified. Further peaks at higher binding energy values at around 18 and 19.5 eV are noticed in the reconstructed spectra. These peaks are not suitable for a quantitative comparison with the experimental spectra, since in this binding energy range the experimental spectra are affected by a significant background from inelastically scattered electrons as well as potentially very small or partially unavailable photoionization cross sections for all elements expected at these binding energies (cf. Table 1).

8.2 Chapter summary: a comparison to their imidazolium-based analogs

The general shape of the reconstructed and experimental XPS and UPS (He II) valence band spectra of [XMPyrr]Tf₂N is observed as close to those of the reconstructed spectra from a [XMIIm]Tf₂N ion pair due to a dominating contribution of the [Tf₂N] anion. All contributions of the anion are reconstructed with a similar progression for both ionic liquids. Nevertheless, for the pyrrolidinium- and imidazolium-based cations different peak positions and curve progressions are identified using both radiation sources. As a result of this, for the cation-related elements of carbon and nitrogen clearly different peak structures are recognized within the XPS and UPS (He II) valence band spectra, which are principally overlaid by the strong anion contributions. For an increase of the longer alkyl chain, which is most probably directed towards the vacuum, the respective additional contributions are assigned to unequal binding energy ranges for these two kinds of ionic liquids. Nonetheless, both have demonstrated a shift towards lower binding energies with increasing alkyl chain length.

Part IV

Results of the reconstruction of valence band spectra of ionic liquids with metals and alkali metals

Additional metal and alkali metal atoms in ionic liquids present a concept with a multitude of potential applications. These involve for example the field of electrochemistry and materials science with usages in electroplating [158, 159] as well as highly efficient batteries and supercapacitors [158, 159, 160] or catalytic applications [128, 141]. For this purpose, atoms can be added to ionic liquids in several ways: they can be (electrochemically) dissolved in, deposited from the gaseous phase onto the ionic liquid or incorporated as an entire part of one or both of the ions. The solubility of materials in ionic liquids is in principal higher if the species have featured an ionic character [161]. Ionic liquids with dissolved or likewise evaporated metal atoms have gained interest for the generation of nanoparticles and deposition of layers of these materials, e.g. by use of an electrochemical or plasma treatment of these liquids [147, 159, 162]. A special arrangement in the near surface region for ionic liquids with the dissolved species, i.e. a strong enrichment or depletion of the respective atoms, can be expected [163]. For this analysis copper is chosen as a representative for metals, which has possessed a broad application potential and is compared to the experimental spectra. Lithium and potassium, which belong to the group of alkali metals, are selected because of their technological relevance.

The investigated (alkali) metal atoms have offered different charge states, which has led to various spin arrangements. For the charged alkali atoms their partial charge is fixed to a single positive charge, but for the copper species the charge of either Cu^+ or Cu^{2+} is uncertain. An assignment of the exact charge state is complicated, since the related $\text{Cu}2p$ states are accompanied by shake-up structures. All of the neutral atoms on the one hand are present with a clearly defined charge state and on the other these are accompanied by spin-related challenges for the quantum-chemical calculation due to their unpaired

electron. Nevertheless, the employed calculations have to provide reliable binding energies, since they have covered the basis for the subsequent reconstruction method. Different kinds of interaction between the ionic liquids and the metal or alkali metal atoms as well as their influence on the resulting electronic structure have to be regarded prior to spectra reconstruction and comparison to the experiment.

9 Interaction of ionic liquids with evaporated metal and alkali metal atoms and the resulting valence band spectra

The interaction of an ionic liquid with additional species is apparent. In this chapter, available experimental data are obtained from evaporated atoms on a standard ionic liquid of [EMIm]Tf₂N under inert conditions. The valence band spectra of the neat ionic liquid were already investigated in Chapter 6.2. Ionic liquids are complex materials itself, since they are formed by charged units and have typically contained a number of polyvalent atoms. The deposited neutral atoms have offered an unpaired spin, which has to be considered for the quantum-chemical calculation. The molecular systems have to be balanced in both their overall charge and overall spin due to the previously described requirement that these calculations have to provide reliable binding energies for the subsequent spectra reconstruction. As a result of these conditions, in all cases a cluster of ion pairs from the ionic liquid and metal or alkali metal atoms with a stoichiometric composition of [Cation]₂[Anion]₂Metal₂ is calculated.

In contrast to this, a combination of ions from ionic liquids together with charged metal or alkali metal ions, like Cu⁺/Cu²⁺, Li⁺, Na⁺, and K⁺, which are typically present in case of an electrochemical dissolution or pair formation between these charged atoms and the ionic liquid prior to a subsequent treatment (cf. refs. [148, 164]), would be accompanied by further effects. Their related cluster calculations might require inter alia the use of an unequal number of anions and cations or an overall charge. Both facts would lead to more complex interactions on the one hand in between the ions of the ionic liquid itself and on the other with the metal or alkali metal ions and the ionic liquid. These calculations could be accompanied by an unpredictable charge transfer between the metal or alkali metal ions and the ionic liquid, which might result in

uncontrollable binding energy shifts for the subsequent reconstruction. In this context, a more extensive rescaling procedure has to be introduced due to these multifaceted interactions. The dissolution and plasma processes are additionally associated with a change in charge of the ionic liquid [148], which might feature a further complexity for the determination of the binding energies comparable to the effects during degradation of a neat ionic liquid (cf. Chapter 5). In consequence, a consideration of the evaporated metal and alkali metal atoms will be adequate to analyze their interaction with the ionic liquid on the simplest and all at once still sufficiently complex level. Subsequently, these results may also be partially transferred to their respectively charged species.

9.1 Evaporation of copper onto [EMIm]Tf₂N

Two copper atoms and two ion pairs from [EMIm]Tf₂N are assembled for the calculated charge- and spin-balanced cluster displayed in Figure 51. Herein, the interaction between copper and the ionic liquid is established by means of the central carbon atom C¹ within the [EMIm] cation (for respective nomenclature see Figure 9). The two copper atoms have formed a diatomic structure. In the performed NBO charge analysis (see Chapter 3.2 for the methodical basis), a partial charge in the order of +0.2 e is ascertained to each copper atom. Consequently, a second relative shift for the potentially charged additional species $\Delta\Delta E_{AddSpecies}$ has to be incorporated into the binding energies of the reconstructed spectra. From the rescaling procedure the respective values are obtained in comparison to the neat ionic liquid: the scaling factor of $f = 1.02830$ is found as similar as for the pure ionic liquid ($f = 1.02838$). Whereas, the absolute shift for [Tf₂N]⁻ of $\Delta E = -2.69 eV$ as well as the relative between [EMIm]⁺ and [Tf₂N]⁻ of $\Delta\Delta E_{Cation-Anion} = -1.77 eV$ are found both significantly higher than for the neat ionic liquid ($\Delta E = -1.36 eV$, $\Delta\Delta E_{Cation-Anion} = -1.10 eV$). In contrast to this, a lower shift might be expected due to the transfer of negative charge to both ions of the ionic liquid. It might be concluded that this transferred partial charge is not equally distributed to the atoms within the cation and anion. This could provoke changes in the respective chemical environments for the ions (cf. ref. [165]) or additional effects on the sample charging for the experimental spectra compared to the neat ionic liquid (cf. ref. [35]). The reconstructed copper contribution is additionally shifted relative to those of the [Tf₂N] anion of the ionic liquid by $\Delta\Delta E_{AddSpecies} = -1.00 eV$, which might result from the slight overestimation of the partial charge by circa +0.2 e

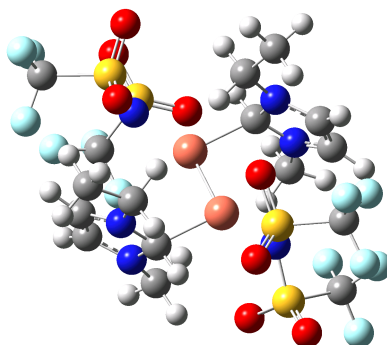


Figure 51: Structure of the calculated charge- and spin-balanced cluster consisting of ionic liquid and copper in the stoichiometric composition of $[\text{EMIm}]_2[\text{Tf}_2\text{N}]_2\text{Cu}_2$.

of the potentially neutral copper (cf. a charge-related shift of around 6 eV/e in ref. [126]).

The reconstructed XPS valence band spectra from the calculated cluster are displayed in Figure 52 with a deconvolution into the ions and the copper (top) and the contained elements (bottom). These have exhibited a similar valence band structure for the $[\text{EMIm}]\text{Tf}_2\text{N}$ contributions compared to the neat ionic liquid (cf. Figure 36). An additional peak, which is obviously not caused by $[\text{EMIm}]\text{Tf}_2\text{N}$, is recognized in the experimental spectrum at a binding energy of approximately 3.5 eV. This peak has originated from copper on the basis of the reconstructed spectrum, which can be assigned to the Cu3d state by means of an experimental peak at a similar binding energy position for the evaporation of copper onto organic systems [166]. A rough estimation of the ratio between copper atoms and ion pairs of $[\text{EMIm}]\text{Tf}_2\text{N}$ in the order of approximately 1:7 is determined with the aid of the peak heights in the valence band. In this context, it has to be noticed that this ratio is estimated in the near surface area with a typical information depth, which has comprised approximately the first 8 nm below the surface and enrichment or depletion effects might additionally occur [163].

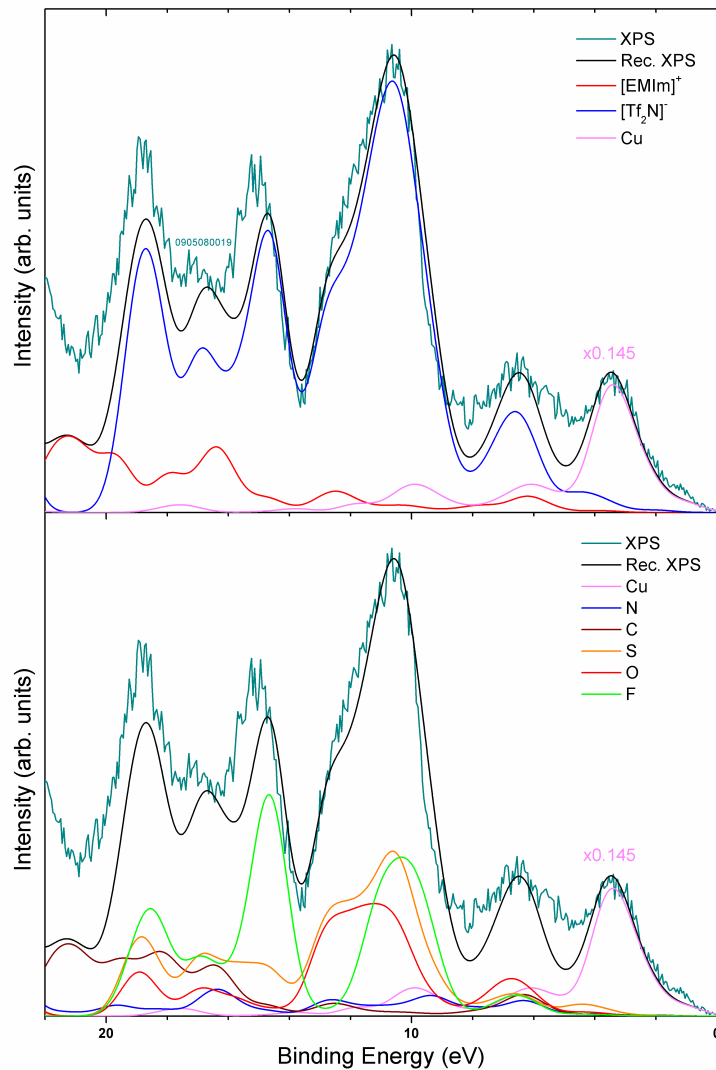


Figure 52: Reconstructed XPS valence band spectra for copper evaporated onto [EMIm]Tf₂N with a deconvolution into the ions (top) and elements (bottom) from the calculated cluster displayed in Figure 51 in comparison to the experimental spectrum. The spectra are normalized to the height of the peak at approximately 10.5 eV. All binding energies of the reconstructed spectra are rescaled by $f = 1.02830$, $\Delta E = -2.69$ eV, and $\Delta\Delta E_{Cation-Anion} = -1.77$ eV, while for the copper contribution a second relative shift of $\Delta\Delta E_{AddSpecies} = -1.00$ eV is applied. The experimental spectrum is obtained from personal communication with Dr. A. Ulbrich.

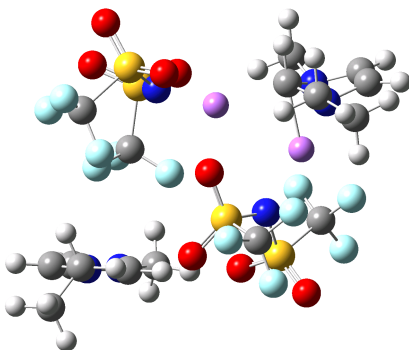


Figure 53: Structure of the calculated charge- and spin-balanced cluster consisting of ionic liquid and lithium in the stoichiometric composition of $[\text{EMIm}]_2[\text{Tf}_2\text{N}]_2\text{Li}_2$.

9.2 Evaporation of lithium onto $[\text{EMIm}]\text{Tf}_2\text{N}$

A calculated charge- and spin-balanced cluster composed of two lithium atoms and two ion pairs of $[\text{EMIm}]\text{Tf}_2\text{N}$ is illustrated in Figure 53. Different interactions between lithium and the ionic liquid are found within this cluster: the first lithium atom is surrounded by oxygen and nitrogen from the $[\text{Tf}_2\text{N}]^-$ anion, while the other has interacted with nitrogen of the second $[\text{Tf}_2\text{N}]^-$ anion and parallel an interaction of minor importance with the C^1 within the $[\text{EMIm}]^+$ cation is established. Herein, the lithium atoms have moved apart from each other. A preferred interaction in between $[\text{Tf}_2\text{N}]^-$ (especially the oxygens) and lithium was suggested in refs. [160, 165, 167]. Whereas, the interaction with the central carbon atom of the cation is supported by ref. [164]. The respective partial charges of both lithium atoms are estimated in the order of $+0.6 e$ based on the NBO charge analysis. This high partial charge might be expected due to the reason that lithium has featured a very low ionization potential.

The reconstructed UPS (He II) and XPS valence band spectra (top/bottom) as well as the respective DOS (middle) of the $[\text{EMIm}]_2[\text{Tf}_2\text{N}]_2\text{Li}_2$ cluster are displayed in Figure 54. In the reconstructed UPS (He II) spectrum, the major elements of $[\text{EMIm}]\text{Tf}_2\text{N}$ are identified in similar way as found in the reconstruction of the neat ionic liquid (cf. Figure 37). No significant contributions are recognized for lithium close to the valence band edge in UPS (He II) due to the comparably low photoionization cross section of the $\text{Li}2s$ orbital (cf. Table 1) as well as the high partial charge preferably found for this orbital. On

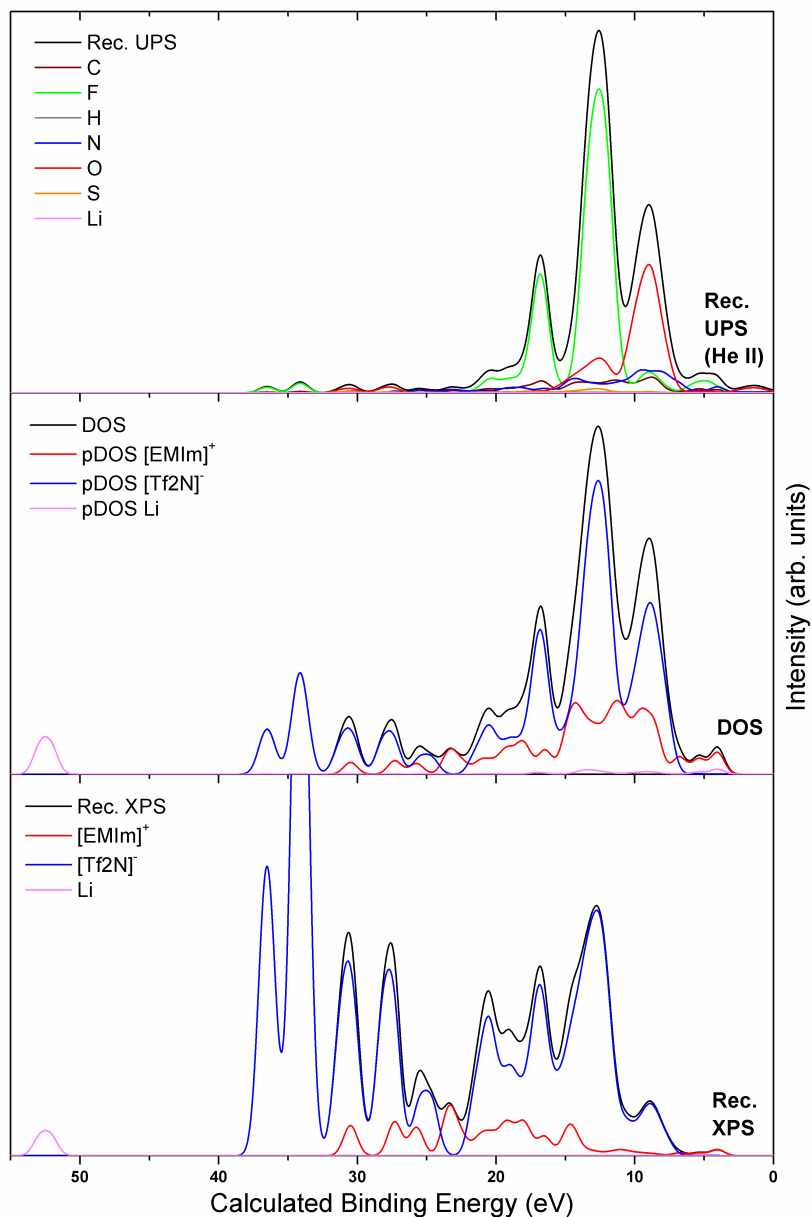


Figure 54: Reconstructed UPS (He II) spectra (top) and XPS valence band spectra (bottom) for lithium evaporated onto [EMIm]Tf₂N in comparison to the respective pDOS (middle) with a deconvolution into the ions or elements. All contributions are achieved from the [EMIm]₂[Tf₂N]₂Li₂ cluster displayed in Figure 53. A rescaling procedure is not applied due to the lack of experimental spectra.

the contrary, for XPS and DOS a clear lithium contribution is noticed at a calculated binding energy of about 52.5 eV. This contribution is addressed to the Li1s state, which is quoted with a binding energy of 59.8 eV by ref. [119]. The contributions related to the Li2s states are identified by the respective partial density of states (pDOS) in a broad range from circa 4 to 17 eV with a minor concentration. In addition, this is caused by the interaction between lithium and the ionic liquid, where a partial transfer of charge out of the Li2s state into the unoccupied orbitals of the ionic liquid has occurred. In the reconstructed XPS valence band spectrum, these contributions have completely disappeared relative to the signal height of all other contained elements or ions due to the well-known small XPS cross sections for elements with a low atomic number (cf. ref. [119]). Nevertheless, the presence of lithium incorporated in [Li-Tf₂N] salts in the near surface region is concluded by T. Kurisaki et al. [160], since the [Tf₂N] anion is preferably found at the surface in the neat ionic liquid, which is further in agreement to the results obtained in Chapter 6.2.2.

9.3 Evaporation of potassium onto [EMIm]Tf₂N

The cluster of [EMIm]₂[Tf₂N]₂K₂ is displayed in Figure 55, which has contained two potassium atoms surrounded by two ion pairs from [EMIm]Tf₂N. Herein, interactions between potassium atoms and nitrogens of the [Tf₂N] anions are established, while the distance in between these are found smaller than in between both potassium atoms. The NBO analysis has revealed a partial charge in the order of +0.1 e for each potassium atom. In consequence, the relative shift $\Delta\Delta E_{AddSpecies}$ for the potassium contribution is expected to be small in comparison to neutral potassium atoms, which are evaporated onto the ionic liquid.

The reconstructed UPS (He II) and XPS valence band spectra (top/bottom) as well as the related DOS (middle) of the [EMIm]₂[Tf₂N]₂K₂ cluster are illustrated in Figure 56 with deconvolution into the ions (left) and the contained elements (right). In general, the reconstructed XPS spectra are received as similar compared to the neat [EMIm]Tf₂N ionic liquid. Their respective binding energies are found at higher values in the range of +1 to +1.5 eV compared to the neat ionic liquid. In contrast, the relative binding energy position of the contributions of the two additional atoms is unknown, but will be corrected by the introduction of an absolute shift ΔE and an relative shift $\Delta\Delta E_{AddSpecies}$

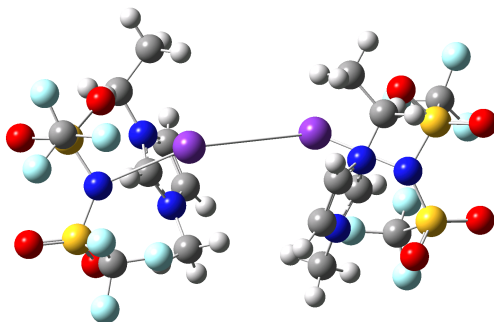


Figure 55: Structure of the calculated charge- and spin-balanced cluster consisting of ionic liquid and potassium in the stoichiometric composition of $[\text{EMIm}]_2[\text{Tf}_2\text{N}]_2\text{K}_2$.

in comparison to the experiment. A significant contribution of potassium is observed at circa 20 eV and has distinctly exceeded the spectral features related to the ionic liquid. This peak is addressed to the K3p state, which is accompanied by a high photoionization cross section (cf. Table 1). A small contribution from potassium is additionally recognized at around 2.5 eV. Decent hints that this contribution has most probably originated from the interaction of potassium with the nitrogen from the anion are provided from the elementwise analysis of the pDOS in Figure 56 and with respect to the calculated cluster displayed in Figure 55. But a further 'shoveling around' of the contributions into other potassium states cannot be excluded without a final comparison to the experimental spectra. In contrast to XPS and DOS, this contribution has nearly disappeared in the reconstructed UPS (He II) spectrum, since the K3p orbital has featured a small photoionization cross section for UPS compared to the elements of the ionic liquid (cf. Table 1).

9.4 Chapter summary

Preferred interactions between the additional atoms and a particular ion of the ionic liquid (cf. refs. [160, 164, 165, 167]) are well reproduced by means of small clusters calculated for the subsequent spectra reconstruction. The reconstructed XPS and UPS (He II) valence band spectra are superimposed by the contributions of the neat ionic liquid and added (alkali) metal atoms with exception of small binding energy ranges, where finger prints of the respective interactions

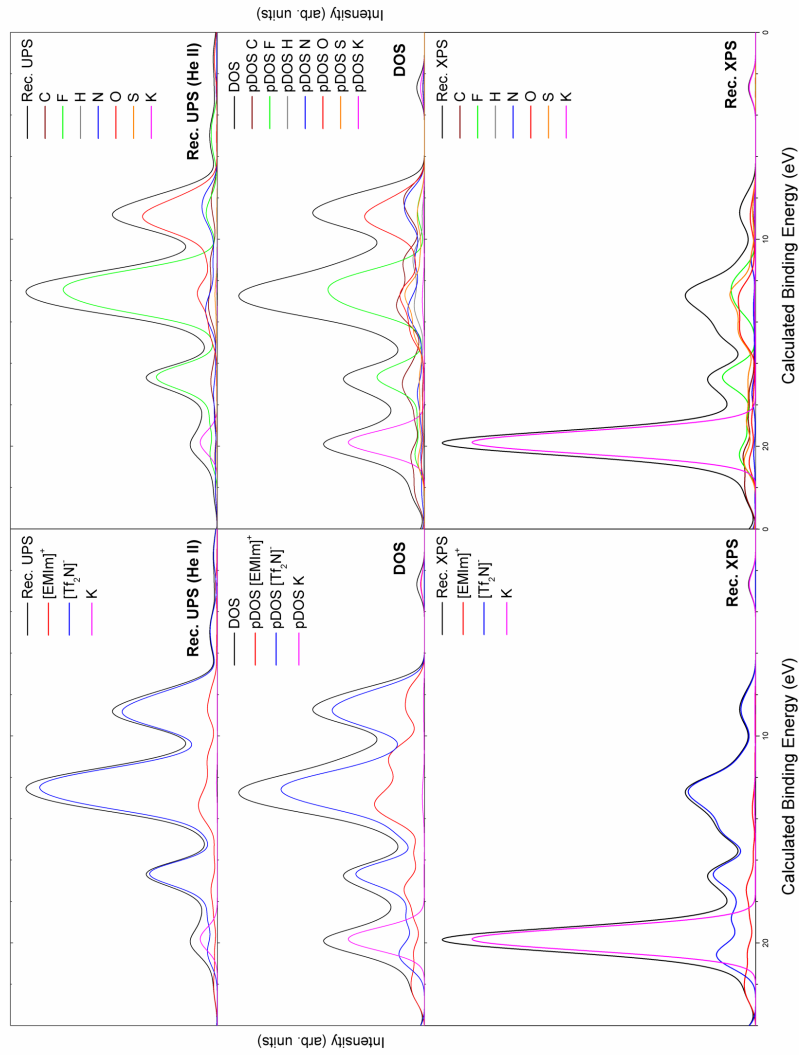


Figure 56: Reconstructed UPS (He II) spectrum (top) and XPS valence band spectrum (bottom) for potassium evaporated onto [EMIm]Te₂N in comparison to the respective pDOS (middle) with a deconvolution into the contributions of the ions (left) and the elements (right). All contributions are achieved from the [EMIm]₂[Te₂N]₂K₂ cluster displayed in Figure 55. A rescaling procedure is not applied due to the lack of experimental spectra.

are present. An introduction of a further shift $\Delta\Delta E_{AddSpecies}$ for the contributions of the additional species relative to those of the ionic liquid in the rescaling procedure has demonstrated its applicability for the reconstructed spectra.

10 Valence band spectra of copper-containing ionic liquids

The reconstructed valence band spectra of copper-containing ionic liquid of $[\text{Cu}(\text{Im}^6)_2]\text{CuCl}_2$ are investigated with respect to the electronic interactions between copper atoms in both cation and anion, which have featured different chemical environments. For the $[\text{Cu}(\text{Im}^6)_4]^+$ the number of imidazolium groups attached to the copper atom in the cation is enhanced compared to the $[\text{Cu}(\text{Im}^6)_2]^+$. Thus, the contributions of the respective ions and elements as well as their binding energy positions in the valence band are of particular interest for those copper-containing ionic liquids.

10.1 Reconstructed valence band spectra

10.1.1 XPS valence band spectra

The reconstructed XPS valence band spectrum of $[\text{Cu}(\text{Im}^6)_2]\text{CuCl}_2$ is illustrated in Figure 57 with a deconvolution into the respective ions (top) and contained elements (bottom). Herein, a dominating contribution by the $[\text{CuCl}_2]$ anion is recognized. A clear separation of the anion contribution into peaks at circa 16 eV (primary Cl3s state) and below 4 eV (primary Cl3p state) is noticed in Figure 57 (bottom). These two peaks have varied in height due to the effect of 'shoveling around' of contributions between these two orbitals in the calculation, while a similar behavior was already observed for the contributions of carbon and nitrogen in $[\text{XMIIm}]\text{Tf}_2\text{N}$ (cf. Chapter 6.2.1). Moreover, this effect is dependent on the applied basis set and functional (cf. Chapter A.1 in the Appendix). Additional contributions are calculated below the experimental valence band edge, which are caused either by a charge transfer from cation to anion or a potential 'shoveling around' of contributions from occupied states into regularly unoccupied ones. In the reconstructed spectra of the anion, the contributions from chlorine and copper are detected with similar progression. A significant interaction between these two elements is concluded from the fact of a preferred ionic bonding, while also the cations' copper atom might partially be included. Herein, the copper atom of the anion is present within the peak at around 4 eV, while the one from the cation is primarily present in the peak at circa 7 eV. Nevertheless, a small interaction in between the two copper atoms in cation and anion is observed by occasional parallel progression in the reconstructed XPS

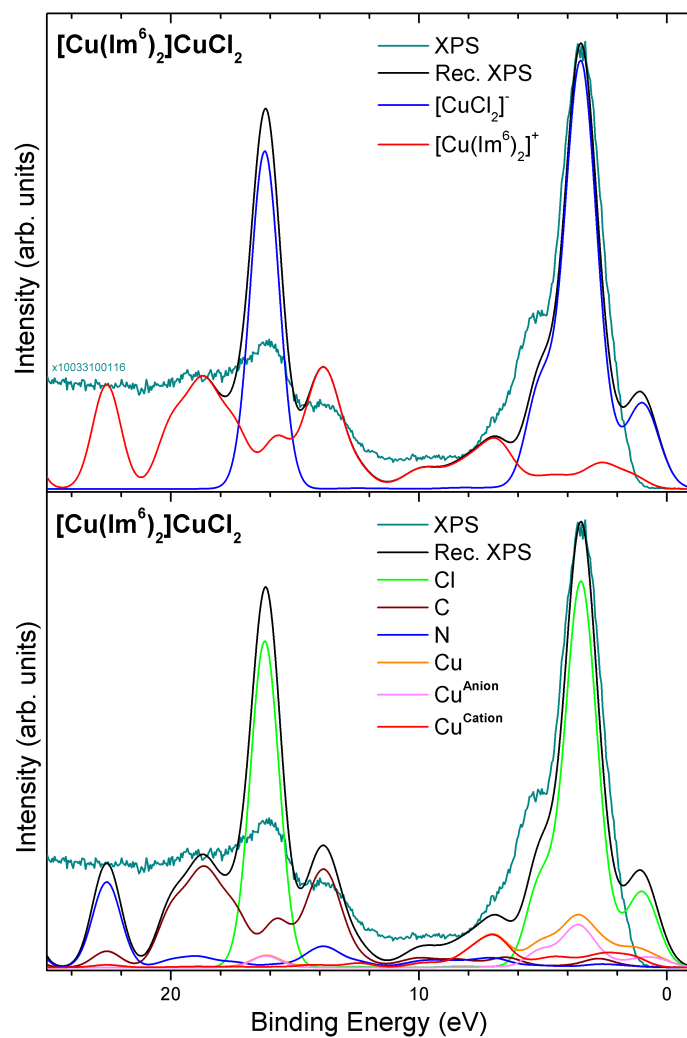


Figure 57: Reconstructed XPS valence band spectra of $[\text{Cu}(\text{Im}^6)_2]\text{CuCl}_2$ with a deconvolution into ions (top) and elements (bottom). The spectra are normalized to the height of the peak at about 4 eV. All binding energies of reconstructed spectra are modified by $f = 1.03045$, $\Delta E = -3.02 \text{ eV}$, and $\Delta\Delta E_{\text{Cation}-\text{Anion}} = -1.05 \text{ eV}$. The experimental spectrum is obtained from personal communication with Dr. M. Himmerlich.

spectrum between circa 1 and 6 eV, which has led to a partial delocalization of the copper-related states over both atoms.

For the reconstruction of the XPS valence band spectra of the $[\text{Cu}(\text{Im}^6)_2]$ cation, all peaks are accompanied by distinctly lower heights than for the $[\text{CuCl}_2]$ anion, which are caused by the smaller cross sections of carbon, nitrogen, and hydrogen. The first cation-related contribution with distinct intensity is observed near the valence band edge and a second one is found at about 7 eV. Both are mainly shaped by the cations' copper atom. Significant contributions of the cations' nitrogen and carbon atoms are detected above 12 eV due to the perceptible cross section for the N2s and C2s states. However, these states are found in a broad range with remarkable intensity. It has to be mentioned that the experimental spectrum has not featured distinct peak structures above 18 eV, since it is already affected by inelastically scattered electrons.

The reconstructed XPS valence band spectra of the ionic liquid $[\text{Cu}(\text{Im}^6)_4]\text{-PF}_6$ are depicted in Figure 58 together with a deconvolution into the respective ions (top) and contained elements (bottom). A first peak is recognized at approximately 4 eV in the experimental spectrum, while the experimental valence band edge is detected around 2 eV. However, the related reconstruction has revealed that this peak is exclusively caused by the copper atom, but this peak is only reproduced with a slight amount of the experimental intensity. A second broad peak is shaped nearly equally by both ions in a binding energy range from approximately 7 to 11 eV. This peak is dominated by both fluorine from the anion and copper from the cation. Two peaks at circa 13 and 16.5 eV have originated from the anions' phosphorus and fluorine contributions in equal shares, while the second peak is shaped by carbon with similar intensity than found for the $[\text{PF}_6]$ anion. The carbon contributions have dominated the spectra above 14 eV due to the significantly higher photoionization cross section for the C2s compared to the C2p orbitals. A distinct difference between reconstructed and experimental spectra has remained, which is especially found for the peaks at around 4 and 13 eV. Nevertheless, from the applied spectra reconstruction an assignment of the contributions to the respective ions and elements is enabled for these ionic liquids.

10.1.2 UPS (He II) spectra

The reconstructed UPS (He II) spectra of the valence band of $[\text{Cu}(\text{Im}^6)_2]\text{CuCl}_2$ are displayed in Figure 59 with a deconvolution into the contained ions (top)

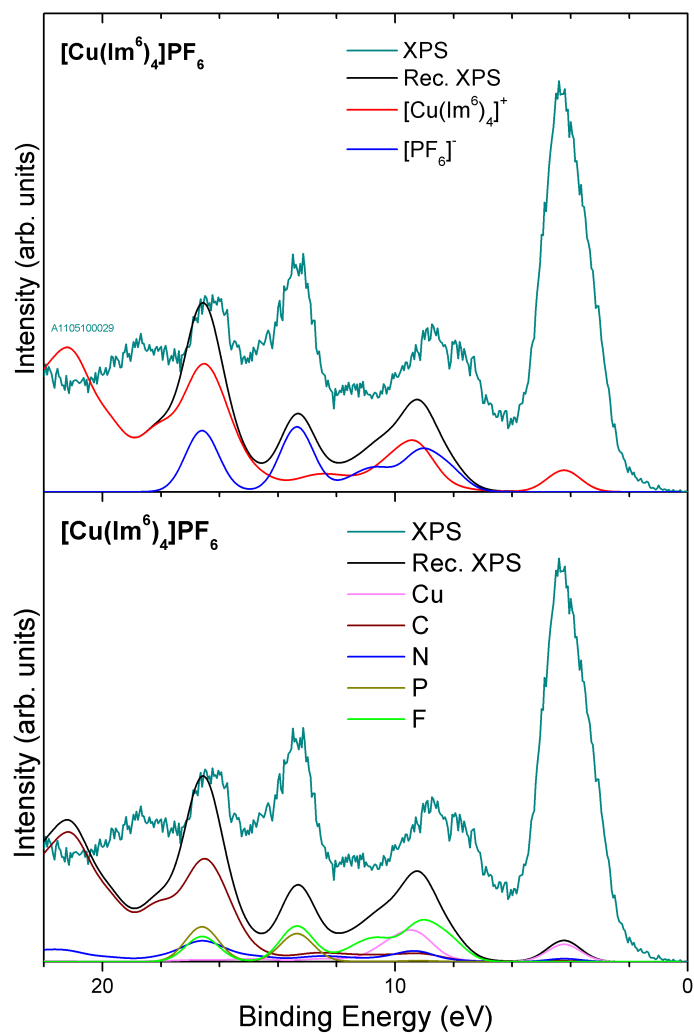


Figure 58: Reconstructed XPS valence band spectra of $[\text{Cu}(\text{Im}^6)_4]\text{PF}_6$ with a deconvolution into the ions (top) and elements (bottom). The spectra are normalized to the height of the peak at approximately 16.5 eV. All binding energies of reconstructed spectra are modified by $f = 1.02427$, $\Delta E = +0.25 \text{ eV}$, and $\Delta\Delta E_{\text{Cation}-\text{Anion}} = -0.60 \text{ eV}$. The experimental spectrum is obtained from personal communication with Dr. A. Ulbrich.

and elements (bottom). Contributions of the anion are recognized at binding energies of around 4 and 16.5 eV, which are caused by the Cl3p and Cl3s states, respectively. The intensity of these two states is regarded as minor compared to the cation contributions at the respective binding energies. Thus, cation-related states are found to dominate in the whole binding energy range from the valence band edge up to 18 eV. Herein, a broad structure with two peaks at circa 6.5 eV and 9.5 eV as well as another peak at about 13.5 eV are addressed to $[\text{Cu}(\text{Im}^6)_2]^+$. These three peaks have originated from primary carbon and additionally from nitrogen, which is typically present with an intensity in the order of 60 to 75 % of those of the carbon. Minor hydrogen contributions are observed in the binding energy range from 5 to 15 eV. No significant contribution is detected for copper in both cation and anion in the reconstructed UPS (He II) spectra due to the very low photoionization cross section for the Cu4s orbital. However, the Cu3d orbital with its much higher photoionization cross section has not contributed with a perceptible amount.

The reconstructed UPS (He II) spectra of $[\text{Cu}(\text{Im}^6)_4]\text{PF}_6$ are illustrated in Figure 60 with a decomposition into the contributions of the ions (top) and the elements (bottom). A first peak at around 4 eV and a second one at about 6.5 eV are assigned to the $[\text{Cu}(\text{Im}^6)_4]^+$, where the latter is only present as a shoulder in the experimental spectra. Both peaks are primarily shaped by the carbon within the cation, while the peak at around 4 eV has contained a significant amount of nitrogen, too. Nevertheless, both peaks are reconstructed with much lower intensity than present in the experimental spectrum. This might lead to the assumption that the experimental spectra of the ionic liquid $[\text{Cu}(\text{Im}^6)_4]\text{PF}_6$ could be affected by additional contributions or unexpected effects. At higher binding energies, two main peaks close to 8 eV and at about 9 eV are recognized in the experiment, which are accompanied by additional shoulder peaks. These peaks from 7 eV up to 13.5 eV are predominantly provoked by the $[\text{PF}_6]$ anion and especially the fluorine atoms therein, which are accompanied by high UPS (He II) photoionization cross section for the F2p orbital. However, the two major peaks are not clearly separated in the reconstruction compared to the experiment. A broad double peak structure caused by carbon and nitrogen of the cation is observed in addition to the strong anion contribution in the binding energy range from circa 7 to 13 eV. At a binding energy of approximately 16.5 eV, a further peak is detected, which has predominantly originated from the cation with its carbon and nitrogen atoms rather than from the an-

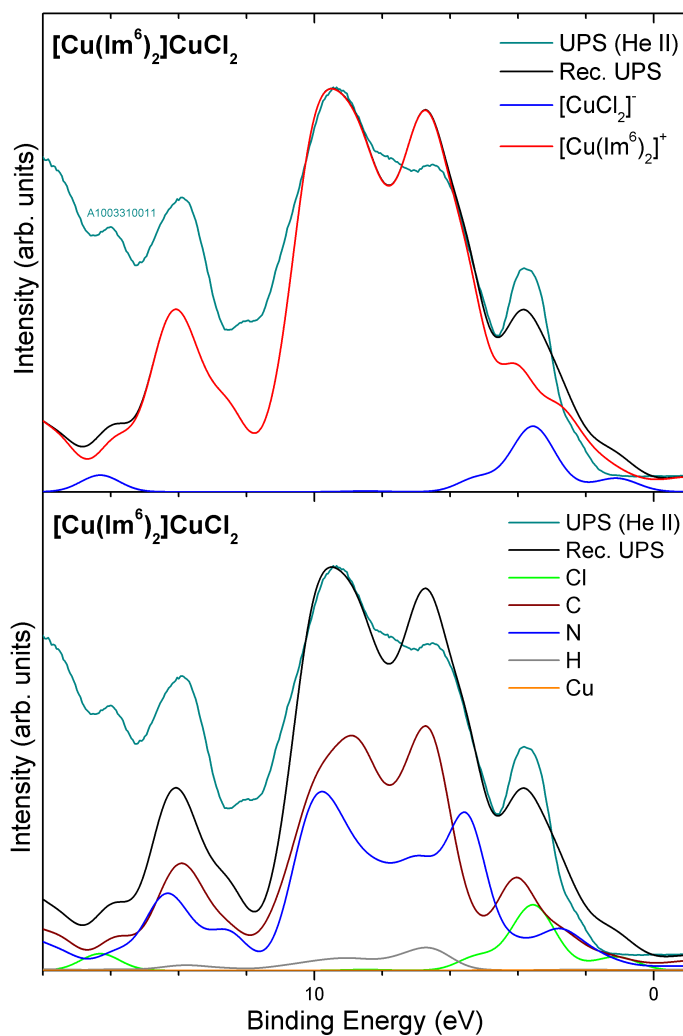


Figure 59: Reconstructed UPS (He II) spectra of $[\text{Cu}(\text{Im}^6)_2]\text{CuCl}_2$ with a deconvolution into the ions (top) and elements (bottom). The spectra are normalized to the height of the peak at approximately 9.5 eV. All binding energies of the reconstructed spectra are modified by $f = 1.03045$, $\Delta E = -2.92 \text{ eV}$, and $\Delta\Delta E_{\text{Cation}-\text{Anion}} = -1.05 \text{ eV}$. The experimental spectrum is obtained from personal communication with Dr. M. Himmerlich.

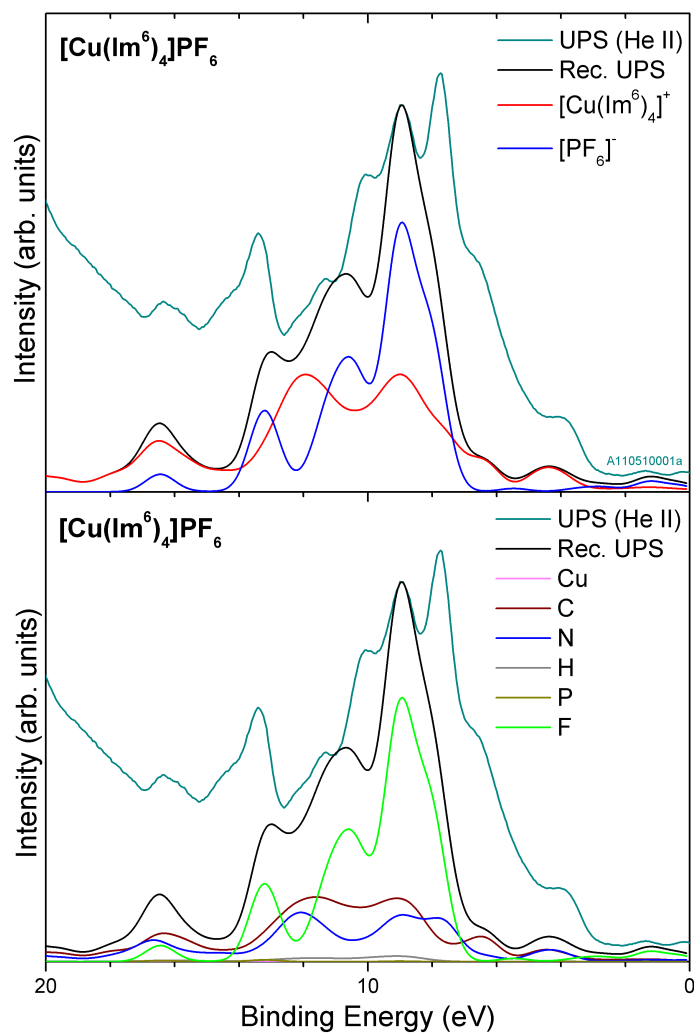


Figure 60: Reconstructed UPS (He II) spectra of $[\text{Cu}(\text{Im}^6)_4]\text{PF}_6$ with a deconvolution into the ions (top) and elements (bottom). The spectra are normalized to the height of the peak at approximately 9 eV. All binding energies of the reconstructed spectra are modified by $f = 1.02427$, $\Delta E = +0.10$ eV, and $\Delta\Delta E_{\text{Cation}-\text{Anion}} = -0.60$ eV. The experimental spectrum is obtained from personal communication with Dr. A. Ulbrich.

ion states. Potential reasons for all of the mentioned differences found between reconstructed and experimental XPS and UPS (He II) valence band spectra of the copper-containing ionic liquids will be further investigated and discussed in Chapter 10.2 and Chapter 10.3, respectively.

10.2 Effect of photoionization cross sections and their calculation methods on the valence band spectra

The reconstructed XPS valence band spectra of $[\text{Cu}(\text{Im}^6)_2]\text{CuCl}_2$ are displayed in Figure 61 for which the photoionization cross sections from two different sources, i.e. I. M. Band et al. [120] as well as J. J. Yeh and I. Lindau [119], are employed. Potential effects of the different photoionization cross sections for the reconstructed XPS valence band spectra are investigated here. Whereby, especially the contributions below or near the valence band edge will be regarded. Partially different methodical approaches, which were quoted in the two references [119, 120], are illustrated for the photoionization process and related cross section calculation: I. M. Band et al. [120] have considered first order perturbation theory using a one photon and one electron approach together with electron wave functions from relativistic self-consistent Dirac-Slater potentials of the uncharged atom. All multipoles are taken into account for these calculations. Relativistic effects are reasoned with their particular importance for low photon energies and have additionally accounted for differences in the asymmetry parameters compared to a non-relativistic treatment (cf. ref. [120]). This approach is further adapted for circular and unpolarized photons and certain solid state effects. Whereas, in the work of J. J. Yeh and I. Lindau [119] a simplified method is utilized regarding Hartree-Fock-Slater states. The photoionization cross sections are obtained from wave functions calculated according to F. Herman and S. Skillman [168], which are used together with a dipole length approximation. Only dipoles instead of multipoles, which might possess a strong effect on low binding energy orbitals of elements of large atomic number, together with a non-relativistic treatment are considered in this approach. In particular, this method is specified for linearly polarized photons.

In Figure 61, the comparison of reconstructed spectra using the abovementioned different methods for the calculation of photoionization cross sections has resulted in no significant differences. This fact has most probably arisen from the minor relative differences between the relativistic and non-relativistic

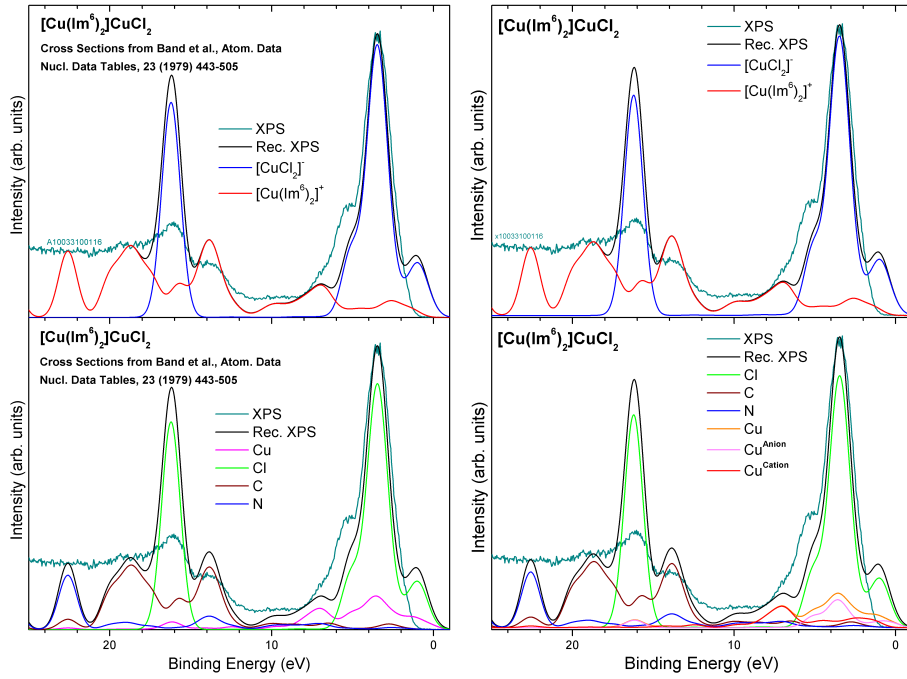


Figure 61: Reconstructed XPS valence band spectra of $[\text{Cu}(\text{Im}^6)_2]\text{CuCl}_2$ with a deconvolution into ions (top) and elements (bottom). For these reconstructions different photoionization cross sections from I. M. Band et al. [120] (left) and from J. J. Yeh and I. Lindau [119] (right, already displayed in Figure 57) are utilized. The spectra are normalized to the height of the peak at around 4 eV for both methods. All binding energies of the reconstructed spectra are modified by $f = 1.03045$, $\Delta E = -3.02 \text{ eV}$, and $\Delta\Delta E_{\text{Cation}-\text{Anion}} = -1.05 \text{ eV}$. The experimental spectrum is obtained from personal communication with Dr. M. Himmerlich.

treatments as well as considerations on the one hand of multipoles or dipoles and on the other circular-/non-polarized or linearly polarized radiation. No improvements regarding the contributions present above the experimental valence band edge are obtained in the reconstruction. In addition, no advances for the height ratios of the Cl3s and Cl3p states are achieved by the utilization of photoionization cross sections obtained by the two partially different calculation approaches. Stronger effects might be found for other elements with large atomic numbers, which are significantly higher than copper with $Z = 29$. Thus, the detected differences have to be attributed to other reasons. The quantum-chemical calculations could exemplarily be responsible for some of the deviations, since they have shaped the basis of the subsequent reconstruction. The contained elements with an uncertain charge state, such as copper, and the elements for which the quantum-chemical description is commonly known as inappropriate or highly complex, such as chlorine, might force the calculation close to the limit for providing reliable results. Moreover, potential impurities can be regarded as another reason for the differences between experimental and reconstructed spectra, which will be analyzed in detail hereinafter.

10.3 Effect of sample impurities on the valence band spectra

In the experimental survey spectra displayed in Figure 62, impurities from silicon and oxygen are identified, which both are not attributed to the initial ingredients of $[\text{Cu}(\text{Im}^6)_4]\text{PF}_6$. The mentioned species were most probably introduced through the synthesis or purification process, where SiO_2 -containing materials were partially involved. The high solubility of oxidic materials in ionic liquids has resulted from the slightly ionic character of these oxides [161]. These SiO_2 -based impurities might contribute with additional spectral features in the valence band, which have been analyzed in Chapter 10.1. Thus, experimental spectra of pure SiO_2 or oxidized silicon recorded with radiation sources of the same or similar photon energy will be utilized to investigate the potential differences between reconstructed and measured valence band spectra of copper-containing ionic liquids.

The valence band spectra of oxidized Si(111) surfaces produced via temperature treatment under an appropriate oxygen partial pressure are studied by

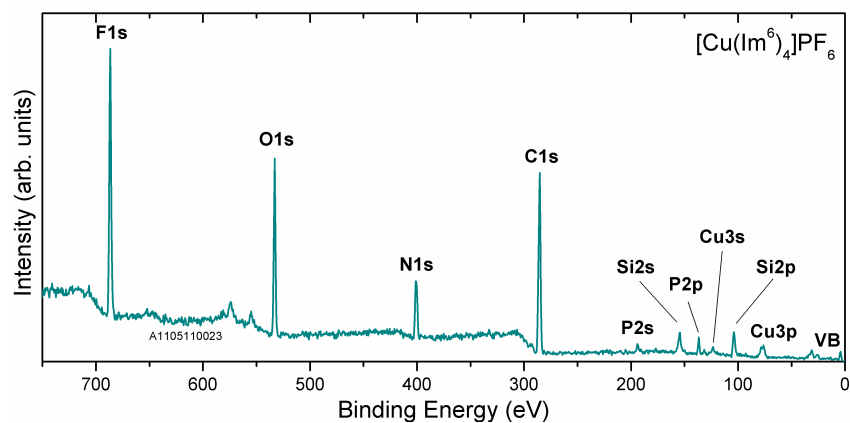


Figure 62: XPS survey spectra of $[\text{Cu}(\text{Im}^6)_4]\text{PF}_6$ with an assignment of the peaks to the respective atomic orbitals. The experimental spectrum is obtained from personal communication with Dr. A. Ulbrich.

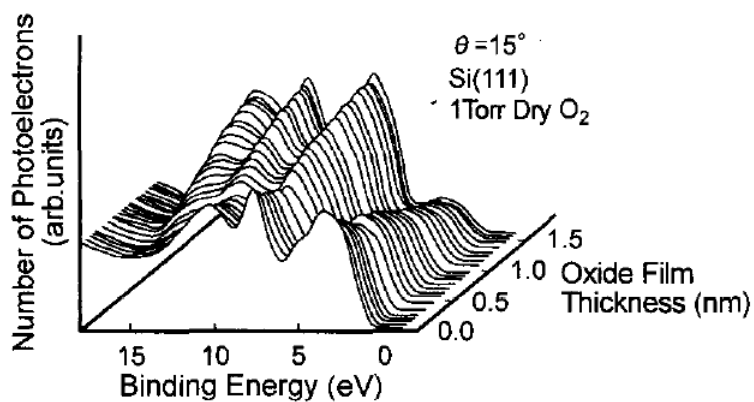


Figure 63: Effect of oxidation progression on the valence band spectra of Si(111) studied by XPS using Al K_α radiation. (With the courtesy of: Elsevier, H. No-hira and T. Hattori, Appl. Surf. Sci., 117/118 (1997) 119-122, page 120 [169])

XPS using Al K_{α} radiation in Figure 63. Herein, spectral features of SiO_2 at binding energies of approximately 4, 8, 10.5, and 12.5 eV are identified, while the latter is only found at enhanced oxidation progression. An additional contribution found in the strong peak at around 4 eV in the experimental XPS valence band spectra of $[\text{Cu}(\text{Im}^6)_4]\text{PF}_6$ can be attributed to the SiO_2 impurities. The SiO_2 peak at 8 eV may be associated with the shoulder at around 7.5 eV in the experimental spectra, which is not found in the reconstructed spectra for $[\text{Cu}(\text{Im}^6)_4]\text{PF}_6$. An intensity plateau between 10 and 12 eV in the experiment can be related to the SiO_2 peak at 10.5 eV, whereas from the reconstruction of the pure ionic liquid a reduced intensity is expected in this range. A modification of the experimental spectra is obviously caused by the SiO_2 peak at 13 eV, where only half of the experimentally detected intensity is achieved from the reconstruction. In this context, it is regarded that the background by inelastically scattered electrons might begin in this binding energy range. At this binding energy a peak with slightly smaller height compared to those at 8 and 10.5 eV is ascertained in the reference study [169].

In a study by M. L. O'Brien et al. [170], 6H- and 4H-SiC treated by an oxygen plasma as well as SiO_2 layers deposited on both substrates by PECVD are investigated using UPS (He I) radiation displayed in Figure 64. In this context, it has to be noticed that this kind of comparison is performed between UPS (He II) and UPS (He I) spectra, which might be affected by slightly different photoionization cross sections (cf. ref. [119]). Both radiation sources have offered a comparable photon energy and, thus, the spectra have featured similar photoionization cross sections, which are sufficient for the performed qualitative comparison. Two main peaks are found for oxidized 6H- or 4H-SiC at approximately 6.5 and 11 eV, while the valence band edge is identified at around 5 eV. Those peaks are recognized at around 7.5 and 11.5 eV as well as 8 and 12 eV for the PECVD-deposited SiO_2 layers on 6H- and 4H-SiC, respectively. The first peak is characterized by a comparably broad shape and, herein, the valence band edge is observed at higher coverage in the binding energy range of 4 to 5 eV. In the experimental spectra, this fact has become evident by the additional spectral features ranging from approximately 5 to 8 eV, which are not present in the reconstruction of the neat copper-containing ionic liquids. The second peak at around 11-12 eV is assigned with a significantly smaller intensity than the first one. Thus, the XPS and UPS (He II) valence band spectra of $[\text{Cu}(\text{Im}^6)_4]\text{PF}_6$ are significantly influenced by the SiO_2 impurities. Regarding these additional spectral features the differences between reconstructed and experimental spec-

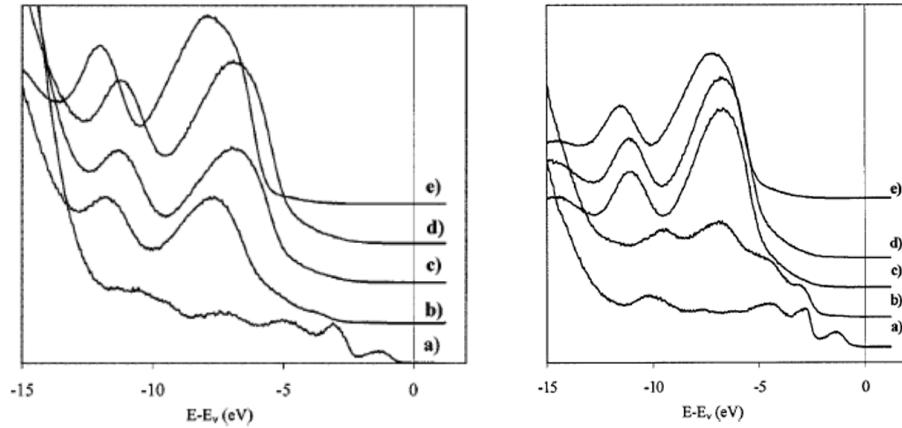


Figure 64: Effect of oxidation on the valence band spectra of 4H n-type SiC (left) and 6H n-type SiC (right) studied by UPS (He I). Herein, the spectra of the $\sqrt{3} \times \sqrt{3}$ reconstructed SiC (a), SiC exposed to oxygen (b), after a 30 s oxygen plasma treatment (c), after a 1 min oxygen plasma treatment (d), and a 1.5 nm PECVD-generated layer of SiO₂ (e) are displayed. (With the courtesy of: The American Vacuum Society, M. L. O'Brien et al., J. Vac. Sci. Technol. B, 18 (2000) 1776-1784, page 1781/1782 [170])

tra of the copper-containing ionic liquids have resulted by approximation of a superposition of their respective contributions.

10.4 Chapter summary

A partial overlap between the contributions of both copper atoms in cation and anion is determined for [Cu(Im⁶)₂]CuCl₂. However, noticeable differences in the valence band between reconstructed and experimental XPS and UPS (He II) spectra are observed due to various reasons: for [Cu(Im⁶)₂]CuCl₂ additional minor contributions of copper and chlorine are detected below the experimental valence band edge, which have demonstrated that these calculations of polyvalent and complex atoms are close to the limit for reliable reconstruction results. Photoionization cross sections calculated by partially different methodical approaches [119, 120] have not improved the reconstructed XPS valence band spectra. On the contrary, the experimental spectra of [Cu(Im⁶)₄]PF₆ are strongly influenced by the presence of SiO₂-based impurities. Nevertheless, the reconstructed spectra of the copper-containing ionic liquids are principally found in

agreement to the experimental ones with consideration of the additional spectral contributions of the model species for these impurities.

Part V

Summary and outlook

11 Summary

A suitable method for the reconstruction of X-ray and ultraviolet photoelectron spectra (XPS and UPS) by means of incorporation of photoionization cross sections and a Gelius intensity approach is introduced in the present thesis. This reconstruction method is a very powerful tool, since it is based on quantum-chemical calculations of fundamental units, like single ion pairs for neat ionic liquids [33, 36, 90] or small charge- and spin-balanced clusters for the consideration of ionic liquids with additional atoms. The preferred interaction sites between the ions as well as in between the additional atoms and the ionic liquid are calculated in agreement with other studies [75, 87, 95, 137, 150, 160, 164, 165, 167]. In particular, a quantitative reproduction of the valence band spectra with their intertwined contributions originating from different contained elements is exclusively provided by this technique [33, 36, 90]. Three rescaling parameters are utilized to adapt the calculated binding energies of neat ionic liquids to the experimental ones [36, 90], while the evidence for a further shift is obtained from the cluster calculations.

The structure of C1s and N1s core levels of several ionic liquids is analyzed with the aid of the developed reconstruction method in comparison to the experiment and has revealed the origin of the detected order of states. This order is defined by their chemical environment, interaction partners, and partial charges. Herein, a direct relationship between the binding energy and the distance between a particular carbon atom and the two nitrogens in the imidazolium-based cation is ascertained for [XMIm]Tf₂N (see Chapter 4.1). This dependence has further propagated through the whole alkyl chain [90] and has featured the dominating effect for the present order of binding energies rather than a general distinction into 'aromatic' and 'aliphatic' carbons [14, 15] or a conceivable influence of different carbon partial charges [30, 87]. In Chapter 4.2, a stronger interaction with additional contributions to the pure distance to the central nitrogen atom is observed by means of the C1s core levels of [XMPyrr]Tf₂N compared to the imidazolium-based analog, which is not in contradiction to another study [140]. The various partial charges of the nitrogen atoms in the

copper-containing ionic liquids with two and four attached imidazolium rings have led to different separations of their N1s states, which are recognized in both reconstructed and experimental spectra (cf. Chapter 4.3). The reconstructed core level spectra from fragments of the cation and anion of [EMIm]Tf₂N in Chapter 5 have confirmed the degradation mechanisms concluded from the experiment [125] and have provided decent hints towards co-occurring degradation mechanisms accompanied with comparable binding energy shifts.

For the valence band spectra using the examples of imidazolium- and pyrrolidinium-based ionic liquids, a quantitative deconvolution into the contributions of the respective ions and contained elements is enabled by this reconstruction method for the first time. The reconstructed valence band spectra are independent from the relative ion pair geometry for the ionic liquids of [XMIm]Tf₂N. In contrast, an influence of the geometry on the separation between Cl3s and Cl3p states is noticed for the imidazolium-based cation with the chlorine anion present in highly defined geometries. A determination of the preferred orientation of the ions at the surface is achieved with the aid of difference spectra (cf. Chapter 6.2.2) or relative changes in the experimental intensity (cf. Chapter 7.1), since the reconstruction has provided absolute heights on which the experimental spectra can be normalized: in both cases the cations' longer alkyl chain protrudes towards the vacuum, while the [Tf₂N] anion is also present at surface due to its considerable dimensions. On the contrary, the small [Cl] anion is buried beneath the cations' longer alkyl chain. All identified orientations and surface arrangements are in agreement with the results of other authors obtained by different experimental methods [14, 15, 31, 42, 63, 155] and molecular dynamics simulations [79, 80, 84]. In Chapter 8, clear differences are recognized in the valence band for the binding energy positions of the contributions related to the increased alkyl chains of imidazolium- and pyrrolidinium-based ionic liquids.

The reconstructed valence band spectra of the ionic liquids with additional atoms are primarily superimposed by their contributions, while the respective interactions are found in small binding energy ranges (cf. Chapter 9). A final analysis of the valence band spectra for copper-containing ionic liquids in Chapter 10 is complicated due to either the effect of 'shoveling around' or SiO₂-based impurities in the sample liquids. Nevertheless, the reconstruction method has enabled a principal assignment of the respective contributions within the experimental spectra under consideration of the additional spectral features caused by the contained impurities.

12 Outlook

The developed reconstruction method can be further applied for the analysis of XPS, UPS (He II), and UPS (He I) spectra of organic species, which has compromised a broad set of substances ranging from small molecules up to polymeric materials. For this purpose, optimized basic units, such as a monomer of the studied polymers, are utilized for the subsequent reconstruction. A sufficient agreement for a quantitative analysis of the valence band spectra is achieved by these basic units and has revealed the respective chemical environment with characteristic bonds [171].

The Kohn-Sham states resulting from the DFT calculations do not essentially fulfill Koopmans' theorem. But the employed hybrid functional B3-LYP has contained an exchange term, which has partially satisfied this theorem. Thus, the calculated binding energies can be modified by means of the employed rescaling procedure for neat ionic liquids using three parameters (f , $\Delta E_{XPS/UPS}$, and $\Delta\Delta E_{Cation-Anion}$). An improvement can be achieved for the calculated binding energies by use of Koopmans-compliant functionals, which have provided suitable results for the binding energies of small organic molecules [127]. Finally, only a single absolute shift $\Delta E_{XPS/UPS}$ has to be applied as a rescaling parameter to compensate the remaining major deviation caused by potential surface charging in the experiment [35].

Appendix

Additional information on the reconstructed spectra

(A.1) Effect of applied basis set and functional on the separation of Cl3s and Cl3p states in [OMIm]Cl in the reconstructed XPS valence band spectrum

By comparison with the experimental spectra, the effect of an inappropriate separation of Cl3s and Cl3p states was already detected in the reconstructed XPS spectrum (cf. Figure 41), where the calculation was executed by use of the basis set 6-31G** and the hybrid-functional B3-LYP. A potential improvement might be achieved by the choice of a different basis set or functional for the calculation of an identical ion pair, which is exemplarily performed for [OMIm]Cl here. The respective results of the Cl3s-Cl3p separation are listed in Table 14. For all reconstructed XPS valence band spectra, where both peaks can be identified, an overestimation in comparison to the experimentally derived separation in the order of 1-2.5 eV is obtained. The regularly applied functional B3-LYP has revealed a deviation of circa 2 eV from the experimental values, while other functionals have demonstrated more precise results for the Cl3s-Cl3p separation (cf. ref. [33]). In some spectra using basis sets different from 6-31G**, the Cl3p peak has completely disappeared, whereas the Cl3s state is enlarged in height or partially other molecular orbitals are occupied by these initial contributions. An analogous effect has occurred for the nitrogen and carbon contributions in the valence band from [XMIIm]Tf₂N (see Chapter 6.2.1) as well as the halogen and copper contribution of copper-containing ionic liquids (see Chapter 10). This effect has consequently denoted as 'shoveling around' of element-specific contributions. These misassignments are more evident if more flexible basis sets are used. In contrast to this, a manageable influence by the effect of 'shoveling around' is demonstrated for the basis set 6-31G** and functional B3-LYP employed in the present thesis. Thus, the choice of this basis set together with the particular hybrid-functional has seemed as reasonable for the calculation of ionic liquids.

$\Delta E_{Cl3s-Cl3p}$ (eV)		$\Delta E_{Cl3s-Cl3p}$ (eV)	
Functional	6-31G ^{**}	Basis set	B3-LYP
B3PW91	12.6	6-31G ^{**++}	12.6
BPV86	11.7	6-311G [*]	n.a.
MPW1PW91	12.8	6-311G ^{**}	n.a.
TPSS	11.9	cc-pVDZ	n.a.
WB97XD	13.1	SDD	n.a.
B3-LYP [#]	12.6	6-31G ^{**#}	12.6
Experiment	10.6	Experiment	10.6

Table 14: Energetic separation between Cl3s and Cl3p states (in eV) in the reconstructed XPS valence band spectra of [OMIm]Cl in their 'as calculated' state, which are exemplarily listed for different functionals (with the 6-31G^{**} basis set) and priorily more extensive basis sets (with the B3-LYP functional) in comparison to the experimental data. ([#]) The basis set 6-31G^{**} together with the functional B3-LYP are utilized for spectra reconstruction in the present thesis. A nomenclature of 'n.a.' has corresponded to an inability for the determination of the separation between Cl3s and Cl3p states in the valence band due to a missing Cl3p contribution.

(A.2) Carbon contributions in the UPS (He II) spectrum

The reconstructed UPS (He II) spectra of the ionic liquid [EMIm]Cl with a deconvolution of the carbon contributions, which are denoted as the dominating species and followed in height by the Cl3p peak, are depicted in Figure 65. Binding energy-specific contributions of carbon atoms in different chemical environments are recognized in the deconvoluted spectra. The peak at the onset of the spectrum has originated from a superposition with the Cl3p orbital and, thereby, has proven the favored interaction site of chlorine in the vicinity of the central carbon (C¹), which is also recognized in the spectra prior to application of the rescaling procedure. For the first neat cation peak at approximately 5 eV, primarily those carbon contributions within the imidazolium ring are assigned. Carbon is present as the main species in UPS (He II) within the significant double structure featuring peaks at around 8 and 10.5 eV. Herein, the alkyl carbons, i.e. C³ and C⁴, are recognized inside the lower binding energy peak, which was already inferred by the differences in the spectra for various alkyl chain lengths in the two sets of imidazolium-based ionic liquids of [XMIm]Tf₂N and [XMIm]Cl. Furthermore, this conclusion is indicated by the C⁴, which is found at lower binding energy compared to C³. The peak at higher binding energy of circa 10.5 eV is significantly shaped by those carbons directly attached

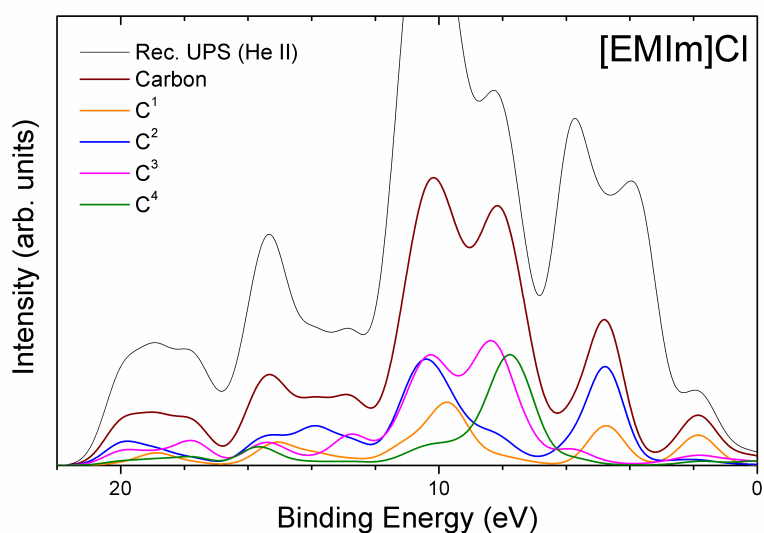


Figure 65: Deconvolution of the reconstructed UPS (He II) spectrum of [EMIm]Cl into the respective carbon positions within the imidazolium-based cation. The respective nomenclature of the different carbons is illustrated in Figure 9. Rescaling parameters of $f = 1.03040$, $\Delta E = -1.41 \text{ eV}$, and $\Delta\Delta E_{\text{Cation}-\text{Anion}} = -1.95 \text{ eV}$ are incorporated. The detailed spectra of the anion as well as the nitrogen and hydrogen contributions are not shown here.

to the nitrogens. This fact has supported the choice of this peak for a height normalization prior to the calculation of difference spectra using UPS (He II) in Figure 39. All four different carbon positions have contributed with their approximate stoichiometry at binding energies above 12 eV. While, an appropriate agreement with the experiment can not be achieved in this binding energy range caused by the obvious background due to inelastically scattered electrons, which are detected with a different binding energy than their elastically scattered/unscattered analogs.

(A.3) Influence of water onto the UPS (He II) valence band spectrum of [EMIm]Cl

The inclusion of water in an ionic liquid at room temperature is conceivable, since ionic liquids are present in a liquid or solid state at this temperature by definition [1]. The water might be either encapsulated in the solid material or is dissolved in the ionic liquid in its liquid state. [EMIm]Cl, which is investigated here, has offered a melting point of 41 °C [130] and most of the imidazolium-based ionic liquids are well known for their hygroscopic behavior [8]. Thus, a capture of water can be expected for these ionic liquids. A potential interaction between ionic liquid and water is established through hydrogen bondings between the anions and the water molecules, where potentially different clusters are formed (see ref. [56] and references therein).

A strong influence on the charge distribution and the arrangement of the ions at the surface was recognized in the presence of water [56, 172]: for low water concentrations of approximately 2,500 ppm a surface structure similar to the pure ionic liquid, i.e. on the one hand the cation with its longer alkyl chain protruding towards the vacuum and on the other chlorine is buried beneath the alkyl chains, is detected. At increased water concentrations of 6,000 to 10,000 ppm, the chlorine anion has occupied the outer surface in [HMIm]Cl, while the [HMIm] cation has changed its orientation with the longer alkyl chain pointing towards the bulk liquid. Beyond that, differences are recognized in the orientation of the imidazolium ring for hydrophobic and hydrophilic imidazolium-based ionic liquids at increased water contents.

The UPS (He II) spectrum for a system composed of one ion pair of [EMIm]Cl together with one water molecule is deconvoluted into the main constituents in Figure 66. Herein, the cation and anion contributions have not significantly var-

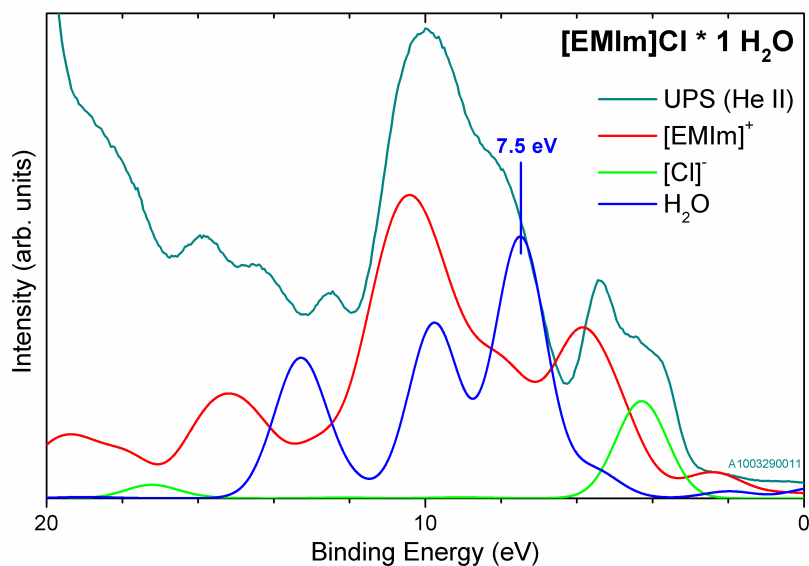


Figure 66: Reconstructed UPS (He II) spectra with a deconvolution into contributions of the different species (ions/water) from [EMIm]Cl with additional water in comparison to the experimental spectrum. The rescaling of the binding energies is performed with the aim to meet the position of the Cl3p peak with the parameters of $f = 1.03040$, $\Delta E = -1.25 \text{ eV}$, and $\Delta\Delta E_{\text{Cation}-\text{Anion}} = -1.95 \text{ eV}$, which were partially borrowed from the neat ionic liquid. A supplementary relative binding energy shift for the additional water molecule $\Delta\Delta E_{\text{AddSpecies}} = +1.20 \text{ eV}$ is incorporated to adapt the binding energy of the most intense water peak to a position of 7.5 eV referring to the approximate position in the experimental UPS (He I) spectra (cf. ref. [173]). The height ratios of the reconstructed spectra of the respective ions and water molecule are arbitrarily considered due to a lack of knowledge about the exact stoichiometry in the experiment. It has to be noted that the O1s state from XPS is the only, but not exclusive hint for the water content, since other impurities, such as SiO₂-based species found in one of the copper-containing ionic liquids, might contribute. The experimental spectrum is obtained from personal communication with Dr. M. Himmerlich.

ied in comparison to the neat ionic liquid. A difference between experimental and reconstructed UPS (He II) spectrum of the neat ionic liquid is recognized under the shoulder at the lower binding energy side of the highest peak with an approximate range from 6.5 to 9 eV. The water contribution, which is shifted to a binding energy of 7.5 eV according to the peak position in ref. [173], would fit to the missing contribution in the reconstructed UPS (He II) spectrum. However, these assignments have to be treated as first hints towards an analysis. A distinct statement about the stoichiometry between ionic liquid and water can not be provided by the UPS (He II) spectrum, since the different contributions are significantly intertwined and the spectra are additionally affected by a background from inelastically scattered electrons. The final ratio between water and ionic liquid has to be determined on the basis of the experimental XPS core level spectra. This would comprise in particular the O1s states, which might be overlaid by potential oxygen-containing contaminations (cf. Chapter 10). In addition, depletion or enrichment effects might occur for water in the near surface area as recognized for other species (cf. ref. [163]).

Additional information on the investigated ionic liquids and rescaling parameters

All ionic liquids investigated in the present thesis are listed with their full name, abbreviation, and stoichiometric composition in Table 15. The respective cation structures are displayed for imidazolium-based and pyrrolidinium-based ionic liquids in Figure 1 as well as for copper-containing ionic liquids in Figure 19 (left). While, the structure of the $[\text{Tf}_2\text{N}]$ anion is illustrated in Figure 29.

The rescaling parameters according to the stepwise procedure described in Chapter 3.3 are listed in Table 16. Herein, the values of the scaling factor f , the relative shift ΔE for the different radiation sources (XPS, UPS (He II), and UPS (He I)), the shift between cation and anion $\Delta\Delta E_{\text{Cation}-\text{Anion}}$ as well as the potential shifts of the additional species like evaporated or dissolved atoms $\Delta\Delta E_{\text{AddSpecies}}$ are itemized for the adaption of the reconstructed spectra onto the experimental ones. The origin of these rescaling parameters and their respective compensation potential are thoroughly discussed in Chapter 3.3.

Ionic liquid	Abbreviation	Stoichiometric composition
[1-ethyl-3-methyl-imidazolium] bis(trifluorosulfonyl)imide	[EMIm][Tf ₂ N]	[C ₆ N ₂ H ₁₁][N(SO ₂ CF ₃) ₂]
[1-octyl-3-methyl-imidazolium] bis(trifluorosulfonyl)imide	[OMIm][Tf ₂ N]	[C ₁₂ N ₂ H ₂₃][N(SO ₂ CF ₃) ₂]
[N-butyl-N-methyl-pyrrolidinium] bis(trifluorosulfonyl)imide	[BMP _{yr}][Tf ₂ N]	[NC ₉ H ₂₀][N(SO ₂ CF ₃) ₂]
[N-octyl-N-methyl-pyrrolidinium] bis(trifluorosulfonyl)imide [#]	[OMP _{yr}][Tf ₂ N]	[NC ₁₃ H ₂₈][N(SO ₂ CF ₃) ₂]
[N-octyl-N-methyl-pyrrolidinium] chloride [#]	[OMP _{yr}][Cl]	[NC ₁₃ H ₂₈][Cl]
[1-ethyl-3-methyl-imidazolium] chloride	[EMIm][Cl]	[C ₆ N ₂ H ₁₁][Cl]
[1-butyl-3-methyl-imidazolium] chloride	[BMIm][Cl]	[C ₈ N ₂ H ₁₅][Cl]
[1-hexyl-3-methyl-imidazolium] chloride	[HMIm][Cl]	[C ₁₀ N ₂ H ₁₉][Cl]
[1-octyl-3-methyl-imidazolium] chloride	[OMIm][Cl]	[C ₁₂ N ₂ H ₂₃][Cl]
[1-ethyl-3-methyl-imidazolium] chloride · water	[EMIm][Cl · H ₂ O]	[C ₆ N ₂ H ₁₁][Cl · H ₂ O]
[1-ethyl-3-methyl-imidazolium] [bis(trifluorosulfonyl)imide] copper	[EMIm] ₂ [Tf ₂ N] ₂ Cu ₂	[C ₆ N ₂ H ₁₁] ₂ [N(SO ₂ CF ₃) ₂] ₂ Cu ₂
[1-ethyl-3-methyl-imidazolium] [bis(trifluorosulfonyl)imide] potassium [§]	[EMIm] ₂ [Tf ₂ N] ₂ K ₂	[C ₆ N ₂ H ₁₁] ₂ [N(SO ₂ CF ₃) ₂] ₂ K ₂
[1-ethyl-3-methyl-imidazolium] [bis(trifluorosulfonyl)imide] lithium [§]	[EMIm] ₂ [Tf ₂ N] ₂ Li ₂	[C ₆ N ₂ H ₁₁] ₂ [N(SO ₂ CF ₃) ₂] ₂ Li ₂
[bis(1-hexyl-imidazole)cupronium] dichloridecuprate	[Cu(Im ⁶) ₂][CuCl ₂]	[Cu(C ₉ N ₂ H ₁₆) ₂][CuCl ₂]
[bis(1-hexyl-imidazole)cupronium] dibromidecuprate [#]	[Cu(Im ⁶) ₂][CuBr ₂]	[Cu(C ₉ N ₂ H ₁₆) ₂][CuBr ₂]
[tetra(1-hexyl-imidazole)cupronium] hexafluorophosphate	[Cu(Im ⁶) ₄][PF ₆]	[Cu(C ₉ N ₂ H ₁₆) ₄][PF ₆]

Table 15: Full name, abbreviation, and stoichiometric composition of the ionic liquids investigated in the present thesis. ([#]) The ionic liquids are studied for reason of comparison. ([§]) All of those ionic liquids are examined by the reconstruction method with the focus on a perspective analysis of the related experimental XPS and UPS spectra.

Ionic liquid	Scaling factor f	Absolute binding energy shift		Relative binding energy shift	
		ΔE_{XPS}	$\Delta E_{UPS(HeII)}$	$\Delta E_{UPS(HeI)}$	$\Delta\Delta E_{Cation-Anion}$
[EMIm][Tf ₂ N]	1.02838	-1.36 eV	-1.26 eV	-0.90 eV	-1.10 eV
[OMIm][Tf ₂ N]	1.02838	-1.39 eV	-1.29 eV	-	-1.10 eV
[BMPyr][Tf ₂ N]	1.02963	-0.79 eV	-0.77 eV	-	-1.47 eV
[OMPyr][Tf ₂ N] [§]	1.02936	-0.77 eV	-0.77 eV	-	-1.47 eV
[OMPyr][Cl] [§]	1.02936	-1.75 eV	-	-	-
[EMIm]Cl	1.03040	-1.41 eV	-1.41 eV	-	-1.95 eV
[BMIm]Cl	1.03040	-1.41 eV	-1.41 eV	-	-1.95 eV
[HMIm]Cl	1.03040	-1.41 eV	-1.41 eV	-	-1.95 eV
[OMIm]Cl	1.03040	-1.41 eV	-1.41 eV	-	-1.95 eV
[EMIm]Cl · H ₂ O	1.03040	-	-1.25 eV	-	-1.95 eV
[EMIm] ₂ [Tf ₂ N] ₂ Cu ₂	1.02830	-2.69 eV	-	-	-1.77 eV
[Cu(Im ⁶) ₂][CuCl ₂]	1.03045	-3.02 eV	-2.92 eV	-	-1.05 eV
[Cu(Im ⁶) ₂][CuBr ₂] [§]	1.03181	-3.29 eV	-2.99 eV	-	+0.24 eV
[Cu(Im ⁶) ₄][PF ₆]	1.02427	+0.25 eV	+0.10 eV	-	-0.60 eV

Table 16: Scaling factor f , absolute binding energy shift ΔE (in eV), and relative binding energy shift $\Delta\Delta E_{Cation-Anion}$ (in eV) between the contribution of the anion (fixed) and cation for XPS and UPS (He II) spectra of the ionic liquids investigated in the present thesis. A second relative shift for potential charge influenced species $\Delta\Delta E_{AddSpecies}$, which is incorporated for metal atoms like copper or water in an ionic liquid. ([§]) Ionic liquids, which are used for reason of comparison, are listed without a direct comparison due to partially unavailable experimental spectra and, thus, are arbitrarily adapted to the experiment. The binding energies of those ionic liquids are modified according to the scaling factor and the relative shift of their analogs, which are completely investigated.

Acknowledgements

First of all, I would like to thank my supervisor Priv.-Doz. Dr. Wichard J. D. Beenken for a multitude of fruitful discussions concerning spectra reconstructions for ionic liquids as well as during the preparation of this thesis. In addition, I would like to acknowledge him for providing me with the opportunity to widely work out my ideas independently. I would like to thank Univ.-Prof. Dr. Erich Runge for his multifaceted support over the course of the last years.

I acknowledge Univ.-Prof. Dr. Stefan Krischok, Dr. Angela Ulbrich, Assoc.-Prof. Dr. Tomonori Ikari, André Zühlsdorff, and Dr. Marcel Himmerlich for the very positive and successful interaction between experiment and theory. They have provided the measured spectra and the experimental details, whereon the developed reconstruction method is established and the rescaling procedure is executed. The cooperative interaction with researchers from the Universities in Clausthal, Erlangen-Nuremberg, Leipzig, Rostock, Gießen, and Chemnitz within the priority research program SPP1191 'Ionic Liquids' of the German Research Foundation (DFG) has to be appreciated at this point.

I am thankful to Andrea Guhl for her support in the finalization of this thesis. She has identified the typing and grammar mistakes, which are unpreventable, and suggested potential improvements. Furthermore, I give thanks to my father Hans Jürgen Reinmöller for proof-reading of the German version of the abstract.

I thank the members of the chairs 'Theoretical Physics I / II' for their help surrounding my research. Herein, I acknowledge especially Julia Preiß and Dr. David Leipold with their contributions to the software packages, which I have used for the reconstruction of XPS, UPS (He II), and UPS (He I) spectra on the basis of previous ion pair and cluster calculations. During this period, the 'coffee fellows', who are Claudia and Steve Lenk, Dr. Martin Körner, and Dr. Thomas Hänsel plus their families as well as a number of non-permanent members, have discussed many facets of physics and beyond like highlights in baby equipment. Moreover, I thank our secretary Dagmar Böhme for her helpful, always positive mood even in the context of partially nerve-wracking paperwork.

Beyond that, I am thankful for the support from outside the university, especially by my own little family. Furthermore, I would like to thank my parents and my grand parents for their motivation, the latter would be proud of this thesis.

References

- [1] P. Walden. Ueber die Molekulargrösse und elektrische Leitfähigkeit einiger geschmolzenen Salze. *Bulletin de l'Académie Impériale des Sciences de St.-Pétersbourg*, 8:405–422, 1914.
- [2] N. V. Plechkova and K. R. Seddon. Applications of ionic liquids in the chemical industry. *Chemical Society Reviews*, 37:123–150, 2008.
- [3] F. Endres and S. Z. El Abedin. Air and water stable ionic liquids in physical chemistry. *Physical Chemistry Chemical Physics*, 8:2101–2116, 2006.
- [4] H.-P. Steinrück and P. Wasserscheid. Ionic liquids in catalysis. *Catalysis Letters*, 145:380–397, 2015.
- [5] A. Stark. Ionic liquid structure-induced effects on organic reactions. *Topics in Current Chemistry*, 290:41–81, 2009.
- [6] J. D. Holbrey and K. R. Seddon. Ionic liquids. *Clean Products and Processes*, 1:223–226, 1999.
- [7] P. Wasserscheid and W. Keim. Ionic liquids - new "solutions" for transition metal catalysis. *Angewandte Chemie International Edition*, 39:3772–3789, 2000.
- [8] T. Welton. Room-temperature ionic liquids. Solvents for synthesis and catalysis. *Chemical Reviews*, 99:2071–2084, 1999.
- [9] T. Welton. Ionic liquids in catalysis. *Coordination Chemistry Reviews*, 248:2459–2477, 2004.
- [10] R. Hayes, G. G. Warr, and R. Atkin. Structure and nanostructure in ionic liquids. *Chemical Reviews*, 115:6357–6426, 2015.
- [11] H.-P. Steinrück. Surface science goes liquid ! *Surface Science*, 604:481–484, 2010.
- [12] C. S. Santos and S. Baldelli. Gas-liquid interface of room-temperature ionic liquids. *Chemical Society Reviews*, 39:2136–2145, 2010.
- [13] G. Andersson and C. Ridings. Ion scattering studies of molecular structure at liquid surfaces with applications in industrial and biological systems. *Chemical Reviews*, 114:8361–8387, 2014.
- [14] K. R. J. Lovelock, C. Kolbeck, T. Cremer, N. Paape, P. S. Schulz, P. Wasserscheid, F. Maier, and H.-P. Steinrück. Influence of different substituents on the surface composition of ionic liquids studied using ARXPS. *Journal of Physical Chemistry B*, 113:2854–2864, 2009.

- [15] C. Kolbeck, T. Cremer, K. R. J. Lovelock, N. Paape, P. S. Schulz, P. Wasserscheid, F. Maier, and H.-P. Steinrück. Influence of different anions on the surface composition of ionic liquids studied using ARXPS. *Journal of Physical Chemistry B*, 113:8682–8688, 2009.
- [16] E. F. Smith, F. J. M. Rutten, I. J. Villar-Garcia, D. Briggs, and P. Licence. Ionic liquids in vacuo: analysis of liquid surfaces using ultra-high-vacuum techniques. *Langmuir*, 22:9386–9392, 2006.
- [17] E. F. Smith, I. J. Villar-Garcia, D. Briggs, and P. Licence. Ionic liquids in vacuo; solution-phase X-ray photoelectron spectroscopy. *Chemical Communications*, :5633–5635, 2005.
- [18] O. Höfft, S. Bahr, M. Himmerlich, S. Krischok, J. A. Schaefer, and V. Kempter. Electronic structure of the surface of the ionic liquid [EMIM][Tf₂N] studied by metastable impact electron spectroscopy (MIES), UPS, and XPS. *Langmuir*, 22:7120–7123, 2006.
- [19] D. S. Silvester, T. L. Broder, L. Aldous, C. Hardacre, A. Crossley, and R. G. Compton. Using XPS to determine solute solubility in room temperature ionic liquids. *Analyst*, 132:196–198, 2007.
- [20] V. Lockett, R. Sedev, C. Bassell, and J. Ralston. Angle-resolved X-ray photoelectron spectroscopy of the surface of imidazolium ionic liquids. *Physical Chemistry Chemical Physics*, 10:1330–1335, 2008.
- [21] J. M. Gottfried, F. Maier, J. Rossa, D. Gerhard, P. S. Schulz, P. Wasserscheid, and H.-P. Steinrück. Surface studies on the ionic liquid 1-ethyl-3-methylimidazolium ethylsulfate using X-ray photoelectron spectroscopy (XPS). *Zeitschrift für Physikalische Chemie*, 220:1439–1453, 2006.
- [22] C. Kolbeck, M. Killian, F. Maier, N. Paape, P. Wasserscheid, and H.-P. Steinrück. Surface characterization of functionalized imidazolium-based ionic liquids. *Langmuir*, 24:9500–9507, 2008.
- [23] S. Krischok, M. Eremtchenko, M. Himmerlich, P. Lorenz, J. Uhlig, A. Neumann, R. Ötting, W. J. D. Beenken, O. Höfft, S. Bahr, V. Kempter, and J. A. Schaefer. Temperature-dependent electronic and vibrational structure of the 1-ethyl-3-methylimidazolium bis(trifluoromethylsulfonyl)amide room-temperature ionic liquid surface: a study with XPS, UPS, MIES, and HREELS. *Journal of Physical Chemistry B*, 111:4801–4806, 2007.
- [24] T. Cremer, M. Killian, J. M. Gottfried, N. Paape, P. Wasserscheid, F. Maier, and H.-P. Steinrück. Physical vapor deposition of [EMIM][Tf₂N]: a new approach to the modification of surface properties with ultrathin ionic liquid films. *ChemPhysChem*, 9:2185–2190, 2008.
- [25] S. Caporali, U. Bardi, and A. Lavacchi. X-ray photoelectron spectroscopy and low energy ion scattering studies on 1-butyl-3-methyl-imidazolium

- bis(trifluoromethane) sulfonimide. *Journal of Electron Spectroscopy and Related Phenomena*, 151:4–8, 2006.
- [26] N. Paape, W. Wei, A. Bösmann, C. Kolbeck, F. Maier, H.-P. Steinrück, P. Wasserscheid, and P. S. Schulz. Chloroalkylsulfonate ionic liquids by ring opening of sultones with organic chloride salts. *Chemical Communications*, :3867–3869, 2008.
- [27] K. R. J. Lovelock, I. J. Villar-Garcia, F. Maier, H.-P. Steinrück, and P. Licence. Photoelectron spectroscopy of ionic liquid-based interfaces. *Chemical Reviews*, 110:5158–5190, 2010.
- [28] T. Ikari, A. Keppler, M. Reinmöller, W. J. D. Beenken, S. Krischok, M. Marschewski, W. Maus-Friedrichs, O. Höfft, and F. Endres. Surface electronic structure of imidazolium-based ionic liquids studied by electron spectroscopy. *e-Journal of Surface Science and Nanotechnology*, 8: 241–245, 2010.
- [29] S. Krischok, R. Ötting, W. J. D. Beenken, M. Himmerlich, P. Lorenz, O. Höfft, S. Bahr, V. Kempter, and J. A. Schaefer. A comparative study on the electronic structure of the 1-ethyl-3-methylimidazolium bis(trifluoromethylsulfonyl)amide RT-ionic liquid by electron spectroscopy and first principles calculations. *Zeitschrift für Physikalische Chemie*, 220: 1407–1416, 2006.
- [30] T. Cremer, C. Kolbeck, K. R. J. Lovelock, N. Paape, R. Wölfel, P. S. Schulz, P. Wasserscheid, H. Weber, J. Thar, B. Kirchner, F. Maier, and H.-P. Steinrück. Towards a molecular understanding of cation-anion interactions - probing the electronic structure of imidazolium ionic liquids by NMR spectroscopy, X-ray photoelectron spectroscopy and theoretical calculations. *Chemistry - A European Journal*, 16:9018–9033, 2010.
- [31] V. Lockett, R. Sedev, S. Harmer, J. Ralston, M. Horne, and T. Rodopoulos. Orientation and mutual location of ions at the surface of ionic liquids. *Physical Chemistry Chemical Physics*, 12:13816–13827, 2010.
- [32] S. Men, B. B. Hurisso, K. R. J. Lovelock, and P. Licence. Does the influence of substituents impact upon the surface composition of pyrrolidinium-based ionic liquids? An angle resolved XPS study. *Physical Chemistry Chemical Physics*, 14:5229–5238, 2012.
- [33] A. Ulbrich, M. Reinmöller, W. J. D. Beenken, and S. Krischok. Surface electronic structure of [XMI]Cl probed by surface sensitive spectroscopy. *ChemPhysChem*, 13:1718–1724, 2012.
- [34] H.-P. Steinrück. Recent developments in the study of ionic liquid interfaces using X-ray photoelectron spectroscopy and potential future directions. *Physical Chemistry Chemical Physics*, 14:5010–5029, 2012.

- [35] I. J. Villar-Garcia, E. F. Smith, A. W. Taylor, F. Qiu, K. R. J. Lovelock, R. G. Jones, and P. Licence. Charging of ionic liquid surfaces under X-ray irradiation: the measurement of absolute binding energies by XPS. *Physical Chemistry Chemical Physics*, 13:2797–2808, 2011.
- [36] A. Ulbrich, M. Reinmöller, W. J. D. Beenken, and S. Krischok. Photoelectron spectroscopy on ionic liquid surfaces - theory and experiment. *Journal of Molecular Liquids*, 192:77–86, 2014.
- [37] S. Krischok, A. Ulbrich, T. Ikari, V. Kempter, M. Marschewski, and O. Höfft. Surface structure of [XMIIm]Tf₂N ultrathin ionic liquid films probed by metastable He atoms and photoelectron spectroscopies (XPS and UPS). *Nuclear Instruments and Methods in Physics Research B*, 340: 51–57, 2014.
- [38] T. Cremer, M. Stark, A. Deyko, H.-P. Steinrück, and F. Maier. Liquid/solid interface of ultrathin ionic liquid films: [C₁C₁Im][Tf₂N] and [C₈C₁Im][Tf₂N] on Au(111). *Langmuir*, 27:3662–3671, 2011.
- [39] T. Iwahashi, T. Nishi, H. Yamane, T. Miyamae, K. Kanai, K. Seki, D. Kim, and Y. Ouchi. Surface structural study on ionic liquids using metastable atom electron spectroscopy. *Journal of Physical Chemistry C*, 113:19237–19243, 2009.
- [40] T. Nishi, T. Iwahashi, H. Yamane, Y. Ouchi, K. Kanai, and K. Seki. Electronic structures of ionic liquids [C_nmim]⁺BF₄⁻ and [C_nmim]⁺PF₆⁻ studied by ultraviolet photoemission, inverse photoemission, and near-edge X-ray absorption fine structure spectroscopies. *Chemical Physics Letters*, 455:213–217, 2008.
- [41] D. Yoshimura, T. Yokoyama, T. Nishi, H. Ishii, R. Ozawa, H. Hamaguchi, and K. Seki. Electronic structure of ionic liquids at the surface studied by UV photoemission. *Journal of Electron Spectroscopy and Related Phenomena*, 144:319–322, 2005.
- [42] C. Aliaga and S. Baldelli. Sum frequency generation spectroscopy of dicyanamide based room-temperature ionic liquids. Orientation of the cation and the anion at the gas-liquid interface. *Journal of Physical Chemistry B*, 111:9733–9740, 2007.
- [43] C. Aliaga, G. A. Baker, and S. Baldelli. Sum frequency generation studies of ammonium and pyrrolidinium ionic liquids based on the bis-trifluoromethanesulfonimide anion. *Journal of Physical Chemistry B*, 112: 1676–1684, 2008.
- [44] S. Baldelli. Influence of water on the orientation of cations at the surface of a room-temperature ionic liquid: a sum frequency generation vibrational spectroscopic study. *Journal of Physical Chemistry B*, 107:6148–6152, 2003.

- [45] T. Iimori, T. Iwahashi, K. Kanai, J. Sung, D. Kim, H. Hamaguchi, and Y. Ouchi. Local structure at the air/liquid interface of room-temperature ionic liquids probed by infrared-visible sum frequency generation vibrational spectroscopy: 1-alkyl-3-methylimidazolium tetrafluoroborates. *Journal of Physical Chemistry B*, 111:4860–4866, 2007.
- [46] Y. Jeon, J. Sung, W. Bu, D. Vaknin, Y. Ouchi, and D. Kim. Interfacial restructuring of ionic liquids determined by sum-frequency generation spectroscopy and X-ray reflectivity. *Journal of Physical Chemistry C*, 112:19649–19654, 2008.
- [47] I. S. Martinez and S. Baldelli. On the arrangement of ions in imidazolium-based room temperature ionic liquids at the gas-liquid interface, using sum frequency generation, surface potential, and surface tension measurements. *Journal of Physical Chemistry C*, 114:11564–11575, 2010.
- [48] C. S. Santos and S. Baldelli. Gas-liquid interface of hydrophobic and hydrophilic room-temperature ionic liquids and benzene: sum frequency generation and surface tension studies. *Journal of Physical Chemistry C*, 112:11459–11467, 2008.
- [49] J. Bowers and M. C. Vergara-Gutierrez. Surface ordering of amphiphilic ionic liquids. *Langmuir*, 20:309–312, 2004.
- [50] E. Sloutskin, B. M. Ocko, L. Tamam, I. Kuzmenko, T. Gog, and M. Deutsch. Surface layering in ionic liquids: an X-ray reflectivity study. *Journal of the American Chemical Society*, 127:7796–7804, 2005.
- [51] Y. F. Yano and H. Yamada. Surface structure of a neat ionic liquid investigated by grazing-incidence X-ray diffraction. *Analytical Sciences*, 24:1269–1271, 2008.
- [52] T. J. Gannon, G. Law, P. R. Watson, A. J. Carmichael, and K. R. Seddon. First observation of molecular composition and orientation at the surface of a room-temperature ionic liquid. *Langmuir*, 15:8429–8434, 1999.
- [53] G. Law, L. M. Watson, A. J. Carmichael, and K. R. Seddon. Molecular composition and orientation at the surface of room-temperature ionic liquids: effect of molecular structure. *Physical Chemistry Chemical Physics*, 3:2879–2885, 2001.
- [54] M. Reichelt, T. Hammer, and H. Morgner. Influence of water on the surface structure of 1-hexyl-3-methylimidazolium chloride. *Surface Science*, 605:1402–1411, 2011.
- [55] C. Ridings, V. Lockett, and G. Andersson. Effect of the aliphatic chain length on electrical double layer formation at the liquid/vacuum interface in the $[C_n\text{mim}][\text{BF}_4]$ ionic liquid series. *Physical Chemistry Chemical Physics*, 13:17177–17184, 2011.

- [56] C. Ridings, V. Lockett, and G. Andersson. Significant changes of the charge distribution at the surface of an ionic liquid due to the presence of small amounts of water. *Physical Chemistry Chemical Physics*, 13: 21301–21307, 2011.
- [57] J. Günster, O. Höfft, S. Krischok, and R. Souda. A time-of-flight secondary ion mass spectroscopy study of 1-ethyl-3-methylimidazolium bis(trifluoromethylsulfonyl)imide RT-ionic liquid. *Surface Science*, 602: 3403–3407, 2008.
- [58] R. Souda. The glass-liquid transition of water on hydrophobic surfaces. *The Journal of Chemical Physics*, 129:124707, 2008.
- [59] R. Souda and J. Günster. Temperature-programed time-of-flight secondary ion mass spectrometry study of 1-butyl-3-methylimidazolium trifluoromethanesulfonate during glass-liquid transition, crystallization, melting, and solvation. *The Journal of Chemical Physics*, 129:094707, 2008.
- [60] R. Souda. Glass-liquid transition, crystallization, and melting of a room temperature ionic liquid: thin films of 1-ethyl-3-methylimidazolium bis[trifluoromethanesulfonyl]imide studied with TOF-SIMS. *Journal of Physical Chemistry B*, 112:15349–15354, 2008.
- [61] I. J. Villar-Garcia, S. Fearn, G. F. De Gregorio, N. L. Ismail, F. J. V. Gschwend, A. J. S. McIntosh, and K. R. J. Lovelock. The ionic liquid-vacuum outer atomic surface: a low-energy ion scattering study. *Chemical Science*, 5:4404–4418, 2014.
- [62] H. Hashimoto, A. Ohno, K. Nakajima, M. Suzuki, H. Tsuji, and K. Kimura. Surface characterization of imidazolium ionic liquids by high-resolution Rutherford backscattering spectroscopy and X-ray photoelectron spectroscopy. *Surface Science*, 604:464–469, 2010.
- [63] K. Nakajima, A. Ohno, H. Hashimoto, M. Suzuki, and K. Kimura. Observation of surface structure of 1-alkyl-3-methylimidazolium bis(trifluoromethanesulfonyl)imide using high-resolution Rutherford backscattering spectroscopy. *The Journal of Chemical Physics*, 133: 044702, 2010.
- [64] V. Halka, R. Tsekov, and W. Freyland. Peculiarity of the liquid/vapour interface of an ionic liquid: study of surface tension and viscoelasticity of liquid BMImPF₆ at various temperatures. *Physical Chemistry Chemical Physics*, 7:2038–2043, 2005.
- [65] M. Tariq, M. G. Freire, B. Saramago, J. A. P. Coutinho, J. N. Canoniga Lopes, and L. P. N. Rebelo. Surface tension of ionic liquids and ionic liquid solutions. *Chemical Society Reviews*, 41:829–868, 2012.

- [66] R. Atkin, S. Z. El Abedin, R. Hayes, L. H. S. Gasparotto, N. Borisenko, and F. Endres. AFM and STM studies on the surface interaction of [BMP]TFSA and [EMIM]TFSA ionic liquids with Au(111). *Journal of Physical Chemistry C*, 113:13266–13272, 2009.
- [67] F. Endres, N. Borisenko, S. Z. El Abedin, R. Hayes, and R. Atkin. The interface ionic liquid(s)/electrode(s): in situ STM and AFM measurements. *Faraday Discussions*, 154:221–233, 2012.
- [68] S. Bovio, A. Podestà, C. Lenardi, and P. Milani. Evidence of extended solidlike layering in [Bmim][NTf₂] ionic liquid thin films at room-temperature. *Journal of Physical Chemistry B*, 113:6600–6603, 2009.
- [69] R. Foulston, S. Gangopadhyay, C. Chiutu, P. Moriarty, and R. G. Jones. Mono- and multi-layer adsorption of an ionic liquid on Au(110). *Physical Chemistry Chemical Physics*, 14:6054–6066, 2012.
- [70] E. I. Izgorodina. Towards large-scale, fully ab initio calculations of ionic liquids. *Physical Chemistry Chemical Physics*, 13:4189–4207, 2011.
- [71] K. Fumino, S. Reimann, and R. Ludwig. Probing molecular interaction in ionic liquids by low frequency spectroscopy: Coulomb energy, hydrogen bonding and dispersion forces. *Physical Chemistry Chemical Physics*, 16:21903–21929, 2014.
- [72] K. Fumino, T. Peppel, M. Geppert-Rybczynska, D. H. Zaitsau, J. K. Lehmann, S. P. Verevkin, M. Köckerling, and R. Ludwig. The influence of hydrogen bonding on the physical properties of ionic liquids. *Physical Chemistry Chemical Physics*, 13:14064–14075, 2011.
- [73] R. M. Lynden-Bell, M. Del Pòpolo, T. G. A. Youngs, J. Kohanoff, C. G. Hanke, J. B. Harper, and C. C. Pinilla. Simulations of ionic liquids, solutions, and surfaces. *Accounts of Chemical Research*, 40:1138–1145, 2007.
- [74] S. Zahn, M. Brehm, M. Brüssel, O. Hollóczki, M. Kohagen, S. Lehmann, F. Malberg, A. S. Pensado, M. Schöppke, H. Weber, and B. Kirchner. Understanding ionic liquids from theoretical methods. *Journal of Molecular Liquids*, 192:71–76, 2014.
- [75] B. Qiao, C. Krekeler, R. Berger, L. Delle Site, and C. Holm. Effect of anions on static orientational correlations, hydrogen bonds, and dynamics in ionic liquids: a simulational study. *Journal of Physical Chemistry B*, 112:1743–1751, 2008.
- [76] W. Zhao, F. Leroy, B. Heggen, S. Zahn, B. Kirchner, S. Balasubramanian, and F. Müller-Plathe. Are there stable ion-pairs in room-temperature ionic liquids? Molecular dynamics simulations of 1-n-butyl-3-methylimidazolium hexafluorophosphate. *Journal of the American Chemical Society*, 131:15825–15833, 2009.

- [77] W. Zheng, A. Mohammed, L. G. Hines, D. Xiao, O. J. Martinez, R. A. Bartsch, S. L. Simon, O. Russina, A. Triolo, and E. L. Quitevis. Effect of cation symmetry on the morphology and physicochemical properties of imidazolium ionic liquids. *Journal of Physical Chemistry B*, 115:6572–6584, 2011.
- [78] S. S. Sarangi, S. G. Raju, and S. Balasubramanian. Molecular dynamics simulations of ionic liquid-vapour interfaces: effect of cation symmetry on structure at the interface. *Physical Chemistry Chemical Physics*, 13:2714–2722, 2011.
- [79] R. M. Lynden-Bell and M. Del Pópolo. Simulation of the surface structure of butylmethylimidazolium ionic liquids. *Physical Chemistry Chemical Physics*, 8:949–954, 2006.
- [80] A. S. Pensado, P. Malfreyt, and A. A. H. Pádua. Molecular dynamics simulations of the liquid surface of the ionic liquid 1-hexyl-3-methylimidazolium bis(trifluoromethanesulfonyl)amide: structure and surface tension. *Journal of Physical Chemistry B*, 113:14708–14718, 2009.
- [81] M. E. Perez-Blanco and E. J. Maginn. Molecular dynamics simulations of CO₂ at an ionic liquid interface: adsorption, ordering, and interfacial crossing. *Journal of Physical Chemistry B*, 114:11827–11837, 2010.
- [82] C. D. Wick, T.-M. Chang, and L. X. Dang. Molecular mechanism of CO₂ and SO₂ molecules binding to the air/liquid interface of 1-butyl-3-methylimidazolium tetrafluoroborate ionic liquid: a molecular dynamics study with polarizable potential models. *Journal of Physical Chemistry B*, 114:14965–14971, 2010.
- [83] T. Yan, S. Li, W. Jiang, X. Gao, B. Xiang, and G. A. Voth. Structure of the liquid-vacuum interface of room-temperature ionic liquids: a molecular dynamics study. *Journal of Physical Chemistry B*, 110:1800–1806, 2006.
- [84] G. Hantal, M. N. D. S. Cordeiro, and M. Jorge. What does an ionic liquid surface really look like? Unprecedented details from molecular simulations. *Physical Chemistry Chemical Physics*, 13:21230–21232, 2011.
- [85] X. Paredes, J. Fernández, A. A. H. Pádua, P. Malfreyt, F. Malberg, B. Kirchner, and A. S. Pensado. Bulk and liquid-vapor interface of pyrrolidinium-based ionic liquids: a molecular simulation study. *Journal of Physical Chemistry B*, 118:731–742, 2014.
- [86] C. Cadena, J. L. Anthony, J. K. Shah, T. I. Morrow, J. F. Brennecke, and E. J. Maginn. Why is CO₂ so soluble in imidazolium-based ionic liquids? *Journal of the American Chemical Society*, 126:5300–5308, 2004.
- [87] P. A. Hunt, B. Kirchner, and T. Welton. Characterising the electronic structure of ionic liquids: an examination of the 1-butyl-3-methylimidazolium chloride ion pair. *Chemistry - A European Journal*, 12:6762–6775, 2006.

- [88] T. Köddermann, C. Wertz, A. Heintz, and R. Ludwig. Ion-pair formation in the ionic liquid 1-ethyl-3-methylimidazolium bis(triflyl)imide as a function of temperature and concentration. *ChemPhysChem*, 7:1944–1949, 2006.
- [89] S. B. C. Lehmann, M. Roatsch, M. Schöppke, and B. Kirchner. On the physical origin of the cation-anion intermediate bond in ionic liquids Part I. Placing a (weak) hydrogen bond between two charges. *Physical Chemistry Chemical Physics*, 12:7473–7486, 2010.
- [90] M. Reinmöller, A. Ulbrich, T. Ikari, J. Preiß, O. Höfft, F. Endres, S. Krischok, and W. J. D. Beenken. Theoretical reconstruction and elementwise analysis of photoelectron spectra for imidazolium-based ionic liquids. *Physical Chemistry Chemical Physics*, 13:19526–19533, 2011.
- [91] K. Kanai, T. Nishi, T. Iwahashi, Y. Ouchi, K. Seki, Y. Harada, and S. Shin. Anomalous electronic structure of ionic liquids determined by soft X-ray emission spectroscopy: contributions from the cations and anions to the occupied electronic structure. *The Journal of Chemical Physics*, 129:224507, 2008.
- [92] K. Kanai, T. Nishi, T. Iwahashi, Y. Ouchi, K. Seki, Y. Harada, and S. Shin. Electronic structures of imidazolium-based ionic liquids. *Journal of Electron Spectroscopy and Related Phenomena*, 174:110–115, 2009.
- [93] E. I. Izgorodina, J. Rigby, and D. R. Mac Farlane. Large-scale ab initio calculations of archetypical ionic liquids. *Chemical Communications*, 48:1493–1495, 2012.
- [94] R. Ishimatsu, N. Nishi, and T. Kakiuchi. Interfacial ion pairing at the interface between water and a room-temperature ionic liquid, n-tetradecylisoquinolinium bis(pentafluoroethylsulfonyl)imide. *Langmuir*, 23:7608–7611, 2007.
- [95] R. Katoh, M. Hara, and S. Tsuzuki. Ion pair formation in [bmim]I ionic liquids. *Journal of Physical Chemistry B*, 112:15426–15430, 2008.
- [96] H. V. Spohr and G. N. Patey. Structural and dynamical properties of ionic liquids: the influence of charge location. *The Journal of Physical Chemistry*, 130:104506, 2009.
- [97] L. Sistik, M. Oncak, and P. Slavicek. Simulations of photoemission and equilibrium redox processes of ionic liquids: the role of ion pairing and long-range polarization. *Physical Chemistry Chemical Physics*, 13:11998–12007, 2011.
- [98] P. Hohenberg and W. Kohn. Inhomogeneous electron gas. *Physical Review*, 136:B864–B871, 1964.

- [99] A. D. Becke. Density-functional exchange-energy approximation with correct asymptotic behavior. *Physical Review A*, 38:3098–3100, 1988.
- [100] A. D. Becke. Density-functional thermochemistry. III. The role of exact exchange. *The Journal of Chemical Physics*, 98:5648–5652, 1993.
- [101] C. Lee, W. Yang, and R. G. Parr. Development of the Colle-Salvetti correlation-energy formula into a functional of the electron density. *Physical Review B*, 37:785–789, 1988.
- [102] B. Miehlich, A. Savin, H. Stoll, and H. Preuss. Results obtained with the correlation energy density functionals of Becke and Lee, Yang and Parr. *Chemical Physics Letters*, 157:200–206, 1989.
- [103] J. B. Foresman and Æ. Frisch. *Exploring chemistry with electronic structure methods*. 2nd edition. Gaussian Inc., Pittsburgh, PA, USA, 1996.
- [104] S. Grimme, W. Hujo, and B. Kirchner. Performance of dispersion-corrected density functional theory for the interactions in ionic liquids. *Physical Chemistry Chemical Physics*, 14:4875–4883, 2012.
- [105] D. Strasser, F. Goulay, M. S. Kelkar, E. J. Maginn, and S. R. Leone. Photoelectron spectrum of isolated ion-pairs in ionic liquid vapor. *Journal of Physical Chemistry A*, 111:3191–3195, 2007.
- [106] M. Vogel, F. Schmitt, J. Sauther, B. Baumann, A. Altenhof, S. Lach, and C. Ziegler. Photoionization cross-section weighted DFT simulations as promising tool for the investigation of the electronic structure of open shell metal-phthalocyanines. *Analytical and Bioanalytical Chemistry*, 400: 673–678, 2011.
- [107] S. Mähl, M. Neumann, B. Schneider, V. Schlett, and A. Baalman. Analysis of XPS valence band spectra of polymers using a density-functional theory based calculation of model oligomers. *Journal of Polymer Science Part A: Polymer Chemistry*, 37:95–103, 1999.
- [108] A. Ulbrich. *Oberflächenanalytische Untersuchungen der elektronischen und chemischen Eigenschaften Ionischer Flüssigkeiten sowie deren Wechselwirkung mit Kupferspezies*. PhD thesis, TU Ilmenau, 2014.
- [109] S. Tanuma, C. J. Powell, and D. R. Penn. Calculations of electron inelastic mean free paths. *Surface and Interface Analysis*, 21:165–176, 1993.
- [110] Y. Harada, S. Masuda, and H. Ozaki. Electron spectroscopy using metastable atoms as probes for solid surfaces. *Chemical Reviews*, 97: 1897–1952, 1997.
- [111] S.-W. Wang and G. Ertl. Theory of penning ionization of absorbed CO by metastable helium (2^1S , 2^3S) beams. *Surface Science*, 93:L75–L81, 1980.

- [112] W. Sesselmann, B. Woratschek, J. Küppers, G. Ertl, and H. Haberland. Interaction of metastable noble-gas atoms with transition-metal surfaces: resonance ionization and Auger neutralization. *Physical Review B*, 35: 1547–1559, 1987.
- [113] A. Einstein. Über einen die Erzeugung und Verwandlung des Lichtes betreffenden heuristischen Gesichtspunkt. *Annalen der Physik*, 322:132–148, 1905.
- [114] F. J. Himpsel. Angle-resolved measurements of the photoemission of electrons in the study of solids. *Advances in Physics*, 32:1–51, 1983.
- [115] P. Puschnig, E.-M. Reinisch, T. Ules, G. Koller, S. Soubatch, M. Ostler, L. Romaner, F. S. Tautz, C. Ambrosch-Draxl, and M. G. Ramsey. Orbital tomography: deconvoluting photoemission spectra of organic molecules. *Physical Review B*, 84:235427, 2011.
- [116] D. Briggs and M. P. Seah, editors. *Practicle surface analysis (Volume 1 - Auger and X-ray photoelectron spectroscopy)*. John Wiley & Sons Ltd., Chichester/New York/Brisbane/Toronto/Singapore, 1990.
- [117] U. Gelius. Recent progress in ESCA studies of gases. *Journal of Electron Spectroscopy and Related Phenomena*, 5:985–1057, 1974.
- [118] U. Gelius and K. Siegbahn. ESCA studies of molecular core and valence levels in the gas phase. *Faraday Discussions of the Chemical Society*, 54: 257–268, 1972.
- [119] J. J. Yeh and I. Lindau. Atomic subshell photoionization cross sections and asymmetry parameters: $1 \leq Z \leq 103$. *Atomic Data and Nuclear Data Tables*, 32:1–155, 1985.
- [120] I. M. Band, Y. I. Kharitonov, and M. B. Trzhaskovskaya. Photoionization cross sections and photoelectron angular distributions for X-ray line energies in the range 0.132–4.509 keV targets: $1 \leq Z \leq 100$. *Atomic Data and Nuclear Data Tables*, 23:443–505, 1979.
- [121] M. J. Frisch, G. W. Trucks, H. B. Schlegel, G. E. Scuseria, M. A. Robb, J. R. Cheeseman, G. Scalmani, V. Barone, B. Mennucci, G. A. Petersson, H. Nakatsuji, M. Caricato, X. Li, H. P. Hratchian, A. F. Izmaylov, J. Bloino, G. Zheng, J. L. Sonnenberg, M. Hada, M. Ehara, K. Toyota, R. Fukuda, J. Hasegawa, M. Ishida, T. Nakajima, Y. Honda, O. Kitao, H. Nakai, T. Vreven, J. A. Montgomery Jr., J. E. Peralta, F. Ogliaro, M. Bearpark, J. J. Heyd, E. Brothers, K. N. Kudin, V. N. Staroverov, R. Kobayashi, J. Normand, K. Raghavachari, A. Rendell, J. C. Burant, S. S. Iyengar, J. Tomasi, M. Cossi, N. Rega, M. J. Millam, M. Klene, J. E. Knox, J. B. Cross, V. Bakken, C. Adamo, J. Jaramillo, R. Gomperts, R. E. Stratmann, O. Yazyev, A. J. Austin, R. Cammi, C. Pomelli, J. W. Ochterski, R. L. Martin, K. Morokuma, V. G. Zakrzewski, G. A. Voth,

- P. Salvador, J. J. Dannenberg, S. Dapprich, A. D. Daniels, Ö. Farkas, J. B. Foresman, J. V. Ortiz, J. Cioslowski, and D. J. Fox. Gaussian 09, Revision D.01. *Gaussian, Inc., Wallingford, CT, USA*, 2009.
- [122] M. J. Frisch, G. W. Trucks, H. B. Schlegel, G. E. Scuseria, M. A. Robb, J. R. Cheeseman, J. A. Montgomery Jr., T. Vreven, K. N. Kudin, J. C. Burant, J. M. Millam, S. S. Iyengar, J. Tomasi, V. Barone, B. Men-
nucci, M. Cossi, G. Scalmani, N. Rega, G. A. Petersson, H. Nakatsuji, M. Hada, M. Ehara, K. Toyota, R. Fukuda, J. Hasegawa, M. Ishida, T. Nakajima, Y. Honda, O. Kitao, H. Nakai, M. Klene, X. Li, J. E. Knox, H. P. Hratchian, J. B. Cross, V. Bakken, C. Adamo, J. Jaramillo, R. Gom-
perts, R. E. Stratmann, O. Yazyev, A. J. Austin, R. Cammi, C. Pomelli, J. W. Ochterski, P. Y. Ayala, K. Morokuma, G. A. Voth, P. Salvador, J. J. Dannenberg, V. G. Zakrzewski, S. Dapprich, A. D. Daniels, M. C. Strain, O. Farkas, D. K. Malick, A. D. Rabuck, K. Raghavachari, J. B. Foresman, J. V. Ortiz, Q. Cui, A. G. Baboul, S. Clifford, J. Cioslowski, B. B. Ste-
fanov, G. Liu, A. Liashenko, P. Piskorz, I. Komaromi, R. L. Martin, D. J. Fox, T. Keith, M. A. Al-Laham, C. Y. Peng, A. Nanayakkara, M. Challa-
combe, P. M. W. Gill, B. Johnson, W. Chen, M. W. Wong, C. Gonzalez, and J. A. Pople. Gaussian 03, Revision C.02. *Gaussian, Inc., Wallingford, CT, USA*, 2003.
- [123] A. Szabo and N. S. Ostlund. *Modern quantum chemistry*. Dover Publica-
tions, Mineola, NY, USA, 1996.
- [124] F. Weinhold and C. R. Landis. Natural bond orbitals and extensions of
localized bonding concepts. *Chemistry Education: Research and Practice
in Europe*, 2:91–104, 2001.
- [125] A. Keppler, M. Himmerlich, T. Ikari, M. Marschewski, E. Pachomow,
O. Höfft, W. Maus-Friedrichs, F. Endres, and S. Krischok. Changes of
the near-surface chemical composition of the 1-ethyl-3-methylimidazolium
bis(trifluoromethylsulfonyl)imide room temperature ionic liquid under the
influence of irradiation. *Physical Chemistry Chemical Physics*, 13:1174–
1181, 2011.
- [126] M. Henzler and W. Göpel. *Oberflächenphysik des Festkörpers*. B. G.
Teubner, Stuttgart, Germany, 1991.
- [127] I. Dabo, A. Ferretti, G. Borghi, N. L. Nguyen, N. Poilvert, C.-H. Park,
M. Cococcioni, and N. Marzari. *Piecewise linearity and spectroscopic prop-
erties from Koopmans-compliant functionals*, chapter First-Principles Ap-
proaches to Spectroscopic Properties of Complex Materials / Topics in
Current Chemistry, pages 193–233. Springer, 2014.
- [128] M. Stricker, T. Linder, B. Oelkers, and J. Sundermeyer. Cu(I)/(II) based
catalytic ionic liquids, their metallo-laminate solid state structures and
catalytic activities in oxidative methanol carbonylation. *Green Chemistry*,
12:1589–1598, 2010.

- [129] I. J. B. Lin and C. S. Vasam. Metal-containing ionic liquids and ionic liquid crystals based on imidazolium moiety. *Journal of Organometallic Chemistry*, 690:3498–3512, 2005.
- [130] C. P. Fredlake, J. M. Crosthwaite, D. G. Hert, S. N. V. K. Aki, and J. F. Brennecke. Thermophysical properties of imidazolium-based ionic liquids. *Journal of Chemical Engineering Data*, 49:954–964, 2004.
- [131] H. Tokuda, K. Hayamizu, K. Ishii, M. Abu Bin Hasan Susan, and M. Watanabe. Physicochemical properties and structures of room temperature ionic liquids. 2. Variation of alkyl chain length in imidazolium cation. *Journal of Physical Chemistry B*, 109:6103–6110, 2005.
- [132] S. Zhang, N. Sun, X. He, X. Lu, and X. Zhang. Physical properties of ionic liquids: database and evaluation. *Journal of Physical and Chemical Reference Data*, 35:1475–1517, 2006.
- [133] R. Hagiwara and Y. Ito. Room temperature ionic liquids of alkylimidazolium cations and fluoroanions. *Journal of Fluorine Chemistry*, 105:221–227, 2000.
- [134] K. Fujii, T. Fujimori, T. Takamuku, R. Kanzaki, Y. Umebayashi, and S. Ishiguro. Conformational equilibrium of bis(trifluoromethanesulfonyl) imide anion of a room-temperature ionic liquid: Raman spectroscopic study and DFT calculations. *Journal of Physical Chemistry B*, 110:8179–8183, 2006.
- [135] E. Bodo, L. Gontrani, R. Caminiti, N. V. Plechkova, K. R. Seddon, and A. Triolo. Structural properties of 1-alkyl-3-methylimidazolium bis(trifluoromethyl)sulfonylamide ionic liquids: X-ray diffraction data and molecular dynamics simulations. *Journal of Physical Chemistry B*, 114:16398–16407, 2010.
- [136] S. Men, K. R. J. Lovelock, and P. Licence. X-ray photoelectron spectroscopy of pyrrolidinium-based ionic liquids: cation-anion interactions and a comparison to imidazolium-based analogues. *Physical Chemistry Chemical Physics*, 13:15244–15255, 2011.
- [137] O. Borodin and G. D. Smith. Structure and dynamics of n-methyl-n-propylpyrrolidinium bis(trifluoromethanesulfonyl)imide ionic liquid from molecular dynamics simulations. *Journal of Physical Chemistry B*, 110:11481–11490, 2006.
- [138] J. N. Canongia Lopes, K. Shimizu, A. A. H. Pádua, Y. Umebayashi, S. Fukuda, K. Fujii, and S. Ishiguro. A tale of two ions: the conformational landscapes of bis(trifluoromethanesulfonyl)amide and n,n-dialkylpyrrolidinium. *Journal of Physical Chemistry B*, 112:1465–1472, 2008.

- [139] Y. Umebayashi, T. Mitsugi, K. Fujii, K. Seki, K. Chiba, H. Yamamoto, J. N. Canongia Lopes, A. A. H. Pádua, M. Takeuchi, R. Kanzaki, and S. Ishiguro. Raman spectroscopic study, DFT calculations and MD simulations on the conformational isomerism of n-alkyl-n-methylpyrrolidinium bis-(trifluoromethanesulfonyl) amide ionic liquids. *Journal of Physical Chemistry B*, 113:4338–4346, 2009.
- [140] A. R. Santos, R. K. Blundell, and P. Licence. XPS of guanidinium ionic liquids: a comparison of charge distribution in nitrogenous cations. *Physical Chemistry Chemical Physics*, 17:11839–11847, 2015.
- [141] S. Men, K. R. J. Lovelock, and P. Licence. Directly probing the effect of the solvent on a catalyst electronic environment using X-ray photoelectron spectroscopy. *RSC Advances*, 5:35958–35965, 2015.
- [142] A. Romero, A. Santos, J. Tojo, and A. Rodríguez. Toxicity and biodegradability of imidazolium ionic liquids. *Journal of Hazardous Materials*, 151:268–273, 2008.
- [143] J. R. Harjani, J. Farrell, M. T. Garcia, R. D. Singer, and P. J. Scammells. Further investigation of the biodegradability of imidazolium ionic liquids. *Green Chemistry*, 11:821–829, 2009.
- [144] K. J. Baranyai, G. B. Deacon, D. R. MacFarlane, J. M. Pringle, and J. L. Scott. Thermal degradation of ionic liquids at elevated temperatures. *Australian Journal of Chemistry*, 57:145–147, 2004.
- [145] P. Stepnowski and A. Zaleska. Comparison of different advanced oxidation processes for the degradation of room temperature ionic liquids. *Journal of Photochemistry and Photobiology A: Chemistry*, 170:45–50, 2005.
- [146] E. M. Siedlecka and P. Stepnowski. The effect of alkyl chain length on the degradation of alkyimidazolium- and pyridinium-type ionic liquids in a fenton-like system. *Environmental Science and Pollution Research*, 16:453–458, 2009.
- [147] N. S. von Brisinski, O. Höfft, and F. Endres. Plasma electrochemistry in ionic liquids: from silver to silicon nanoparticles. *Journal of Molecular Liquids*, 192:59–66, 2014.
- [148] O. Höfft and F. Endres. Plasma electrochemistry in ionic liquids: an alternative route to generate nanoparticles. *Physical Chemistry Chemical Physics*, 13:13472–13478, 2011.
- [149] A. Guleria, A. K. Singh, S. Adhikari, and S. K. Sarkar. Radiation induced physicochemical changes in FAP (fluoro alkyl phosphate) based imidazolium ionic liquids and their mechanistic pathways: influence of hydroxyl group functionalization of the cation. *Dalton Transactions*, 43:609–625, 2014.

- [150] H. Weingärtner. Understanding ionic liquids at the molecular level: facts, problems, and controversies. *Angewandte Chemie International Edition*, 47:654–670, 2008.
- [151] F. R. McFeely, S. P. Kowalczyk, L. Ley, R. G. Cavell, R. A. Pollak, and D. A. Shirley. X-ray photoemission studies of diamond, graphite, and glassy carbon valence bands. *Physical Review B*, 9:5268–5278, 1974.
- [152] C. S. Fadley and D. A. Shirley. *Electronic density of states*, chapter Electronic density of states from X-ray photoelectron spectroscopy, pages 163–177. National Bureau of Standards, Special Publication 323, 1971.
- [153] S. Tougaard. Quantitative analysis of the inelastic background in surface electron spectroscopy. *Surface and Interface Analysis*, 11:453–472, 1988.
- [154] X. Li, Z. Zhang, and V. E. Henrich. Inelastic electron background function for ultraviolet photoelectron spectra. *Journal of Electron Spectroscopy and Related Phenomena*, 63:253–265, 1993.
- [155] C. Aliaga, C. S. Santos, and S. Baldelli. Surface chemistry of room-temperature ionic liquids. *Physical Chemistry Chemical Physics*, 9:3683–3700, 2007.
- [156] M. Bühl, A. Chaumont, R. Schurhammer, and G. Wipff. Ab initio molecular dynamics of liquid 1,3-dimethylimidazolium chloride. *Journal of Physical Chemistry B*, 109:18591–18599, 2005.
- [157] Y. Umebayashi, T. Fujimori, T. Sukizaki, M. Asada, K. Fujii, R. Kanzaki, and S. Ishiguro. Evidence of conformational equilibrium of 1-ethyl-3-methylimidazolium in its ionic liquid salts: Raman spectroscopic study and quantum chemical calculations. *Journal of Physical Chemistry A*, 109:8976–8982, 2005.
- [158] M. Armand, F. Endres, D. R. MacFarlane, H. Ohno, and B. Scrosati. Ionic-liquid materials for the electrochemical challenges of the future. *Nature Materials*, 8:621–629, 2009.
- [159] A. P. Abbott, K. El Ttaib, G. Frisch, K. J. McKenzie, and K. S. Ryder. Electrodeposition of copper composites from deep eutectic solvents based on chlorine chloride. *Physical Chemistry Chemical Physics*, 11:4269–4277, 2009.
- [160] T. Kurisaki, D. Tanaka, Y. Inoue, H. Wakita, B. Minofar, S. Fukuda, S. Ishiguro, and Y. Umebayashi. Surface analysis of ionic liquids with and without lithium salt using X-ray photoelectron spectroscopy. *Journal of Physical Chemistry B*, 116:10870–10875, 2012.
- [161] A. P. Abbott, G. Frisch, J. Hartley, and K. S. Ryder. Processing of metal and metal oxides using ionic liquids. *Green Chemistry*, 13:471–481, 2011.

- [162] M. Brettholle, O. Höfft, L. Klarhöfer, S. Mathes, W. Maus-Friedrichs, S. Z. El Abedin, S. Krischok, J. Janek, and F. Endres. Plasma electrochemistry in ionic liquids: deposition of copper nanoparticles. *Physical Chemistry Chemical Physics*, 12:1750–1755, 2010.
- [163] F. Maier, J. M. Gottfried, J. Rossa, D. Gerhard, P. S. Schulz, W. Schwieger, P. Wasserscheid, and H.-P. Steinrück. Surface enrichment and depletion effects of ions dissolved in ionic liquids: an X-ray photoelectron spectroscopy study. *Angewandte Chemie International Edition*, 45: 7778–7780, 2006.
- [164] D. R. MacFarlane, M. Forsyth, P. C. Howlett, J. M. Pringle, J. Sun, G. Annat, W. Neil, and E. I. Izgorodina. Ionic liquids in electrochemical devices and processes: managing interfacial electrochemistry. *Accounts in Chemical Research*, 40:1165–1173, 2007.
- [165] M. Olschewski, R. Gustus, M. Marschewski, O. Höfft, and F. Endres. Spectroscopic characterization of the interaction of lithium with thin films of the ionic liquid 1-octyl-3-methylimidazolium bis(trifluoromethylsulfonyl)amide. *Physical Chemistry Chemical Physics*, 16:25969–25977, 2014.
- [166] D.-Q. Yang, S. Poulin, E. Sacher, and C. Hyett. Interfacial reaction between evaporated copper and Dow Cyclotene 3022. *Applied Surface Science*, 165:116–126, 2000.
- [167] O. Borodin, G. D. Smith, and W. Henderson. Li⁺ cation environment, transport, and mechanical properties of the LiTFSI doped n-methyl-n-alkylpyrrolidinium⁺TFSI⁻ ionic liquids. *Journal of Physical Chemistry B*, 110:16879–16886, 2006.
- [168] F. Herman and S. Skillman. *Atomic structure calculations*. Prentice-Hall Publishing, Englewood Cliffs, NJ, USA, 1963.
- [169] H. Nohira and T. Hattori. SiO₂ valence band near the SiO₂/Si(111) interface. *Applied Surface Science*, 117/118:119–122, 1997.
- [170] M. L. O’Brien, C. Koitzsch, and R. J. Nemanich. Photoemission of the SiO₂-SiC heterointerface. *Journal of Vacuum Science & Technology B*, 18:1776–1784, 2000.
- [171] T. Haensel, M. Reinmöller, P. Lorenz, W. J. D. Beenken, S. Krischok, and S. I. U. Ahmed. Valence band spectra of cellulose and lignin studied by XPS and DFT. *Cellulose*, 19:1005–1011, 2012.
- [172] S. Rivera-Rubero and S. Baldelli. Influence of water on the surface of hydrophilic and hydrophobic room-temperature ionic liquids. *Journal of the American Chemical Society*, 126:11788–11789, 2004.

- [173] A. Borodin, O. Höfft, S. Krischok, and V. Kempter. Ionization and solvation of CsCl interacting with solid water. *Journal of Physical Chemistry B*, 107:9357–9362, 2003.

List of Figures

1	Three-dimensional representation of the composition of ionic liquids by choice of cation and anion with the opportunity of an adjustment of certain properties by variation of the length and functionality of the alkyl chains. All largely displayed cations or bold styled anions and respective cation alkyl chains are investigated in the present thesis. (Referring to the illustration in A. Stark, <i>Top. Curr. Chem.</i> 290 (2009) 41-81, page 44 [5]) . . .	9
2	Three hypothetical arrangements of ions at the ionic liquid surface (ionic liquid-vacuum interface): cations are closer to the surface (a), anions are closer to the surface (b) or a mixed arrangement of the ions (c). (Referring to the illustration in C. S. Santos and S. Baldelli, <i>Chem. Soc. Rev.</i> 39 (2010) 2136-2145, page 2137 [12])	11
3	Illustration of the idealized principle of photoelectron spectroscopy (one electron approximation) for a molecular system, like ionic liquids.	16
4	Experimental setup for the executed XPS, UPS, and MIES investigation with indication of the relevant geometrical parameters (angles γ and θ_e) for reconstruction and comparison to experimental spectra.	18
5	Schematic illustration of the steps within the Auger deexcitation (AD) process: initial state (left), energy transfer/exchange interaction (middle), and final state (right).	19
6	The density of states (DOS) calculated from a single ion pair of [EMIm]Tf ₂ N is related to the experimental XPS valence band spectrum (all spectra are taken from the illustration in M. Reinmüller et al., <i>Phys. Chem. Chem. Phys.</i> , 13 (2011) 19526-19533, page 19530 [90]). For comparison the reconstructed XPS spectrum is displayed, which is obtained according to the reconstruction method described in Chapter 2.4. DOS and reconstructed XPS valence band spectrum are normalized to the peak at approximately 11 eV. The binding energies of DOS and reconstructed XPS spectrum are modified according to the rescaling procedure described in Chapter 3.3 with the parameters $f = 1.02838$, $\Delta E = -1.36 \text{ eV}$, and $\Delta\Delta E_{\text{Cation}-\text{Anion}} = -1.10 \text{ eV}$. . .	20
7	A comparison of the reconstructed XPS core level and valence band spectrum of [EMIm]Tf ₂ N together with the experimental spectrum. Binding energies are rescaled according to Chapter 3.3 with the parameters $f = 1.02838$, $\Delta E = -1.36 \text{ eV}$, and $\Delta\Delta E_{\text{Cation}-\text{Anion}} = -1.10 \text{ eV}$. Slight deviations might be caused by the background in the experimental spectrum and potentially different broadening mechanisms for core levels and valence band. The experimental spectrum is obtained from personal communication with Dr. A. Ulbrich.	27

8	Illustration of the effects of the three steps of the rescaling procedure for the calculated binding energies of [EMIm]Tf ₂ N with introduction of a scaling factor $f = 1.02838$, an absolute shift $\Delta E = -1.36 \text{ eV}$, and a relative ion shift $\Delta\Delta E_{\text{Cation-Anion}} = -1.10 \text{ eV}$. The experimental and reconstructed spectra are taken from the illustration in M. Reinmöller et al., Phys. Chem. Chem. Phys., 13 (2011) 19526-19533, page 19530 [90].	32
9	The DOS of the C1s core level spectra for [EMIm]Tf ₂ N (left) and [OMIm]Tf ₂ N (right) obtained from the single ion pairs visualized in the top left. Signatures of different carbon positions C ¹ -C ⁿ (see inset) within the imidazolium-based cations are grouped together depicted by means of similar color. Rescaling of the calculated binding energies is performed with parameters of $f = 1.02838$, $\Delta E = -1.36 \text{ eV}$ for [EMIm]Tf ₂ N and $\Delta E = -1.39 \text{ eV}$ for [OMIm]Tf ₂ N, while here $\Delta\Delta E_{\text{Cation-Anion}} = 0 \text{ eV}$. (With the courtesy of: The Royal Society of Chemistry, M. Reinmöller et al., Phys. Chem. Chem. Phys., 13 (2011) 19526-19533, page 19527 [90])	39
10	Conformers of the [N-alkyl-N-methylpyrrolidinium] cation and [Tf ₂ N] anion. (With the courtesy of: The American Chemical Society, Y. Umebayashi et al., J. Phys. Chem. B, 113 (2009) 4338-4346, page 4339 [139])	43
11	Three-dimensional isosurfaces of the density of different elements in [PMPyrr]Tf ₂ N, which are also denoted as spatial distribution functions (SDF): nitrogen (isovalue: 4.0, color: red), fluorine (2.1, green), carbon from [Tf ₂ N] ⁻ (2, silver/yellow), and carbons of the neighboring pyrrolidinium-based cation (2.2, blue). (With the courtesy of: The American Chemical Society, O. Borodin and G. D. Smith, J. Phys. Chem. B, 110 (2006) 11481-11490, page 11486 [137])	44
12	Normalization of experimental C1s binding energies to those of [OMPyrr]Tf ₂ N (left) and C1s core level spectra from a set of pyrrolidinium-based ionic liquids [XMPyrr]Tf ₂ N with varied alkyl chain length (right). (With the courtesy of: The Royal Society of Chemistry, S. Men et al., Phys. Chem. Chem. Phys., 13 (2011) 15244-15255, page 15250 [136])	45
13	Nomenclature for the different carbon atoms in [BMPyrr]Tf ₂ N: C ¹ -C ⁷ in the [BMPyrr] cation (left) and C ^{Tf₂N} inside the [Tf ₂ N] anion (right), which is modified compared to the assignment in S. Men et al. [136].	45

14	Reconstructed C1s spectra (left) in comparison to the respective ion pair geometry (right). All utilized ion pairs have featured a twist conformer of the [BMPyrr] cation (see nomenclature in Figure 10) for sake of comparison. Herein, the calculated binding energies are utilized due to the reason that a rescaling procedure can only be executed for a particular ion pair, since the related parameters (f , ΔE , and $\Delta\Delta E_{Cation-Anion}$) might change and will be incomparable to those of ion pairs with significantly different geometry.	47
15	Reconstructed C1s core level spectra of different ion pairs from [BMPyrr]Tf ₂ N (visualized in Figure 16), which have featured a distinct double peak structure in the contributions of the cation. A deconvolution of the contributions of carbon atoms in different chemical environment within the [BMPyrr] cation is executed (for the respective nomenclature see Figure 13). Herein, the calculated binding energies are utilized due to the reason that a rescaling procedure can only be executed for a particular ion pair, since the related parameters (f , ΔE , and $\Delta\Delta E_{Cation-Anion}$) might slightly vary for the ion pairs investigated here.	49
16	Ion pairs from [BMPyrr]Tf ₂ N, which have featured a distinct double peak structure in their reconstructed C1s core level spectra (see Figure 15), are visualized by two different directions (side and top view, separated by a dotted line). The ion pairs in line A have offered a cis conformer of the [Tf ₂ N] anion, while those with a trans conformer are depicted in line B.	50
17	Reconstructed C1s core level spectra of [BMPyrr]Tf ₂ N and [OMPyrr]Tf ₂ N (carbon atoms in a conformable chemical environment are grouped together according to the inset). Herein, the binding energies are modified by the rescaling parameters $f = 1.02963$, $\Delta E = -0.79 eV$ for [BMPyrr]Tf ₂ N and $\Delta E = -0.77 eV$ for [OMPyrr]Tf ₂ N, respectively, and $\Delta\Delta E_{Cation-Anion} = -1.47 eV$ for both ionic liquids.	52
18	Crystal structure of [Cu(Im ¹²) ₂]CuBr ₂ with indication of the unit cell. (With the courtesy of: The Royal Society of Chemistry, M. Stricker et al., Green Chem. 12 (2010) 1589-1598, page 1591 [128])	60

19	Structure (left) and reconstructed N1s core levels together with the experimental spectrum (right) of the copper-containing ionic liquids $[\text{Cu}(\text{Im}^6)_2]\text{CuCl}_2$ (top) and $[\text{Cu}(\text{Im}^6)_4]\text{PF}_6$ (bottom). The reconstructed spectra are normalized to the peak N^{Im} and, thus, the related rescaling parameters of $f = 1.03045$, $\Delta E = -3.02 \text{ eV}$, and $\Delta\Delta E_{\text{Cation}-\text{Anion}} = -1.05 \text{ eV}$ for $[\text{Cu}(\text{Im}^6)_2]\text{CuCl}_2$ as well as $f = 1.02427$, $\Delta E = +0.25 \text{ eV}$, and $\Delta\Delta E_{\text{Cation}-\text{Anion}} = -0.60 \text{ eV}$ for $[\text{Cu}(\text{Im}^6)_4]\text{PF}_6$ are employed. The experimental spectra of $[\text{Cu}(\text{Im}^6)_2]\text{CuCl}_2$ and $[\text{Cu}(\text{Im}^6)_4]\text{PF}_6$ are obtained from personal communication with Dr. M. Himmerlich and Dr. A. Ulbrich, respectively.	62
20	Experimental core level spectra indicating the degradation of $[\text{EMIm}]\text{Tf}_2\text{N}$ by treatment of monochromated X-rays over time with comparison to the respective non-monochromated radiation. (With the courtesy of: The Royal Society of Chemistry, A. Kepler et al., Phys. Chem. Chem. Phys., 13 (2011) 1174-1181, page 1177 [125])	65
21	Reconstructed XPS core level spectra (N1s and C1s) for the degradation of the alkyl chain of the $[\text{EMIm}]$ cation in $[\text{EMIm}]\text{Tf}_2\text{N}$. The alkyl parts, which are removed, are indicated (left) and the calculated geometry of the residual fragment is depicted (right). For comparison the spectra and geometry of the reference ion pair are displayed (top line) and the initial peak positions of $[\text{EMIm}]\text{Tf}_2\text{N}$ are illustrated by guidance lines. All spectra are modified by the same rescaling parameters as used for $[\text{EMIm}]\text{Tf}_2\text{N}$ ($f = 1.02838$, $\Delta E = -1.36 \text{ eV}$, and $\Delta\Delta E_{\text{Cation}-\text{Anion}} = -1.10 \text{ eV}$).	68
22	Reconstructed XPS core level spectra (N1s and C1s) for the degradation of a single hydrogen atom of the $[\text{EMIm}]$ cation in $[\text{EMIm}]\text{Tf}_2\text{N}$. The hydrogen atom, which is removed, is indicated (left) and the calculated geometry of the residual fragment is depicted (right). For comparison the spectra and geometry of the reference ion pair are displayed (top line) and the initial peak positions of $[\text{EMIm}]\text{Tf}_2\text{N}$ are illustrated by guidance lines. All spectra are modified by the same rescaling parameters as used for $[\text{EMIm}]\text{Tf}_2\text{N}$ ($f = 1.02838$, $\Delta E = -1.36 \text{ eV}$, and $\Delta\Delta E_{\text{Cation}-\text{Anion}} = -1.10 \text{ eV}$).	70

23	Reconstructed XPS core level spectra (N1s and C1s) for the degradation of a single hydrogen atom of the [EMIm] cation in [EMIm]Tf ₂ N. The hydrogen atom, which is removed, is indicated (left) and the calculated geometry of the residual fragment is depicted (right). For comparison the spectra and geometry of the reference ion pair are displayed (top line) and the initial peak positions of [EMIm]Tf ₂ N are illustrated by guidance lines. All spectra are modified by the same rescaling parameters as used for [EMIm]Tf ₂ N ($f = 1.02838$, $\Delta E = -1.36 eV$, and $\Delta\Delta E_{Cation-Anion} = -1.10 eV$)	72
24	Reconstructed XPS core level spectra (N1s, C1s, and S2p) for the degradation of a single fluorine atom of the [Tf ₂ N] anion in [EMIm]Tf ₂ N. The fluorine atom, which is removed, is indicated (left) and the calculated geometry of the residual fragment is depicted (right). For comparison the spectra and geometry of the reference ion pair are displayed (top line) and the initial peak positions of [EMIm]Tf ₂ N are illustrated by guidance lines. All spectra are modified by the same rescaling parameters as used for [EMIm]Tf ₂ N ($f = 1.02838$, $\Delta E = -1.36 eV$, and $\Delta\Delta E_{Cation-Anion} = -1.10 eV$)	74
25	Reconstructed XPS core level spectra (N1s, C1s, and S2p) for the degradation of multiple fluorine atoms of the [Tf ₂ N] anion in [EMIm]Tf ₂ N. The fluorine atoms, which are removed, are indicated (left) and the calculated geometry of the residual fragment is depicted (right). For comparison the spectra and geometry of the reference ion pair are displayed (top line) and the initial peak positions of [EMIm]Tf ₂ N are illustrated by guidance lines. All spectra are modified by the same rescaling parameters as used for [EMIm]Tf ₂ N ($f = 1.02838$, $\Delta E = -1.36 eV$, and $\Delta\Delta E_{Cation-Anion} = -1.10 eV$)	76
26	Reconstructed XPS core level spectra (N1s, C1s, and S2p) for the degradation of the oxygen atoms of the [Tf ₂ N] anion in [EMIm]-Tf ₂ N. The oxygen atoms, which are removed, are indicated (left) and the calculated geometry of the residual fragment is depicted (right). For comparison the spectra and geometry of the reference ion pair are displayed (top line) and the initial peak positions of [EMIm]Tf ₂ N are illustrated by guidance lines. All spectra are modified by the same rescaling parameters as used for [EMIm]-Tf ₂ N ($f = 1.02838$, $\Delta E = -1.36 eV$, and $\Delta\Delta E_{Cation-Anion} = -1.10 eV$)	78

27	Reconstructed XPS core level spectra (N1s, C1s, and S2p) for the degradation of trifluoromethyl groups of the [Tf ₂ N] anion in [EMIm]Tf ₂ N. The CF ₃ groups, which are removed, are indicated (left) and the calculated geometry of the residual fragment is depicted (right). For comparison the spectra and geometry of the reference ion pair are displayed (top line) and the initial peak positions of [EMIm]Tf ₂ N are illustrated by guidance lines. All spectra are modified by the same rescaling parameters as used for [EMIm]Tf ₂ N ($f = 1.02838$, $\Delta E = -1.36 eV$, and $\Delta\Delta E_{Cation-Anion} = -1.10 eV$)	80
28	Reconstructed XPS core level spectra (N1s, C1s, and S2p) for the degradation of larger groups of the [Tf ₂ N] anion in [EMIm]Tf ₂ N. The groups, which are removed, are indicated (left) and the calculated geometry of the residual fragment is depicted (right). For comparison the spectra and geometry of the reference ion pair are displayed (top line) and the initial peak positions of [EMIm]Tf ₂ N are illustrated by guidance lines. All spectra are modified by the same rescaling parameters as used for [EMIm]Tf ₂ N ($f = 1.02838$, $\Delta E = -1.36 eV$, and $\Delta\Delta E_{Cation-Anion} = -1.10 eV$)	81
29	Nomenclature for the preferred carbon positions inside the imidazolium ring in [EMIm] ⁺ (left) with distinction of the C ² carbons into the one closer to the methyl group, denoted as C ^{2M} , and the other closer to the ethyl chain, denoted as C ^{2E} , as well as cis conformer (middle) and trans conformer (right) of the [Tf ₂ N] anion.	85
30	Three-dimensional spatial distribution function (SDF) for the anion around the [EMIm] cation obtained from molecular dynamics simulations of ionic liquids with the anions of [Cl] ⁻ (left), [BF ₄] ⁻ (middle), and [Tf ₂ N] ⁻ (right). Isovalues for the closest distances between the geometrical centers of the ions ($r = 0 - 0.54 nm$) are drawn as ten-times the average density (blue) and five-times the average density (red). While, areas with a larger distance between the centers of cation and anion ($r = 0.54 - 0.66 nm$) are indicated by densities of eight-times (green) and four-times the average density (yellow). The simulations were performed with a number of 288 ion pairs per calculation box and at temperatures of 450, 380, and 350 K, respectively. (With the courtesy of: The American Chemical Society, B. Qiao et al., J. Phys. Chem. B, 112 (2008) 1743-1751, page 1746 [75])	85
31	Different ion pair geometries of [EMIm]Tf ₂ N with the [Tf ₂ N] anion in vicinity of the C ¹ carbon (total energy and relative differences as well as the respective anion conformers and interaction sites are listed in Table 8).	86

32	Different ion pair geometries of [EMIm]Tf ₂ N with the [Tf ₂ N] anion in vicinity of the C ^{2M} and C ^{2E} carbons (total energy and relative differences as well as the respective anion conformers and interaction sites are listed in Table 9).	88
33	Reconstructed XPS and UPS (He II) valence band spectra from ion pairs of [EMIm]Tf ₂ N with the [Tf ₂ N] anion in C ¹ (a, c) and C ^{2M} /C ^{2E} position (b, d). A rescaling procedure is not applied for the binding energy scale of the reconstructed spectra due to potentially different values for the scaling factor f , absolute binding energy shift ΔE , and relative binding energy shift between both ions $\Delta\Delta E_{Cation-Anion}$	91
34	Reconstructed XPS valence band spectra (top) and UPS (He II) spectra (bottom) for visualization of the nearly uniform shifts in the binding energy positions for the three limiting cases of ion pair geometry (C ¹ position (A1), C ^{2M} position (F1), and an intermediate position, which does not belong to any of those groups of geometries depicted in Figure 31 and Figure 32).	92
35	Reconstructed XPS valence band spectra in the binding energy range between 20 and 28 eV with a decomposition of the spectra displayed in Figure 34 into the contained elements. Herein, the three limiting cases of ion pair geometry are illustrated: C ¹ position (A1, top), C ^{2M} position (F1, bottom), and an intermediate position, which does not belong to any of the groups of ion pair geometry depicted in Figure 31 and Figure 32.	94
36	Reconstructed XPS valence band spectra of [EMIm]Tf ₂ N (left) and [OMIm]Tf ₂ N (right) with a deconvolution into the ions in comparison to the experiment (top) and into the contained elements (bottom). The comparison with the calculated density of states (DOS), which is broadened by the peak width of the reconstructed spectra, is performed for both ionic liquids (top). All spectra are normalized in height to the most prominent peak at about 11 eV. The contributions of hydrogen are not displayed, since their photoionization cross section is marginal compared to those of the other elements. Herein, rescaling parameters of $f = 1.02838$, $\Delta E = -1.36 eV$ for [EMIm]Tf ₂ N and $\Delta E = -1.39 eV$ for [OMIm]Tf ₂ N as well as $\Delta\Delta E_{Cation-Anion} = -1.10 eV$ are applied. (With the courtesy of: The Royal Society of Chemistry, M. Reinmöller et al., Phys. Chem. Chem. Phys., 13 (2011) 19526-19533, page 19530 [90])	96

37	Reconstructed UPS (He II) spectra of [EMIm]Tf ₂ N (left) and [OMIm]Tf ₂ N (right) with a deconvolution into the ions in comparison to the experiment (top) and into the contained elements (bottom). All spectra are normalized in height to the most prominent peak at about 11 eV. The presence of the He II β -line is considered by means of a duplicate of the reconstructed He II α -line combined with a shift of -7.56 eV and a height of 4% of the initial α -line intensity in the reconstruction. Herein, rescaling parameters of $f = 1.02838$, $\Delta E = -1.26 eV$ for [EMIm]Tf ₂ N and $\Delta E = -1.29 eV$ for [OMIm]Tf ₂ N as well as $\Delta\Delta E_{Cation-Anion} = -1.10 eV$ are applied. (With the courtesy of: The Royal Society of Chemistry, M. Reinmöller et al., Phys. Chem. Chem. Phys., 13 (2011) 19526-19533, page 19531 [90])	99
38	Reconstructed UPS (He I) spectrum of [EMIm]Tf ₂ N in comparison to the experimental spectrum (left) and with a decomposition into the contributions of the ions (left) and the respective elements (right). The binding energies of the reconstructed spectra are modified by identical values of $f = 1.02838$ and $\Delta\Delta E_{Cation-Anion} = -1.10 eV$ applied for XPS and UPS (He II) as well as a different absolute shift of $\Delta E = -0.90 eV$. The intensity of the reconstructed spectra has considered the final state density by means of a multiplicative factor using the approximation $1/\rho_f \approx 1/\sqrt{E_{kin}} \approx 1/\sqrt{\hbar\omega - E_{bind}}$, since the approximation $\rho_f \approx \sqrt{E_{kin}}$ is valid for the experimental spectra (cf. ref. [152]). The experimental spectrum is obtained from personal communication with Dr. M. Himmerlich.	100
39	Difference spectra between [OMIm]Tf ₂ N and [EMIm]Tf ₂ N obtained from the normalized experimental UPS (He II) spectra (left) and MIES spectra (right) are compared to the reconstructed UPS (He II) spectra and partial density of states (pDOS) of selected parts of the ions. For UPS (He II) the experimental spectra are normalized onto the most prominent peak at about 11 eV of the respective reconstructed spectrum (left) and for MIES onto each other using the shoulder present at circa 12.5 eV (right). The binding energies of the depicted contributions of the additional alkyl chain (C ⁴ H ₂ -C ⁹ H ₂) and the fluorine atoms in [OMIm]Tf ₂ N are rescaled by the parameters of $f = 1.02838$, $\Delta E = -1.29 eV$, and $\Delta\Delta E_{Cation-Anion} = -1.10 eV$ for both methods. (With the courtesy of: The Royal Society of Chemistry, M. Reinmöller et al., Phys. Chem. Chem. Phys., 13 (2011) 19526-19533, page 19532 [90])	104
40	Calculated ion pairs from a series of [XMIIm]Cl (from left to right): [EMIm]Cl, [BMIIm]Cl, [HMIIm]Cl, and [OMIm]Cl.	108

41	Experimental XPS, UPS (He I), and UPS (He II) valence band spectra (left) and reconstructed XPS and UPS (He II) valence band spectra as well as the respective density of states (DOS) (right) of [XMIIm]Cl. All experimental and reconstructed spectra are normalized to the intensity at about 10 eV. The binding energies of the reconstructed spectra of XPS, UPS (He II), and the DOS are modified by a scaling factor of $f = 1.03040$, an identical absolute shift of $\Delta E = -1.41 \text{ eV}$, and an equivalent relative shift between the ions of $\Delta\Delta E_{\text{Cation-Anion}} = -1.95 \text{ eV}$. (With the courtesy of: Wiley-VCH, A. Ulbrich et al., ChemPhysChem, 13 (2012) 1718-1724, page 1721 [33]).	108
42	The partial density of states (pDOS) from the outer part of the alkyl chain (C^4H_3 or $\text{C}^4\text{H}_2\text{-C}^n\text{H}_3$) of [XMIIm]Cl ionic liquids. Herein, the binding energies are modified by the rescaling parameters of $f = 1.03040$, $\Delta E = -1.41 \text{ eV}$, and $\Delta\Delta E_{\text{Cation-Anion}} = -1.95 \text{ eV}$. (With the courtesy of: Wiley-VCH, A. Ulbrich et al., ChemPhysChem, 13 (2012) 1718-1724, page 1721 [33]).	110
43	Six different ion pair geometries for [EMIm]Cl (respective total energy and relative difference for the ion pairs are listed in Table 10).	112
44	Reconstructed XPS valence band spectra from six different ion pair geometries of [EMIm]Cl (displayed in Figure 43). The calculated binding energies of the Cl3s and Cl3p states are indicated for the reconstructed spectra. A rescaling procedure is not applied here.	114
45	Reconstructed UPS (He II) spectra from six different ion pair geometries of [EMIm]Cl (displayed in Figure 43). The calculated binding energies of the peaks and some related shoulders are indicated for the reconstructed spectra. A rescaling procedure is not applied here.	115
46	Side view (top) and top view (bottom) of two conformers of the [EMIm] cation with planar (left) and nonplanar geometry (right).	118
47	Ion pairs of [OMIm]Cl with artificially incorporated changes, i.e. kinks and/or torsions, in the longer alkyl chain (respective changes as well as total energy and relative difference are listed in Table 13).	119
48	Reconstructed UPS (He II) spectra of ion pairs of [OMIm]Cl with artificially incorporated kinks and torsions (displayed in Figure 47). A rescaling procedure is not applied here.	120

49	Reconstructed XPS valence band spectrum of [BMPyrr]Tf ₂ N together with the experimental spectrum (left) and for comparison only the reconstructed spectrum is shown for [OMPyrr]Tf ₂ N (right). Herein, the reconstructed spectrum is decomposed into the ions (top) and elements (bottom). The reconstructed spectrum of [BMPyrr]Tf ₂ N is normalized to the respective height of the experimental peak at approximately 12 eV. All reconstructed spectra for [BMPyrr]Tf ₂ N are modified by the rescaling parameters of $f = 1.02963$, $\Delta E = -0.79 \text{ eV}$, and $\Delta\Delta E_{\text{Cation-Anion}} = -1.47 \text{ eV}$ to fit the value of $N^{\text{Tf}_2\text{N}}$. The same values except of $\Delta E = -0.77 \text{ eV}$ (due to minor deviations) are used for [OMPyrr]Tf ₂ N, since for this ionic liquid no experimental spectra are available. For comparison to ionic liquids of the sets of [XMIm]Tf ₂ N and [XMIm]Cl, the rescaling parameters for ion pairs featuring an analogous geometry are almost identical within one set (cf. Table 16). The experimental spectrum is obtained from personal communication with Dr. M. Himmerlich.	123
50	Reconstructed UPS (He II) spectrum of [BMPyrr]Tf ₂ N together with the experimental spectrum (left) and for comparison only the reconstructed spectrum is shown for [OMPyrr]Tf ₂ N (right). Herein, the reconstructed spectrum is decomposed into the ions (top) and elements (bottom). The presence of the He II β -line is considered in the reconstructed spectra by means of a duplicate of the reconstructed He II α -line combined with a shift of -7.56 eV and a height of 4% of the initial α -line intensity. The spectrum of [BMPyrr]Tf ₂ N is normalized to height of the peak at approximately 11 eV. All reconstructed spectra for [BMPyrr]Tf ₂ N are modified by the rescaling parameters of $f = 1.02963$, $\Delta E = -0.99 \text{ eV}$, and $\Delta\Delta E_{\text{Cation-Anion}} = -1.47 \text{ eV}$ to fit the value of $N^{\text{Tf}_2\text{N}}$. The same values are used for [OMPyrr]Tf ₂ N, since for this ionic liquid no experimental spectra are available. For comparison to ionic liquids of the sets of [XMIm]Tf ₂ N and [XMIm]Cl, the rescaling parameters for ion pairs featuring an analogous geometry are almost identical within one set (cf. Table 16). The experimental spectrum is obtained from personal communication with Dr. M. Himmerlich.	126
51	Structure of the calculated charge- and spin-balanced cluster consisting of ionic liquid and copper in the stoichiometric composition of [EMIm] ₂ [Tf ₂ N] ₂ Cu ₂	132

52	Reconstructed XPS valence band spectra for copper evaporated onto [EMIm]Tf ₂ N with a deconvolution into the ions (top) and elements (bottom) from the calculated cluster displayed in Figure 51 in comparison to the experimental spectrum. The spectra are normalized to the height of the peak at approximately 10.5 eV. All binding energies of the reconstructed spectra are rescaled by $f = 1.02830$, $\Delta E = -2.69$ eV, and $\Delta\Delta E_{Cation-Anion} = -1.77$ eV, while for the copper contribution a second relative shift of $\Delta\Delta E_{AddSpecies} = -1.00$ eV is applied. The experimental spectrum is obtained from personal communication with Dr. A. Ulbrich.	133
53	Structure of the calculated charge- and spin-balanced cluster consisting of ionic liquid and lithium in the stoichiometric composition of [EMIm] ₂ [Tf ₂ N] ₂ Li ₂	134
54	Reconstructed UPS (He II) spectra (top) and XPS valence band spectra (bottom) for lithium evaporated onto [EMIm]Tf ₂ N in comparison to the respective pDOS (middle) with a deconvolution into the ions or elements. All contributions are achieved from the [EMIm] ₂ [Tf ₂ N] ₂ Li ₂ cluster displayed in Figure 53. A rescaling procedure is not applied due to the lack of experimental spectra.	135
55	Structure of the calculated charge- and spin-balanced cluster consisting of ionic liquid and potassium in the stoichiometric composition of [EMIm] ₂ [Tf ₂ N] ₂ K ₂	137
56	Reconstructed UPS (He II) spectrum (top) and XPS valence band spectrum (bottom) for potassium evaporated onto [EMIm]Tf ₂ N in comparison to the respective pDOS (middle) with a deconvolution into the contributions of the ions (left) and the elements (right). All contributions are achieved from the [EMIm] ₂ [Tf ₂ N] ₂ -K ₂ cluster displayed in Figure 55. A rescaling procedure is not applied due to the lack of experimental spectra.	138
57	Reconstructed XPS valence band spectra of [Cu(Im ⁶) ₂]CuCl ₂ with a deconvolution into ions (top) and elements (bottom). The spectra are normalized to the height of the peak at about 4 eV. All binding energies of reconstructed spectra are modified by $f = 1.03045$, $\Delta E = -3.02$ eV, and $\Delta\Delta E_{Cation-Anion} = -1.05$ eV. The experimental spectrum is obtained from personal communication with Dr. M. Himmerlich.	141
58	Reconstructed XPS valence band spectra of [Cu(Im ⁶) ₄]PF ₆ with a deconvolution into the ions (top) and elements (bottom). The spectra are normalized to the height of the peak at approximately 16.5 eV. All binding energies of reconstructed spectra are modified by $f = 1.02427$, $\Delta E = +0.25$ eV, and $\Delta\Delta E_{Cation-Anion} = -0.60$ eV. The experimental spectrum is obtained from personal communication with Dr. A. Ulbrich.	143

59	Reconstructed UPS (He II) spectra of $[\text{Cu}(\text{Im}^6)_2]\text{CuCl}_2$ with a deconvolution into the ions (top) and elements (bottom). The spectra are normalized to the height of the peak at approximately 9.5 eV. All binding energies of the reconstructed spectra are modified by $f = 1.03045$, $\Delta E = -2.92 \text{ eV}$, and $\Delta\Delta E_{\text{Cation}-\text{Anion}} = -1.05 \text{ eV}$. The experimental spectrum is obtained from personal communication with Dr. M. Himmerlich.	145
60	Reconstructed UPS (He II) spectra of $[\text{Cu}(\text{Im}^6)_4]\text{PF}_6$ with a deconvolution into the ions (top) and elements (bottom). The spectra are normalized to the height of the peak at approximately 9 eV. All binding energies of the reconstructed spectra are modified by $f = 1.02427$, $\Delta E = +0.10 \text{ eV}$, and $\Delta\Delta E_{\text{Cation}-\text{Anion}} = -0.60 \text{ eV}$. The experimental spectrum is obtained from personal communication with Dr. A. Ulbrich.	146
61	Reconstructed XPS valence band spectra of $[\text{Cu}(\text{Im}^6)_2]\text{CuCl}_2$ with a deconvolution into ions (top) and elements (bottom). For these reconstructions different photoionization cross sections from I. M. Band et al. [120] (left) and from J. J. Yeh and I. Lindau [119] (right, already displayed in Figure 57) are utilized. The spectra are normalized to the height of the peak at around 4 eV for both methods. All binding energies of the reconstructed spectra are modified by $f = 1.03045$, $\Delta E = -3.02 \text{ eV}$, and $\Delta\Delta E_{\text{Cation}-\text{Anion}} = -1.05 \text{ eV}$. The experimental spectrum is obtained from personal communication with Dr. M. Himmerlich.	148
62	XPS survey spectra of $[\text{Cu}(\text{Im}^6)_4]\text{PF}_6$ with an assignment of the peaks to the respective atomic orbitals. The experimental spectrum is obtained from personal communication with Dr. A. Ulbrich.	150
63	Effect of oxidation progression on the valence band spectra of Si(111) studied by XPS using Al K_α radiation. (With the courtesy of: Elsevier, H. Nohira and T. Hattori, Appl. Surf. Sci., 117/118 (1997) 119-122, page 120 [169])	150
64	Effect of oxidation on the valence band spectra of 4H n-type SiC (left) and 6H n-type SiC (right) studied by UPS (He I). Herein, the spectra of the $\sqrt{3} \times \sqrt{3}$ reconstructed SiC (a), SiC exposed to oxygen (b), after a 30 s oxygen plasma treatment (c), after a 1 min oxygen plasma treatment (d), and a 1.5 nm PECVD-generated layer of SiO_2 (e) are displayed. (With the courtesy of: The American Vacuum Society, M. L. O'Brien et al., J. Vac. Sci. Technol. B, 18 (2000) 1776-1784, page 1781/1782 [170])	152
65	Deconvolution of the reconstructed UPS (He II) spectrum of $[\text{EMIm}]\text{Cl}$ into the respective carbon positions within the imidazolium-based cation. The respective nomenclature of the different carbons is illustrated in Figure 9. Rescaling parameters of $f = 1.03040$, $\Delta E = -1.41 \text{ eV}$, and $\Delta\Delta E_{\text{Cation}-\text{Anion}} = -1.95 \text{ eV}$ are incorporated. The detailed spectra of the anion as well as the nitrogen and hydrogen contributions are not shown here.	159

66 Reconstructed UPS (He II) spectra with a deconvolution into contributions of the different species (ions/water) from [EMIm]Cl with additional water in comparison to the experimental spectrum. The rescaling of the binding energies is performed with the aim to meet the position of the Cl3p peak with the parameters of $f = 1.03040$, $\Delta E = -1.25 \text{ eV}$, and $\Delta\Delta E_{\text{Cation-Anion}} = -1.95 \text{ eV}$, which were partially borrowed from the neat ionic liquid. A supplementary relative binding energy shift for the additional water molecule $\Delta\Delta E_{\text{AddSpecies}} = +1.20 \text{ eV}$ is incorporated to adapt the binding energy of the most intense water peak to a position of 7.5 eV referring to the approximate position in the experimental UPS (He I) spectra (cf. ref. [173]). The height ratios of the reconstructed spectra of the respective ions and water molecule are arbitrarily considered due to a lack of knowledge about the exact stoichiometry in the experiment. It has to be noted that the O1s state from XPS is the only, but not exclusive hint for the water content, since other impurities, such as SiO₂-based species found in one of the copper-containing ionic liquids, might contribute. The experimental spectrum is obtained from personal communication with Dr. M. Himmerlich. 161

List of Tables

1	Asymmetry-corrected photoionization cross sections (in barn) are calculated by use of the parameters from J. J. Yeh and I. Lindau [119] for atomic orbitals of all elements, which are incorporated in ionic liquids investigated in the present thesis. The photoionization cross sections are tabulated for three radiation sources: XPS Al K_{α} ($\hbar\omega=1486.7$ eV, $\gamma=80^{\circ}$), UPS (He II) ($\hbar\omega=40.8$ eV, $\gamma=42.5^{\circ}$), and UPS (He I) ($\hbar\omega=21.2$ eV, $\gamma=42.5^{\circ}$).	25
2	Asymmetry-corrected photoionization cross sections (in barn) are calculated by use of the parameters from I. M. Band et al. [120] for atomic orbitals of selected elements of ionic liquids. These are listed for XPS using Al K_{α} radiation ($\hbar\omega=1486.7$ eV, $\gamma=80^{\circ}$). . .	26
3	Rescaled binding energies for the N1s and C1s core levels obtained from ion pairs of [EMIm]Tf ₂ N and [OMIm]Tf ₂ N (displayed in Figure 9) together with those of the single cation [OMIm] ⁺ in comparison to the experimental values. The nomenclature for all positions within the imidazolium-based cations is depicted in Figure 9 (top right). (^{&}) A normalization of the binding energies from [EMIm]Tf ₂ N and [OMIm]Tf ₂ N onto the experimental N ^{Tf₂N} core level is performed by a scaling factor of $f = 1.02838$ and respective absolute shifts of $\Delta E = -1.36$ eV for [EMIm]Tf ₂ N and $\Delta E = -1.39$ eV for [OMIm]Tf ₂ N. A relative shift is not incorporated at this stage ($\Delta\Delta E_{Cation-Anion} = 0$ eV). ([#]) The normalization of the binding energies for the isolated cation of [OMIm] ⁺ is achieved by the identical scaling factor and a shift of $\Delta E = -4.90$ eV. (With the courtesy of: The Royal Society of Chemistry, M. Reinmöller et al., Phys. Chem. Chem. Phys., 13 (2011) 19526-19533, page 19529 [90])	41
4	Rescaled binding energies of the different carbon atoms in the reconstructed core level spectra of [BMPyrr]Tf ₂ N and [OMPyr]Tf ₂ N in Figure 17 with a partial comparison to the experimental data. For the positions within the pyrrolidinium cations see inset in Figure 17. ([#]) The value of N ^{Tf₂N} in [BMPyrr]Tf ₂ N is utilized as reference for the rescaling procedure. Herein, the binding energies are adapted by the following rescaling parameters: a scaling factor of $f = 1.02963$, an absolute shift of $\Delta E = -0.79$ eV for [BMPyrr]Tf ₂ N and $\Delta E = -0.77$ eV for [OMPyr]Tf ₂ N, and a relative shift of $\Delta\Delta E_{Cation-Anion} = -1.47$ eV. The binding energies of the neat pyrrolidinium-based cations are obtained by an identical scaling factor as used for [BMPyrr]Tf ₂ N and they are finally shifted by $\Delta E = -5.66$ eV for [BMPyrr] ⁺ and $\Delta E = -5.61$ eV for [OMPyr] ⁺ to match the value of N ^{Pyrr} of the ion pair.	53

5	NBO partial charges (in e) for different carbons of the [OMPyr]-Tf ₂ N ion pair and the isolated cation [OMPyr] ⁺ . For respective nomenclature of carbon atoms see inset in Figure 17.	56
6	The geometrical distances (in Å) between the atoms within the [BMPyr] cation and selected atoms of the [Tf ₂ N] anion, which are tabulated for the utilized ion pair from [BMPyr]Tf ₂ N (for the affiliation of the carbon atoms see inset in Figure 17).	57
7	The binding energies (in eV) of the carbon atoms of the [OMPyr] cation, which have shaped a similar ion pair together with an anion of [Tf ₂ N] ⁻ or [Cl] ⁻ , are related to the respective geometrical distances (in Å) to the anion. (#) All reconstructed spectra are normalized onto the binding energy value of N ^{Pyr} for [BMPyr]Tf ₂ N in Table 4. Herein, an identical scaling factor of $f = 1.02963$ and for the pyrrolidinium-based cation in [OMPyr]-Tf ₂ N an absolute of $\Delta E = -0.77 eV$ as well as a relative shift of $\Delta\Delta E_{Cation-Anion} = -1.47 eV$ are employed. In contrast to this, the contributions of [OMPyr]Cl are modified by an overall shift $\Delta E = -1.75 eV$	59
8	Total energy and relative difference (in eV) of different ion pair geometries of [EMIm]Tf ₂ N featuring a position in vicinity of the central carbon atom (C ¹ position). The respective conformer of the [Tf ₂ N] anion is indicated as cis, trans or intermediate (i.e. in between the other two distinct cases). (#) An optimization of the ion pairs A1-D4 was performed by means of the Gaussian03 program package [122] and the respective energy difference is estimated related to the ion pair geometry B4 in Figure 31. (§) For all ion pairs E1-E4 the optimization was executed by the Gaussian09 program package [121] and, thus, the energy difference is accomplished according to the ion pair E4 in Figure 31.	87
9	Total energy and relative difference (in eV) of different ion pair geometries of [EMIm]Tf ₂ N featuring a position in vicinity of the carbon atoms at the imidazolium rings' bottom (C ^{2M} and C ^{2E} position). The respective conformer of the [Tf ₂ N] anion is indicated as cis or trans, while an intermediate shape (i.e. in between the other two distinct cases) is not observed here. Optimization of the ion pairs was performed by means of the Gaussian09 program package [121]. The energy difference is calculated relative to the favored geometry of E4 (Figure 31) and Table 8. (&) A further interaction is established in particular between the [Tf ₂ N] anion and hydrogens of the ethyl chain rather than the methyl group.	89
10	Total energy and relative difference (in eV) of the calculated ion pairs of [EMIm]Cl displayed in Figure 43 in dependence of the respective geometry.	112

11	The calculated binding energy positions of the first state related to the [EMIm] cation (at lowest binding energy) and of the Cl3p orbital in the reconstructed UPS (He II) spectra of various ion pair geometries of [EMIm]Cl displayed in Figure 43 as well as the resulting difference between these contributions.	116
12	The total energy and relative difference (in eV) from the planar and nonplanar conformers of the [EMIm] cation displayed in Figure 46.	118
13	Total energy and relative difference (in eV) of ion pairs of [OMIm]-Cl displayed in Figure 47 with artificially incorporated kinks (K) and/or torsions (T) in the longer alkyl chain. (#) The ion pairs of B1 and B3 have featured the same total energy due to symmetry reasons, since their octyl chain is rotated around the C-N bond.	118
14	Energetic separation between Cl3s and Cl3p states (in eV) in the reconstructed XPS valence band spectra of [OMIm]Cl in their 'as calculated' state, which are exemplarily listed for different functionals (with the 6-31G** basis set) and priorily more extensive basis sets (with the B3-LYP functional) in comparison to the experimental data. (#) The basis set 6-31G** together with the functional B3-LYP are utilized for spectra reconstruction in the present thesis. A nomenclature of 'n.a.' has corresponded to an inability for the determination of the separation between Cl3s and Cl3p states in the valence band due to a missing Cl3p contribution.	158
15	Full name, abbreviation, and stoichiometric composition of the ionic liquids investigated in the present thesis. (#) The ionic liquids are studied for reason of comparison. (§) All of those ionic liquids are examined by the reconstruction method with the focus on a perspective analysis of the related experimental XPS and UPS spectra.	163
16	Scaling factor f , absolute binding energy shift ΔE (in eV), and relative binding energy shift $\Delta\Delta E_{\text{Cation-Anion}}$ (in eV) between the contribution of the anion (fixed) and cation for XPS and UPS (He II) spectra of the ionic liquids investigated in the present thesis. A second relative shift for potential charge influenced species $\Delta\Delta E_{\text{AddSpecies}}$, which is incorporated for metal atoms like copper or water in an ionic liquid. (§) Ionic liquids, which are used for reason of comparison, are listed without a direct comparison due to partially unavailable experimental spectra and, thus, are arbitrarily adapted to the experiment. The binding energies of those ionic liquids are modified according to the scaling factor and the relative shift of their analogs, which are completely investigated.	164